5-14-2018

Endorectal Digital Prostate Tomosynthesis

Joseph Robert Steiner
Louisiana State University and Agricultural and Mechanical College, joseph.r.steiner@gmail.com

Recommended Citation

Steiner, Joseph Robert, "Endorectal Digital Prostate Tomosynthesis" (2018). *LSU Doctoral Dissertations*. 4582.
https://digitalcommons.lsu.edu/gradschool_dissertations/4582

ENDORECTAL DIGITAL PROSTATE TOMOSYNTHESIS

A Dissertation

Submitted to the Graduate Faculty of the
Louisiana State University and
Agricultural and Mechanical College
in partial fulfillment of the
requirements for the degree of
Doctor in Philosophy

in

The Department of Physics and Astronomy

by
Joseph Robert Steiner
B.S., Buffalo State College, 2010
August 2018

Acknowledgment

I acknowledge and thank my supervisory committee members, Drs. Guang Jia, Kenneth Matthews II, Jonas Fontenot, and J. Gregory Stacy. I thank Dr. Jia for his support for and excitement about this work, Dr. Matthews for his invaluable expertise, guidance, and particularly his help in editing this dissertation, Dr. Fontenot for ensuring my project goals were always clear, and Dr. Stacy for ensuring I always maintained a clear and reasonable timeline and set of milestones. I thank the staff of the Louisiana State University Physics and Astronomy Department, the Mary Bird Perkins Cancer Center, Pennington Biomedical Research Center, and XDR Radiology for providing the equipment, facilities, resources, and/or instruction required to complete this investigation. I thank Dr. Fontenot and Dan Neck at Mary Bird Perkins Cancer Center for use of their CT scanner, LINAC, and TLD reader, Dr. Owen Carmichael, Blanca Desharnais, and Kevin McKlveen at Pennington Biomedical Research Center for use of their radiography unit and MRI scanner, and Dr. Doug Yoon and Joel Karafin at XDR Radiology for their loan of an intraoral dental sensor and software for preliminary testing. I am grateful for my classmates and peers, with whom I had many enlightening and passionate discussions regarding this project. I thank Krystal Kirby, Desmond Fernandez, Addie Barron, John Doiron, Justin Sick, and Elizabeth Hilliard for their help in using equipment that I was unfamiliar with. Finally, and most importantly, I thank my wife Alicia for her unconditional understanding and encouragement.

This research was funded in part through a Leveraging Innovation for Technology Transfer (LIFT^2) grant #LSU-2018-LIFT-005 from Louisiana State University.

Table of Contents

List of Tables

List of Figures

Abbreviations and Acronyms

ANOVA – analysis of variance

ASF – artifact spread function

Ax. – axial

BG - background

BP – backprojection

BPH – benign prostate hyperplasia

BT – brachytherapy

CEUS – contrast enhanced ultrasound

Cor. – coronal

CT – computed tomography

DBT – digital breast tomosynthesis

DCE-MRI – dynamic contrast enhanced MRI

DRE – digital rectal exam

endoDPT – endorectal digital prostate tomosynthesis

ESD – entrance skin dose

ESF – edge spread function

FBP – filtered backprojection

FoV – field of view

HU – Hounsfield unit

ID – inner diameter

Inc. – spatial step size

LDRBT – low dose rate brachytherapy

LINAC – linear accelerator

LSF – line spread function

MR – magnetic resonance

MRI – magnetic resonance imaging

MTF – modulation transfer function

MU – monitor units

NEQ – noise equivalent quanta

NPS – noise power spectrum

OAR – organs at risk

OD – outer diameter

OID – object-to-image plane distance

OOP – out-of-plane

ROI – region of interest

PCa – prostate cancer

pCT – perfusion computed tomography

PET – positron emission tomography

PI-RADS – prostate imaging reporting and data system

PPAT – periprostatic adipose tissue

PSA – prostate specific antigen

SAA – shift and add

SID – source-to-image plane distance

SPECT – single photon computed tomography

T1W – T1 weighted

T2W – T2 weighted

TE – echo time

TL – thermoluminescence

TLD – thermoluminescent dosimeter

TR – repetition time

TRUS – transrectal ultrasound

Abstract

Several areas of prostate cancer (PCa) management, such as imaging permanent brachytherapy implants or small, aggressive lesions, benefit from high image resolution. Current PCa imaging methods can have inadequate resolution for imaging these areas. Endorectal digital prostate tomosynthesis (endoDPT), an imaging method that combines an external x-ray source and an endorectal x-ray sensor, can produce three-dimensional images of the prostate region that have high image resolution compared to typical methods. This high resolution may improve PCa management and increase positive outcomes in affected men.

This dissertation presents the initial development of endoDPT, including system design, image quality assessment, and examples of possible applications to prostate imaging. Experiments using computational phantoms, physical phantoms, and canine prostate specimens were conducted.

Initial system design was performed computationally and three methods of endoDPT image reconstruction were developed: shift and add (SAA), backprojection (BP), and filtered BP (FBP). A physical system was developed using an XDR intraoral x-ray sensor and a GE radiography unit. The resolution and radiation dose of endoDPT were measured and compared to a GE CT scanner. Canine prostate specimens that approximated clinical cases of PCa management were imaged and compared using endoDPT, the above CT scanner, and a GE MRI scanner.

This study found that the resolution of endoDPT was significantly higher than CT. The radiation dose of endoDPT was significantly lower than CT in the regions of the phantom that were not in the endoDPT field of view (FoV). Inside the endoDPT FoV, the radiation dose ranged from significantly less than to significantly greater than CT. The endoDPT images of the canine prostate specimens demonstrated qualitative improvements in resolution compared to CT and MRI, but endoDPT had difficulty in visualizing larger structures, such as the prostate border.

Overall, this study has demonstrated endoDPT has high image resolution compared to typical methods of PCa imaging. Future work will be focused on development of a prototype system that improves scanning efficiency that can be used to optimize endoDPT and perform pre-clinical studies.

Chapter 1. Background

1.1 The Prostate Gland

The prostate is a muscular exocrine gland that is located medially within the male pelvis, fused and inferior to the urinary bladder, and anterior to the rectum. In adults, the healthy prostate is approximately walnut-shaped with diameters of 4 cm lateral, 3 cm cranial-caudal, and 2 cm ventral-dorsal (Tortora 2014).

Approximately two-thirds of the prostate is glandular tissue that slowly secretes and accumulates prostatic fluid, which nourishes, protects, and improves motility of the sperm (Tortora 2014). This glandular tissue is divided into the peripheral zone, central zone, and transition zone, which comprise about 70%, 20-25%, and 5-10% of the glandular tissue volume, respectively (McNeal 1981, McNeal 1988). Most of the remaining third of the prostate volume is the anterior fibromuscular stroma, a non-glandular stromal tissue (McNeal 1981). The anterior fibromuscular stroma aids in the expulsion of semen, a fluid comprised primarily of sperm, seminal fluid, and prostatic fluid, during ejaculation (Tortora 2014). A pseudo-capsule composed of an outer sheath of collagen over a smooth muscle layer surrounds most of the prostate (Udeh 1982, Ayala 1989).

The four most common diseases of the prostate are prostatitis, prostatic atrophy, benign prostate hyperplasia (BPH), and prostate cancer (PCa). Prostatitis is any temporary pain or swelling in the prostate region and is most commonly associated with inflammation (Sutcliffe 2015). Atrophy is a reduction in size of the prostate glandular volume due to cell degeneration (McNeal 1988). BPH is the non-malignant hyperplasia of glandular tissue in the TZ (Mcneal 1978, Roehrborn 2005). PCa is the primary motivation for this study.

1.2 Current State of Prostate Cancer Management

In the United States, PCa is the most common non-skin malignancy and the third leading cause of cancer-related death in men, with an estimated 161,360 new PCa diagnoses and 26,730 PCa deaths in 2017 (Siegel 2017). The 5-year survival rates for all races diagnosed with local, regional, or metastatic PCa are >99%, >99%, and 29%, respectively (Siegel 2017). At the time of diagnosis, 80% of PCa presents as local only, 12% presents with regional spread to the pelvic lymph nodes, 4% presents with distant metastasis, and 4% is not staged (Howlader 2016, Siegel 2017). These figures underestimate the total number of men with PCa, as autopsy studies have shown that the rate of incidental PCa, which is often symptomless, is much higher than clinically diagnosed PCa (McNeal 1969).

PCa is usually detected in suspected or at-risk individuals using the digital rectal exam (DRE) and/or through measurement of prostate specific antigen (PSA) levels in the blood serum. The DRE is the digital palpation of the prostate through the rectum. Any abnormalities compared to typical anatomy, such as increased stiffness or nodularity, can indicate PCa (Qaseem 2013). The PSA serum analysis measures of the amount of PSA, an antigen made by the secretory epithelial cells in the prostate, per unit volume of blood serum (Kuriyama 1980, Kuriyama 1981). Elevated PSA levels, velocity, and density in the blood serum have been correlated to increased incidence and grade of PCa (De Angelis 2007). Both DRE and PSA serum analysis are inexpensive and simple to perform, and have been effective at increasing the detection rates of PCa (Roobol 2015). However, neither test provides a definitive diagnosis. Other diseases or disruptions to the prostate, such as BPH, can change tissue stiffness or nodularity (Sharma 2014), or can increase PSA levels (Scarpato 2016). In addition, some cancers cannot be felt through palpation (Sharma 2014) and/or do not elevate serum PSA levels (Scarpato 2016).

Biopsy, generally using ultrasound guidance and systematic random sampling, is the only method in clinical use that can definitively diagnose PCa *in situ*, other than a pathological examination after surgical excision (Bhavsar 2014, Futterer 2015). The biopsy samples are scored using the Gleason histological grading system, which provides a measure of disease aggressiveness and is the dominant predictor for patient prognosis (Gleason 1966, Humphrey 2004). The Gleason score classifies PCa based on histologic appearance (level of differentiation) of malignant cells prior to any treatment on a scale of Pattern 1 to Pattern 5, with Pattern 5 being most malignant and least differentiated (Gleason 1966). Because PCa is usually multi-focal in origin, the reported Gleason score is the sum of the first and second most common pattern numbers (Gleason 1966).

PCa is also staged to characterize the extent of disease, assess prognosis, and guide treatment (Reese 2016). Current staging uses the TNM model defined by the American Joint Committee on Cancer, where the T value indicates the extent of local disease, the N value indicates if the regional lymph nodes were assessed and if PCa has invaded this site, and the M value indicates if and where the disease has metastatic involvement (Reese 2016). There is a strong correlation between high Gleason scores, advanced stage, and increased PCa mortality (Gleason 1974).

After clinical diagnosis, PCa can be treated or closely monitored. The two main curative treatments for PCa are radical prostatectomy, which is the surgical excision of the prostate gland, and radiation therapy, which is the treatment of PCa using external beam radiation therapy and/or brachytherapy (BT). Curative rates for radical prostatectomy and radiation therapy are high but these treatments also result in a high incidence of both urinary incontinence and erectile dysfunction (McLaughlin 2005, Gomella 2016). Chemotherapy and hormonal therapy are common adjuvants to radical prostatectomy and radiation therapy for cases of curative intent, and can be used palliatively for advanced disease (Catalona 1994, Bilusic 2016). Several new therapies, such as high intensity focused ultrasound (Monn 2016) and cryotherapy (Chipollini 2016), are under investigation because they can be used focally, sparing normal prostatic tissue and reducing side effects (Mendhiratta 2016).

Delaying or precluding PCa treatment by monitoring the prostate can improve quality of life by not subjecting the patient to procedures that may damage their urinary, sexual, or reproductive integrity until medically necessary (Adolfsson 2008). The two monitoring techniques used for PCa management are watchful waiting and active surveillance (Klotz 2005, Adolfsson 2008). Watchful waiting is prescribed for elderly patients with short life expectancies and/or competing comorbidities. PCa treatment in these patients is either precluded or, if the disease advances, palliative. Active surveillance is prescribed for patients with low-risk PCa and longer life expectancy. Treatment in these patients is delayed until deemed necessary by the physician, and when treatment occurs, it is of curative intent.

After definitive treatment, PCa can recur as local, regional, or metastatic disease (Kitajima 2013). Biochemical relapse, which is the elevation of PSA serum levels above nadir, is usually the first sign of recurrence (Kitajima 2013). Biochemical relapse occurs in one in three men within 10 years of definitive treatment (Freedland 2007).

1.3 Current State of PCa Imaging

The most common PCa imaging modalities are magnetic resonance imaging (MRI), transrectal ultrasound (TRUS), computed tomography (CT), and nuclear medicine. The general application of these modalities to PCa imaging is described in this section; specific concerns that directly relate to endorectal digital prostate tomosynthesis, the subject matter of this dissertation, are detailed in Chapter 2.

1.3.1 Magnetic Resonance Imaging

MRI is the gold standard diagnostic modality for PCa imaging due to excellent soft tissue contrast and the ability to collect multiple anatomical and functional image sets during a single multiparametric MRI examination (Futterer 2015, Dulaney 2016). Prostate MRI is often completed with an endorectal probe, which improves image quality but results in additional time, cost, and patient discomfort (Heijmink 2011).

There are several MRI scan types useful for local PCa imaging, including T1 weighted (T1W) imaging, T2 weighted (T2W) imaging, diffusion weighted imaging, dynamic contrast enhanced MRI (DCE-MRI), and magnetic resonance spectroscopy. Anatomic T1W and T2W scans and functional diffusion weighted imaging and DCE-MRI scans are often combined into a multiparametric MRI examination (Bhavsar 2014). The examination results are compiled into a standardized scoring matrix known as the Prostate Imaging Reporting and Data System (PI-RADS) to assess disease extent, aggressiveness, and prognosis (Weinreb 2015).

Due to limitations in sensitivity and specificity, MRI cannot be used as the sole modality for PCa detection, staging, and diagnosis (de Rooij 2014, de Rooij 2016). However, some studies have reported MRI as effective at identifying significant (aggressive) PCa, thus reducing unnecessary treatment and biopsy for low-risk disease and improving guidance for biopsy and treatment (Thompson 2014, Dulaney 2016, Mendhiratta 2016). The potential benefits of MRI for imaging low-risk disease remain controversial; screening or routine MRI examinations are not indicated for potential low-risk cases (Porten 2014).

1.3.2 Transrectal Ultrasound

TRUS collects images of the prostate using a transrectal probe and is the most common imaging method for the prostate because it is fast, inexpensive, and does not use ionizing radiation (Sankineni 2016). Several common methods of TRUS prostate imaging are standard grayscale imaging, Doppler ultrasound, and contrast enhanced ultrasound (CEUS).

The most common applications of TRUS are biopsy guidance, BT implant guidance, and measuring the prostate volume (Sankineni 2016). Overall, TRUS cannot consistently identify PCa and is heavily dependent on operator skill, which precludes the use of TRUS as a sole modality for PCa detection, staging, and diagnosis (Halpern 2006, Harvey 2012).

1.3.3 Computed Tomography

CT has no standard or established use in the current practice of local PCa diagnosis due to poor soft-tissue contrast between PCa and normal tissues (Heijmink 2011, Luczynska 2014). CT can be used to image advanced local PCa with severe extra-prostatic extension, seminal vesicle invasion, or invasion into nearby anatomy such as the bladder (Sharma 2014). CT is commonly used to image the pelvic lymph nodes and other distant areas to stage metastatic involvement or recurrence (Jung 2012, Eifler 2016).

1.3.4 Nuclear Medicine Imaging

Positron emission tomography (PET) and single photon emission computed tomography (SPECT) are currently used to image PCa by attaching radioisotopes to macromolecules that have preferential uptake by or preferentially react with PCa. PCa cells exhibit increased uptake of choline, acetate, some amino acids, and androgen analogs such as dihydrotestosterone compared to normal prostatic tissues (Catalona 1994, Krause 2013). Some compounds, such as capromab pentetide (more commonly known as ProstaScint®, Cytogen Corporation, Princeton, New Jersey) preferentially react with the prostate specific membrane antigen, which is overexpressed in PCa, (Tang 2016). Despite the many radiotracers available for PCa imaging, the utility of PET and SPECT remains low due to nonspecific uptake of radiopharmaceuticals by other diseases such as BPH, limited resolution, and background accumulations of radiopharmaceuticals in nearby anatomy such as the bladder and urethra (Krause 2013, Sharma 2014, Eifler 2016).

1.4 Overview of Tomosynthesis

Conventional tomography (Littleton 1996) provides the foundation for tomosynthesis (Dobbins 2003). In conventional tomography, a patient is positioned between a film and an x-ray source. A single exposure is collected as the film and x-ray source move in unison in an opposed manner; a linear scan (Fig. 1.1) is one possible motion pattern. Structures within the plane of the fulcrum of the film and x-ray source motion project to fixed locations on the film, generating a single tomographic image plane; structures above and below this plane are blurred from visibility. This reduces the appearance of structures above and below the image plane, providing an advantage over projection radiographs. Residual blur artifacts from the structures located outside the tomographic image plane and the generation of only one tomographic image plane per scan were problematic limitations. Tomosynthesis was developed as an extension to conventional tomography to address some of these limitations.

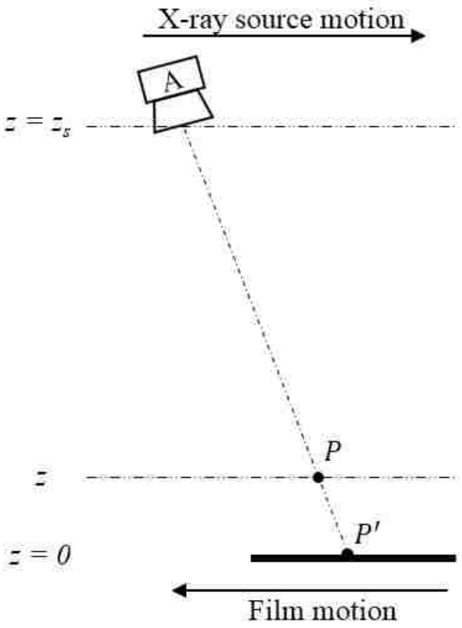

Figure 1.1: Conventional tomography with linearly opposed motion. The x-ray source and film occupy planes that are parallel and separated by distance z_s. The tomographic image plane z containing the object P is generated by moving the x-ray source and film such that z is located at the fulcrum of motion, assuming a parallel x-ray beam. This results in P projecting to the same location P' on the film during the entire exposure.

Tomosynthesis originated as the discretization of conventional tomography (Ziedses des Plantes 1935, Ziedses Des Plantes 1938, Grant 1972). A single set of projection images on separate films was collected as the x-ray source moved in known, discrete steps. Tomographic image planes located at any height z above and parallel to the image acquisition (film) plane were reconstructed by shifting and overlaying the films on a film reader. The direction and magnitude of the shift was dependent both on z and on the film and x-ray source locations for each discrete image.

This method of analog tomosynthesis imaging saw limited use because it was bulky and slow, thus difficult to implement clinically (Garrison 1969, Miller 1971, Miller 1974). Film was phased out in favor of x-ray image intensifiers in the 1970s and 1980s which improved efficiency but suffered from poor image quality (Sone 1991), particularly in comparison to CT which was rapidly becoming a mainstay in the medical imaging community (Goodsitt 2014). In the early 1990s, primarily due to the advent of digital flat panel detectors capable of high-resolution and high frame-rate scans, tomosynthesis truly became clinically feasible (Dobbins 2003).

Linear parallel tomosynthesis, shown in Fig. 1.2, is the simplest implementation of digital tomosynthesis and is widely used (Niklason 1997, Dobbins 2003, Wu 2004, Dobbins 2009a). A typical linear parallel tomosynthesis imaging system consists of an x-ray source that travels along a linear path in a plane above and parallel to a *stationary* digital x-ray detector, with projection images acquired at discrete x-ray source locations. Key parameters used to define the scan are the x-ray source travel and the spatial step size. The x-ray source travel is the distance the x-ray source moves in one dimension during the scan (for example, travel in $\hat{x}$ from $-x_{max} = -40$ cm to $x_{max} = 40$ cm, where $-x_{max}$ is the starting source position and x_{max} is the ending source position). This motion is typically termed sweep angle in the digital breast tomosynthesis (DBT) literature; sweep angle is the half-angle that the central ray of the x-ray beam sweeps over, and ranges from 7.5° to 45° (Reiser 2007, Gennaro 2016). The spatial step size defines the number of projection images typically acquired at equal increments (for example, every 2 cm). This is analogous to the DBT term angular increment. Typically, the spatial or angular spacing will be such that 9-60 images are acquired (Reiser 2007, Gennaro 2016). In general, smaller values of x-ray source travel and spatial step size improve in-plane image resolution at the cost of decreased resolution in the slice thickness ($\hat{z}$) direction (Reiser 2007).

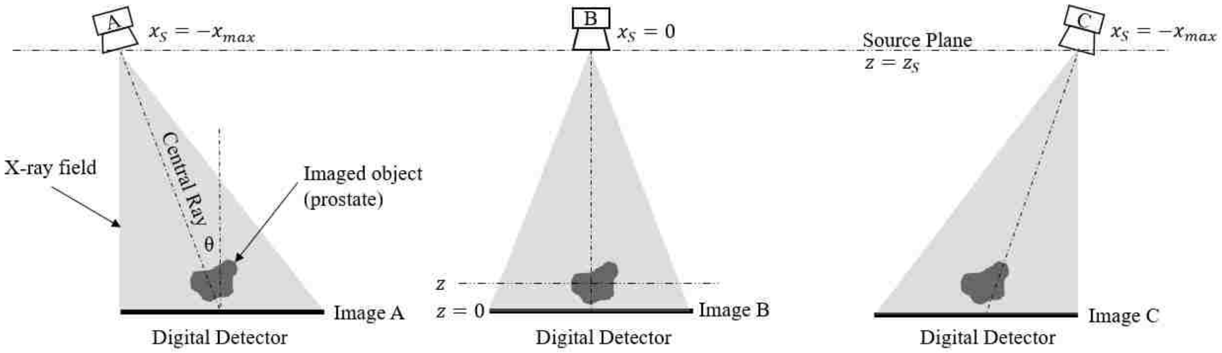

Figure 1.2: Tomosynthesis scanning geometry, showing three projection image acquisitions.

Once the projection data are acquired, tomosynthesis image planes can be reconstructed using two broad categories of algorithms – analytical and algebraic. Analytic methods assume the system is ideal and a solution can be derived exactly. Some common analytic methods include the shift and add (SAA) algorithm (Niklason 1997), backprojection (BP) and filtered backprojection (FBP) (Lauritsch 1998), and matrix inversion tomosynthesis (Dobbins 1990). The more advanced analytical techniques such as FBP and matrix inversion tomosynthesis better remove blur artifacts from the reconstructed images. Algebraic methods numerically find the approximate solution of discrete voxels within the reconstructed volume, usually with iterative techniques that reduce the error matrix between the solution and the true projection data to below a predetermined threshold (Colsher 1977). Some common algebraic algorithms are expectation maximum and total variation minimization (Reiser 2007).

Tomosynthesis has been applied for imaging much of the human body, with the most common applications to the breast and chest (Goodsitt 2014). DBT was initially demonstrated in 1997

(Niklason 1997) and over the past two decades has experienced rapid growth because it supplies depth information with in-plane resolution and radiation dose comparable to two-field projection mammography (Dobbins 2003, Wu 2003, Reiser 2007, Chen 2013). Chest tomosynthesis has been widely used to assess lung lesions, primarily in the differentiation of small nodules from calcifications that benefit from high resolution and removal of tissue superposition, at a lower radiation dose than CT (Sone 1993, Dobbins 2009b, Horvath 2016).

Several efforts have been reported to image the prostate region using tomosynthesis, although not with an endorectal x-ray sensor. Such uses have included radiotherapy treatment verification as an alternative to cone-beam CT or portal imaging (Yoo 2009), and prostate BT implant localization. The latter prostate tomosynthesis application is discussed further in Chapter 2.

Despite substantial interest in tomosynthesis due to allowing high resolution and depth information at comparable radiation dose to projection radiography, tomosynthesis is limited by sampling over a small angular range. This results in a non-isotropic reconstructed volume, with resolution in the depth direction (normal to reconstructed image planes) an order of magnitude worse than in-plane resolution; a significant blur artifact can result from out-of-plane (OOP) structures (Reiser 2007, Dobbins 2009a, Sechopoulos 2013a). The limited angular sampling makes it difficult to quantitatively determine the density of the imaged volume (Reiser 2007) unlike CT, and hinders removal of blurring artifacts in reconstructed images (Dobbins 2003).

1.5 Radiographic Image Quality and Dose

Many metrics are available to assess image quality of radiographic images; many methods provide quantitative measures to compare images taken under known conditions. In this work, modulation transfer function (MTF), noise power spectrum (NPS), artifact spread function (ASF), and radiation dose were used to quantify the image quality of endoDPT.

Classically, the limiting spatial resolution of an imaging system is described as the minimum object size visible or the minimum separation required to differentiate two objects (Bushberg 2012). There are several methods to directly measure this quantity, such as use of line pair phantoms. However, it is often more convenient to quantify the resolution of the imaging system through measurement of the MTF. The MTF of an imaging system describes how well the system can map frequency domain characteristics of the input signal (the object) to the output signal (the image of the object) (Qian 2013). Measurement of the MTF is the accepted standard for characterization of spatial resolution in digital x-ray imaging systems such as radiography, mammography, and CT (Bushberg 2012, Qian 2013). The frequency value at which the MTF reaches 10% of its zero-frequency magnitude is often quoted as the limiting resolution of an imaging system (Bushberg 2012).

Noise is unwanted signal or unwanted variations in signal in an image (Bushberg 2012). Unwanted variations in signal are primarily due to the stochastic nature of x-ray photon interactions. The noise per pixel element, σ, in the detector system is directly related to the number of photons, N, incident on that pixel element by $\sigma \propto \sqrt{N}$ (Bushberg 2012). Higher x-ray source energies and currents result more incident photons on a given detector element, which results less relative noise compared to measured signal; the increase in the signal-to-noise ratio is proportional to $N/\sigma = \sqrt{N}$. The level of noise in images is often quantified in the frequency domain through measurement of the NPS. The NPS reports the variance of an image as a function of frequency in the frequency domain, and is a primary image quality metric for medical imaging (Chen 2014).

As noted, the primary disadvantage of tomosynthesis is that limited sampling of the imaged volume results in OOP structure blur artifacts in the reconstructed planes (Dobbins 2003, Wu 2004). OOP structures present as a ghosting artifact that replicates the imaging geometry (Reiser

2007). In linear parallel tomosynthesis, the artifact appears as a band of repeated structures, and this effect is particularly significant when the OOP structures have high space density (Sechopoulos 2013b). The severity of blurring artifact decreases with increasing distance of the OOP object to the reconstruction plane, and can be quantified using the ASF, which is commonly used as a metric to assess slice thickness resolution in DBT (Wu 2004, Sechopoulos 2013a).

One of the primary disadvantages of x-ray imaging is exposing the patient to radiation dose. Dose is the energy from ionizing radiation absorbed in a medium per unit mass and is measured in Gy (Attix 1986). Radiation dose can induce negative health effects (Hall 2006). Deterministic effects occur if a specific threshold ionizing radiation dose is breached, increase in severity as ionizing radiation dose is increased, and can present as early or late effects, such as skin erythema and cataract genesis, respectively. Stochastic effects can occur at any level of ionizing radiation dose, where the probability of the effect increases as a function of ionizing radiation dose; the severity is binary, for example, cancer is either induced or not induced. Stochastic effects are the principle concern at the dose levels encountered with radiological imaging. Because of this, it is important to reduce the dose to the lowest level that still allows for diagnostic evaluation of x-ray images.

Chapter 2. Project Overview and Hypothesis

2.1 Introduction and Goals

This dissertation describes the development of endorectal digital prostate tomosynthesis (endoDPT), a high-resolution method for imaging the prostate region. endoDPT utilizes a stationary endorectal x-ray sensor combined with an external x-ray source (Fig. 2.1). A typical endoDPT scan consists of discrete projection images collected of the prostate region as the x-ray source moves along a linear path in a plane above and parallel to the x-ray sensor. These projection images are reconstructed into image planes above and parallel to the x-ray sensor through the prostate region using tomosynthesis.

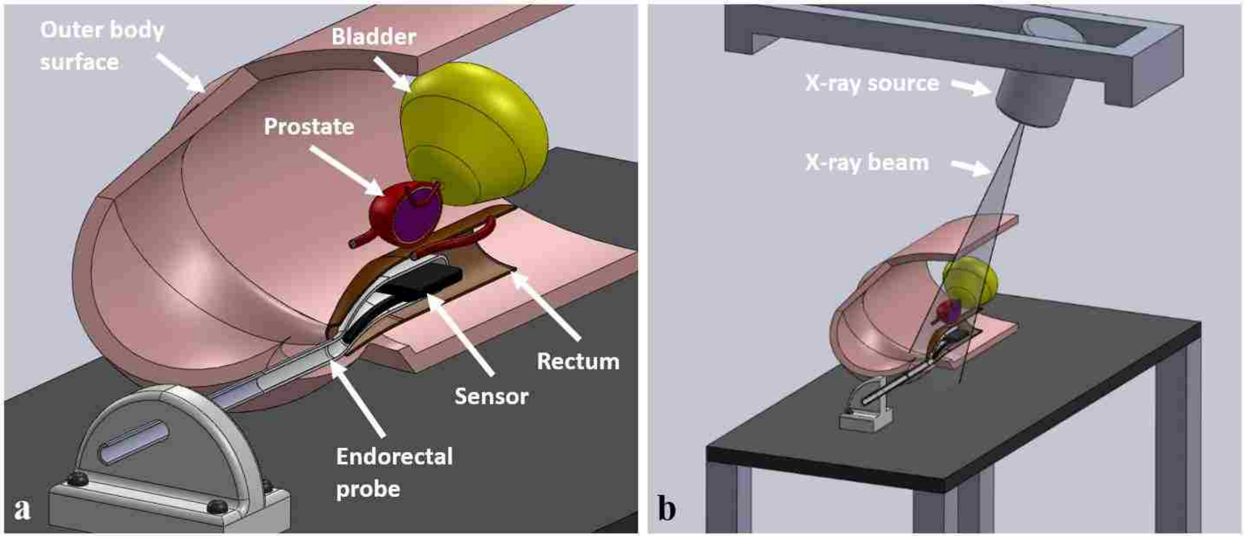

Figure 2.1: (a) Anticipated clinical implementation of endoDPT. A probe system places an x-ray sensor within the rectum directly adjacent to the prostate. (b) X-rays from various source positions enter the anterior of the patient to create projection images of the prostate region. One source position is shown.

There have been several efforts to develop endorectal x-ray or gamma-ray sensor probe systems like endoDPT, with the most similar being BrachyView. BrachyView consists of several small, high-resolution gamma-ray sensors that are coupled with pinhole collimators to form miniature gamma cameras that can be used to determine the location of low dose rate or high dose rate BT sources (Petasecca 2013, Safavi-Naeini 2013, Safavi-Naeini 2015, Alnaghy 2017). Recent efforts have demonstrated that if the planar detectors used in BrachyView are located outside of the rectum using a male pelvic phantom, radiographic contrast between prostate-simulating and other soft tissue-simulating gels can be observed (Loo 2014), but this system has not been used or assessed for endorectal tomosynthesis imaging of the prostate region.

endoDPT has the potential to provide high-resolution images of the prostate due to 1) the utilization of a high-resolution x-ray sensor and 2) a large source-to-image plane distance (SID) with a small object-to-image plane distance (OID) which minimizes focal spot blur (see Appendix A for details on focal spot blur reduction). Increased resolution of the prostate region may aid physicians in PCa cancer diagnosis, treatment, and management by improving the conspicuity of small structures within the prostate that may not be visible or, if visible, not easily discernable, with conventional imaging methods.

The goals of this study were to develop endoDPT, to assess the image quality and dose of endoDPT, and to image representative simulations of typical PCa management cases. Ideally, endoDPT will provide higher in-plane resolution with less radiation dose compared to CT. While CT currently has no standard clinical use in local PCa diagnosis due to poor soft tissue contrast between PCa and normal prostate tissues (Luczynska 2014), CT is still a widely used technique for visualizing the prostate region, including applications such as post-implant imaging of permanent BT sources (Yu 1999, Nath 2009).

To achieve these goals, first the endoDPT imaging system was computationally designed, tomosynthesis image reconstruction algorithms were derived, and the theoretical image resolution of the system was measured using simulated phantoms. Next, a small, high-resolution x-ray sensor and a commercial radiography source were used to physically assess image quality in endoDPT, focusing on measurement of image resolution and dose. These metrics were compared to equivalent measurements made using a typical CT scanner. Finally, *ex vivo* canine prostate specimens were imaged and compared using endoDPT, CT, and MRI. The deliverable associated with achieving the project goals is a well-characterized test bed imaging system that can move towards prototyping and clinical implementation.

2.2 Clinical Motivation

The motivation for this study arises from three areas of PCa that may benefit from high-resolution: imaging of low dose rate brachytherapy (LDRBT) seeds after implantation into the prostate; imaging of the periprostatic adipose tissue (PPAT) layer surrounding the prostate; and imaging of increased microvessel density within PCa lesions using contrast agents.

2.2.1 Low Dose Rate Brachytherapy

LDRBT is a PCa treatment in which 40-100 radioactive metal pellets encased in a thin metal shell (collectively known as seeds) are implanted permanently into the prostate to deliver dose to local disease while sparing nearby critical structures such as the bladder and rectum (Zaorsky 2016). The seeds are small, with lengths from 3 mm to 5 mm and diameters of approximately 0.8 mm (shell) and 0.5 mm (core), with the shell having a thickness on the order of 0.05 mm (Khan 2014). The seeds deliver dose at a low rate (defined as < 2 Gy/hr but typically << 2 Gy/hr) over a relatively long decay time (weeks to months). The number of seeds implanted is dependent on seed type, desired coverage of the prostate, and physician preference. Implantation of seeds is typically done manually by the physician using needle applicators through the perineum with TRUS guidance.

Due to uncertainties in seed implantation, the seeds are imaged after the procedure to assess dose to the prostate and to nearby organs at risk (OAR) such as the rectum, bladder, and urethra (Yu 1999). Initially, seed locations were determined stereoscopically through use of radiographs taken at multiple angles. This technique was not optimal because the prostatic borders could not be visualized with radiography, and so it was difficult to compute dose to the prostate (Yu 1999). Currently, the American Brachytherapy Society recommends that post-implant dosimetry be performed with CT within 60 days of the treatment (Davis 2012). CT is preferred because the high-density seed cores show up extremely well and the prostate border can usually be distinguished (Nath 2009). Despite being the current standard for imaging of seeds, the in-plane and slice thickness resolutions are on the order of seed diameter and seed length, respectively, which leads to partial volume averaging that makes it difficult to identify seed orientations or to differentiate neighboring seeds in close proximity (Nath 2009, Collins Fekete 2014). This can be problematic because the seeds emit radiation anisotropically due to source construction (Collins Fekete 2014, Khan 2014). The American Association of Physicists in Medicine recommends a two-dimensional dose calculation formalism that models this anisotropy for post-implant dosimetry (Nath 2009). Because of the limited resolution of CT, it is assumed that the long axis of the seeds is aligned with the axis of the CT scanner (Chng 2012). Any variations in seed orientation, and therefore anisotropic dose distributions, are ignored (Nath 1997, Nath 2009, Davis 2012, Collins Fekete 2014). Variations in seed tilt from the CT scanner axis are expected to have a negligible to small effect on the final dose to the prostate and OAR due to the large number of seeds used (Ellis 2002, Chng 2012), but it has been shown that dose to OAR can vary by up to 10% (2.1% on average) when seed tilt is explicitly modeled (Collins Fekete 2014).

TRUS, projection x-ray imaging, and MRI have all been assessed for use as an adjunct or sole modality for LDRBT implant dosimetry. The potential benefits of these methods include higher resolution images capable of determining seed orientation and differentiating adjacent seeds, a reduction or removal of ionizing radiation dose to the patient, and the possibility of intraoperatively assessing dose distribution in the prostate in real-time.

TRUS post-implant dosimetry is attractive because the TRUS probe is already in the rectum during the implantation procedure and the prostate border is easily identifiable (Han 2003b). This allows for real-time dosimetry and modification of treatment plans while in the operating suite (Mitri 2009, Mehrmohammadi 2014). However, TRUS has difficulty in visualizing seeds both at certain angles and when many seeds are implanted within the prostate (Han 2003b). New techniques, such as vibro-acoustography TRUS, have shown improvement in this area, but seed detection rates are suboptimal (75%-90%) so TRUS is not sufficient for real-time dosimetry (Mehrmohammadi 2014).

Techniques using projection x-ray imaging with an x-ray sensor external to the body such as radiography, fluoroscopy, and tomosynthesis provide excellent resolution and contrast of the high-density seeds and can be used intraoperatively to assess dosimetry in real-time. Radiography and fluoroscopy typically consist of images acquired for at least three angles to stereoscopically assess seed position using a variety of seed matching algorithms (Su 2004, Lee 2011, Kuo 2014). Tomosynthesis removes the need for complex seed matching algorithms as seed depth can be visualized in the reconstructed image planes. Tomosynthesis seed imaging is typical performed in the operating suite with C-arm radiography units and several studies have automatically localized seeds with good spatial accuracy. Fusing the tomosynthesis images to CT or TRUS images facilitates dose assessment to the prostate volume (Tutar 2003, Brunet-Benkhoucha 2009).

MRI provides excellent soft tissue contrast of the prostate region which can be used to accurately assess prostate volume for dose calculation. MRI is not used for LDRBT procedures (De Brabandere 2006); in general, seeds are difficult to visualize in MRI. Fusion of CT seed images to MRI anatomical images (Kunogi 2015, Quivrin 2015, Schieda 2015) and use of MRI specific high-contrast markers paired with seeds (Lim 2016) is common. Replacing CT entirely is one of the most attractive possibilities of MRI LDRBT imaging, because it removes the radiation dose from CT to the body; it also removes variability caused by registration and patient setup when fusing images between modalities. A recent study has shown no significant differences in dosimetric results between post-implant dosimetry computed using only MRI and an MRI-CT fusion (De Brabandere 2012).

The primary benefit of endoDPT is that the high-resolution images obtained using the endorectal sensor may allow for better determination of seed tilt and position. The raw data collected during the endoDPT scan can be reconstructed using tomosynthesis or can be analyzed using stereoscopic techniques to find seed locations and orientations. Due to the small size of the detector, a small x-ray beam can be used which reduces whole body radiation dose to the patient. endoDPT may be able to offer more insight into the effect of seed anisotropy and orientation (tilt) on LDRBT implant dosimetry, along with the potential to improve efficiency of seed counting, particularly for seeds near one another. Like other radiographic techniques, the primary difficulty encountered by endoDPT is determination of the prostate border to calculate dose to the prostate region. The endoDPT detector could be conjoined with an TRUS probe to determine prostate volume, if prostate volume cannot be determined by endoDPT alone.

2.2.2 Periprostatic Adipose Tissue

PPAT is a visceral fat that partially or fully surrounds the prostate. Research efforts to determine if PPAT is a valuable biomarker for PCa are relatively recent and sparse; most studies have focused on linking PCa with obesity (Bhindi 2012). Some work has been published using CT, TRUS, and MRI that shows positive correlations of increased levels of PPAT to increased incidence and aggressiveness of PCa (van Roermund 2010, van Roermund 2011, Bhindi 2012, Woo 2015). While the exact mechanism that links increased PPAT to PCa is unknown, it is believed that the adipose tissue surrounding the prostate acts not just as an energy reservoir but also produces hormones and cytokines that increase PCa growth (Finley 2009, Laurent 2016). Several studies have shown that increased PPAT secretions correlated to higher Gleason scores (Finley 2009) and to increased likelihood of metastasis (Ribeiro 2012, Laurent 2016). Using CT, patients with the highest risk PCa were reported to have the largest areas of PPAT coverage over the prostate; the correlation between PPAT and PCa was stronger than the correlation between subcutaneous fat (obesity) and PCa (van Roermund 2011). Using TRUS, it was reported that for each millimeter of increased PPAT layer thickness, there was an approximate 12% increase in detecting PCa and a 20% increase in detecting high-grade PCa, with a mean PPAT thickness of 5.3 mm (Bhindi 2012). It was also reported that the thickness, measured with TRUS, of the anterior PPAT layer between the rectal wall and the prostate was a good predictor of recurrence (Sumitomo 2010). Using MRI, it was reported that obese patients with more PPAT had higher blood vessel density in the PPAT and increased proliferation of PCa cells, indicating increased risk for metastasis (Venkatasubramanian 2014). Additionally, it was reported that the Gleason score was positively correlated with PPAT layer thickness measured using MRI (Woo 2015).

These studies show an apparent association of the amount of PPAT surrounding the prostate to PCa risk and aggressiveness. endoDPT could prove to be a useful alternative or adjunct method for imaging this fat layer, potentially identifying sub-millimeter trends in fat thickness with improved spatial resolution.

2.2.3 Microvessel Density Imaging of PCa

As malignant tumors approach diameters of 1-2 mm diameter, they leave their avascular state and enter a more aggressive and faster growing angiogenic state (Folkman 1990). This occurs because existing vasculature cannot supply adequate nutrients and oxygen to sustain tumor growth

(Folkman 1990, West 2001). Increased angiogenesis can be observed through measurement of the microvessel density of thin tissue sections viewed at 40x-100x magnification (Silberman 1997) and is usually reported as the mean number of blood vessels (Brawer 1993) or the area of blood vessels (Tretiakova 2013) in a given area. Multiple groups have reported microvessel density was increased in PCa compared to normal prostatic tissue (Bigler 1993, Siegal 1995, Borre 1998) and that microvessel density increases with stage and Gleason score of PCa (Brawer 1993, Weidner 1993, Borre 1998, Mucci 2009).

Perfusion imaging can be used to view these areas of increased angiogenesis and increased microvessel density *in vivo*, providing a valuable biomarker to assess PCa extent and aggressiveness (Halpern 2006). Perfusion imaging measures the wash-in and wash-out of contrast media from areas of interest, where perfusion is a function of the same factors that increase microvessel density, primarily the number, surface area, and permeability of small blood vessels (Padhani 2005, Petralia 2010). Many clinical studies have demonstrated DCE-MRI, CEUS, and perfusion CT (pCT) can detect PCa by enhancing areas of increased angiogenesis.

DCE-MRI assesses tissue vascularity by rapidly obtaining T1W images before, during, and after a gadolinium chelate contrast agent is injected intravenously. PCa presents as an area of intense and rapid signal enhancement when the contrast agent perfuses into the lesion, which is easily differentiable from the slow and progressive uptake of normal prostatic tissues (Bittencourt 2014). Studies have shown DCE-MRI improves PCa detection and localization (Futterer 2006, Tan 2015) and increases detection rates using biopsy and success rates of treatments by providing improved image guidance (Hara 2005, Haider 2008, Yakar 2010). DCE-MRI is attractive because it can be combined with T2W imaging and diffusion weighted imaging to provide high-contrast images of the entire prostate region. However, MRI has many contraindications such as pacemakers and stents, which are much more common in the aging population of men most at risk for PCa (Luczynska 2014). MRI has high operating costs to the patient (Luczynska 2014). Several authors have commented that improvements in resolution would be desirable for improved detection of small, aggressive PCa tumors (Bittencourt 2014, Barentsz 2016).

CEUS assesses tissue vasculature by measuring the reflected signal of gas microbubbles (1-10 μm diameters) that are introduced intravenously and then trapped within capillaries vessels (Errico 2015). Because the microbubbles have enhanced reflectivity of sound waves compared to normal tissue by a factor of about 1000, areas of increased angiogenesis are highlighted using this method (Ferrara 2007), including blood vessels that are too small to be imaged directly with Doppler ultrasound (Halpern 2006, Wells 2006). Several recent studies have shown that targeted biopsies to densely sample areas of high microbubble concentration resulted in more positive PCa findings compared to systematic biopsy (Sano 2011, Zhao 2013, Sharma 2014). CEUS had better lesion detection rates than standard grayscale TRUS and Doppler imaging (Strazdina 2011). Despite theoretical image resolution on the order of 50 μm (Halpern 2006), CEUS cannot typically image PCA lesions smaller than 1 cm in diameter (Strazdina 2011). Image quality depends heavily on operator skill level (Sankineni 2016). Doppler imaging can also be used to image increased angiogenesis (Heijmink 2011) but is not described further because CEUS using microbubbles outperforms Doppler imaging (Strazdina 2011).

Use of pCT with iodine contrast was shown to be feasible using a dynamic contrast enhanced protocol and a single detector row CT scanner (Prando 2000). Improvements in CT technology, primarily the advent of wide multi-detector arrays, has made pCT into a more viable method (Ives 2005), but scanners with axial detector lengths greater than 4 cm, required to image the prostate with no table motion, are costly and limited in availability (Osimani 2012). Two recent studies have shown pCT was able to identify areas of increased microvessel density at doses of 10 mSv (Osimani 2012) and 16 mSv (Luczynska 2014); these doses are comparable to typical CT scans.

endoDPT has theoretical resolution that is high compared to pCT and DCE-MRI (true perfusion methods) and is similar to clinical CEUS (which does not supply a true measure of perfusion). Currently DCE-MRI and CEUS can detect lesions with diameters greater than 1 cm (Strazdina 2011, Eifler 2016), with no literature assessing minimum tumor diameters detectable with pCT. Detecting PCa using perfusion imaging between the beginning of angiogenesis (1-2 mm diameter) and after several doubling times (~1 cm diameter) is currently difficult. The high resolution of endoDPT combined with true perfusion imaging may allow for detection of lesions at 1-2 m diameter as they leave the avascular state and enter the angiogenic state. Perfusion imaging using endoDPT could occur at extremely fast rates by using multiple sources and electronic voltage switching, as demonstrated in tuned aperture tomosynthesis (Klotz 1976, Groh 1977). Other advantages of endoDPT may include reduced dose compared to CT, reduced cost compared to CT and MRI, and greater flexibility in operator skill levels compared to TRUS. This could make endoDPT a valuable alternative or addition to current patient care.

2.3 Hypothesis

We hypothesized that endoDPT would provide images of the prostate region with significantly higher in-plane resolution ($p < 0.05$) and significantly lower dose ($p < 0.05$) compared to a typical CT scan of the prostate region. CT was chosen for comparison because CT is the most similar of the typical prostate imaging techniques to endoDPT in terms of image acquisition and processing. CT is also the only other common prostate imaging technique that results in dose from x-rays. Providing a demonstrable improvement in spatial resolution at a reduced dose compared to CT will place endoDPT in an excellent position for prototyping and pre-clinical studies. The effort of this research is divided into three specific aims that examine and test the hypothesis.

2.4 Specific Aims

The first aim was to develop a computational endoDPT system, to derive tomosynthesis reconstruction methods for endoDPT, and to assess the theoretical image resolution of endoDPT using simulated phantoms. To accomplish this aim, clinically available technology was modeled; specifically, an intraoral dental sensor, which has high resolution and a small form factor, and a commercial radiography source. Analytic reconstruction methods SAA, BP, and FBP were implemented because these algorithms are common in clinical tomosynthesis implementations, are widely understood, and are robust. The theoretical resolution was assessed through measurement of the MTF using methods previously utilized for resolution measurements in radiography and DBT.

The second aim was to characterize experimentally the image quality of endoDPT in terms of spatial resolution, noise, and artifacts. Radiation dose was also measured. Specifically, the detector MTF was measured using an edge method and was combined with the reconstruction algorithm resolution from Aim 1 to find the system resolution of endoDPT. The NPS was measured using a featureless acrylic phantom, while the ASF was measured using high-density, small metal spheres. Dose was measured using thermoluminescent dosimeters (TLDs). For comparison resolution of CT was measured using a commercial CT performance phantom; CT dose measured using TLDs. Where appropriate, measurements were made as a function of x-ray source potential (measured in kVp) of x-ray time integrated current (measured in mAs). At the end of this aim, the hypothesis was tested using the student t-test.

The third aim was to compare endoDPT, CT, and MRI images of canine prostates implanted with LDRBT seeds, surrounded by thin PPAT layers, and embedded with surrogate vasculature. The qualitative differences between the modalities, including relevant artifacts, were assessed. One comparison was the ability to visualize, differentiate, and count the LDRBT seeds. Another was the visibility and discernibility of the PPAT layer. A third comparison was the visibility and discernibility of small diameter silicone rubber tubing filled with contrast agent.

Chapter 3. Aim 1, Development of Imaging System and Reconstruction Method

3.1 Overview

In this aim, endoDPT was computationally designed. A computational test bed system was modeled on existing clinical technologies, specifically, a dental intraoral digital x-ray sensor and a standard radiography unit. Analytical tomosynthesis reconstruction algorithms based on existing methods of image reconstruction for DBT and chest tomosynthesis were derived for the test bed system. To test the effectiveness of the test bed system and image reconstruction algorithms, two computational phantoms were modeled and simulated projection images of both were collected. The simulated image sets were processed and/or reconstructed as appropriate, and the computational detector and reconstruction algorithm MTFs were determined. The commercial software package MATLAB® R2015A (The MathWorks Inc., Natick, Massachusetts) was used for all computational modeling, image reconstruction, and image analysis.

3.2 System Geometry

endoDPT, as shown in Fig. 3.1, has the geometry of a linear parallel tomosynthesis system. Linear parallel tomosynthesis is the typical tomosynthesis method for imaging the chest and abdomen (Dobbins 2009a, Dobbins 2009b) and is often considered the best starting point for derivation of new or modified image reconstruction algorithms with new imaging methods (Nett 2007). Minimizing the motion in the directions $(\hat{y}, \hat{z})$ not associated with the scan motion $(\hat{x})$ reduces the propensity for error.

Assuming the patient is positioned as shown in Fig. 2.1 a, $\hat{x}, \hat{y},$ and $\hat{z}$ are perpendicular to the patient's sagittal, axial, and coronal planes, respectively. The detection plane is the coronal plane at $z = 0$ cm. The center of the detection plane has the coordinates $(x_D, y_D, z_D) =$ (0 cm, 0 cm, 0 cm). During the tomosynthesis scan, N projection images are obtained, with the i^{th} source location at $\left(x_{S_i}, y_S, z_S\right)$. The x-ray source is nominally located at a constant $z_S = 100$ cm and $y_S = 0$ cm. The x-ray source is directed at the center of the detection plane for each source location. During the tomosynthesis scan, the x-ray source travel in $\hat{x}$ has a maximum range of $\pm x_{max}$. For this dissertation, 41 projection images were collected with $x_{max} = 40$ cm and a spatial step size of 2 cm. This range of motion is consistent with other tomosynthesis methods (Reiser 2007, Dobbins 2009b, Chen 2013, Choi 2015, Gennaro 2016), including prostate tomosynthesis with an external x-ray sensor (Brunet-Benkhoucha 2009), and represents a maximum angle of incidence (central ray) of $\theta_{\max} \approx 21.8°$.

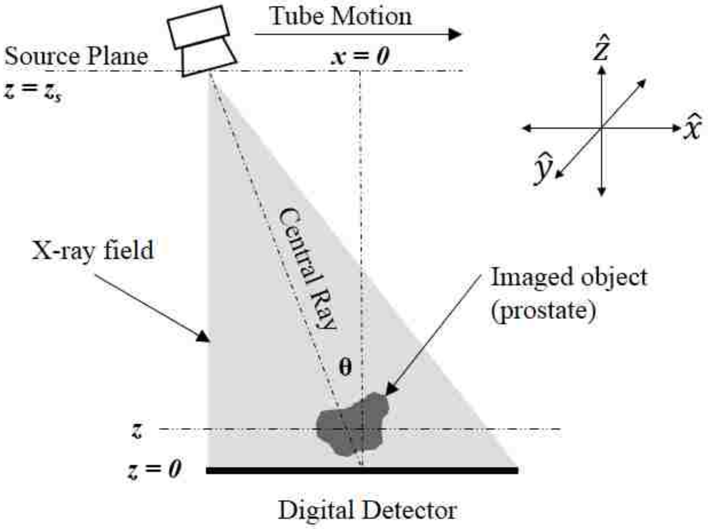

Figure 3.1: endoDPT system geometry. The detection plane remains stationary and the x-ray source travels along $\hat{x}$ with no motion along $\hat{y}$ or $\hat{z}$.

3.3 Computational System Design

The geometry shown in Fig. 3.1 was computationally modeled for assessment of both the digital detector MTF and the reconstruction algorithm MTF. Similar computational studies have been widely employed in tomosynthesis (Tutar 2003, Chen 2005, Orman 2006, Reiser 2007, Zhou 2007, Chen 2008, Zhao 2008, Cong 2011, Mainprize 2011, Choi 2015) and radiography (Samei 1998, Saunders 2003) because they are simple and cost-effective to implement.

The endoDPT test bed imaging system was developed by modeling a small, digital x-ray sensor and a point source with the travel of a typical radiography source. The physical x-ray sensor and radiography unit for these models are discussed in Chapter 4. The x-ray sensor was modeled as a two-dimensional detection plane with 2.5992 cm width (along $\hat{x}$), 3.6024 cm length (along $\hat{y}$), and 19 µm pixel size and pitch. This form factor and pixel size are consistent with most intraoral dental sensors (Farman 2005a). The x-ray source was modeled as a monoenergetic point source with a uniform diverging beam. The central ray of the x-ray source was directed towards the center of the detector array for each x-ray source position during the endoDPT scan.

3.4 Computational Phantoms and Simulated Scanning

Two computational phantoms were modeled to assess endoDPT resolution. The first phantom was a sharp, attenuating edge. Such simulated edge phantoms are commonly used to measure of the detector resolution in radiography (Samei 1998, Saunders 2003, Saunders 2005) and DBT (Chen 2007a). The second phantom was a simulated point impulse suspended above the center of the detector. Such point impulse phantoms have been previously used to assess reconstruction algorithm resolution in DBT (Chen 2005, Chen 2007a, Chen 2008, Chen 2014).

3.4.1 Edge Phantom Design and Image Simulation

The edge phantom was modeled and imaged using a two-part simulator, similar to previously developed techniques (Tutar 2003, Mainprize 2011). In part one of the simulator, an edge phantom that was 1 mm thick, 3 mm wide, and 20 mm long was modeled with voxel dimensions of 10 µm by 10 µm by 10 µm in the center of an arbitrary computational space. The voxel size was chosen to be smaller than the computational detector pixel size to reduce artifacts in projection imaging (Reiser 2014). The edge phantom was rotated by $\theta = 1.5^{\circ}$ with respect to the $\hat{y}$-axis using a 3D rotation matrix. A translation matrix was used to place the center point of the 20 mm long edge on the centermost pixel of the computational detector, with the edge in direct contact with the computational detector. The plan view of this computational phantom is shown in Fig. 3.2.

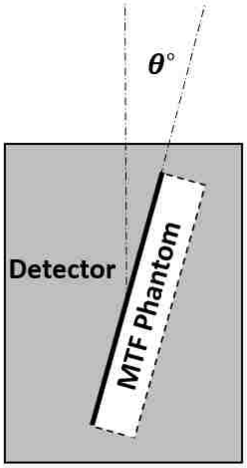

Figure 3.2: Edge phantom modeled on computational detector. The solid line marks the edge used for the MTF calculation.

In part two of the simulator, projection images of the edge phantom were created. The analytic photon path to each computational detector element through the edge phantom was determined with the source located at $(x_S, y_S, z_S) = (0 \text{ cm}, 0 \text{ cm}, 100 \text{ cm})$ using a layer-by-layer ray tracing method (Siddon 1985). Computationally, this was calculated by adding an index of 1 to each computational detector element for each layer of the phantom traversed. The resultant pixel values were then multiplied by the path length through one layer, which is constant for a given ray traveling from a single computational detector element to the x-ray source location.

The modeled x-ray sensor recorded values in 12-bit format with no signal being the value 1 and the maximum recordable signal being the value 4096. It was assumed that for an x-ray beam with perpendicular incidence on the surface of the x-ray sensor, the signal value of a pixel element under the 1 mm thick edge was 600 and the value of an unobstructed pixel element was 2400, representing a transmission factor of 25%. While a transmission factor of 10% was used in the study that this experiment was modeled after (Samei 1998), 25% transmission was chosen because it more closely matched the image signal of high-density metal structures compared to background signal in a preliminary imaging study with the intraoral dental sensor.

Using this transmission factor, an approximate attenuation coefficient for the simulated edge phantom material was calculated as

$$-\frac{\ln(\mathrm{I}/I_0)}{t} = \mu \tag{3.1}$$

where I is the beam intensity after attenuation $(I = 25\%)$, I_0 is the incident beam intensity $(I_0 = 100\%)$, t is the thickness of the phantom $(t = 0.1\text{ cm})$, and $\mu\ (\text{cm}^{-1})$ is the unknown attenuation coefficient of the edge. Solving Eq. 3.1 for these variables results in $\mu = 13.86\text{ cm}^{-1}$. μ was completely arbitrary and was based solely on the step function with 25% transmission.

The projection image was formed by analytically calculating the photon transmission for each pixel (m, n) on the computational detector, with the pixel value for pixel (m, n) calculated as

$$v(m,n) = \mathrm{I} = \mathrm{I}_0 e^{-\mu t_{total(m,n)}} \tag{3.2}$$

where $t_{total(m,n)}$ was the total path length through the edge phantom defined as the sum of path lengths through each layer of the edge phantom from the point source to each pixel (m, n), and I_0 was 2400. The full unattenuated photon fluence with a signal intensity of 2400 was assigned to any computational detector element where the path did not intersect the edge phantom. After image formation, a correction for r_0^2/r^2 photon fluence falloff was applied, where $r_0 = 100\text{ cm}$ and r was the distance from the x-ray source to a given computational detector pixel (m, n). At the centermost pixel, $r_0^2/r^2 = 1$.

Following simulation of this noiseless projection image, a noisy projection image was created by sampling a random number from a Poisson distribution for each pixel element (m, n) on the detector, subtracting the distribution mean from the random number, and then adding the mean-subtracted random number value to the pixel element (Samei 1998, Reiser 2007). The mean of the sampled Poisson distribution for each pixel was equal to the value of the detector element (m, n). The noisy projection image is shown in Fig. 3.3. The projection image data was output with a 12-bit pixel depth identical to the output from the x-ray sensor used in Chapter 4.

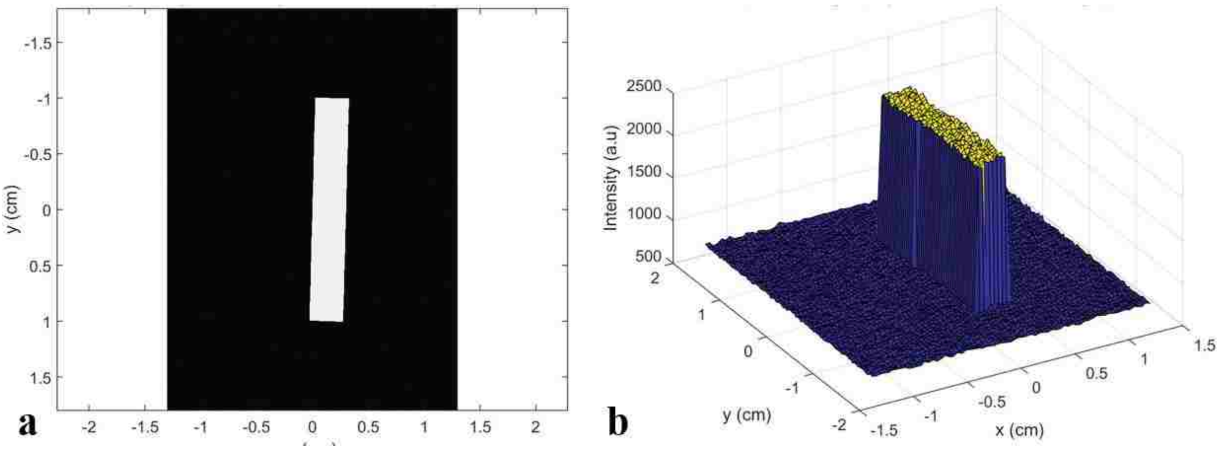

Figure 3.3: (a) Projection image of the edge phantom with added Poisson noise at $x_S = 0$ cm. (b) Surface plot of the projection image with added Poisson noise. The color scale in the (b) is illustrative only.

3.4.2 Point Impulse Phantom Design and Image Simulation

The point impulse phantom was designed using a method previously developed for DBT (Chen 2005, Chen 2007a, Chen 2007b, Chen 2008, Chen 2014), which provided a convenient method to evaluate reconstruction algorithm resolution while controlling or removing sources of error, such as error in source location (Reiser 2014). The simulated point impulse was created by modeling nine delta functions in a plane 1.5 cm above and parallel to the computational detector. The delta functions were modeled such that for the simulated x-ray source located at $(x_S, y_S, z_S) = (0\text{ cm}, 0\text{ cm}, 100\text{ cm})$, the delta functions projected to the center of the computational detector as shown in Fig. 3.4, where $L = (0.019/3)$ mm. For this source position, the centermost delta function projected to $(x_D, y_D, z_D) = (0\text{ cm}, 0\text{ cm}, 0\text{ cm})$. Nine delta functions evenly distributed within an area the size of a single pixel, rather than a single delta function, were used to estimate the average overall point impulse with less sensitivity to location versus pixel boundaries (Chen 2014).

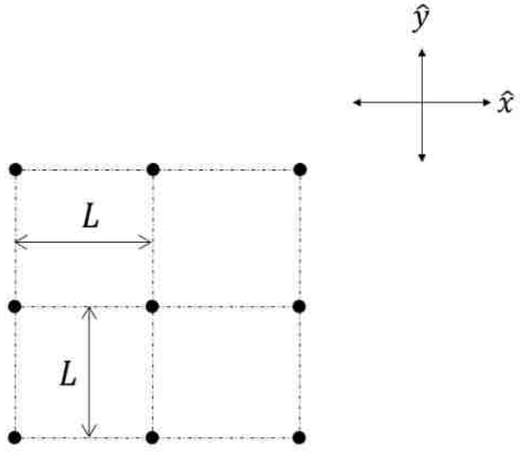

Figure 3.4: Projection of nine simulated delta functions onto the computational detector with the source located at $(x_S, y_S, z_S) = (0\text{ cm}, 0\text{ cm}, 100\text{ cm})$. The projections of the delta functions are equally spaced with $L = (0.019/3)$ mm.

Ray tracing was used to collect an ideal image set of each of the nine delta functions with the source located at 41 discrete locations along $\hat{x}$ with x-ray source travel of ± 40 cm and a spatial step size of 2 cm with $(y_S, z_S) = (0\text{ cm}, 100\text{ cm})$. For delta functions that did not project to an integer computational detector element, linear interpolation was used to proportionately split the delta function magnitude between the nearest four computational detector elements. No noise was added to the projection images; this phantom was used to measure and assess differences between the ideal frequency response of the reconstruction algorithms. By summing the projections of each of the nine delta functions for each discrete source location, the simulated point impulse projection image set was formed. This image set was normalized by the number of delta functions that were modeled and was saved in the same format as the simulated edge phantom images. The projection image of the composite point impulse acquired at $(x_S, y_S, z_S) = (0\text{ cm}, 0\text{ cm}, 100\text{ cm})$ is shown in Fig. 3.5.

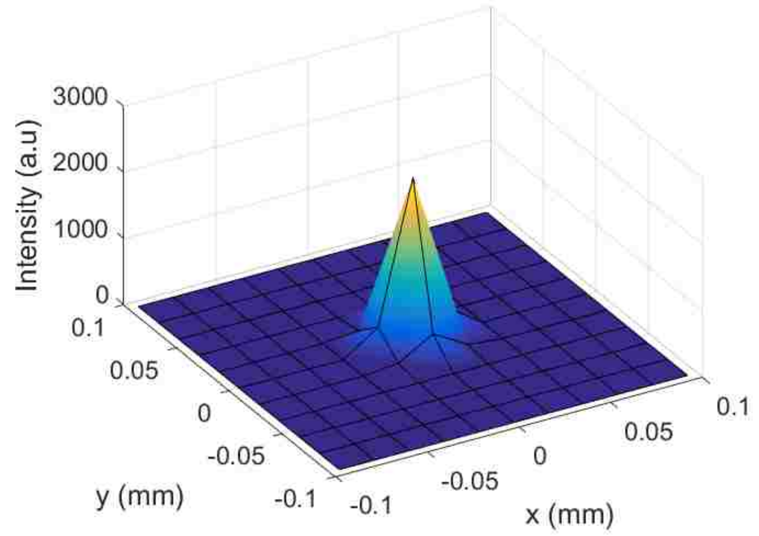

Figure 3.5: Composite point impulse projection image with source location $(x_S, y_S, z_S) = (0\text{ cm}, 0\text{ cm}, 100\text{ cm})$. Only a 0.2 mm by 0.2 mm of the detector is shown for clarity. The color scale is illustrative only.

3.4.3 Source Location Error

In addition to the ideal composite simulated point impulse set created in Section 3.4.2, additional image sets were generated by applying systematic offsets to the source location (x_S, y_S, z_S) during the projection imaging process. This step was performed to assess the impact of systematic source location offset error on reconstruction algorithm resolution. A total of 12 simulated point impulses was created with systematic offsets from the nominal 41 discrete source locations as summarized in Table 3.1. Systematic offsets were only applied in one direction for $\hat{x}$ and $\hat{y}$ because these projection images were symmetric. Offsets in $\hat{z}$ were not symmetric and so projection image sets were created with the source location offset by amounts both closer to and further from the computational detector. Simultaneous source offset errors in $\hat{x}$ and $\hat{z}$ were also investigated by modeling offsets of 1 mm and 3 mm along diagonals in the $\hat{x}, \hat{z}$ plane; preliminary work found that source offset error in $\hat{y}$ had little effect on the reconstruction algorithm MTF, so offsets in the $(\hat{y}, \hat{z})$ plane and $(\hat{x}, \hat{y})$ plane were not investigated.

Table 3.1: Systematic source offsets used to create simulated projection images sets of the nine delta functions. Source location errors in projection x-ray imaging of these typical magnitudes have been previously reported (Lee 2011).

Simulated Point Impulse Number	**Offset in $\hat{x}$ (mm)**	**Offset in $\hat{y}$ (mm)**	**Offset in $\hat{z}$ (mm)**
1	1	0	0
2	3	0	0
3	0	1	0
4	0	3	0
5	0	0	1
6	0	0	3
7	0	0	-1
8	0	0	-3
9	$1/\sqrt{2}$	0	$1/\sqrt{2}$
10	$3/\sqrt{2}$	0	$3/\sqrt{2}$
11	$1/\sqrt{2}$	0	$-1/\sqrt{2}$
12	$3/\sqrt{2}$	0	$-3/\sqrt{2}$

3.5 Tomosynthesis Reconstruction

Three analytical methods of linear parallel tomosynthesis reconstruction were implemented for endoDPT: shift and add (SAA), backprojection (BP), and filtered backprojection (FBP). These analytic techniques are well understood, easily implementable, and often used for evaluation of tomosynthesis imaging systems (Niklason 1997, Wu 2004, Levakhina 2013). For all three reconstruction algorithms, image planes were reconstructed above and parallel to the detector face; these planes have the highest possible in-plane resolution (Dobbins 2003).

3.5.1 Image Pre-Processing

All image reconstruction algorithms used the same image pre-processing prior to reconstruction. The primary purpose of pre-processing was to read in the projection data, to convert the pixel values from 12-bit unsigned integer values to double precision, and to perform a logarithmic transform on the data. This process is summarized in Fig. 3.6.

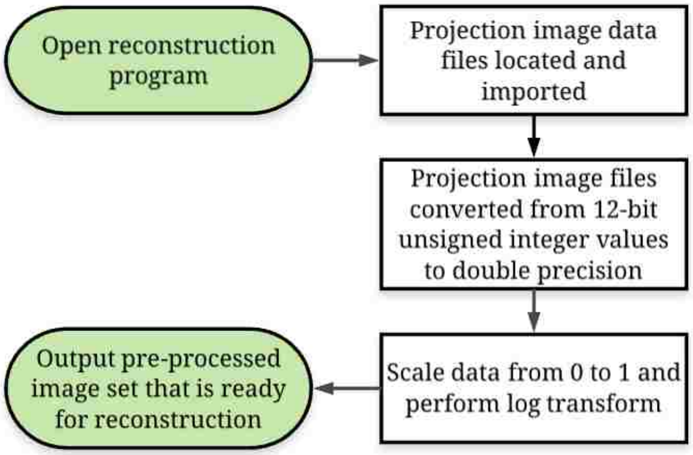

Figure 3.6. Summary of projection image pre-processing used for all endoDPT image reconstruction methods.

The pixel values were converted to double values to maintain precision and to avoid truncation errors during calculations. The logarithmic transform was performed because the value of a given detector pixel in a single projection image is the line integral of all attenuation values over the path length from source to pixel. Unlike CT, the reconstruction algorithms used in this work reconstruct only an approximate attenuation coefficient in the reconstructed image plane through the addition of pixel values from every projection image. Addition of line integrals to find an approximate attenuation coefficient is not a linear process whereas addition of the logarithmic transformed data (which removes the exponential term) is. Dobbins and Godfrey described why this is particularly important in tomosynthesis (Dobbins 2003), and their result is rederived in Appendix B.

3.5.2 Shift and Add

SAA was the first x-ray imaging method capable of reconstructing any arbitrary plane in an imaged volume from a single set of discrete projection images (Ziedses Des Plantes 1938) and remains in clinical use today (Dobbins 2009a). SAA has been thoroughly described and widely used clinically (Niklason 1997, Dobbins 2003, Wu 2004, Chen 2008, Chen 2013, Zhou 2015) and is often a starting point for more advanced algorithms (Dobbins 1990, Chen 2006, Godfrey 2006b).

Image acquisition and reconstruction using SAA with linear parallel tomosynthesis is shown in Fig. 3.7. During image acquisition, the radiographic shadows of the two structures in the imaged volume (the square and triangle) project to the stationary detector, forming projection images. To reconstruct a plane through the imaged volume, the projection images are shifted by amounts dependent on x_{S_i}, z_S, and z (where z is the height of the reconstructed plane above the detector) and are then superimposed. Structures located within the reconstruction plane register while structures located outside of the reconstructed plane blur or smear out.

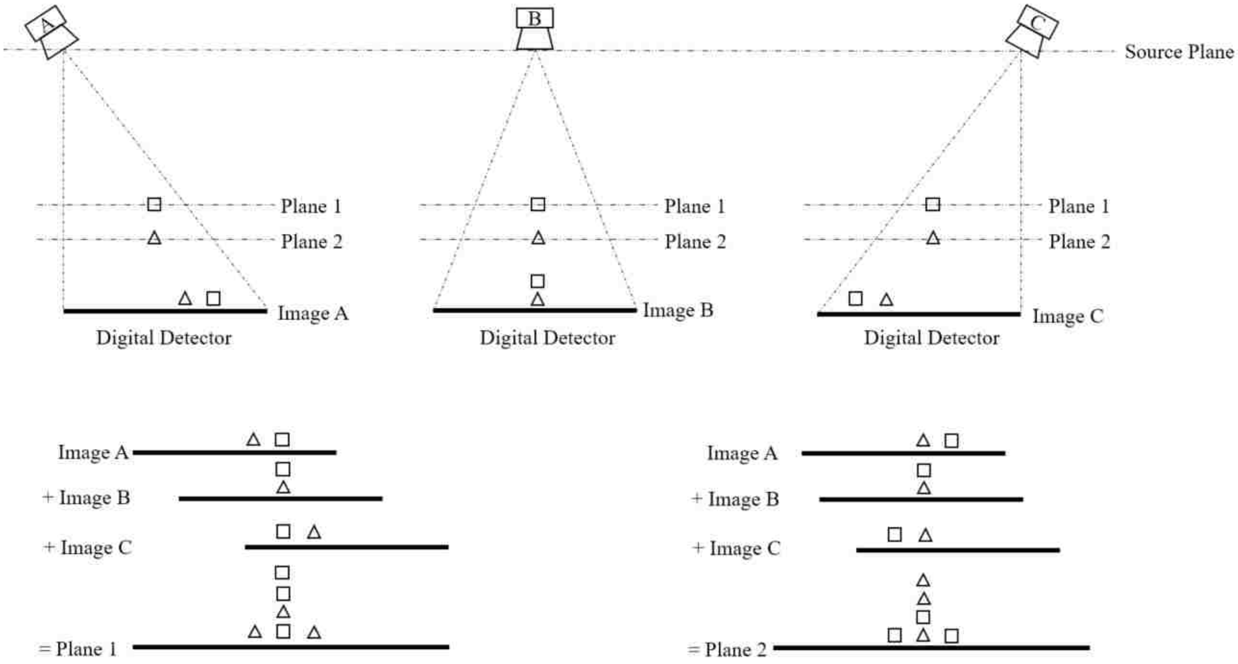

Figure 3.7: Image acquisition and SAA reconstruction of two discrete planes, adapted from (Miller 1971) and (Dobbins 2003).

Fig. 3.7 illustrates the reconstruction of the planes containing either the square or the triangle in the bottom row. Because the square is located farther from the detector, larger shifts are required to register the projection images such that the squares overlap while the triangles blur out across the image. SAA relies on this blurring of OOP structures to make them less noticeable to the observer.

Fig. 3.8 summarizes the SAA algorithm developed for endoDPT. This algorithm can reconstruct any arbitrary image plane located at z above and parallel to the detector plane. The shift $S(x_{S_i}, z_S, z)$ for the i^{th} of N projection images, occurs in the direction of x-ray source motion. $S(x_{S_i}, z_S, z)$ depends only the x-ray source location (x_{S_i}, y_S, z_S) and z. The shift was calculated using a parallel beam assumption. This assumption was required for SAA because each discrete image experiences a single shift (Dobbins 2003). This improved the efficiency of the reconstruction, but results in reduced image quality as one moves off axis in $\hat{x}$ or $\hat{y}$ because beam divergence was ignored

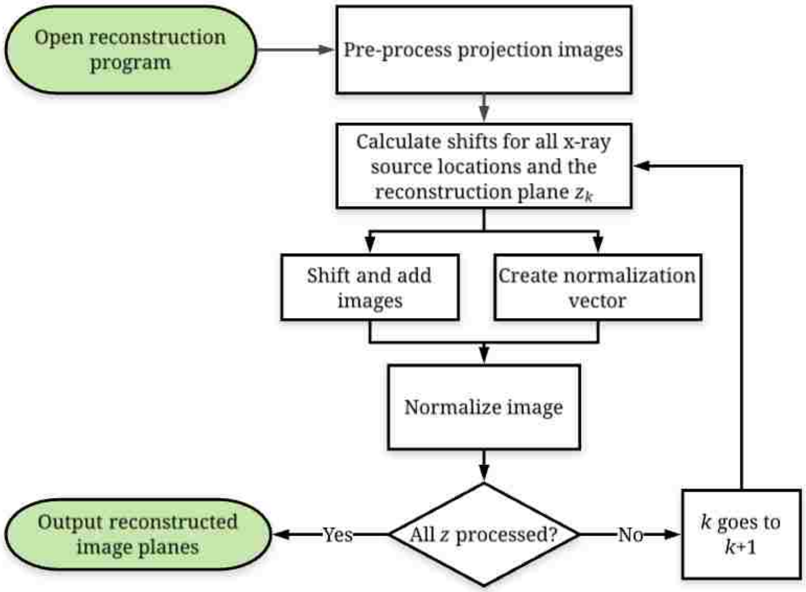

Figure 3.8: Process diagram for the SAA algorithm. Shifts are calculated based on acquisition geometry and the height of reconstruction planes. Images are shifted and added together. The reconstructed image is normalized based on the number of additions that occur for each reconstructed voxel.

Fig. 3.9 shows how the shift was determined for a given projection image. Assuming a parallel beam, the structure P located at height z above the detector plane projects to the detector pixel located at x_{P_0} for source location (x_{S_0}, y_S, z_S). For source location (x_{S_1}, y_S, z_S), P projects to the detector pixel located at x_{P_1}. The difference of x_{P_0} and x_{P_1} was the shift required to register the images such that P_0 and P_1 superimposed in the reconstructed plane. The shift was calculated as

$$S(x_{S_i}, z_S, z) = x_{p_1} - x_{p_0} = \left(\frac{x_{S_i}}{z_S}\right) z \tag{3.3}$$

Due to the parallel beam assumption, the shift was constant for all pixels for a given projection image and occurred only in $\hat{x}$.

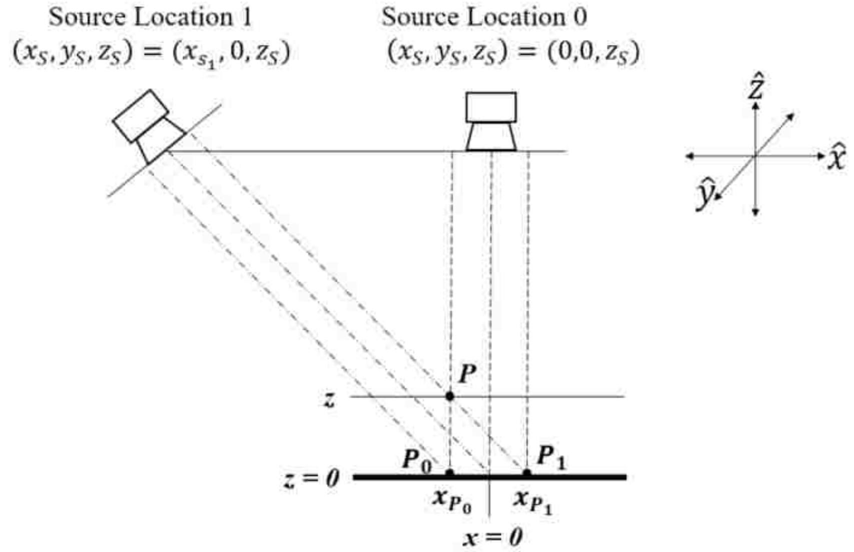

Figure 3.9: SAA shift determination example for a structure P located at height z above the detector plane, using the parallel beam assumption.

After the shifts for each projection image were determined for a given z, the individual projections were shifted relative to the projection obtained at $(0,0,z_S)$ in Fig. 3.9 and summed. Bilinear interpolation was used between the two nearest pixel elements within each row to get the shifted values for the additions. Each reconstructed voxel was normalized by the number of additions occurring in that voxel. This normalization factor was not constant for the entire reconstructed image plane due to the small size of the XDR sensor; for some source locations, some rays projected beyond the detector's edge. Normalizing by the N projection images would result in a severe banding artifact at the image edges perpendicular to the source motion, known as truncation artifact (Sechopoulos 2013b). To minimize this artifact, the number of additions per reconstruction voxel was tracked, similar to a previously developed method for DBT (Li 2007). The primary limitations of endoDPT SAA reconstruction are the parallel beam assumption and the lack of a mechanism for removal of OOP structure blur.

3.5.3 Backprojection

BP is an extension of the SAA algorithm in which beam divergence is modeled. BP has been widely used in tomosynthesis reconstruction (Lauritsch 1998, Dobbins 2003, Wu 2004, Chen 2007b, Chen 2008, Levakhina 2013, Choi 2015, Zhou 2015). Linear parallel tomosynthesis using BP to reconstruct planes above and parallel to the detector plane is illustrated in Fig. 3.10.

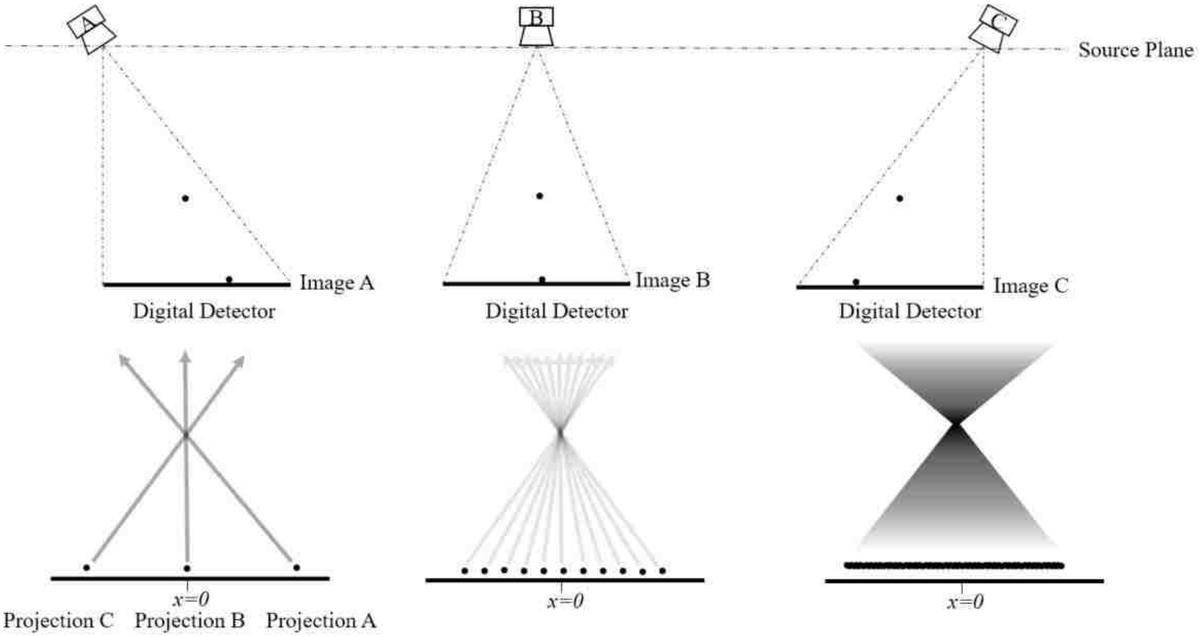

Figure 3.10: Projection imaging (top) and backprojection (bottom) of a point impulse in linear parallel tomosynthesis. The top row shows the acquisition of three discrete projection images. The bottom row shows that the point impulse can be reconstructed by backprojecting the projection image pixel values to the source, going from a very discrete case (three projections, left), a reconstruction more typical of tomosynthesis (11 projections, middle), and the continuous case (infinite projections, right).

The top row of Fig. 3.10 shows the projection imaging process for linear parallel tomosynthesis in two dimensions. The projection imaging process maps the three-dimensional object $f(x, y, z)$

to the projection images $p_i(x_D, y_D, 0)$. The signal values recorded by each detector element (m, n) for each discrete image i are the line integrals of attenuation through $f(x, y, z)$ from the source location (x_{S_i}, y_S, z_S) to $p_i(x_D, y_D, 0)$. To reconstruct $f(x, y, z)$ from the projection images using BP, this process is reversed. For each projection image, rays are traced from each detector element (m, n) to the assumed point source located at (x_{S_i}, y_S, z_S). The value of each detector element (m, n) is added to the voxel in the reconstruction plane, located at height z above and parallel to the detector, that the ray from (m, n) to (x_{S_i}, y_S, z_S) traverses. This operation is performed for all N projection images and is illustrated in the bottom row of Fig. 3.10. Each voxel in the reconstructed image plane is the average of all ray sums that traverse that voxel during the BP process over the entire projection image set. The bottom row of Fig. 3.10 also demonstrates the primary blur artifact associated with the backprojection process. This blur artifact is a primary limitation of image quality for BP.

Assuming a parallel beam, if a point input is located at $(0,0,z)$ above the detector plane and if the x-ray source travels continually over $\pm x_{S,max}$ during a single exposure, an integrating detector records the image as a line of length l given by

$$l = 2z\left(\frac{x_{S,max}}{z_S - z}\right) \tag{3.4}$$

where l describes the imaging geometry as shown in Fig. 3.11. If a constant exposure rate to the integrating detector is assumed for the entire continuous scan and it is assumed that the integrating detector has a linear response, the integrated intensity of the background subtracted complement of line l will be a constant value C. This results in any discrete portion of l, dl, having signal intensity that is inversely proportional to the x-ray source travel distance and the ratio z/z_S for a constant z_S. In the limiting case where the x-ray source travel distance is 0 or $z/z_S = 0$, l becomes a delta function.

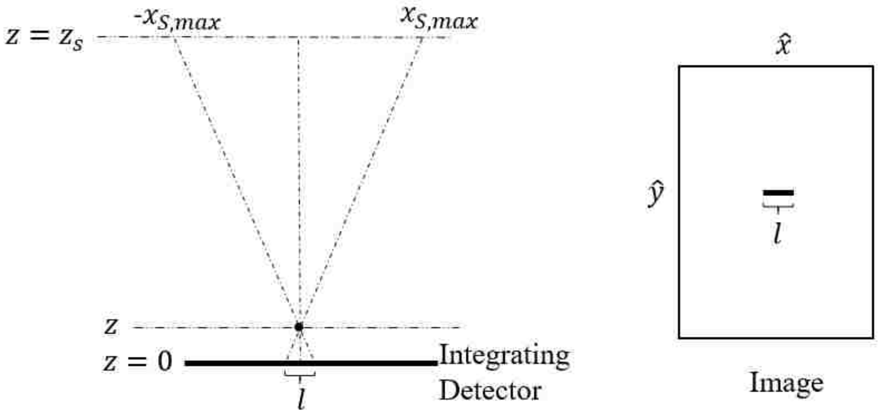

Figure 3.11: Imaging geometry of a point impulse that results in a line of length l on an integrating detector.

Overall, this shows that the line l is a rect function with a constant integrated area of C, which decreases in width and increases in magnitude for smaller x-ray source travel distances and smaller ratios of z/z_S. This is the spatial domain equivalent of the slice transfer function (Grant 1972). The slice transfer function is defined as the Fourier transform of the image of the impulse response; it describes how structures are transferred to reconstructed image planes surrounding the plane they occupy (Grant 1972, Mertelmeier 2014). In linear parallel tomosynthesis, the slice transfer function is the Fourier transform of Eq. 3.4, which is a sinc function given by

$$\int_{-\frac{l}{2}}^{\frac{l}{2}} \mathrm{rect}(x) * e^{-j\omega_x x} dx = \frac{\sin\left(\frac{l}{2} * \omega_x\right)}{\frac{l}{2} * \omega_x} = \mathrm{sinc}\left(\frac{l}{2} * \omega_x\right) \tag{3.5}$$

where $\widehat{\omega}_x$ is the frequency space analog of $\hat{x}$ in the spatial domain. The slice transfer function is constant in $\widehat{\omega}_y$, the frequency space analog of $\hat{y}$ in the spatial domain, due to the parallel beam assumption (Grant 1972).

In linear parallel tomosynthesis, the point impulse response (spatial domain transfer function) can be used to assess how an object located in the plane at z will affect (or be transmitted to) a plane located at $z \pm dz$, where dz is a non-zero value. This is the point spread function, $h_p(x,z)$ (Grant 1972, Haerer 2002, Mertelmeier 2014), given by

$$h_p(x,z) = \frac{1 + \frac{(z_0 - z)^2}{(x_0 - x)^2}}{2\tan\theta_{max} * |(x_0 - x)| \sqrt{1 + \frac{(z_0 - z)^2}{(x_0 - x)^2}}} = \frac{\sqrt{1 + \frac{z^2}{x^2}}}{2\tan\theta_{max} * |x|} \qquad (3.6)$$

for the two-dimensional case shown in Fig. 3.11 with invariance in $\hat{y}$, with the point of interest in the imaged volume located at (x_0, z_0). $h_p(x,z)$ is bound to the sampled region of $(x_0 - x)/(z_0 - z) < \tan(\theta_{max})$, where $\theta_{max} = \tan^{-1}(l/2z)$. This is shown in Fig. 3.12 and is identical to the result obtained by Haerer, Lauritsch, and Zellerho (Haerer 2002).

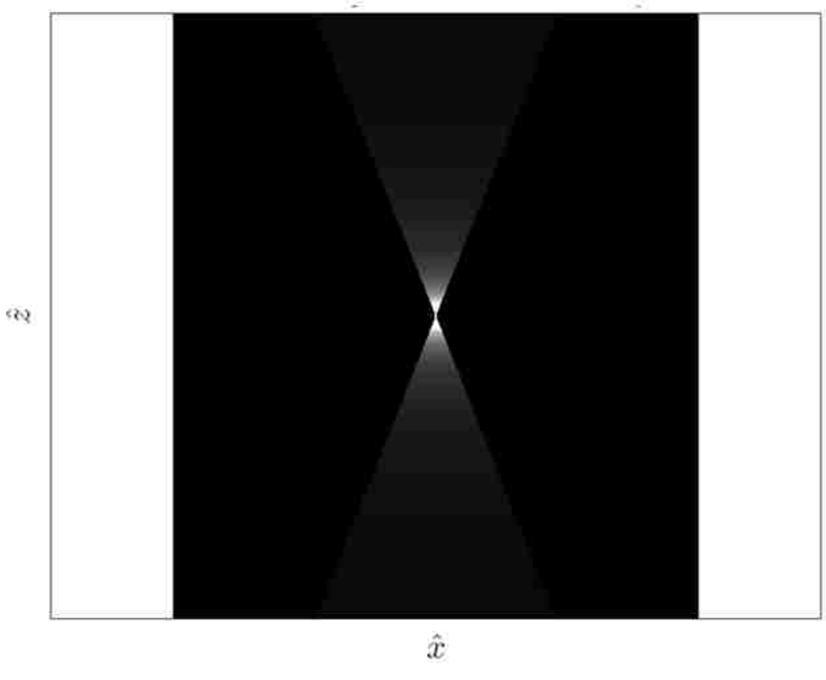

Figure 3.12: The reconstructed point spread function of a point impulse located at $(x_0, 0, z_0)$ in a volume imaged with linear parallel tomosynthesis using endoDPT geometry.

This study used a pixel-by-pixel BP algorithm. The algorithm had the ability to reconstruct any arbitrary image plane above and parallel to the detector plane. The process of the algorithm is summarized in Fig. 3.13. Image planes $R(x, y, z)$ are reconstructed at z above the detector plane with the reconstructed voxel size set to 20 µm by 20 µm using the formalism

$$R(x, y, z) = \mathcal{N}\left[\sum_{i=1}^{N} \mathcal{B}[p_i(x_D, y_D, 0)]\right] \tag{3.7}$$

where N projection images $p_i(x_D, y_D, z_D)$ are reconstructed into $R(x, y, z)$ using $\mathcal{B}$, the backprojection operator, and then normalized using $\mathcal{N}$, the normalization operator.

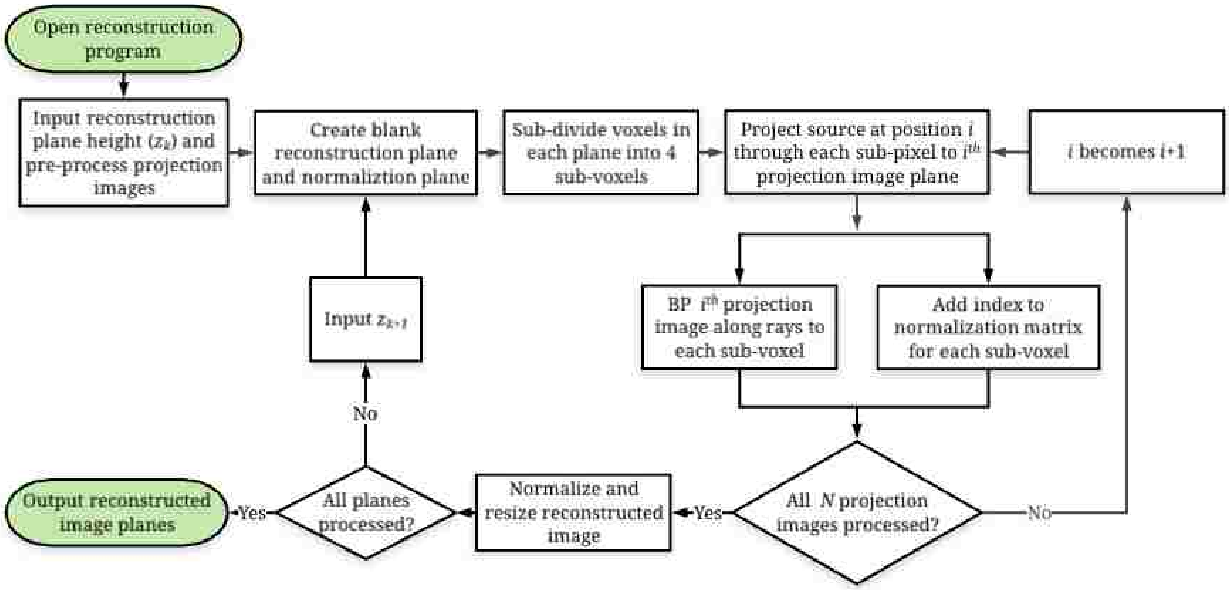

Figure 3.13: Process diagram for the BP Algorithm. Each voxel in the reconstructed plane is divided into 4 sub-voxels. Pixel values from the detector are backprojected to these sub-voxels to form the reconstructed image, which is normalized based on the number of sub-voxels and the number of additions occurring for each sub-voxel.

Prior to backprojection, each voxel in the reconstruction plane was split into four sub-voxels (10 µm per side) to improve sampling from the projection image. To perform the backprojection for each i^{th} source position, a ray was projected from (x_{S_i}, y_S, z_S) through the known center of each sub-voxel in $R(x, y, z)$ to the detector (x_D, y_D, z_D). If the ray projected to the center of a detector pixel, the value of the pixel in the projection image corresponding to (x_D, y_D, z_D) was added to the sub-voxel in the reconstruction plane; if the ray did not project to the center of a detector pixel, linear interpolation between the nearest four detector pixels was used to add a proportional value to the sub-voxel in the reconstruction plane. The (x_D, y_D, z_D) for each source location and each sub-voxel was found by

$$\frac{x_{S_i} - x}{z_S - z} = \frac{x_{S_i} - x_D}{z_S - z_D} = \frac{x_{S_i} - x_D}{z_S} \to x_D = x_{S_i} - \left(\frac{x_{S_i} - x}{z_S - z}\right) * z_S \tag{3.8}$$

and

$$\frac{y_S - y}{z_S - z} = \frac{y_S - y_D}{z_S - z_D} = \frac{y_S - y_D}{z_S} \to y_D = y_S - \left(\frac{y_S - y}{z_S - z}\right) * z_S \tag{3.9}$$

noting that $z_D = 0$, and that the $\hat{x}$ and $\hat{y}$ components are separable. These relationships are illustrated in Fig. 3.14.

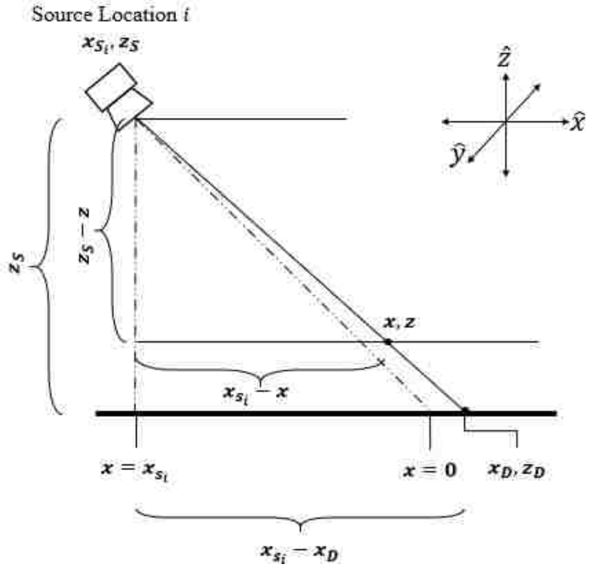

Figure 3.14: Geometry of the backprojection process. Similar triangles were used to derive the equations for projection from the source through the reconstructed image plane to the projection image.

This process was repeated for every sub-voxel in the reconstructed image plane. The sub-voxels were then summed back into their parent voxel in the reconstructed image plane and normalized. This process was repeated for all N projection images, building the reconstructed image plane as the sum of backprojected values from all projections. Like the SAA algorithm, the final reconstructed image voxels were normalized based on the number of additions occurring for each reconstructed voxel to minimize the truncation artifact. BP improves upon SAA by incorporating beam divergence, but like SAA there is no mechanism for blur reduction.

3.5.4 Filtered Backprojection

To reduce the blur inherent in the BP process, a filter can be applied that modifies the projection images prior to BP. FBP is the most common tomosynthesis reconstruction method used for tomosynthesis blur reduction (Dobbins 2003, Chen 2013, Sechopoulos 2013b, Mertelmeier 2014). In tomosynthesis, FBP only reduces the blur; unlike CT, FBP cannot completely remove the blur due to limited sampling (Lauritsch 1998, Wu 2004, Mertelmeier 2014).

Filter design for tomosynthesis reconstruction has been extensively described (Lauritsch 1998, Claus 2004, Wu 2004, Claus 2006, Erhard 2012, Mertelmeier 2014). Typically, the first step in the filtering process is the transformation of the projection images $p_i(x_D, y_D, z_D)$, which are two-dimensional because $z_D = 0$, to frequency space images $P_i(\omega_x, \omega_y)$. A parallel beam is often assumed for filtration because inaccuracies due to limited sampling overpower the inaccuracies due to the divergent x-ray beam, particularly when the source-to-object and SID are large and the detection plane area is small (Stevens 2001, Zhao 2008, Mertelmeier 2014). This is the case for the geometry of endoDPT, which has an assumed source to object (center of prostate) distance of 98.5 cm, a SID of 100 cm, and a detector size of 2.5992 cm by 3.6024 cm. Using the parallel beam assumption, the transformation of the spatial domain projection images to the frequency domain is completed using a one-dimensional Fourier transform along $\hat{x}$. The frequency space projections are filtered with the blur-reduction function, are inverse Fourier transformed along $\widehat{\omega}_x$, and then are backprojected to form reconstructed image planes.

The frequency space projection images are related to the entire frequency space object by the central slice theorem (CST) (Hsieh 2009, Mertelmeier 2014). Due to the limited sampling in tomosynthesis (in endoDPT, the imaged volume is sampled over ± 21.8°), the frequency space projections do not completely sample the frequency space object. A typical tomosynthesis scan results in lines of information in the frequency space as shown in Fig. 3.15, which is often referred to as a double-wedge (Mertelmeier 2014). Because frequency space is not fully sampled, it is impossible to remove all of the blur from BP by filtration (Mertelmeier 2014) and additional considerations are required for the sharp discontinuity between the sampled and unsampled space (Lauritsch 1998) which can result in a ringing artifact in the spatial domain (Mertelmeier 2014).

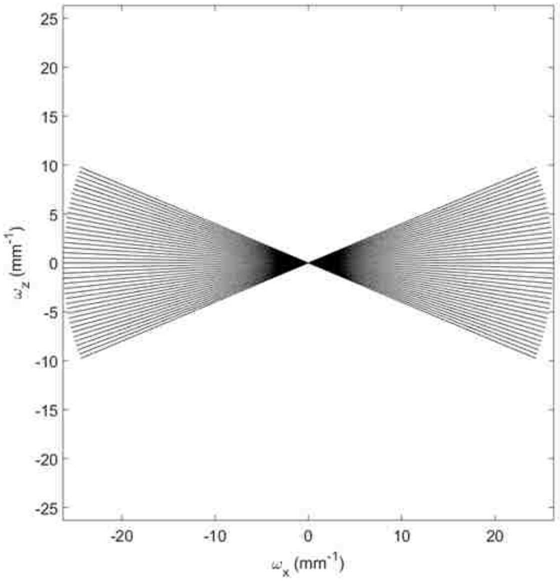

Figure 3.15: Incomplete Fourier space data from projection images collected at different source positions in tomosynthesis. This figure shows the frequency coverage of projections collected over ±40 cm in 2 cm steps with endoDPT geometry.

The steps for tomosynthesis filter design have been described in detail in several previous studies (Lauritsch 1998, Wu 2004, Mertelmeier 2014). The filter design starts with the system equation given by

$$G(\boldsymbol{\omega}) = H(\boldsymbol{\omega}) * F(\boldsymbol{\omega}) \tag{3.10}$$

where $G(\boldsymbol{\omega})$ is the reconstructed object in the frequency domain, $H(\boldsymbol{\omega})$ is the system MTF due to the projection and backprojection imaging process, $F(\boldsymbol{\omega})$ is the true object in the frequency domain, and $\boldsymbol{\omega} = (\omega_x, \omega_y, \omega_z)$.

$H(\boldsymbol{\omega})$ can be split into a projection-backprojection term $H_{P\to BP}(\boldsymbol{\omega})$ which describes how the object blurs due to the projection-backprojection process and a filter term $H_f(\boldsymbol{\omega})$, where $H(\boldsymbol{\omega}) = H_{P\to BP}(\boldsymbol{\omega}) * H_f(\boldsymbol{\omega})$. The goal of the filter term is to approximately invert the blur caused by the projection-backprojection term, $H_f(\boldsymbol{\omega}) \approx [H_{P\to BP}(\boldsymbol{\omega})]^{-1}$, so that the reconstructed object approximates the true object, $G(\boldsymbol{\omega}) \approx F(\boldsymbol{\omega})$.

Because of the invariance in $\widehat{\omega}_y$ due to the parallel beam assumption, $H_f(\boldsymbol{\omega})$ becomes $H_f(\omega_x, \omega_z)$. In tomosynthesis, $H_f(\omega_x, \omega_z)$ is typically divided into three discrete filter functions (Lauritsch 1998, Mertelmeier 2014): $H_{inverse}(\omega_x, \omega_z)$ inverts the Fourier transform of the point impulse response $h_p(x, z)$ from Eq. 3.6 to deblur the reconstructed images; $H_{spectral}(\omega_x)$ reduces noise exacerbated by $H_{inverse}(\omega_x, \omega_z)$; and $H_{profile}(\omega_z)$ addresses the sharp discontinuity observed in Fig. 3.15 between the sampled and unsampled data in the frequency space. In the simplest form, $H_{spectral}(\omega_x)$ and $H_{profile}(\omega_z)$ are windowing functions (Mertelmeier 2014), such as Hanning windows given by

$$H_{spectral}(\omega_x) = \begin{cases} \frac{1}{2}\left(1 + \cos\left(\frac{\pi\omega_x}{A}\right)\right), & \text{if } |\omega_x| \leq A \\ 0 & \text{otherwise} \end{cases} \tag{3.11}$$

and

$$H_{profile}(\omega_z) = \begin{cases} \frac{1}{2}\left(1 + \cos\left(\frac{\pi\omega_z}{B}\right)\right), & \begin{array}{c}\text{if } |\omega_z| \leq B \text{ and} \\ |\omega_z| < \tan(\theta_{max})\,|\omega_x|\end{array} \\ 0 & \text{otherwise} \end{cases} \tag{3.12}$$

where A and B are tunable parameters.

Because the axis of the x-ray source was on the central pixel of the x-ray sensor for endoDPT, the two-dimensional filter can be reduced to single-dimensionality through use of the cosine function (Wu 2004) as

$$H_f(\omega_x, \omega_z) = H_f(\omega_x) * \cos(\theta_i) \tag{3.13}$$

where $-\frac{1}{2\Delta} \leq \omega_x \leq \frac{1}{2\Delta}$, Δ is the pixel size, and θ_i is the angle the parallel x-ray beam makes relative to $\hat{z}$ for the i^{th} projection image. A filter with single-dimensionality was chosen for initial development of endoDPT because it reduced the number of tunable parameters; conceptually, application of $H_f(\omega_x) * \cos(\theta_i)$ to the frequency space projection images is equivalent to filtration in CT which is robust and well understood (Wu 2004). Full details on this transformation are reported by Wu *et al.* (Wu 2004). The filter for endoDPT becomes

$$H_f(\omega_x) * \cos(\theta_i) = H_{inverse}(\omega_x) * H_n(\omega_x) * \cos(\theta_i) \tag{3.14}$$

where $H_{inverse}(\omega_x)$ is the inverse of the point spread function given in Eq. 3.6 in the frequency domain at $\omega_Z = 0$ and is given by (Haerer 2002)

$$H_{inverse}(\omega_x) = 2 \tan \theta_{max} * |\omega_x| \tag{3.15}$$

and $H_n(\omega_x)$ is a Hanning window given by

$$H_n(\omega_x) = \begin{cases} \frac{1}{2}\left(1 + \cos\left(\frac{\pi\omega_x}{a}\right)\right), & \text{if } \omega_x \leq a \\ 0 & \text{otherwise} \end{cases} \tag{3.16}$$

where a is a tunable cutoff parameter. For this work, $a = 20\ \text{mm}^{-1}$; $20\ \text{mm}^{-1}$ corresponds to 0.025 mm in the spatial domain and was twice the spatial frequency (one-half the size) of the smallest structure expected to be visualized in this study, the shell of a typical LDRBT seeds (0.05 mm thickness). The filter used for the projection image taken at $(x_S, y_S, z_S) = (0\ \text{cm}, 0\ \text{cm}, 100\ \text{cm})$ is shown in Fig. 3.16. Wu *et al.* reported that this method of FBP had good results compared to iterative techniques (Wu 2004).

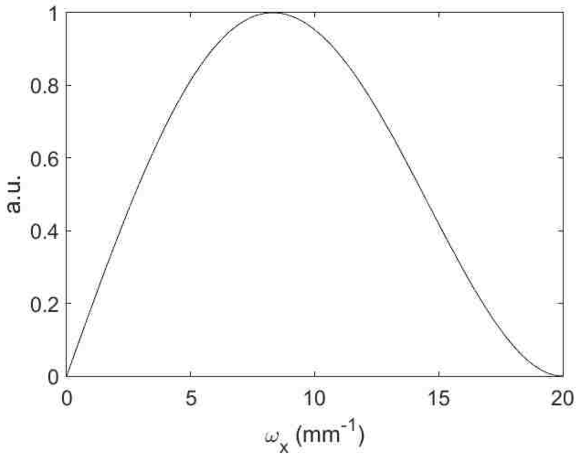

Figure 3.16: endoDPT filter for the image taken at $(x_S, y_S, z_S) = (0\text{ cm}, 0\text{ cm}, 100\text{ cm})$.

The frequency space projection images were filtered by multiplying each row along $\widehat{\omega}_x$ by $H_f(\omega_x) \cdot \cos(\theta_i)$ where $\theta_i = \tan^{-1}(x_{S_i}/z_S)$. Because of the parallel beam assumption, all rows (along $\widehat{\omega}_y$) in a given projection had the same filter applied. After filtration, the frequency space projection images were transformed back to the spatial domain and then reconstructed with BP. Alternatively, one could interpolate in frequency space followed by a two-dimensional transformation directly to the reconstructed image in the spatial domain (no BP needed), but interpolation artifacts in frequency space can be severe (Hsieh 2009).

OOP structure blur is not eliminated in FBP reconstruction, but is reduced compared to SAA and BP. More advanced FBP techniques and algebraic reconstruction methods can further reduce the OOP structure blur, but were not explored in this study. An additional artifact in FBP due to the filtration is an overshoot, or edge-enhancement, artifact (Nett 2007, Reiser 2007, Sechopoulos 2013b, Mertelmeier 2014). This artifact occurs due to the application of $H_{inverse}(\omega)$ on a set of projections that did not fully sample the object (a limited angle scan of less than 180°). The overshoot artifact manifests as a dark border along edges of objects in the direction of x-ray source motion (Mertelmeier 2014).

3.6 Computational Detector Resolution

The detector MTF ($\mathrm{MTF_{detector}}$) was measured using an edge method (Samei 1998) that has been widely employed for measurement of the resolution of digital imaging systems (Saunders 2003, Saunders 2005, Chen 2007a, Chen 2014). To find the computational $\mathrm{MTF_{detector}}$, profiles were measured perpendicular to the sharp edge of the edge phantom modeled in Section 3.4.1. Multiple profiles were averaged to form a composite edge spread function (ESF), which was differentiated to find the line spread function (LSF). The Fourier transform of the LSF is $\mathrm{MTF_{detector}}$.

Proper calculation of $\mathrm{MTF_{detector}}$ requires the profiles to be orthogonal to the edge, so one must account for any tilt angle of the edge relative to the detector pixel grid. To find this angle the image was first cropped to the edge region of interest (Fig. 3.17 a) and then binarized. A MATLAB® function was used to find the edge in the image using Sobel's method (Sobel 1968) (Fig. 3.17 b). The Radon transform (Radon 1917) was used to find the angle of the edge line. First, a coarse Radon transform ($0° \pm 15°$ in $0.5°$ increments) was taken of the edge. A Gaussian function was fit to each angle bin in the resultant sinogram, and the angle bin with the maximum amplitude of the Gaussian peak was the coarse angle of the edge, θ_{coarse}. A second Radon transform ($\theta_{\mathrm{coarse}} \pm 1°$ in $0.01°$ increments) was taken of p_{edge}. A Gaussian function was fit to each angle bin in the resultant sinogram, with the angle bin with the maximum amplitude of the Gaussian peak resulting in the edge angle θ. This method could exactly reproduce the known tilt angle ($1.50°$) of the computational edge phantom.

Eight hundred profiles that were perpendicular to the edge ($\theta + 90°$) and extended 1 mm to either side of the edge were measured over a 1.52 mm length of the edge in increments of 0.1 pixel

(Fig. 3.18 a). Measuring the profiles in increments of 0.1 pixels results in a pre-sampled MTF that minimizes aliasing effects (Samei 1998). A single profile is shown in Fig. 3.18 (b).

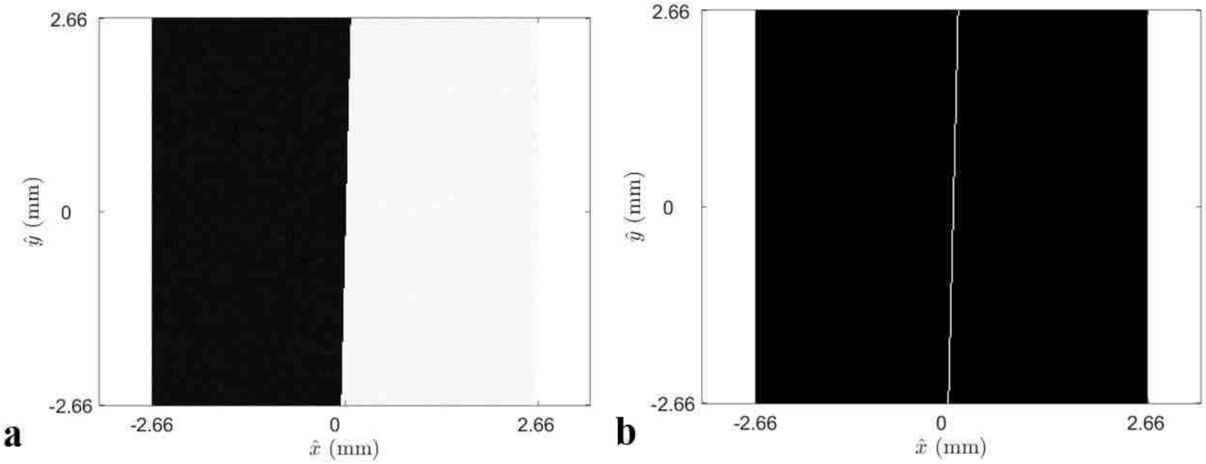

Figure 3.17: (a) Cropped image of the simulated (noisy) projection image of the edge phantom. (b) An edge finding function was applied to the binary image to find the edge.

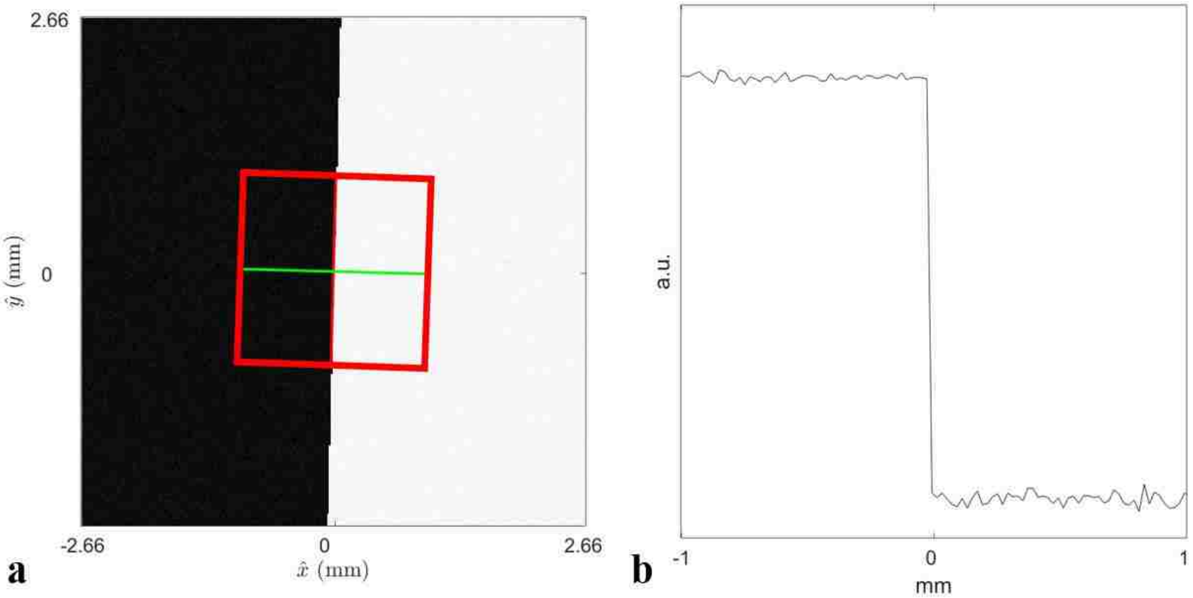

Figure 3.18: (a) The location of one profile (green) and the total region along the edge used for measurement of ESFs (red line). A red box is drawn around the sampled region for clarity. (b) The profile shown by the green line in the left pane, showing Poisson noise. The portion of the profile with more attenuation (under the attenuating edge) shows more noise.

If a measured point on the profile did not fall on the center of a pixel, linear interpolation between the four neighboring pixels was used. The profiles were averaged to form a composite ESF (Fig. 3.19). The composite ESF was differentiated to find the LSF, also shown in Fig. 3.19. The tails of the LSF were fit with a linear function and then corrected for decreased photon fluence due to inverse squared falloff. In addition, a Hanning window (cutoff of 2 mm) was applied to the LSF to reduce the effect of high frequency noise in the tails (Samei 1998). Finally, the LSF was Fourier transformed, resulting in the computational $\mathrm{MTF}_{\mathrm{detector}}$. The MTF was normalized to unit magnitude at zero frequency, as is customary.

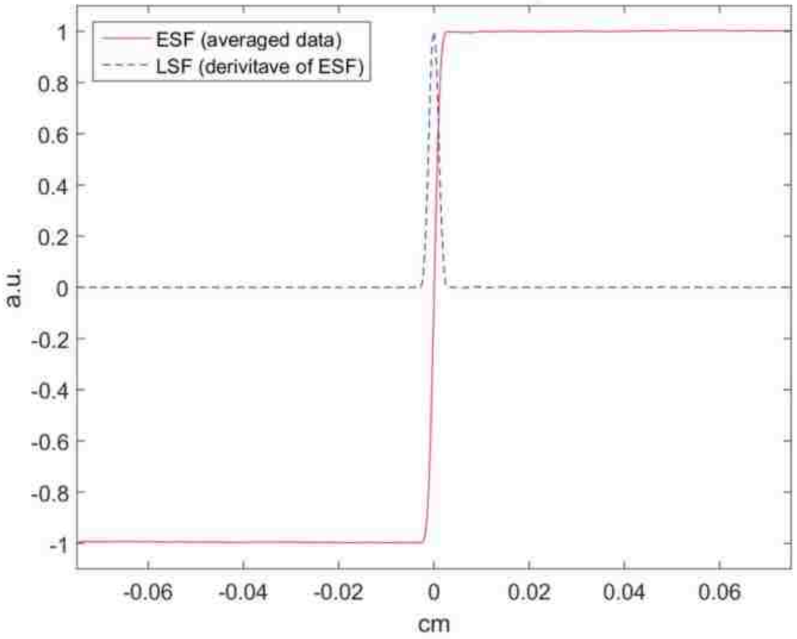

Figure 3.19: The composite ESF and LSF derived from the noisy simulated edge image.

3.7 Reconstruction Algorithm Resolution

The reconstruction algorithm resolution was measured using methodology that has been previously described (Chen 2007a, Chen 2008, Chen 2014). The projection images of the simulated delta functions (see Section 3.4.2 and Section 3.4.3) were reconstructed using SAA, BP, and FBP. All image sets were reconstructed assuming the same geometry as in Section 3.4.2. Fig.

3.20, Fig. 3.21, and Fig. 3.22 show the reconstructed images of the point impulse projection images with no source location error, reconstructed using SAA, BP, and FBP, respectively, at $z = 1.5$ cm above the detection plane.

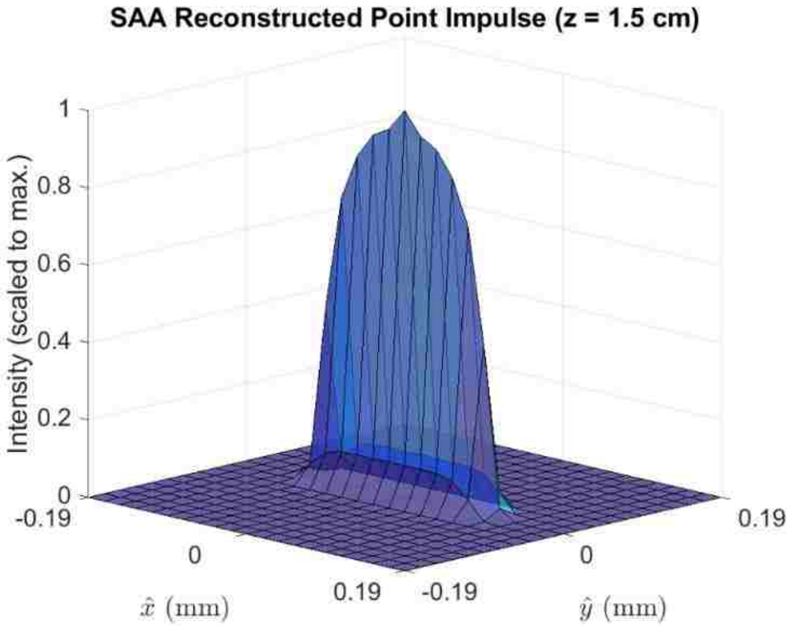

Figure 3.20: Reconstruction of point impulse projection data at $z = 1.5$ cm using SAA. The plot was normalized to the maximum value.

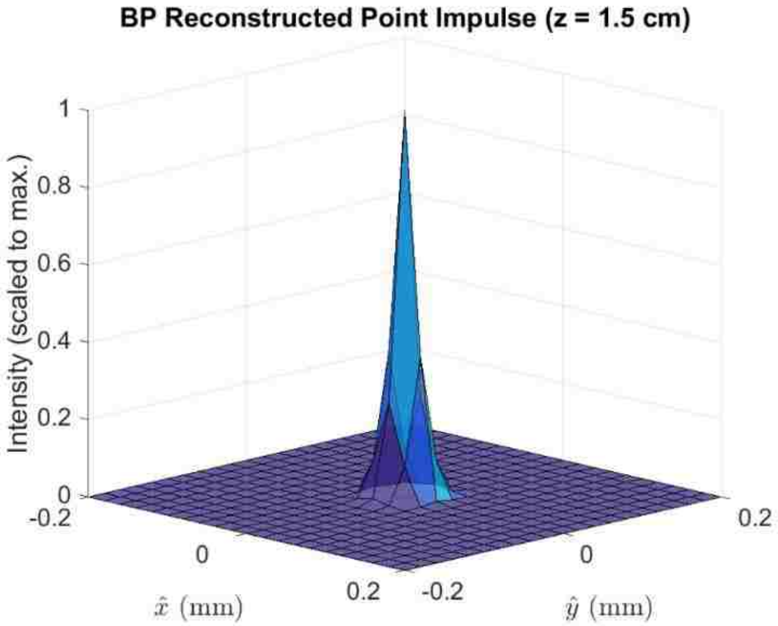

Figure 3.21: Reconstruction of point impulse projection data at $z = 1.5$ cm using BP. The plot was normalized to the maximum value.

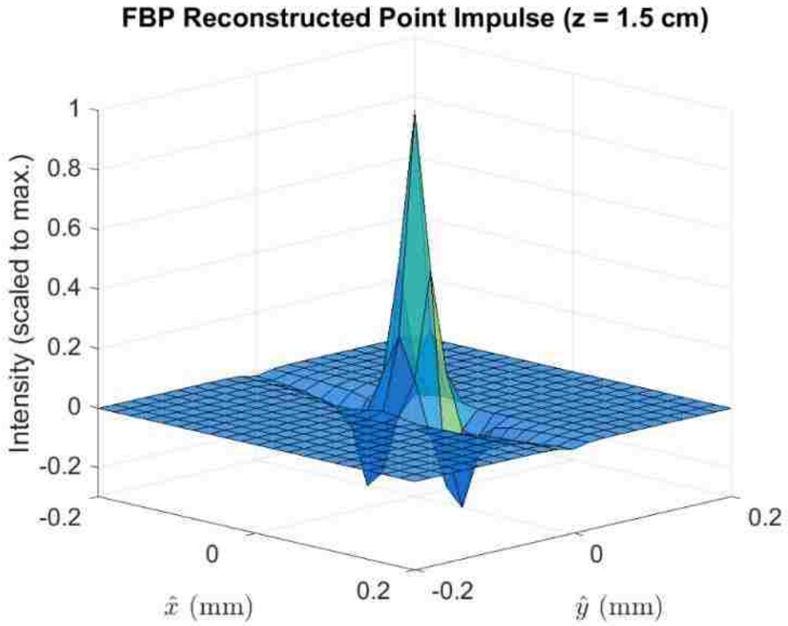

Figure 3.22: Reconstruction of point impulse projection data at $z = 1.5$ cm using FBP. The plot was normalized to the maximum value. The negative side lobes adjacent to the peak are the overshoot artifact.

For these reconstructed point impulses, the entire image set (all 41 images) was used for the reconstruction. Because the SAA algorithm assumed a single shift for each projection image, the point impulse function spreads in the reconstructed plane in the scan direction – this is a limitation of SAA (Chen 2007b). The BP and FBP profiles were sharper in the scan direction due to incorporation of divergent beam geometry. FBP displayed the characteristic edge-enhancement artifact in the direction of scan motion associated with the filtration process (Mertelmeier 2006, Mertelmeier 2014).

In addition to reconstructing the simulated point impulse projection images using all source locations, the point impulse was also reconstructed using smaller x-ray source travel distances and/or larger spatial step sizes to assess the effect of these parameters. The combinations of these parameters are summarized in Table 3.2. The composite point impulse image sets with source location error (Section 3.4.3) were reconstructed using the same procedure and assumed source locations as described above for the ideal image set.

Table 3.2: Combinations of x-ray source travel and spacings used to reconstruct the point impulse phantom.

X-ray source travel (cm)	Spatial step size in $\hat{x}$ between images (cm)	Number of images used
-40 to 40	2	41
-40 to 40	4	21
-40 to 40	8	11
-20 to 20	2	21
-20 to 20	4	11
-10 to 10	2	11

To find the reconstruction algorithm resolution, the profile that traversed the point of maximum intensity in the reconstructed point impulse along $\hat{x}$ was Fourier transformed, which resulted in the reconstruction algorithm MTF $(\mathrm{MTF_{recon}})$. $\mathrm{MTF_{recon}}$ was measured for all point impulse image sets, all reconstruction methods, and all combinations of source travel and step size. $\mathrm{MTF_{recon}}$ was normalized to unit magnitude at zero frequency for SAA and BP, as is customary. For FBP, $\mathrm{MTF_{recon}}$ was normalized to unit magnitude at the point of maximum intensity on the FBP $\mathrm{MTF_{recon}}$ curve; due to the limited sampling of the object, much of the low frequency information in FBP is removed, and the FBP $\mathrm{MTF_{recon}}$ was therefore relative.

3.8 Results

3.8.1 Computational Detector Resolution

Fig. 3.23 shows the pre-sampled computational $\mathrm{MTF_{detector}}$ of the simulated edge images. The frequency values at which $\mathrm{MTF_{detector}}$ was reduced to 90%, 50%, and 10% of the maximum value at zero frequency were 9.3 mm^{-1}, 23.1 mm^{-1}, and 38.6 mm^{-1} for the noiseless image. The addition of Poisson noise did not have a substantial effect on the measured MTF due to the large number of profiles used to determine the average detector MTF; 800 profiles were measured over the 1.52 mm length of the edge in increments of 0.1 pixel.

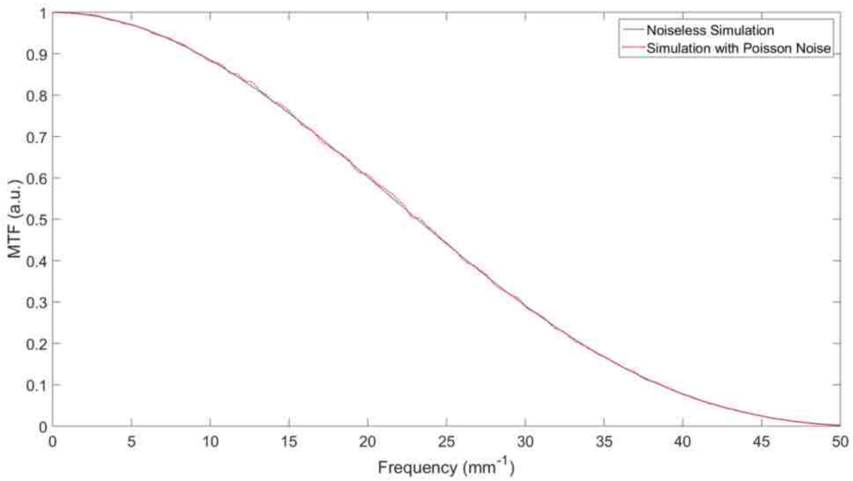

Figure 3.23: Pre-sampled $\mathrm{MTF}_{\mathrm{detector}}$ of the simulated edge image with and without added Poisson noise.

3.8.2 Reconstruction Algorithm Resolution

Fig. 3.24, Fig. 3.25, and Fig. 3.26 show $\mathrm{MTF}_{\mathrm{recon}}$ curves generated from the reconstructed point impulses with no source location error for each reconstruction algorithm using the source travel and step size given in Table 3.2. The 90%, 50%, and 10% $\mathrm{MTF}_{\mathrm{recon}}$ for SAA for all reconstruction parameters are given in Table 3.3. The 90% and 50% $\mathrm{MTF}_{\mathrm{recon}}$ for BP for all reconstruction parameters are given in Table 3.4; note that the BP $\mathrm{MTF}_{\mathrm{recon}}$ was not reduced to 10% over the frequency range investigated, possibly due to aliasing (pre-sampling was not used for measurement of $\mathrm{MTF}_{\mathrm{recon}}$). A similar effect was observed in the study this aim was modeled from (Chen 2007a). Table 3.5 gives the frequency of the point of the maximum $\mathrm{MTF}_{\mathrm{recon}}$ for FBP for all reconstruction parameters. The FBP $\mathrm{MTF}_{\mathrm{recon}}$ was not normalized to $\mathrm{MTF}_{\mathrm{recon}}(0) = 1$; low-frequency information in the projections was removed using the endoDPT filter $2 \tan \theta_{max} * |\omega_x|$ and was not fully reintroduced to the image due to sampling over a limited angular range of $21.8°$. In contrast, CT reconstruction using $> 180°$ angular sampling theoretically fully reintroduces the low frequency information. Normalization to $\mathrm{MTF}_{\mathrm{recon}}(0)$ was therefore not meaningful (Chen 2007a) and the FBP $\mathrm{MTF}_{\mathrm{recon}}$ was normalized to its maximum value; this made it a relative measure that demonstrated an artificially improved frequency response in comparison to BP.

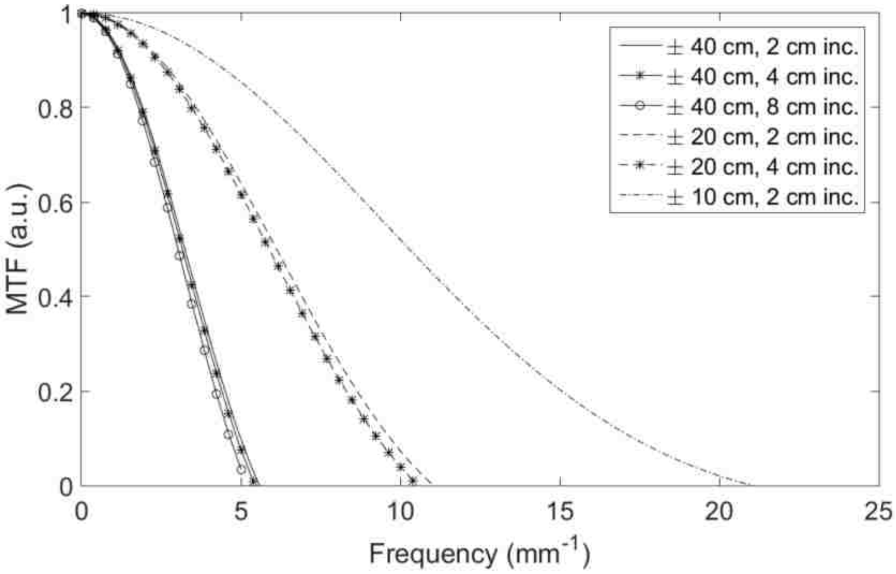

Figure 3.24: $\mathrm{MTF_{recon}}$ for SAA reconstruction with no source localization error for various combinations of x-ray source travel and spatial step size (inc).

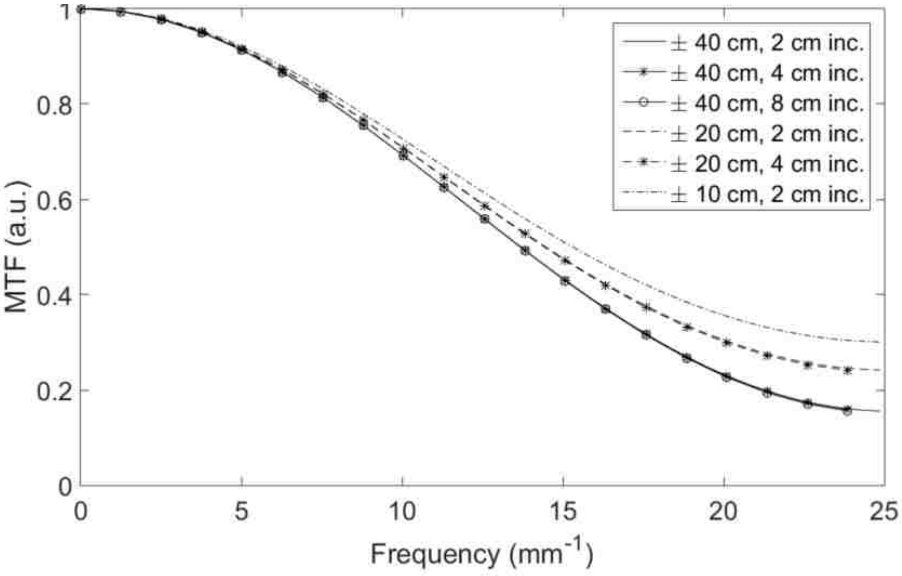

Figure 3.25: $\mathrm{MTF_{recon}}$ for BP reconstruction with no source localization error for various combinations of x-ray source travel and spatial step size (inc).

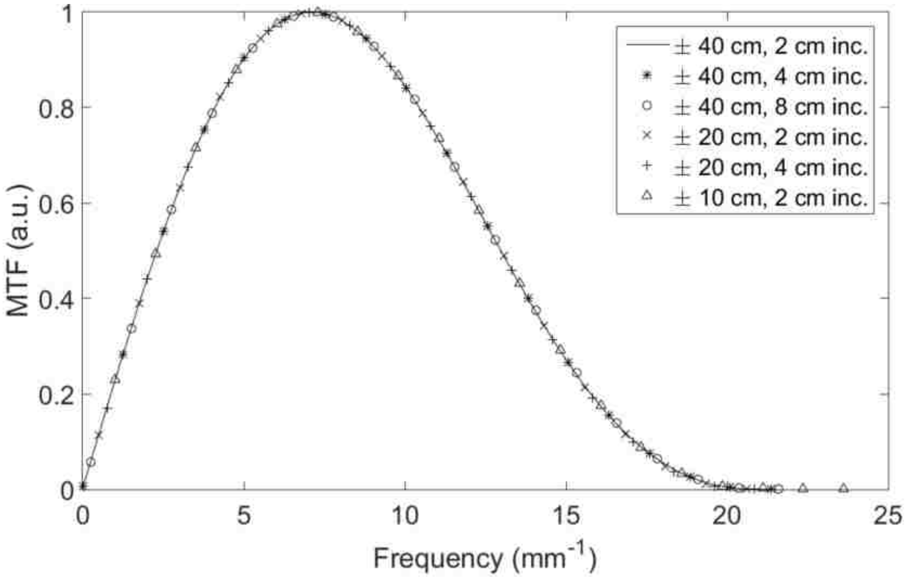

Figure 3.26: MTF curves for FBP reconstruction with no source localization error for various combinations of x-ray source travel and spatial step size (inc).

Table 3.3: Summary of $\mathrm{MTF}_{\mathrm{recon}}$ for SAA using various combinations of x-ray source travel and spatial step size (inc).

Reconstruction Parameters	Frequency of 90% MTF (mm^{-1})	Frequency of 50% MTF (mm^{-1})	Frequency of 10% MTF (mm^{-1})
-40 cm to 40 cm, 2 cm inc.	1.33	3.25	4.99
-40 cm to 40 cm, 4 cm inc.	1.30	3.17	4.88
-40 cm to 40 cm, 8 cm inc.	1.25	3.03	4.66
-20 cm to 20 cm, 2 cm inc.	2.49	6.12	9.68
-20 cm to 20 cm, 4 cm inc.	2.40	5.89	9.29
-10 cm to 10 cm, 2 cm inc.	4.09	10.29	17.32

Table 3.4: Summary of $\mathrm{MTF}_{\mathrm{recon}}$ for BP using various combinations of x-ray source travel and spatial step size (inc).

Reconstruction Parameters	Frequency of 90% MTF (mm^{-1})	Frequency of 50% MTF (mm^{-1})
-40 cm to 40 cm, 2 cm inc.	5.38	13.65
-40 cm to 40 cm, 4 cm inc.	5.38	13.64
-40 cm to 40 cm, 8 cm inc.	5.38	13.62
-20 cm to 20 cm, 2 cm inc.	5.49	14.42
-20 cm to 20 cm, 4 cm inc.	5.49	14.37
-10 cm to 10 cm, 2 cm inc.	5.65	15.25

Table 3.5: Summary of $\mathrm{MTF}_{\mathrm{recon}}$ for FBP using various combinations of x-ray source travel and spatial step size (inc).

Reconstruction Parameters	Frequency of maximum relative MTF (mm^{-1})
-40 cm to 40 cm, 2 cm inc.	7.08
-40 cm to 40 cm, 4 cm inc.	7.08
-40 cm to 40 cm, 8 cm inc.	7.08
-20 cm to 20 cm, 2 cm inc.	7.08
-20 cm to 20 cm, 4 cm inc.	7.08
-10 cm to 10 cm, 2 cm inc.	7.08

3.8.3 Reconstruction Algorithm Resolution with Source Location Error

Fig. 3.27-3.29 show $\mathrm{MTF}_{\mathrm{recon}}$ curves generated from the reconstructed point impulse with no source location error (Section 3.4.2) and with source location error (Section 3.4.3) for SAA reconstruction. Fig. 3.30-3.32 show $\mathrm{MTF}_{\mathrm{recon}}$ curves generated from the reconstructed point impulse with no source location error (Section 3.4.2) and with source location error (Section 3.4.3) for BP reconstruction. Fig. 3.33-3.35 show $\mathrm{MTF}_{\mathrm{recon}}$ curves generated from the reconstructed point impulse with no source location error (Section 3.4.2) and with source location error (Section 3.4.3) for FBP reconstruction.

All the data shown in Fig. 3.27-3.35 are for the tomosynthesis scan with ± 40 cm source travel and 2 cm step size. The same trends seen for various combinations of x-ray source travel and spatial step size are expected, although the source location error can change the magnitude of the trends. The largest x-ray source travel (± 40 cm) and smallest spatial step size (2 cm) were used because they result in the largest reconstructed plane cm field of view (FoV) with the finest sampling. All future endoDPT tomosynthesis scans (Chapter 4 and Chapter 5) were acquired using ± 40 cm source travel and 2 cm step size because a typical prostate has an average diameter of 3 cm; using the largest reconstructed image plane possible reduces the propensity for truncation artifact and other detractors of image quality.

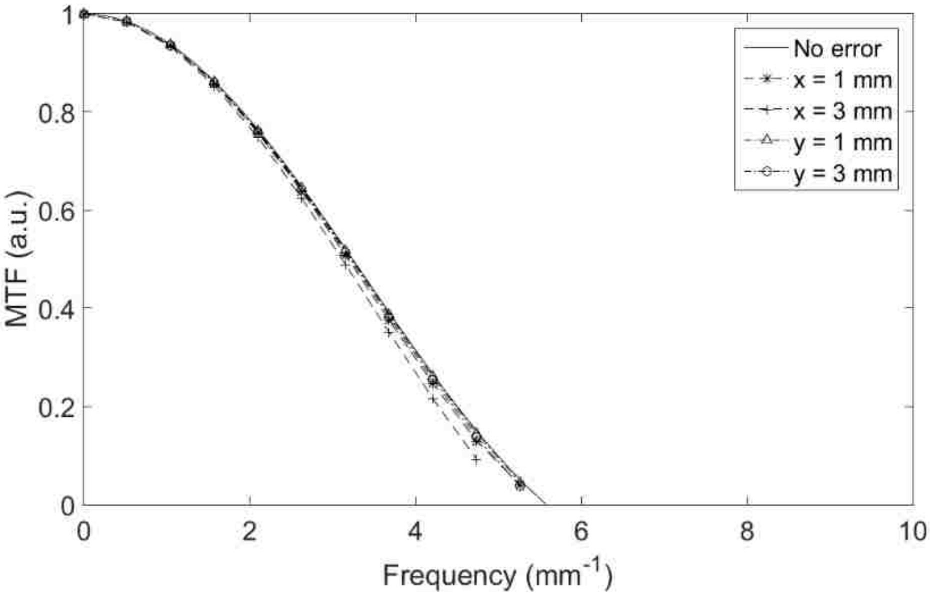

Figure 3.27: $\mathrm{MTF_{recon}}$ for SAA reconstruction with ± 40 cm source travel and 2 cm step size with source location error in $+\hat{x}$ and $+\hat{y}$. MTF curves for error in $-\hat{x}$ and $-\hat{y}$ were not generated because of symmetry in the endoDPT geometry. Note the shorter frequency range compared to BP and FBP, used here for clarity.

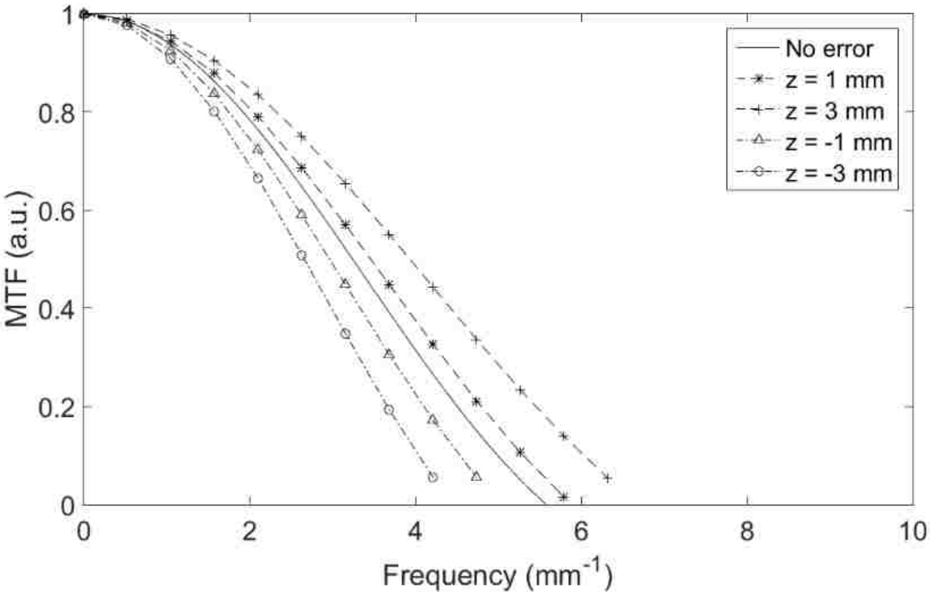

Figure 3.28: $\mathrm{MTF_{recon}}$ for SAA reconstruction with ± 40 cm source travel and 2 cm step size with source location error in $+\hat{z}$ and $-\hat{z}$. Note the shorter frequency range compared to BP and FBP, used here for clarity.

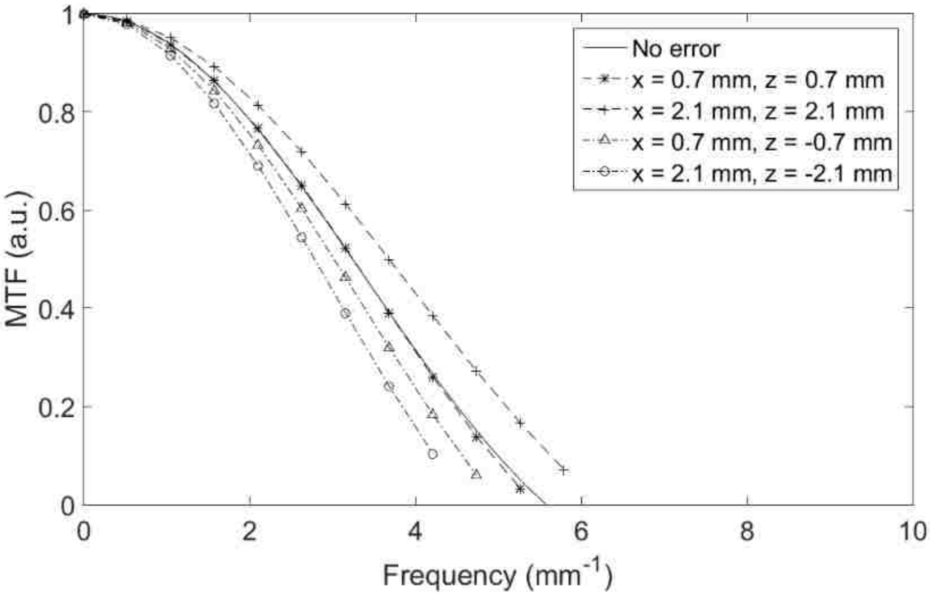

Figure 3.29: $\mathrm{MTF}_{\mathrm{recon}}$ for SAA reconstruction with ± 40 cm source travel and 2 cm step size. The total source location error is $\sqrt{x^2 + z^2}$, where the x and z values used in each plot are given in the legend. Note the shorter frequency range compared to BP and FBP, used here for clarity.

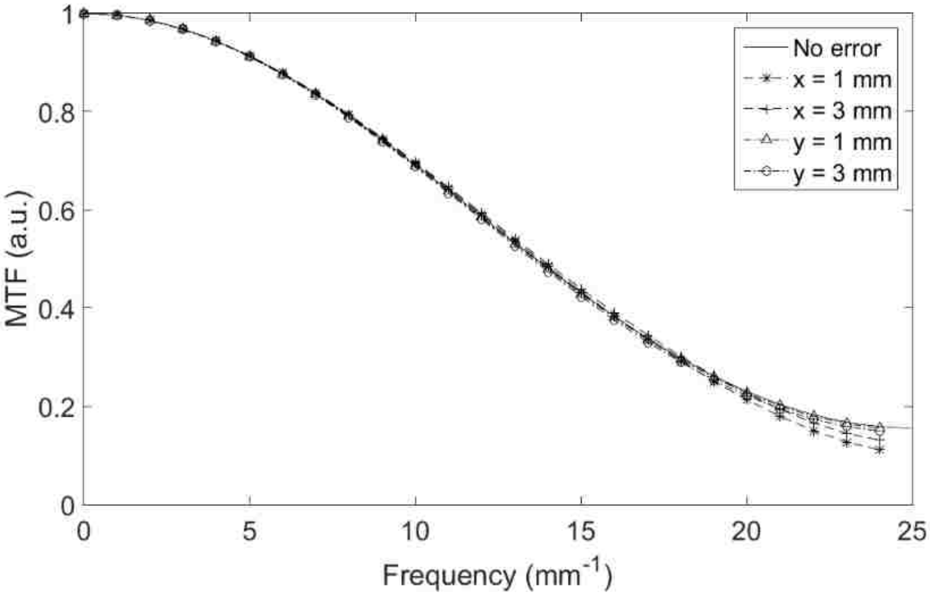

Figure 3.30: $\mathrm{MTF}_{\mathrm{recon}}$ for BP reconstruction with ± 40 cm source travel and 2 cm step size with source location error in $+\hat{x}$ and $+\hat{y}$. MTF curves for error in $-\hat{x}$ and $-\hat{y}$ were not generated because of symmetry in the endoDPT geometry.

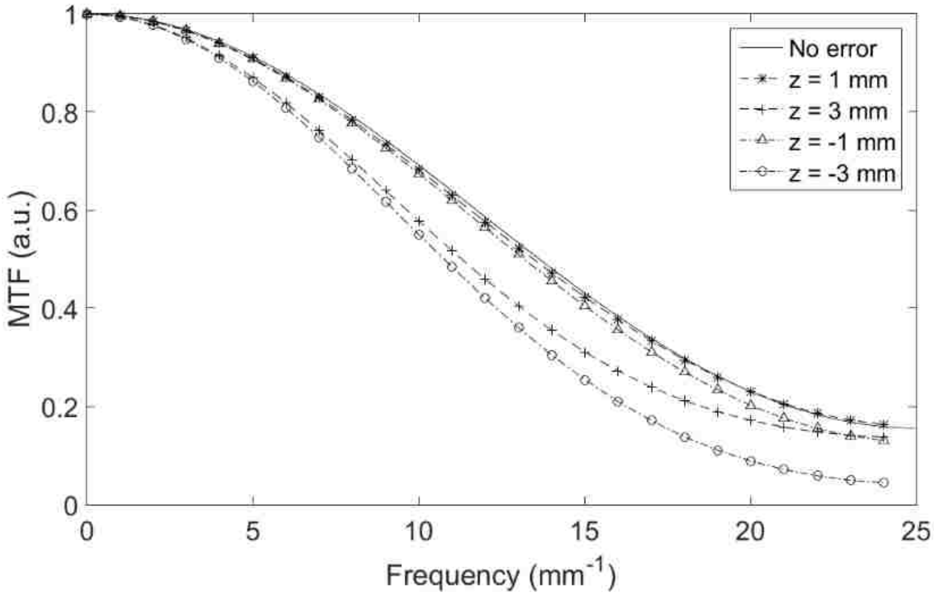

Figure 3.31: $\mathrm{MTF}_{\mathrm{recon}}$ for BP reconstruction with ± 40 cm source travel and 2 cm step size with source location error in $+\hat{z}$ and $-\hat{z}$.

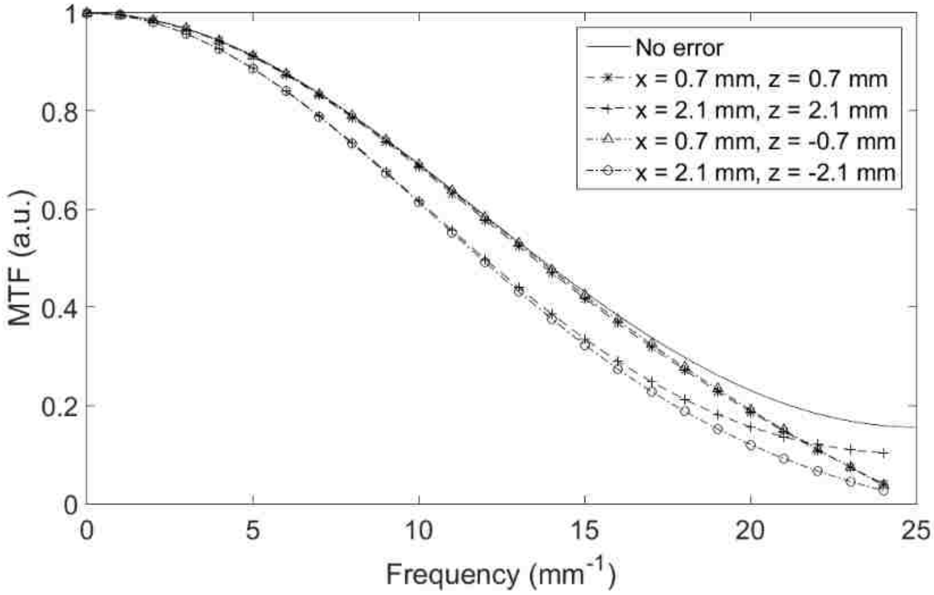

Figure 3.32: $\mathrm{MTF}_{\mathrm{recon}}$ for BP reconstruction with ± 40 cm source travel and 2 cm step size. The total source location error is $\sqrt{x^2 + z^2}$, where the x and z values used in each plot are given in the legend.

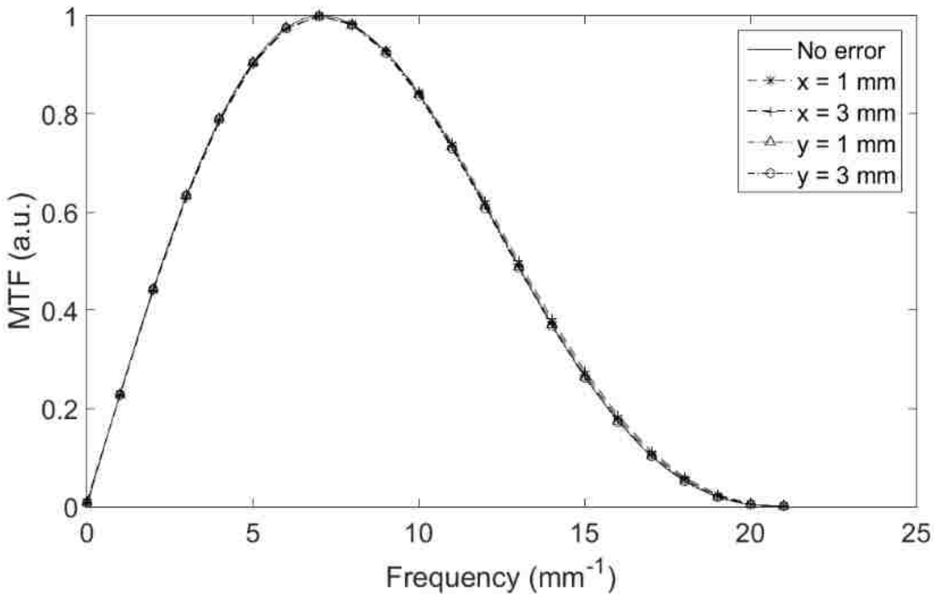

Figure 3.33: $\mathrm{MTF_{recon}}$ for FBP reconstruction with ± 40 cm source travel and 2 cm step size with source location error in $+\hat{x}$ and $+\hat{y}$. MTF curves for error in $-\hat{x}$ and $-\hat{y}$ were not generated because of symmetry in the endoDPT geometry.

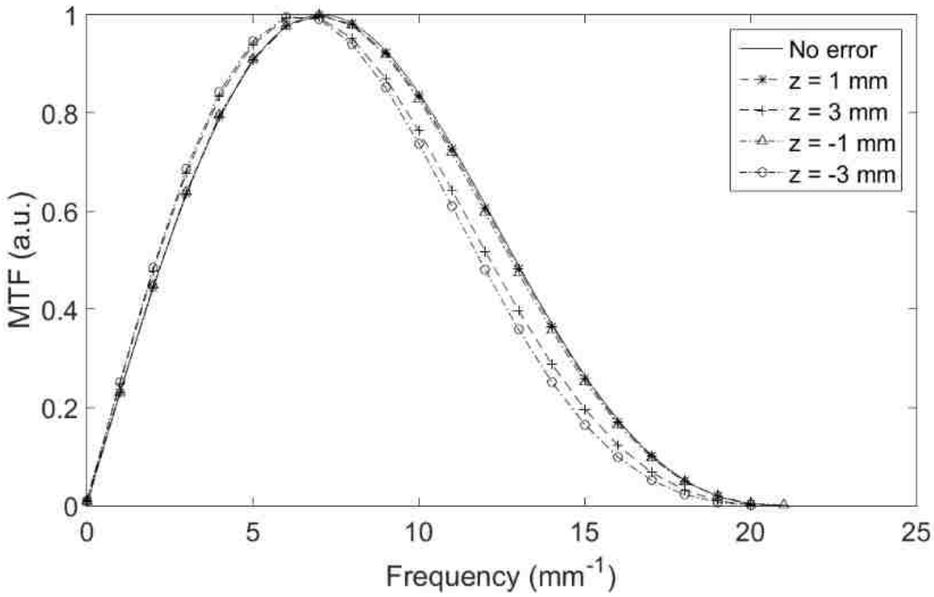

Figure 3.34: $\mathrm{MTF_{recon}}$ for FBP reconstruction with ± 40 cm source travel and 2 cm step size with source location error in $+\hat{z}$ and $-\hat{z}$.

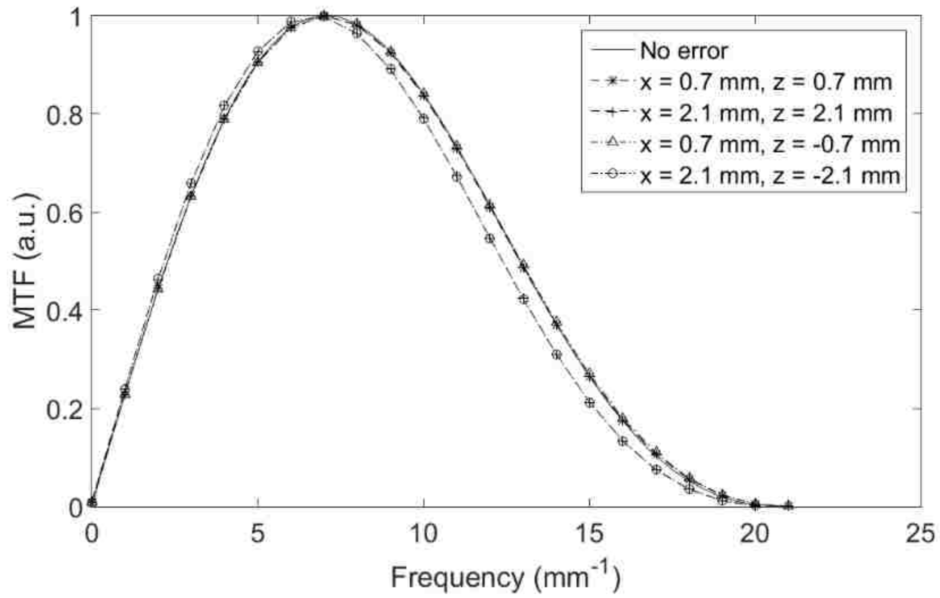

Figure 3.35: $\mathrm{MTF}_{\mathrm{recon}}$ for FBP reconstruction with ± 40 cm source travel and 2 cm step size. The total source location error is $\sqrt{x^2 + z^2}$, where the x and z values used in each plot are given in the legend.

3.9 Discussion

In this aim, the endoDPT system was computationally modeled, endoDPT reconstruction algorithms were derived, and the computational $\mathrm{MTF}_{\mathrm{detector}}$ and $\mathrm{MTF}_{\mathrm{recon}}$ were assessed. The computational system model followed previous efforts in tomosynthesis with x-ray sensors external to the body (Tutar 2003, Chen 2007a, Reiser 2007, Mainprize 2011, Chen 2014) and in radiography (Samei 1998, Saunders 2003). This computational system design allowed for a convenient and cost-effective method to assess endoDPT, including providing comparisons to experimental measurements on a test system (see Chapter 4).

$\mathrm{MTF}_{\mathrm{detector}}$ and $\mathrm{MTF}_{\mathrm{recon}}$ derived using simulated phantoms showed that high image resolution was achievable in endoDPT. The endoDPT $\mathrm{MTF}_{\mathrm{detector}}$ was higher than the computational study (Samei 1998) that this work was based on; Samei and Flynn measured the frequency of the 10% $\mathrm{MTF}_{\mathrm{detector}}$ on a simulated detector with 200 µm pixels to be 22 mm^{-1}

whereas the frequency of 10% $\mathrm{MTF}_{\mathrm{detector}}$ of endoDPT (19 µm pixel) was 38.6 mm^{-1}. There was not a 1:1 correspondence to smaller pixel size because the edge phantom image created by Samei and Flynn was a perfect step function; the image was not created using a divergent beam source. This resulted in a narrower LSF and broader $\mathrm{MTF}_{\mathrm{detector}}$ relative to pixel size. Because many profiles were averaged into the ESF, the added Poisson noise in the study had little effect on the measurement.

$\mathrm{MTF}_{\mathrm{recon}}$ showed high resolution compared to BP $\mathrm{MTF}_{\mathrm{recon}}$ and FBP $\mathrm{MTF}_{\mathrm{recon}}$ measured in the computational study this work was based on (Chen 2007a); Chen created projection images (partial isocentric tomosynthesis with 25 projections equiangularly spaced over $25°$) of nine point impulses spaced within a single pixel (pixel size = 85 µm) located 25 mm above the detection plane and reconstructed using BP and FBP. Chen reported the frequencies of the 50% BP $\mathrm{MTF}_{\mathrm{recon}}$, the maximum of FBP $\mathrm{MTF}_{\mathrm{recon}}$, and the minimum of FBP $\mathrm{MTF}_{\mathrm{recon}}$ to be 4 mm^{-1}, 2.2 mm^{-1}, and 5.8 mm^{-1}, respectively. The corresponding values measured for endoDPT were 13.6 mm^{-1}, 7.08 mm^{-1}, and 20 mm^{-1}, respectively. endoDPT increased $\mathrm{MTF}_{\mathrm{recon}}$ by a factor of three to four compared to Chen’s work, which was expected due to using a pixel size approximately four times smaller in endoDPT.

Both the BP and FBP algorithms showed that retention of higher frequencies than achieved by SAA was possible, although the measured FBP $\mathrm{MTF}_{\mathrm{recon}}$ was relative and FBP was limited to the tunable parameter a of the Hanning window, which resulted in all frequencies above a being reduced to zero. SAA $\mathrm{MTF}_{\mathrm{recon}}$ demonstrated a marked dependence on x-ray source travel. Small travel distances resulted in SAA $\mathrm{MTF}_{\mathrm{recon}}$ approaching BP $\mathrm{MTF}_{\mathrm{recon}}$. Larger travel distances reduced SAA $\mathrm{MTF}_{\mathrm{recon}}$. This occurred because SAA assumes a parallel beam. In all instances for a given amount of travel, increasing the number of images by using a smaller step size improved the $\mathrm{MTF}_{\mathrm{recon}}$. BP showed that larger x-ray source travel distances decreased $\mathrm{MTF}_{\mathrm{recon}}$ in the high frequency region, but to a much lesser extent than that seen in SAA. The BP $\mathrm{MTF}_{\mathrm{recon}}$ is larger than the SAA $\mathrm{MTF}_{\mathrm{recon}}$ because BP incorporates beam divergence. The BP $\mathrm{MTF}_{\mathrm{recon}}$ decreases for larger x-ray source travel distances because this induces a greater blur (the reconstructed image moves closer to what would be visualized in CT compared to radiography for larger source travel distances). No differences were noted for variations in the step size for a given x-ray source travel distance in BP. FBP showed little variation in the $\mathrm{MTF}_{\mathrm{recon}}$ for variations in source travel distances or in the step size. This occurred because the high-frequency range of the image (which was where most of $\mathrm{MTF}_{\mathrm{recon}}$ variation was observed in BP) was attenuated in FBP by the Hanning window.

Due to the limited angular sampling of the object and the filtration process, FBP $\mathrm{MTF}_{\mathrm{recon}}$ was relative and assumed the approximate shape of the point impulse inversion filter windowed by the Hanning function (Mertelmeier 2006, Chen 2007a, Zhou 2007, Cong 2011). This occurred because FBP $\mathrm{MTF}_{\mathrm{recon}}$ was measured across the reconstructed point impulse in the direction of scan motion. The blur artifact of tomosynthesis had a small impact on this view in BP due to the limited angular sampling, whereas in CT, the blur would affect this in-plane view because the blur artifact occurs over the entire reconstructed point impulse. The profile of the FBP reconstructed point impulse had negative values, which resulted in an overshoot or edge-enhancement artifact that translated to the FBP $\mathrm{MTF}_{\mathrm{recon}}$.

Small, systematic errors to source location in $\hat{x}$, $\hat{y}$, and $\hat{z}$ resulted in changes of $\mathrm{MTF}_{\mathrm{recon}}$ that varied for each reconstruction algorithm and were most pronounced in the high frequency range. Source location error in $\hat{x}$ reduced $\mathrm{MTF}_{\mathrm{recon}}$ for SAA and BP. For SAA, a larger source location error in $\hat{x}$ worsened $\mathrm{MTF}_{\mathrm{recon}}$. For BP, the opposite effect occurred; a 1 mm source location error worsened $\mathrm{MTF}_{\mathrm{recon}}$ more so than the 3 mm source location error. This occurred because the geometry of the 3 mm source location error resulted in projection images with the point impulse more closely spaced about a single pixel than with 1 mm source location error. This effect occurred due to the use of discrete detector elements. Source location errors in $\hat{y}$ affected $\mathrm{MTF_{recon}}$ to a much lesser degree than offsets in $\hat{x}$ for SAA due to the parallel beam assumption. In BP, the worsening of $\mathrm{MTF_{recon}}$ with increasing $\hat{y}$ source location error was more evident than SAA because $\mathrm{MTF_{recon}}$ covered a larger frequency range and because BP incorporated divergent beam geometry. Source location error in $\hat{x}$ and $\hat{y}$ showed little effect on the FBP $\mathrm{MTF_{recon}}$; the high-frequency components of the BP $\mathrm{MTF_{recon}}$ were where worsening of the $\mathrm{MTF_{recon}}$ was observed and these components were attenuated by the Hanning window in FBP.

Source location error in $\pm\hat{z}$ showed a much greater effect of the $\mathrm{MTF_{recon}}$ compared to error in $\hat{x}$ and $\hat{y}$. The SAA $\mathrm{MTF_{recon}}$ improved for source location errors that increased the SID; this improved the imaging geometry of SAA by making the x-ray source more like a parallel beam which decreased beam divergence. The SAA $\mathrm{MTF_{recon}}$ worsened for negative $\hat{z}$ source location errors for the same reason. The beam became less parallel and beam divergence played a larger role. The BP $\mathrm{MTF_{recon}}$ and FBP $\mathrm{MTF_{recon}}$ showed a slight worsening for positive $\hat{z}$ source location errors but showed a much larger effect for negative $\hat{z}$ source location errors, due to the larger effect of beam divergence at smaller SID.

Source location error in both $(+\hat{x}, +\hat{z})$ and $(+\hat{x}, -\hat{z})$ combined the effects described above for the SAA $\mathrm{MTF_{recon}}$ and the BP $\mathrm{MTF_{recon}}$. Source location error in $(+\hat{x}, +\hat{z})$ did not affect the FBP $\mathrm{MTF_{recon}}$ but source location error in $(+\hat{x}, -\hat{z})$ decreased the $\mathrm{MTF_{recon}}$. For the FBP $\mathrm{MTF_{recon}}$ source location error in $(+\hat{x}, -\hat{z})$, there was little difference for a 1 mm offset and a 3 mm source location error; this is again believed to be the product of attenuation of the high-frequency components of $\mathrm{MTF_{recon}}$ by the Hanning window. These results demonstrate that for a physical system, precise knowledge of the system geometry will be important to limit potential reductions in system resolution. These results also highlight the usefulness of linear parallel tomosynthesis geometry; a source constrained to move in a straight line along a single direction ($\hat{x}$) should aid minimization of source location error.

This aim had several limitations and sources of error. The primary limitation was that the edge phantom and the point impulse phantom were modeled and imaged geometrically. Material-photon interactions, the polychromatic x-ray spectrum of a kV imaging system, x-ray scatter, focal spot size, pixel fill factor, detector gain, and detector scintillation layer were not considered. In a physical system, the detector resolution will be decreased. Most dental imaging sensors have limiting high-contrast clinical resolutions of approximately 9-20 lp/mm^{-1} (Farman 2005a). This resolution is lower than the computational limits in this study, but is still high compared to other methods for prostate imaging. When the physical detector resolution is combined with the reconstruction algorithm resolution, it is expected that the total system resolution will be higher that than typical methods of prostate imaging.

3.10 Conclusion

The main objectives of this aim were to develop a computational model to perform endoDPT simulations and to develop analytical tomosynthesis reconstruction methods for the endoDPT geometry. Both objectives were completed. The computational endoDPT system developed with idealized parameters demonstrated that high detector resolution is achievable, which was expected due to the small pixel size used. The reconstruction algorithm resolution demonstrated a similar result for the same reason. Further, it was demonstrated that small errors in source location affect the resultant MTF, although not to a large degree. This aim developed the endoDPT concept and provided a clear indication that high resolution is achievable with endoDPT.

Chapter 4. Aim 2: endoDPT Image Quality and Dose Assessment

4.1 Overview

A test system to assess image quality of endoDPT was assembled using an intraoral dental x-ray sensor and a standard radiography unit. The small size and high-resolution of the x-ray sensor and the range of x-ray source travel of the radiography unit were appropriate for testing endoDPT. The MTF, NPS, ASF, and dose were measured using this physical system. The MTF and dose were also measured for a typical CT scanner to provide a comparison to endoDPT. Differences were considered significant for $p < 0.05$.

4.2 endoDPT System Components

The physical system was designed by adapting an intraoral dental sensor and a standard radiography unit to perform endoDPT scans. An intraoral dental sensor was chosen for this study because it had both high resolution (19 µm pixel size) and a form factor similar to the size of large (≈ 24 mm diameter) TRUS probes in clinical use (Koprulu 2012). The size of the intraoral dental sensor was also similar to the size of an endorectal gamma-ray detector (≈ 25 mm width and ≈ 80 mm length) currently under investigation (Safavi-Naeini 2015, Alnaghy 2017). A typical radiography unit was chosen for this study because the x-ray source travel associated with general radiography can easily accommodate the range required for tomosynthesis imaging. A drawback is that the radiography source required manual positioning. Additionally, the technology used in these devices is both readily available and inexpensive, resulting in a high level of technology readiness for implementation of endoDPT.

4.2.1 endoDPT X-ray Sensor

The endoDPT x-ray sensor was an XDR Size 2 Intraoral dental x-ray sensor (S/N: 526388, XDR Radiology, Los Angeles, California), shown in Fig. 4.1. This XDR sensor comprises a layer of scintillating CsI(Tl) needles over a CMOS chip with an optimal energy response for x-ray spectra of 60 kV to 80 kV[i]. The active area is 25.992 mm (1368 pixels) by 36.024 mm (1896 pixels) with pixel size of 19 µm; the overall size was 40 mm length, 30 mm width, 5 mm thickness. The XDR sensor is powered by and interfaces to a personal computer via USB connection.

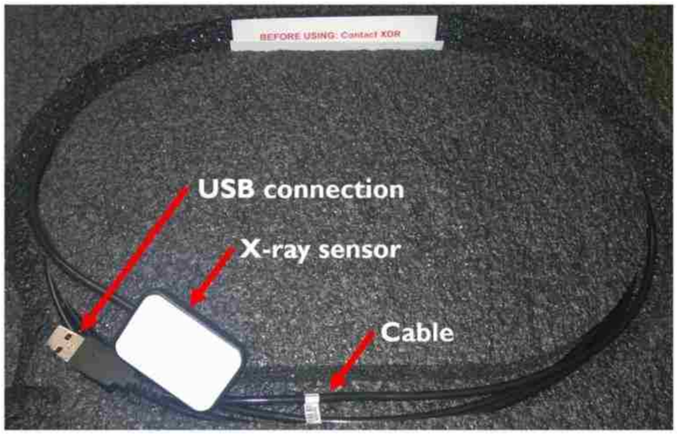

Figure 4.1: The XDR sensor used in the physical endoDPT system.

Projection images were collected with the XDR sensor using the image acquisition software provided by XDR Radiology (XDR Digital Radiographic System, Version 3.2.10, XDR Radiology, Los Angeles, California). This software allowed for the manual collection of a single projection image every 5-7 seconds. Prior to output of the projection image, a gain uniformity correction was applied, which included a linear interpolation step to provide a signal intensity value for any dead pixel elements. This was the only pre-processing step that occurred at the XDR sensor level. The resultant projection images were output at a 12-bit pixel depth (where a pixel value of 4096 indicates no signal has been collected) with a total image size of about 5 MB.

A sample projection image collected with the XDR sensor is shown in Fig. 4.2. Each corner of the image comprised a triangular area of pixels that do not respond to radiation exposure (these areas are covered by sensor clips in intraoral dental imaging). These corner areas of unresponsive pixels were not used in any reconstruction or data analysis steps.

---

[i] Dr. Doug Yoon (XDR Radiology), personal communication, September 3, 2015

Figure 4.2: Representative projection image acquired with the XDR sensor of 10 LDRBT seeds (titanium shell is $\approx$ 5 mm long with diameter $\approx$ 0.8 mm, silver core is $\approx$ 3.5 mm long with diameter $\approx$ 0.3 mm) implanted in a Styrofoam plug.

4.2.2 X-ray Source

For physical testing, a GE Proteus XR/a radiography unit (Model: 6124101, SN: 106888HL1, General Electric Company, Waukesha, Wisconsin), shown in Fig. 4.3, was used. This GE Proteus XR/a is ceiling mounted at Pennington Biomedical Research Center, with the ability to translate the unit source head in three-dimensions. The source can additionally be rotated by θ in the $(\hat{x}, \hat{z})$ plane as shown in Fig. 4.3 for endoDPT imaging. This three-phase 65 kW radiography unit operates from 40 kVp to 150 kVp in 1 kVp increments using x-ray source currents up to 400 mA with the small focal spot setting; the small focal spot setting of 0.6 mm on the rhenium-tungsten target was used for all endoDPT imaging. This radiography unit has an inherent filtration of 1.1 mm aluminum equivalent at 75 kVp in the head (MX100 x-ray tube) and added filtration of 1.5 mm aluminum equivalent at 75 kVp in the collimator (Eclipse Proteus Collimator). No additional filters were used for this study.

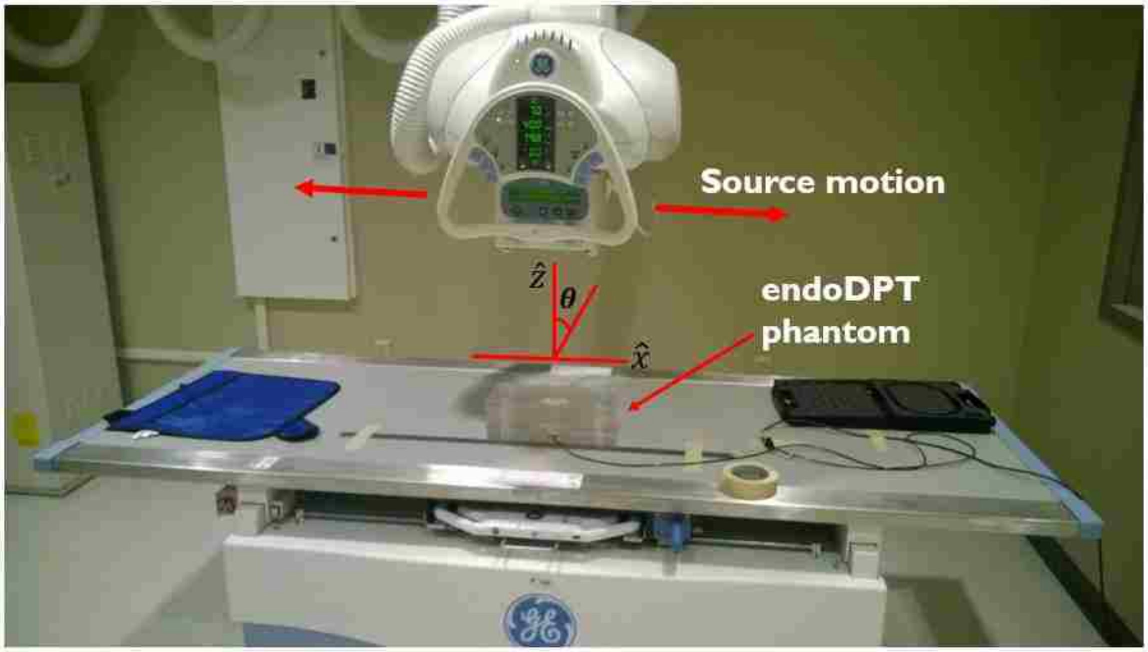

Figure 4.3: The GE Proteus XR/a radiography unit used in the physical endoDPT system.

The digital radiography flat panel x-ray detector associated with this radiography unit, a wireless GE FlashPad (General Electric Company, Waukesha, Wisconsin) with a 40.4 cm by 40.4 FoV and 200 µm pixel size, was also used in this study to verify the x-ray source locations relative to the XDR sensor through use of wire fiducials in the endoDPT phantom. The FlashPad detector was only used for this x-ray source localization.

4.3 CT Scanner

A GE Lightspeed RT16 CT scanner (SID: 22515CT1, General Electric Company, Waukesha, Wisconsin) was used in this study (Fig. 4.4). This is a 16 slice CT scanner used for radiation therapy treatment planning and simulation at Mary Bird Perkins Cancer Center. The scanner operates at 80, 100, 120, or 140 kVp, can use either a constant x-ray source setting or an automatic exposure setting, has both axial and helical scanning modes with 1.25 mm, 2.5 mm, 5 mm, or 10 mm slice thicknesses, and reconstructs objects using a 512 by 512 matrix. In this study, a 25 cm FoV was used for all scans, resulting in a 0.488 mm reconstructed voxel size.

Figure 4.4: The GE LightSpeed RT16 CT scanner used in this study.

4.4 endoDPT Phantoms

4.4.1 Modular Acrylic Phantom

A modular phantom was created using 1” and 2” thick plates of acrylic plastic. This phantom was used to measure the MTF, NPS, ASF, and dose. Acrylic was chosen as the phantom material because it is easily machinable, similar in composition to soft tissue, and is inexpensive (Robertson 2012). The modular phantom had overall dimensions of 11.5” (292.1 mm) width, 5.5” (139.7 mm) depth, and 6” (152.4 mm) height. Some plates were configured for specific purposes, while the remainder were solid material. The combination and ordering of plates could be changed to accommodate the various measurements. Every plate had four identical alignment holes that were used with machined acrylic bolts to clamp the plates together reproducibly.

Two plates were configured as shown in Fig. 4.5, one to hold the wire fiducials for alignment verification and the other to hold the XDR sensor. The fiducial plate was always the base of the phantom (Fig. 4.5 a), with tapped holes to secure the alignment bolts. The 1” thick fiducial plate had two features to facilitate alignment verification of the x-ray source. First, a 150 mm ruled scale was epoxied into a recess milled along one edge to help set up the phantom during imaging. Second, three small recesses were milled into both the top and bottom faces of the plate; 38 mm long sections of 0.8 mm diameter piano wire were epoxied into these recesses for use as fiducial markers to determine imaging geometry with the FlashPad detector (Section 4.5). The detector holder plate was 1” thick with a cut-out for the XDR sensor (Fig. 4.5 b). The cutout was lined with foam to ensure the detector was placed in a reproducible position. The detector holder plate was typically placed directly above the fiducial plate. Fig. 4.6 shows one arrangement of the modular acrylic phantom assembled with two solid acyclic slabs above the fiducial plate and detector holder plate. This phantom was used for measurement of the NPS.

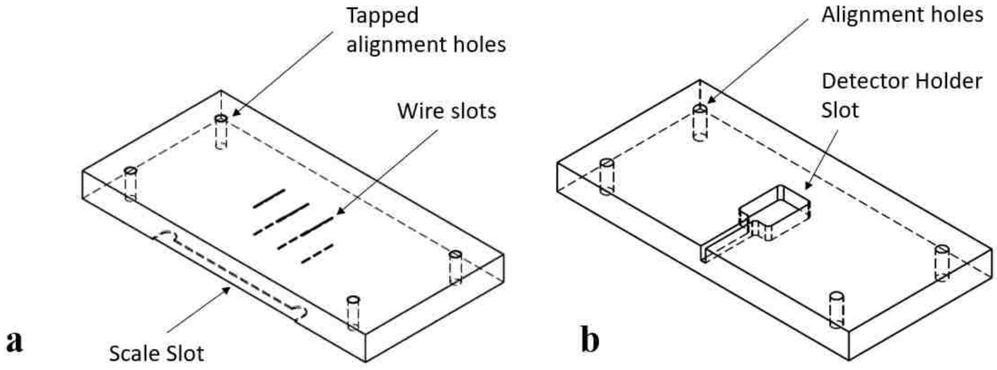

Figure 4.5: (a) Modular acrylic phantom bottom plate, with slots for wire fiducials (localization) and a scale (setup). (b) Plate to hold the XDR sensor.

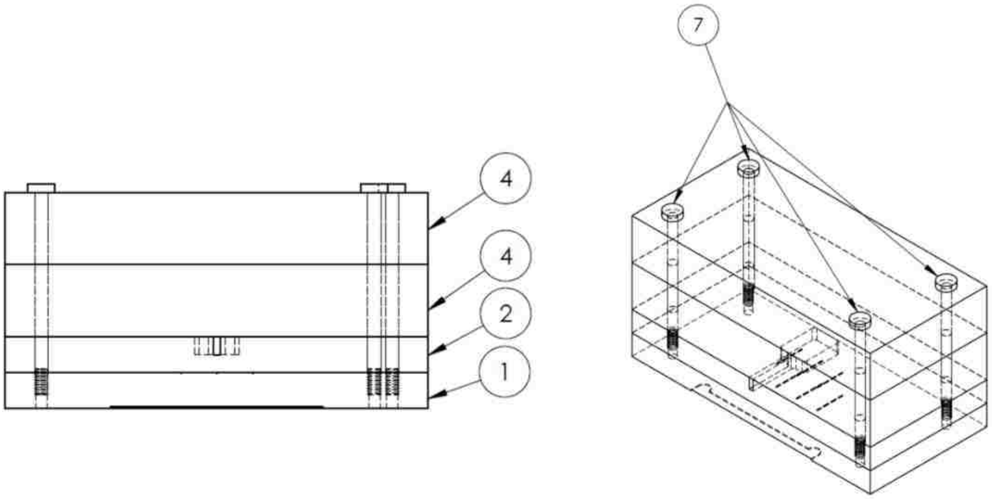

Figure 4.6: Configuration of modular acrylic phantom for measurement of NPS. The fiducial plate (1) and detector holder plate (2) were illustrated in Fig. 4.5. Two solid plates (4) were each 2” thick and 4 acrylic bolts (7) were used to clamp the assembly together.

The sample holder plate is shown in Fig. 4.7. This 2” thick plate had a large cavity (7.75” width, 1-7/16” thickness, 1-13/16” depth) milled into the center of the top face; there was 4.76 mm of acrylic plastic separating the XDR sensor face from the bottom of the cavity during imaging. The cavity housed various objects that were imaged in this work, such as metal spheres suspended in carrageenan gel for measurement of ASF (Section 4.6.3) and canine prostate specimens suspended in carrageenan gel (Chapter 5).

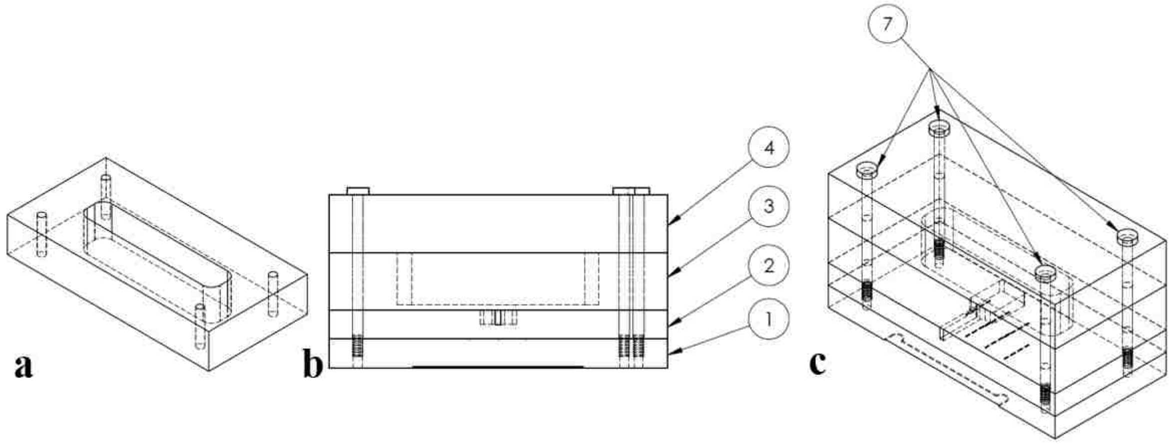

Figure 4.7: (a) Sample holder plate. (b) and (c) Configurations of modular acrylic phantom for ASF measurement and prostate specimen imaging showing fiducial plate (1), detector holder plate (2), sample holder plate (3), and solid plate (4). 4 acrylic bolts (7) were used to clamp the assembly together.

4.4.2 Carrageenan Gel Inserts

Carrageenan gel, which is solid at room temperature, was used to suspend phantom materials within the cavity in the sample holder plate, as well as to create pliable sheets (1” thick) that could be substituted for 1” slabs in the modular acrylic phantom for dose measurements (Section 4.6.4). The recipe for this gel was adapted at our institution (Lamberto 2014) as a variation of a previously reported recipe (Hattori 2013).

The gel was made by first dissolving the materials listed in Table 4.1 in distilled water at room temperature. The solution was heated in a hot water bath to 90°C and continuously stirred at this temperature for 5 minutes to create the gel. To remove air bubbles, the gel rested in a hot water bath at 90°C for 20 additional minutes. The gel was poured either into the sample holder cavity or into a form with the same length and width dimensions as the acrylic plates. The gel was allowed to solidify for 12 hours at 20-25°C. When filling the sample holder, the cavity was overfilled to compensate for shrinkage and any excess gel was trimmed flush with the top face of the sample holder plate. For gel slabs, the form was overfilled and then two 1" thick pieces of acrylic were place on either side of the slab as guides to trim the gel to 1" thick. When not in use for imaging, the gel samples were tightly wrapped in plastic wrap and refrigerated to prevent shrinkage.

Table 4.1: Materials and concentrations used to create a muscle-like gel with T1 and T2 relaxation behavior with a 3T MRI (Lamberto 2014). w/w indicates percent by weight in water. An example calculation for material amounts to create 500 g of gel is given in Appendix C.

Material	**Quantity**	**Purpose**
Agarose	1.200% w/w	Adjusts T2
$GdCl_3$	55.0 µmol/kg	Adjusts T1
Carrageenan	3% w/w	Provides for gelatinization
NaCl	0.291% w/w	Alters conductivity
NaN_3	0.03% w/w	Anti-microbial

Carrageen was the gelatinizing agent used to solidify the gel (Hattori 2013). The amounts of $GdCl_3$, agarose, and NaCl in the recipe controlled the T1 relaxation time, T2 relaxation time, and conductivity, respectively, to produce similar MRI characteristics as human muscle tissue (Lamberto 2014). While these characteristics were not important for endoDPT, they facilitated comparative imaging with MRI (Chapter 5). The NaN_3 was an anti-microbial to prevent mold and mildew (Hattori 2013, Lamberto 2014). The carrageenan was purchased through Research Products International (Mt Prospect, IL) while the other materials were purchased through Fisher Scientific (Fair Lawn, NJ). An example calculation for materials to create 500 g of gel is given in Appendix C.

4.5 X-ray Source Localization

Determining of the x-ray source location relative to the XDR sensor was accomplished with wires in the fiducial plate (Fig. 4.5 a) of the modular acrylic phantom. This method was based on previously developed methods for determining the location of the x-ray source by mapping a three-dimensional fiducial (or set of fiducials) onto a two-dimensional x-ray detector in fluoroscopy (Jain 2005, Kuo 2014, Szczykutowicz 2016, Lee 2017) and tomosynthesis (Li 2010). The wires were in the same positions relative to the XDR sensor for all endoDPT scans.

From the beam's eye view, the wires were located distal to the XDR sensor but before the FlashPad detector, which was located within the table bucky of the Proteus x-ray unit. For each discrete source location $(x_{S_i}, y_{S_i}, z_{S_i})$ during the endoDPT scan a projection image was formed of the wires on the FlashPad detector. An example image is shown in Fig. 4.8. The coordinates of the endpoints of the wires were manually found by displaying each projection image in ImageJ (https://imagej.nih.gov/ij/); ImageJ's cursor tool was used to determine the pixel coordinates, which were converted to spatial coordinates using the 200 µm pixel size of the FlashPad detector.

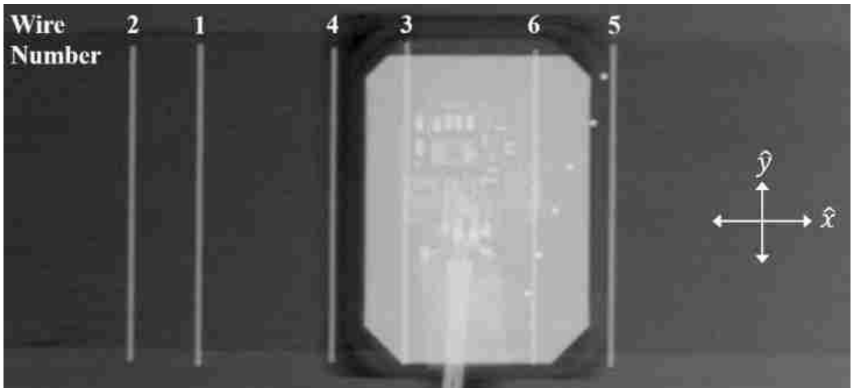

Figure 4.8: Projection image collected on the FlashPad detector to show relative locations of fiducial wires and XDR sensor with the x-ray source located nominally at $(x_S, y_S, z_S) = (40\text{ cm}, 0\text{ cm}, 100\text{ cm})$ relative to the center point of the XDR sensor. The wires are numbered 1-6. This projection image is in the $(\hat{x}, \hat{y})$ plane of endoDPT geometry, with $\hat{z}$ out of the page.

To determine the absolute positions of the wires relative to the XDR sensor, CT scans were taken of the modular acrylic phantom and XDR sensor with CT slices oriented in the $(\hat{x}, \hat{z})$ plane of the phantom (Fig. 4.9 a) and rotated 90° for CT slices in the $(\hat{y}, \hat{z})$ plane (Fig. 4.9 b). In the CT image sets, wire and XDR sensor locations were found manually using ImageJ. The locations of the wire endpoints and the XDR sensor center point are given in Table 4.2.

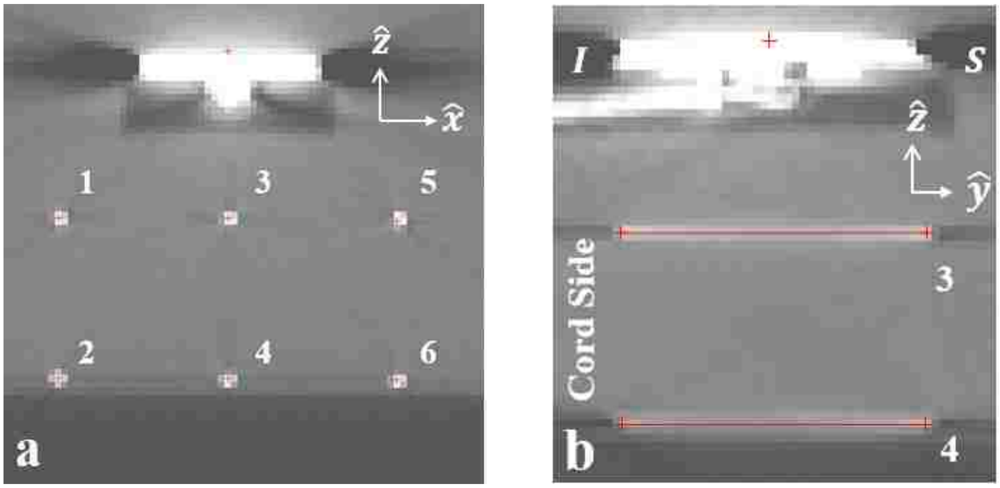

Figure 4.9: CT slices of the modular acrylic phantom and XDR sensor, showing the x-ray source localizing wires relative to the XDR sensor. The + symbol on the XDR sensor marks $(x, y, z) = (0,0,0)$. The labels on the wires (1-6) correspond to the labels in Table 4.2. (a) CT slice in the $(\hat{x}, \hat{z})$ plane. (b) CT slice in the $(\hat{y}, \hat{z})$ plane. The XDR sensor has an inferior (I) and superior (S) side; the cord of the XDR sensor in on the I side.

Table 4.2: Inferior and superior wire endpoint locations. The (x, z) location of the wires did not change along $(\hat{y})$. The wire numbers correspond to the labels in Fig. 4.8 and Fig. 4.9.

	Inferior Wire Endpoint			**Superior Wire Endpoint**		
	x (mm)	**y (mm)**	**z (mm)**	**x (mm)**	**y (mm)**	**z (mm)**
XDR Sensor Center	0	0	0	0	0	0
Wire 1	-25.4	-19.1	-24.9	-25.4	19.8	-24.9
Wire 2	-25.4	-19.8	-48.8	-25.4	20.0	-48.8
Wire 3	0	-18.6	-25.4	0	20.0	-25.4
Wire 4	0	-19.2	-48.8	0	20.0	-48.8
Wire 5	25.4	-18.6	-25.4	25.4	20.0	-25.4
Wire 6	25.4	-19.1	-49.1	25.4	20.0	-49.1

The relative locations of the wires both to one another and to the XDR sensor were drawn in SolidWorks (Dassault Systèmes, Waltham, Massachusetts). The center point of the XDR sensor was placed at the origin of the drawing. This drawing was first used to determine the location of the FlashPad detector along $\hat{z}$ relative to the XDR sensor. This step was performed because leaving both the location of the source and the location of the FlashPad detector unconstrained made the geometrical problem too complex for the modeling software to read and input dimensions from a spreadsheet that contained the wire-to-wire distances (known as a design table). Because the same radiography table, table bucky, FlashPad detector, and endoDPT phantom were used for all endoDPT scans, it was assumed the location of the FlashPad detector relative to the XDR sensor and wires along $\hat{z}$ was constant; this assumed constraint simplified the drawing and made it possible to find the source location using a design table.

The location of the FlashPad detector was found assuming it was in a horizontal plane $(\hat{x}, \hat{y})$ below the endoDPT phantom. By considering only the wire center points in the $(\hat{x}, \hat{z})$ plane because the center points of the wires did not vary along $\hat{y}$, six rays were drawn from an arbitrary source point through each wire's center to a horizontal line (the FlashPad detector). At this stage, the x-ray source location was not constrained (the x-ray source could be located at any x or z) and the FlashPad detector location was constrained only to be parallel to $\hat{x}$ (it could be located at any z). This is shown in Fig. 4.10.

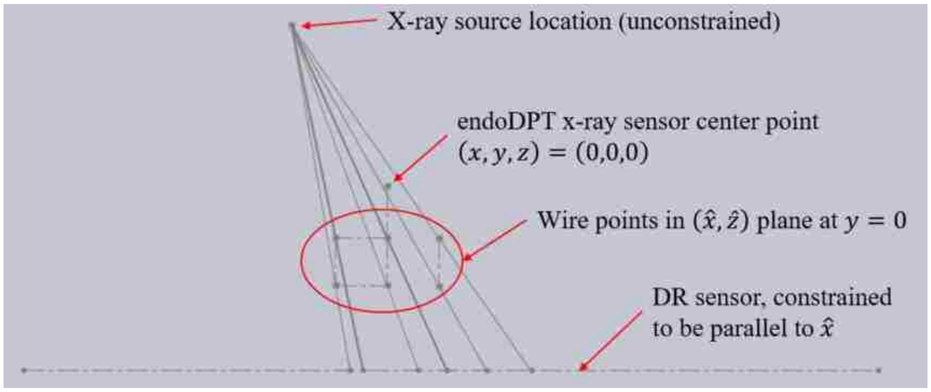

Figure 4.10: $(\hat{x}, \hat{z})$ plane at $y = 0$ (through the XDR sensor center point) of the modular acrylic phantom. For clarity, this figure is not drawn to scale.

To constrain both the x-ray source location (x, z) and the location of the FlashPad detector along $\hat{z}$ in the $(\hat{x}, \hat{z})$ plane, three wire-to-wire distances were required. Three sets of three wire-to-wire distances were selected randomly in each image of a projection image set acquired in the normal manner nominally with $x_{S_i} = \pm 40$ cm in 2 cm increments, $y_S = 0$ cm, and $z_S = 100$ cm. From these 123 measurements the mean z position of the FlashPad detector was $z = -132.2 \pm 0.1$ mm, relative to the XDR sensor located at $z = 0$ mm.

With the location of the FlashPad detector constrained, the complexity of finding the source location $\left(x_{S_i}, y_S, z_S\right)$ was reduced. To further reduce the complexity of finding $\left(x_{S_i}, y_S, z_S\right)$, the source location $\left(x_{S_i}, z_{S_i}\right)$ was first determined; only two wire-to-wire distances were required to constrain the source location in the $(\hat{x}, \hat{z})$ plane for each FlashPad detector image. It was possible to automate this process by choosing wire-to-wire distances that continually increased or decreased over the range of projection images. There were six wire-to-wire distances that continually increased or decreased, resulting in a total of 15 combinations of two wire-to-wire distances that could be used. Of those 15 combinations, 10 combinations were randomly chosen and input into the modeling software. x_{S_i} was taken to be the mean of the 10 measurements of x_{S_i} for each projection image. Because z_S did not vary (the x-ray source did not move in $\hat{z}$ during the scan), the mean value of all measurements of z_{S_i} was used for reconstruction. Typical uncertainties (standard deviation) in x_{S_i} and z_S were on the order of 2 mm to 7 mm. With z_S constrained, a similar process was used to find y_S. Only one distance, the endpoint of one wire to the endpoint of separate wire in a superimposed $(\hat{y}, \hat{z})$ plane, was needed to estimate y_{S_i}. Because no motion occurred in $\hat{y}$, the mean value of all y_{S_i} was used for reconstruction. Typical uncertainties in y_S were on the order of 2 mm to 7 mm. These uncertainties in source location are slightly higher than source location uncertainties (0.3 mm to 3 mm) from similar studies using fiducials to localize an x-ray source (Jain 2005, Lee 2011, Kuo 2014). As an example, a partial set of the measured source locations and uncertainty for the ASF image set (Section 4.6.3) is presented in Table 4.3.

Table 4.3: Measured source locations and uncertainty for the ASF image set. The average (y, z) location for this source was (0.57 cm, 102.48 cm). For all endoDPT image sets, uncertainties in source location ranged from 2-7 mm.

Image Number	x_{S_i} **(cm)**	$\sigma_{x_{S_i}}$ **(cm)**	y_{S_i} **(cm)**	$\sigma_{y_{S_i}}$ **(cm)**	z_{S_i} **(cm)**	$\sigma_{z_{S_i}}$ **(cm)**
1	-40.29	0.35	0.75	0.47	102.07	0.45
2	-38.58	0.53	0.59	0.41	102.59	0.34
3	-36.82	0.43	0.72	0.40	103.03	0.34
4	-33.89	0.45	0.71	0.43	102.81	0.57
5	-31.00	0.39	0.13	0.41	102.40	0.43
⋮	⋮	⋮	⋮	⋮	⋮	⋮
37	32.88	0.53	0.62	0.49	102.17	0.44
38	34.47	0.39	0.82	0.33	102.74	0.55
39	36.09	0.52	0.29	0.48	102.90	0.33
40	38.74	0.53	-0.09	0.58	101.69	0.29
41	40.79	0.46	0.22	0.40	102.04	0.43

4.6 endoDPT Image Quality Metrics

4.6.1 MTF

The system resolution of endoDPT, $\mathrm{MTF}_{\mathrm{endoDPT}}$, was found as

$$\mathrm{MTF}_{\mathrm{endoDPT}}(\omega) = \mathrm{MTF}_{\mathrm{recon}}(\omega) * \mathrm{MTF}_{\mathrm{detector}}(\omega) \tag{4.1}$$

which is the multiplication of two MTF stages; the computational $\mathrm{MTF}_{\mathrm{recon}}$ (determined in Chapter 3) and the physical $\mathrm{MTF}_{\mathrm{detector}}$ of the XDR sensor measured in this section. $\mathrm{MTF}_{\mathrm{endoDPT}}$ was determined for various combinations of reconstruction algorithms (all with x-ray source travel of ±40 cm and spatial step size of 2 cm), x-ray source energy, and x-ray source current.

The physical $\mathrm{MTF}_{\mathrm{detector}}$ was measured with a Leeds MTF-TO test device (Leeds Test Objects LTD, Roecliffe, York, United Kingdom). The test edge device was made of 1 mm thick tungsten with a sharp edge (< 5 µm ripple). For the radiographic unit accelerating voltages of interest (60 kVp to 100 kVp), this edge was considered fully opaque. $\mathrm{MTF}_{\mathrm{detector}}$ was measured from a projection image of the edge using the same procedure discussed in Chapter 3; this procedure is recommended by the International Electrotechnical Commission international standard 62220-1 (IEC 2003). This procedure was previously utilized with opaque edges to measure the MTF of digital detectors that had a scintillating layer and CCD or CMOS chipsets (Neitzel 2004, Illers 2005), and thus is appropriate for the XDR sensor.

Fifteen sets of 10 projection images each were acquired of the test edge device using the x-ray source kVp and mAs settings in Table 4.4. The x-ray source currents for each kVp setting resulted in signal (pixel value) to the exposed XDR sensor of ≈ 3000 (low mAs), ≈ 2000 (medium mAs), and ≈ 1000 (high mAs), allowing for comparison of low, medium, and high signal levels.

Table 4.4: Imaging parameters for the $\mathrm{MTF}_{\mathrm{detector}}$ measurements.

Image Set	**kVp**	**mAs**
1	60	16.0
2	60	32.0
3	60	50.0
4	70	12.5
5	70	20.0
6	70	32.0
7	80	8.0
8	80	12.5
9	80	20.0
10	90	6.3
11	90	10.0
12	90	16.0
13	100	4.0
14	100	8.0
15	100	12.5

The test edge device was placed in contact with the XDR sensor external housing (Fig. 4.11). All images were acquired with the x-ray source located 100 cm above the XDR sensor center point using the small focal spot setting (0.6 mm). To reduce afterglow artifacts, a scrubber image (test edge device removed) was taken between each projection image of the test edge device. The test edge device was rotated through a random angle ($\pm 10^\circ$ relative to $\hat{y}$) for each projection.

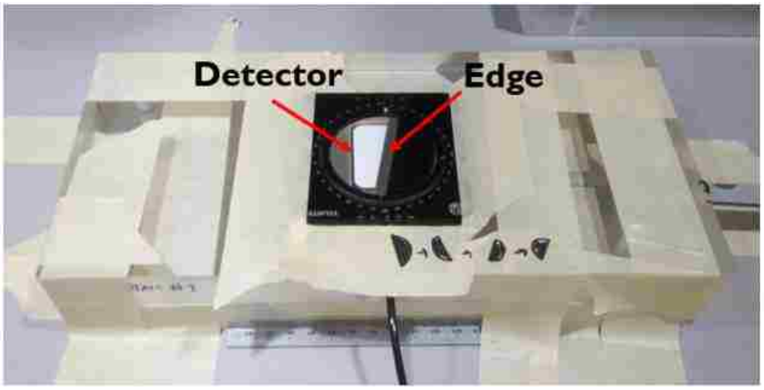

Figure 4.11: Test edge device in position on top of the XDR sensor in the detector holder plate of the modular acrylic phantom.

Eight hundred profiles perpendicular to the edge in the projection images were measured using the same procedure as discussed in Chapter 3. Fig. 4.12 (a) shows a typical projection image of the edge acquired on the XDR sensor and Fig. 4.12 (b) shows an example profile. The profiles collected over the 1.52 mm length were averaged for each projection to obtain the ESF, which was differentiated to find the LSF (Fig. 4.13). The LSF for each projection was Fourier transformed to obtain $\mathrm{MTF_{detector}}$. $\mathrm{MTF_{detector}}$ was normalized to $\mathrm{MTF_{detector}}(0) = 1$. A representative $\mathrm{MTF_{detector}}$ for a single projection is shown in Fig. 4.14. The average $\mathrm{MTF_{detector}}$ for each kVp and mAs setting was found for the 10 projections acquired at each x-ray source setting.

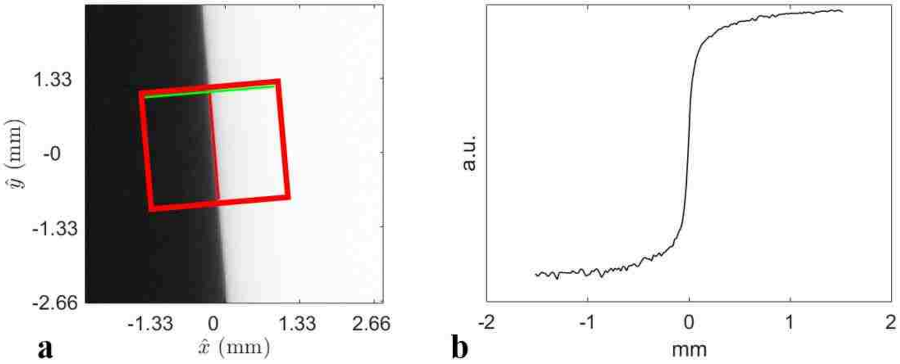

Figure 4.12: (a) The location of one profile (green line) and the total path along the edge upon which profiles were measured (red line) superimposed over one edge image (80 kVp, 12.5 mAs). A red box is drawn around the sampled region for clarity. (b) The ESF profile shown by the green line in the left pane.

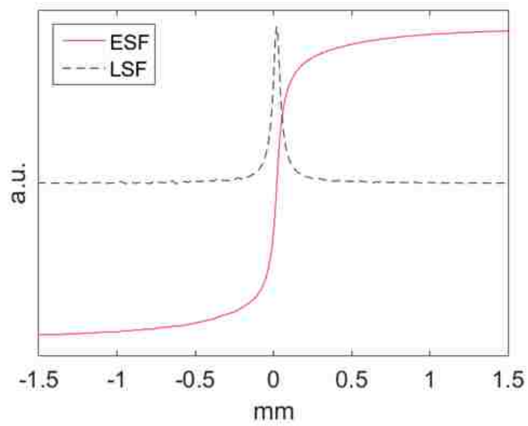

Figure 4.13: The composite ESF and LSF for a single physical edge image taken at 80 kVp, 12.5 mAs.

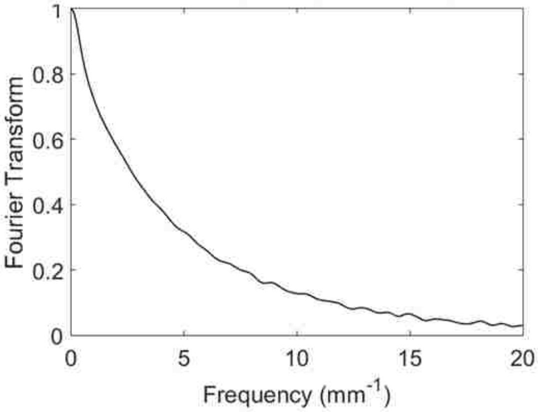

Figure 4.14: $\mathrm{MTF}_{\mathrm{detector}}$ for a single edge image acquired at 80 kVp, 12.5 mAs.

$\mathrm{MTF}_{\mathrm{endoDPT}}$ was found using Eq. 4.1 for each reconstruction algorithm (SAA, BP, and FBP, using an x-ray source travel of ±40 cm and a spatial step size of 2 cm), for each kVp and mAs setting listed in Table 4.4. Because $\mathrm{MTF}_{\mathrm{recon}}$ was computationally determined, there was no associated uncertainty in this term. Uncertainty in $\mathrm{MTF}_{\mathrm{detector}}$ was determined as the standard deviation of the measured frequency values at the 90%, 50%, and 10% MTF from the 10 scans and was propagated to find the uncertainty of $\mathrm{MTF}_{\mathrm{endoDPT}}$.

4.6.2 NPS

The NPS of endoDPT was measured at 80 kVp using three different x-ray source currents (25 mAs, 50 mAs, and 100 mAs) with the small focal spot setting (0.6 mm) using the modular acrylic phantom with two solid plates (Fig. 4.6). These x-ray source currents resulted in detector signals of ≈ 3000 (low mAs), ≈ 2000 (medium mAs), and ≈ 1000 (high mAs). The procedure for imaging the phantom and computing the NPS was adapted from existing methods (Dobbins 1995, Godfrey 2006a, Chen 2014). 10 identical scans for each x-ray source current were acquired in the normal manner with $x_{S_i} = \pm 40$ cm in 2 cm steps, $y_S = 0$ cm, and $z_S = 100$ cm. The central ray of the x-ray source was directed towards this center point on the XDR sensor for each source position.

The $z = 1.5$ cm plane of each projection image set was reconstructed using SAA, BP, and FBP using all 41 projection images. The plane at $z = 1.5$ cm was reconstructed because this is the plane at which the reconstruction algorithm resolution was determined; the NPS and $\mathrm{MTF}_{\mathrm{recon}}$ in the same plane were needed to compute the noise equivalent quanta (NEQ) (see below). The NPS was determined using only the full image set (41 images) because the noise properties of the reconstructed image depend on x-ray exposure to the XDR sensor (Godfrey 2006a).

A mean background subtraction was performed on all reconstructed images for each given x-ray source current and each method of image reconstruction. The purpose of the mean background subtraction was to remove possible structured noise components in the source, phantom, or XDR sensor (Godfrey 2006a, Chen 2014). The mean of each voxel calculated from all reconstructed images for each x-ray source current and reconstruction method was subtracted from the corresponding voxel value of each reconstructed image.

Each mean background-subtracted reconstructed image was divided into 60 regions of interest (ROIs) of 128 by 128 voxels in size (Godfrey 2006a, Chen 2014). The ROIs were placed in the central region of the image, to avoid edge effects and truncation artifacts. Fig. 4.15 shows the central region of the image used for NPS analysis and a single ROI. The ROIs were used to compute NPS for each reconstructed image using

$$\mathrm{NPS}\left(\omega_x, \omega_y\right) = C * \frac{< |\mathcal{F}_{2D}[I(x,y) - \bar{I}]|^2 >}{N_x N_y} \Delta x \Delta y \tag{4.2}$$

where $I(x, y)$ is the ROI, $\bar{I}$ is the global mean intensity, $\mathcal{F}_{2D}$ is the two-dimensional Fourier transform, $\Delta x = \Delta y = 0.019$ mm (voxel size for SAA) or $\Delta x = \Delta y = 0.020$ mm (voxel size for BP and FBP), and $N_x = N_y = 128$ voxels, the size of each ROI (Dobbins 1995). The term corrects for the reduction in image variance after performing the mean background subtraction, with a value of $N/(N - 1)$ where N is the number of repeat scans (10 here).

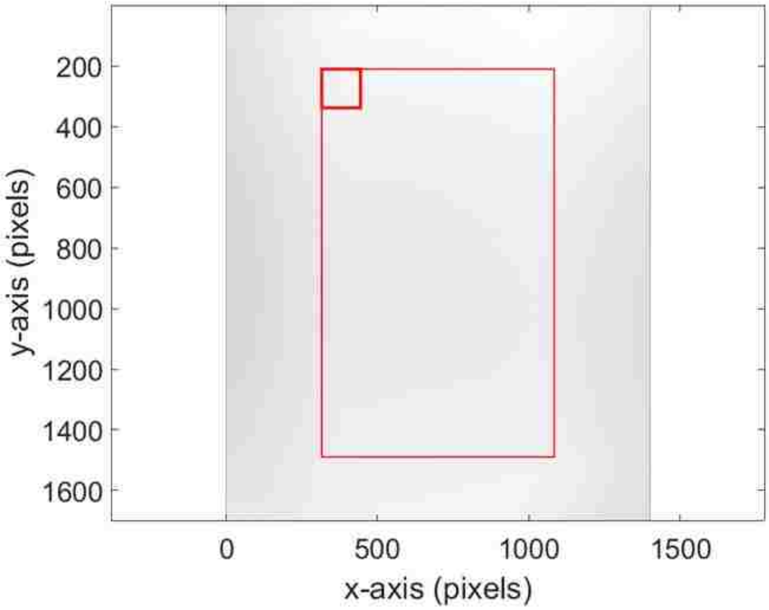

Figure 4.15: BP reconstructed image of the modular acrylic phantom used for measurement of NPS. The central region that comprises all ROIs is drawn with the thin red line. A single ROI is drawn with a bold red line. ROIs were only located in the central FoV to avoid truncation artifacts and edge effects.

The resultant $\mathrm{NPS}\left(\omega_x, \omega_y\right)$ was a two-dimensional function while the NPS is typically reported as a one-dimensional function, $\mathrm{NPS}(\omega)$. $\mathrm{NPS}(\omega)$ was calculated by integrating in $\widehat{\omega}_y$ (Godfrey 2006a). The value of the NPS at $\omega = 0$ was excluded from further analysis because NPS(0) may contain background trends in the data (such as the heel effect) that may have remained after background subtraction (Dobbins 1995). The NPS for each x-ray source current and image reconstruction method was calculated as the mean of the 10 reconstructed images using those parameters.

$\mathrm{NPS}(\omega)$ provided the variance amplitude at a given spatial frequency in the reconstructed image. $\mathrm{NPS}(\omega)$ can be used with $\mathrm{MTF}_{\mathrm{recon}}(\omega)$ and $\mathrm{MTF}_{\mathrm{detector}}(\omega)$ to calculate NEQ, which is analogous to the signal-to-noise ratio (Chen 2014). The NEQ can be used to directly compare image reconstruction algorithms, assuming all image acquisition parameters are identical for each stage (Chen 2014). The NEQ was calculated using

$$\mathrm{NEQ}(\omega)=\frac{\mathrm{MTF}_{\mathrm{recon}}^{2}(\omega)*\mathrm{MTF}_{\mathrm{detector}}^{2}(\omega)*k_1*k_2}{\mathrm{NPS}(\omega)} \tag{4.3}$$

where k_1 was the inverse of the normalization factor that scaled $\mathrm{MTF}_{\mathrm{recon}}(0)=1$ for SAA and BP or the maximum value of $\mathrm{MTF}_{\mathrm{recon}}$ to unity for FBP, and k_2 was the inverse of the normalization factor that scaled $\mathrm{MTF}_{\mathrm{detector}}(0)=1$. This method using the total, unnormalized frequency response allows for comparison between the three reconstruction algorithms for a given level of exposure to the XDR sensor (Chen 2007a).

4.6.3 ASF

The phantom used to measure the ASF consisted of six tungsten BBs of 0.79 mm (1/32”) nominal diameter suspended in carrageenan gel at varying heights above the XDR sensor along the central axis ($\hat{y}$). Similar metal structures such as 0.4 mm diameter steel BBs (Hu 2008) and high-contrast metal balls (Mertelmeier 2006) have been used in phantoms to measure ASF in DBT.

The phantom was constructed by tilting the sample holder plate by approximately $30°$ and then partially filling the cavity with carrageenan gel. After the gel had set, the BBs were implanted in the angled face of the carrageenan gel (Fig. 4.16), spaced such that the BBs would be located at heights ranging from 1.25 cm to 3.50 cm above the XDR sensor in the assembled modular acrylic phantom. The remainder of the sample holder cavity was then filled with carrageenan gel to the surface of the sample holder plate.

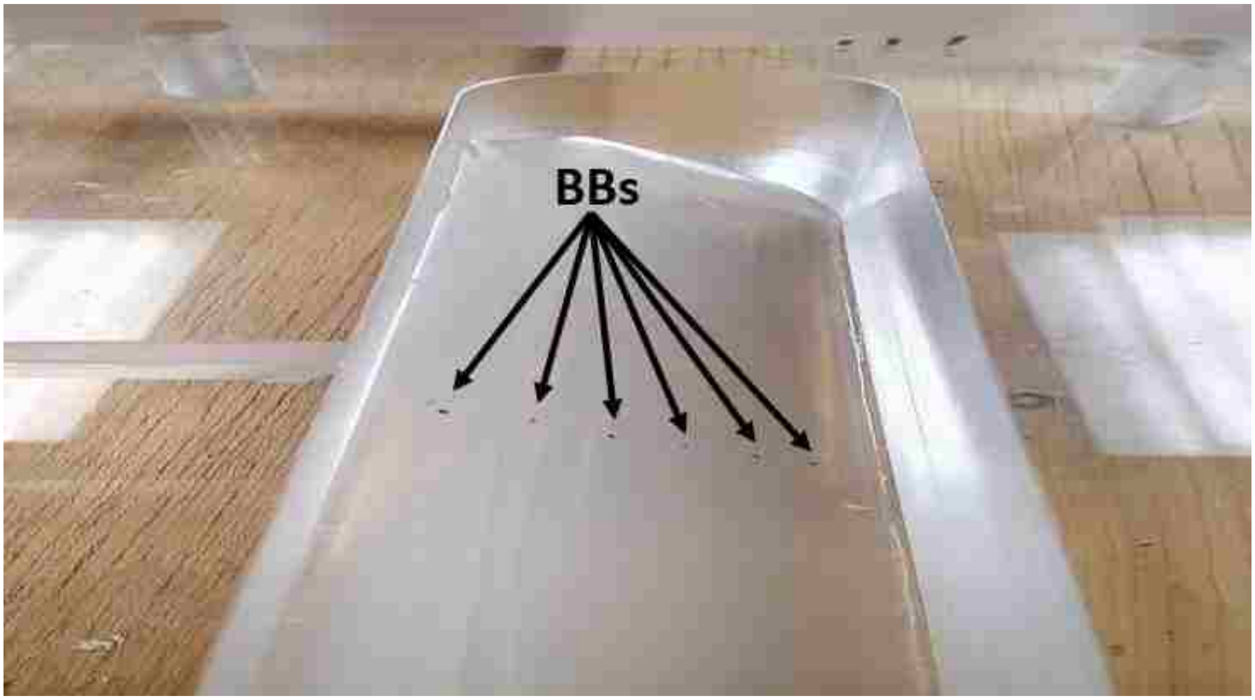

Figure 4.16: View looking down on sample holder plate, showing BBs in place on the slanted surface of the gel slab.

Three endoDPT scans were acquired at 80 kVp using x-ray source currents of 25 mAs, 50 mAs, and 100 mAs (to result in low, medium, and high exposure scans) with the small focal spot setting (0.6 mm). The modular acrylic phantom was configured as shown in Fig. 4.7. A single projection image of the BBs is shown in Fig. 4.17.

Image planes were reconstructed using SAA, BP, and FBP from $z = 0.5$ cm to $z = 4.0$ cm in 0.1 mm increments for all three scan sets using all 41 projection images. After reconstruction, the center points and heights of the BBs were determined for all six BBs. For each BB, an ROI of 30 voxels by 30 voxels was drawn about the center point of the BB. This ROI was used as the signal measurement for computation of the ASF. An ROI of the same size was also drawn 1 cm from each BB center point along $-\hat{x}$ on the reconstructed image. This second ROI was used as a background measurement for computation of the ASF. The mean voxel value of these ROIs was used to compute the ASF. The two ROIs for one of the BBs is shown in Fig. 4.18.

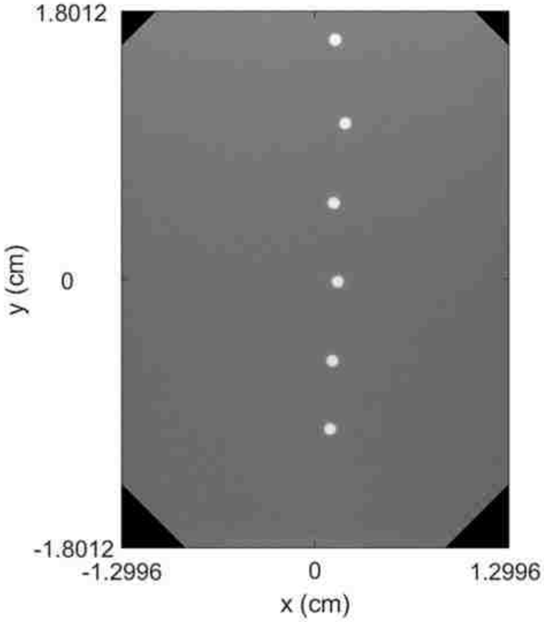

Figure 4.17: Single projection image of BBs, taken at a nominal source location of (0 cm, 0 cm, 100 cm). This image was acquired at 80 kVp with 100 mAs.

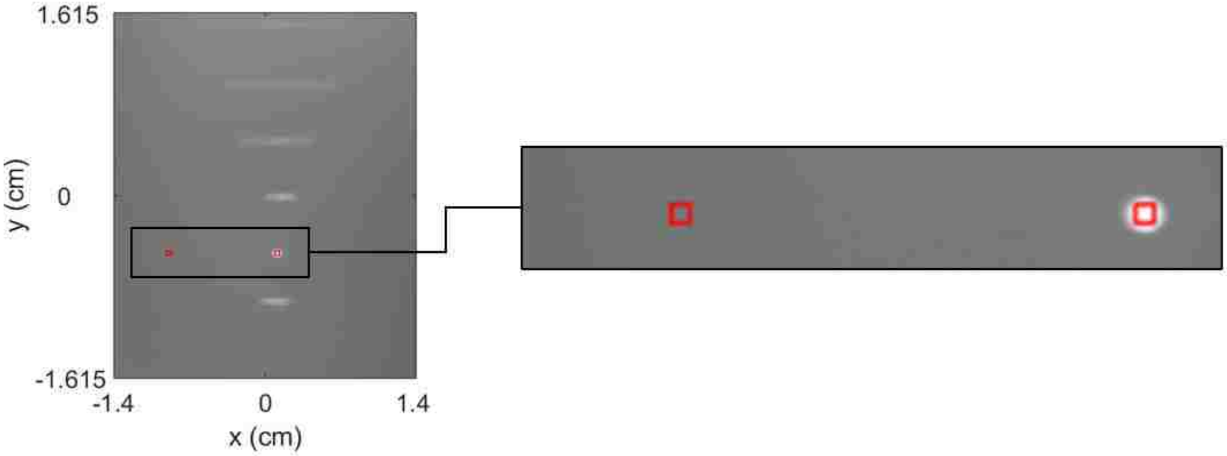

Figure 4.18: Image reconstructed with BP at $z = 1.6$ cm showing ROIs (30 pixel by 30-pixel red boxes) used for computation of the ASF. The left-most ROI is for the background measurement and the right-most ROI is centered over the reconstructed BB.

The ASF was calculated for each BB for every combination of reconstruction algorithm and x-ray source current using

$$ASF(z) = \frac{\bar{\mu}_{artifact}(z) - \bar{\mu}_{BG}(z)}{\bar{\mu}_{feature}(z_0) - \bar{\mu}_{BG}(z_0)} \tag{4.4}$$

where $\bar{\mu}_{feature}(z_0)$ was the mean voxel value of the in-plane BB ROI, $\bar{\mu}_{artifact}(z)$ was the mean voxel value of the BB ROI in other planes, and $\bar{\mu}_{BG}$ was the mean voxel value of the background ROI (Wu 2004).

4.6.4 Dose

An acrylic and carrageenan phantom with packets of TLD powder located both on the surface of the phantom and sandwiched between slabs of the phantom (Fig. 4.19) was used to measure absorbed dose delivered by an endoDPT scan. Carrageenan gel slabs conformed around the TLD packets to prevent air gaps from two layers such as would occur if sandwiching TLD packets between two acrylic plates.

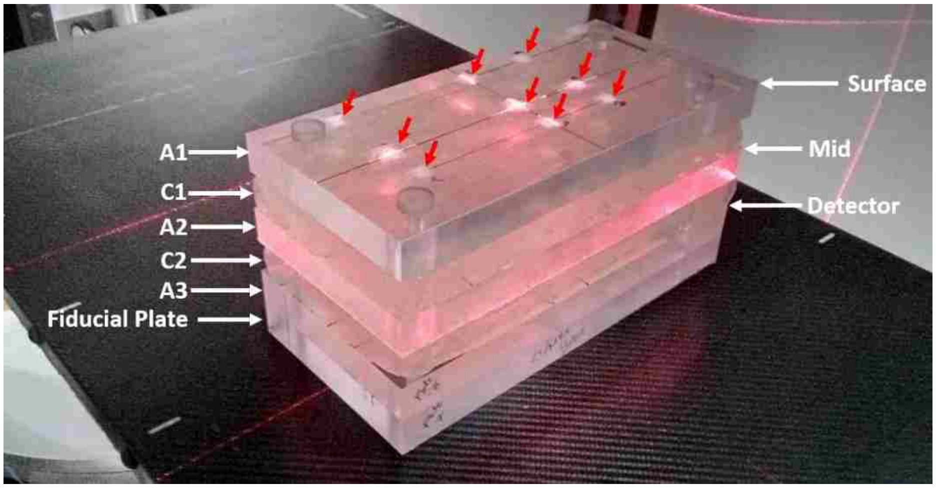

Figure 4.19: Acrylic and carrageenan phantom used to measure ionizing dose from endoDPT and CT scans. 1” thick acrylic slabs (A) and carrageenan slabs (C) were used. TLD packets are located on the surface (red arrows), mid, and detector planes of the phantom.

TLD packets were made from two layers of 1 cm by 1 cm thin plastic sheet and contained 45 mg of TLD100 LiF(Mg,Ti) powder (Rexon Components, Inc., Beachwood, Ohio). The edges of the plastic packets were heat sealed using a plastic film sealer. TLD100 powder is commonly used for patient dosimetry at Mary Bird Perkins Cancer Center; the packet formation followed their clinical process. Each TLD packet was assumed to be a point dosimeter, ignoring the size of the TLD powder sample and the plastic sheet.

Twenty-seven TLD packets were arranged on three planes on and within the phantom (Fig. 4.19). The surface plane TLDs were on the phantom surface, the mid plane TLDs were located 2” (5.08 cm) below the surface, and the detector plane TLDs were located 4” (10.16 cm) below the surface. The XDR sensor was not in place for dose measurements – a solid acrylic plate was used in place of the XDR sensor holder plate. For the mid and detector planes, TLDs were placed on an acrylic plate with a carrageen gel slab placed on top of them (e.g., between A2 and C1, and between A3 and C2).

Nine TLD packets were in each plane in the phantom in the positions shown in Fig. 4.20. These locations were the same for each plane. The gray box shows the endoDPT field size (6 cm by 6 cm) at the detector plane for the x-ray source location of (0 cm, 0 cm, 100 cm).

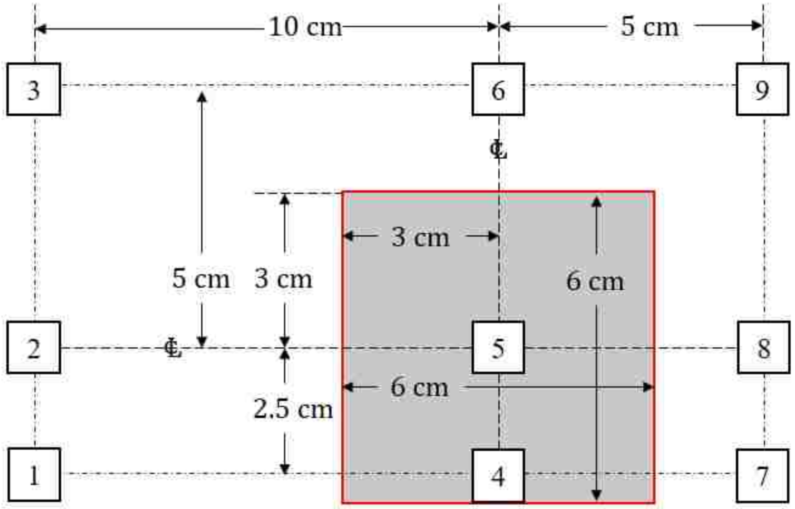

Figure 4.20: TLD locations on each plane of dose phantom. The gray box bounded by a red line shows the endoDPT field size (6 cm by 6 cm) and location of the field at the detector plane for the x-ray source location of (0 cm, 0 cm, 100 cm).

With reference to the projected field for the (0 cm, 0 cm, 100 cm) source location, the TLDs were positioned such that TLD 5 was located above the XDR sensor center point at $x_D = y_D = z_D = 0$, TLD 4 was at and within the field edge, TLDs 6, 7, and 8 were located 2.0 cm from the field edge, and TLDs 1, 2, 3, and 9 were located ≥ 2 cm from the field edge. This pattern of TLDs gave a cross section of the imaging dose in the FoV, near the FoV, and far from the FoV at discrete depths within the phantom.

Ten identical endoDPT scans of the dose phantom were acquired in the normal manner at 80 kVp and 100 mAs with the small focal spot size (0.6 mm) with the TLDs accumulating dose over all ten scans. The multiple scans improved the statistics of the TLD measurement. After irradiation, the TLDs were stored for 24 hours prior to reading. After 24 hours, the 27 irradiated TLD packets, plus one unirradiated (background) TLD packet, were read on a Rexon UL-320 TLD reader (Rexon Components, Inc., Beachwood, Ohio). Each TLD packet was divided into three ~15 mg samples. The mass of each sample was measured using a Mettler Toledo AL54 Electronic Analytical Balance (Mettler Toledo, Columbus, Ohio). Each sample was placed on a planchette, inserted into the TLD reader, and heated through pre-heat and heat cycles. Luminescence as a function of temperature was recorded during the heat cycle, which heated the TLD powder uniformly from 60°C to 240°C over 25 seconds. The edges of the planchette that connect to the electrodes were polished with fine grit sandpaper after each TLD packet (every three readings). The internal portion of the planchette where the powder resides was polished with a cotton swab after each reading. This method followed the clinical procedure used for patient dosimetry at Mary Bird Perkins Cancer Center.

For each TLD packet, the mean thermoluminescence per mass (TL/mass which was measured in counts per mg) and the standard deviation of the luminescence per mass was found using

$$\overline{TL/mass}_i = \frac{1}{N}\sum_{k=1}^{N} TL/mass_{i,k} \tag{4.5}$$

and

$$\sigma_{\overline{TL/mass}_i} = \sqrt{\frac{1}{N-1}\sum_{k=1}^{N}\left(TL/mass_{i,k} - \overline{TL/mass}_i\right)^2} \tag{4.6}$$

for $N = 3$ samples per TLD packet. To find the net mean luminescence per mass for each irradiated TLD packet, the background $\overline{TL/mass}_{BG}$ was subtracted from each irradiated packet's $\overline{TL/mass}$. Because 10 scans were collected at 100 mAs for endoDPT, the net $\overline{TL/mass}$ for each irradiated packet was divided by 10 to give the TLD reading for one endoDPT scan at 100 mAs, by 20 to give the TLD reading for one endoDPT scan at 50 mAs, and by 40 to give the TLD reading for one endoDPT scan at 25 mAs. This assumed that the TLD luminescence was linear to both number of scans and x-ray source current (Attix 1986, Knoll 2010).

To report the mean TLD readings as absorbed dose, a TLD calibration curve was measured using an Elekta Versa linear accelerator (LINAC) (Elekta, Stockholm, Sweden). This was a relative calibration because the LINAC photon energy was 6 MV (minimum energy setting of the LINAC) whereas photons produced at 80 kVp were used to measure endoDPT dose. There is a slight energy dependence of TLD100 powder resulting in kV photons having about 1.1 times more luminescence for a given dose than MV photons (Attix 1986). However, because the objective of this study was to determine dosimetric differences between endoDPT and CT, rather than determining absolute dose, this calibration curve was a satisfactory conversion of luminescence to dose (Gy).

To create the calibration curve, seven TLD packets were irradiated to the doses listed in Table 4.5. All the TLD packets except for Sample 1 (background measurement) were sandwiched at 10 cm depth in a 20 cm thick water equivalent plastic material. The TLD packets were aligned to the center of the field with the source located at 0° (AP beam) at 100 cm above the TLD packet (90 cm source to surface distance) using a 6 MV beam. The dose per MU at 10 cm depth with the 6 MV is 0.8 MU/cGy for the LINAC used in this study.

Table 4.5: TLD packets used to create calibration curve. MU is the monitor unit setting for the LINAC.

Sample	MU	Dose (cGy) at 10 cm depth
1	0	0
2	15	12
3	25	20
4	50	40
5	100	80
6	200	160
7	250	200

The mean luminescence per mass (counts per mg) and the standard deviation of the luminescence per mass were determined using the readout procedure described above (Table 4.6). The calibration curve was generated as a linear fit of the TLD reading to delivered to delivered dose (Fig. 4.21), requiring a y-intercept of zero. TLD100 has a linear response in this dose range (Attix 1986).

Table 4.6: Readings from irradiated TLD packets for calibration curve. BG is background. σ is the uncertainty in the BG subtracted value.

Sample	MU	Dose (cGy)	Raw Counts (TL/mg)	Net BG subtracted counts (TL/mg)	σ (counts)
1	0	0	607	-	
2	15	12	1046	439	78
3	25	20	1165	558	55
4	50	40	1756	1146	52
5	100	80	2785	2178	78
6	200	160	5162	4555	92
7	250	200	6353	5747	73

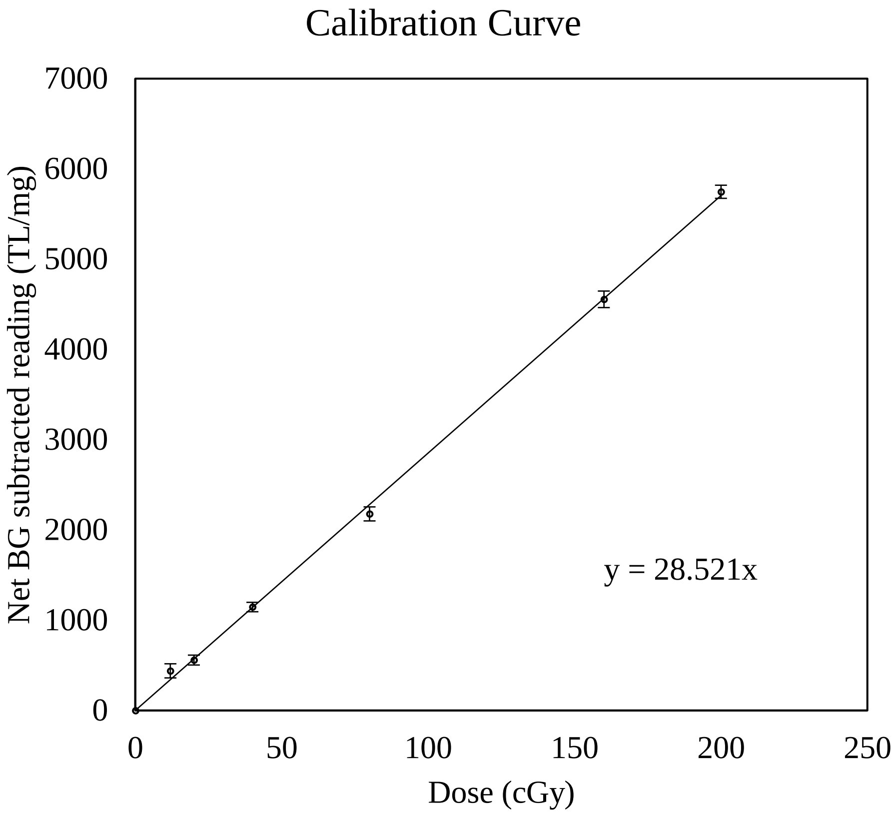

Figure 4.21: TLD calibration curve measured with a 6 MV LINAC. The error bars represent the standard deviation of the net BG subtracted reading.

4.7 CT Image Quality Metrics

Both MTF and dose were measured using a typical scan protocol on a CT scanner. These metrics were statistically compared to endoDPT to test the hypothesis of this study. All CT scans were performed using the CT scanner discussed in Section 4.3.

4.7.1 MTF

The MTF of the CT scanner was measured using an AAPM CT Performance Phantom (Fluke Biomedical, Cleveland, Ohio). The phantom contained a 0.009” (0.23 mm) steel wire surrounded by water. The phantom was oriented on the CT scanner couch such that the wire was perpendicular to the slice plane and parallel to the scanner axis. This wire allowed for measurement of the CT system MTF ($\mathrm{MTF_{CT}}$) in one step (Kayugawa 2013), in contrast to endoDPT which required measurement of $\mathrm{MTF_{recon}}$ and $\mathrm{MTF_{detector}}$.

Multiple slices of the wire were collected using helical scanning mode at 120 kVp, 1.25 mm slice thickness, 0.938 pitch, small reconstruction FoV (512 by 512 matrix, 0.488 mm voxel size), and automatic x-ray source current. A single slice is shown in Fig. 4.22, with the wire located within the top ROI (wire ROI). The bottom ROI was used for background measurement (background ROI). ROIs were collected, rather than single profiles through the wire, to reduce the effect of noise and of small changes in the wire location throughout the scan.

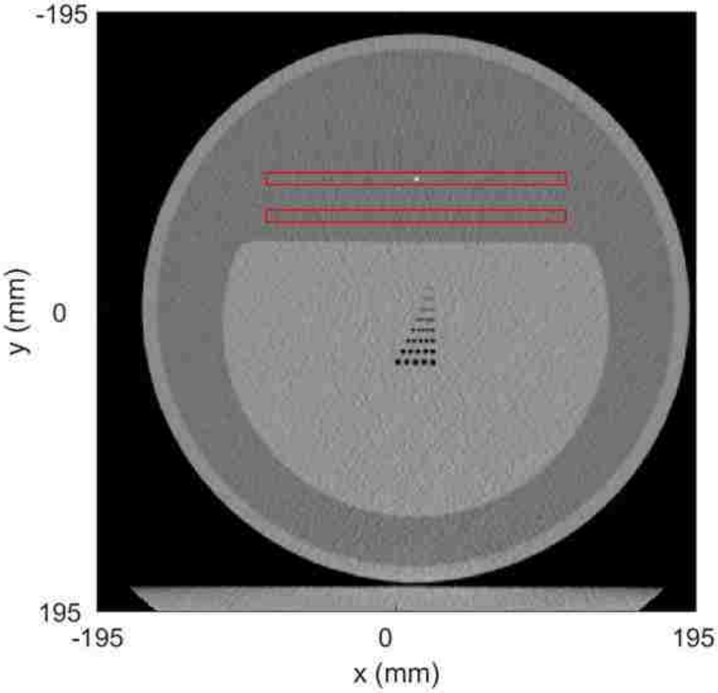

Figure 4.22: AAPM CT Performance Phantom image, showing wire phantom within the top red ROI; the bottom ROI was used for a BG measurement. The ROIs have been drawn larger in $\hat{y}$ for clarity (9 voxels instead of 5 voxels).

The MTF of the CT scanner was measured over 24 slices. To measure the MTF, first the ROIs shown in Fig. 4.22 (101 voxels by 5 voxels) were extracted from each slice. For each slice, the mean value of the background ROI was subtracted from each voxel in the wire ROI. Each column array ($\hat{y}$) in the wire ROI was integrated, creating a single row array that contained the background subtracted wire profile. Similar methods of ROI integration have been previously reported (Kayugawa 2013). The profile was subsampled for every 0.1 voxels and a Hanning window was applied to reduce the effect of high frequency noise in the tails of the profile (with tunable parameter $a = 1.175$ cm $= 200$ subsampled voxels, which was equivalent to the number of voxels used for a in $\mathrm{MTF}_{\mathrm{detector}}$ for endoDPT). $\mathrm{MTF}_{\mathrm{CT}}$ was found by taking the Fourier of the profile. The composite $\mathrm{MTF}_{\mathrm{CT}}$ was the average of the set of $\mathrm{MTF}_{\mathrm{CT}}$ measured over all 24 slices.

4.7.2 Dose

The relative dose of CT was measured using the same acrylic/carrageenan phantom and TLD packet locations as endoDPT. The phantom was irradiated with 15 typical CT scans with the horizontal setup lasers aligned parallel to the detector plane, resulting in similar TLD readings as the 10 endoDPT scans at 100 mAs/image for points within the endoDPT beam. Each CT scan consisted of anterior-posterior and lateral localizing scans and a single acquisition. The localizing scans were performed over a 20 cm range at 120 kVp and 80 mAs/image. The helical scan was performed over the same range at 120 kVp, 1.25 mm slice thickness, 0.938 pitch, and automatic x-ray source current. The x-ray source current was 150 mAs to 170 mAs over the scan duration. The TLD packets were read using the same procedure described above – the readings were background subtracted and then divided by 15 to find the reading for a single, typical CT scan.

4.8 Results

4.8.1 Resolution

Fig. 4.23 shows the mean endoDPT $\mathrm{MTF}_{\mathrm{detector}}$ measured at 80 kVp and 12.5 mAs. This MTF is representative of MTFs found for various kVp and mAs settings. For each set of x-ray source potential and x-ray source current, the mean frequency values ($\overline{\omega}$) and standard deviations ($\sigma_{\overline{\omega}}$) at which the MTF was reduced to 90%, 50%, and 10% are summarized in Table 4.7.

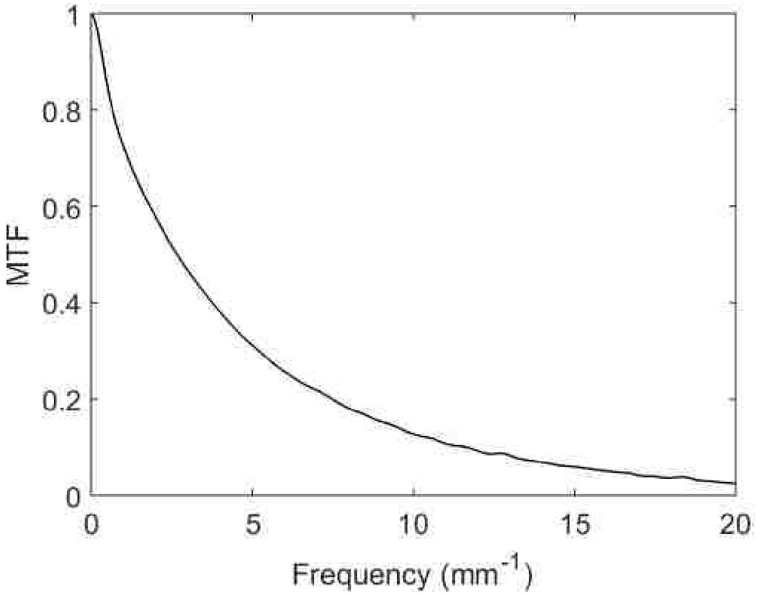

Figure 4.23: Composite $\mathrm{MTF}_{\mathrm{detector}}$ for projection image acquired at 80 kVp and 12.5 mAs. For clarity error bars were not plotted (typical standard deviations were 1% of the frequency values measured at 90%, 50%, and 10% MTF and are listed in Table 4.7).

Table 4.7: Frequency values and standard deviation at the 90%, 50%, and 10% MTF for each of the 15 $\mathrm{MTF}_{\mathrm{detector}}$.

Image Set	**kV**	**mAs**	**Frequency (mm^{-1}) of the 90%, 50% and 10% MTF**					
			$\bar{\omega}_{90\%}$	$\sigma_{\bar{\omega}_{90\%}}$	$\bar{\omega}_{50\%}$	$\sigma_{\bar{\omega}_{50\%}}$	$\bar{\omega}_{10\%}$	$\sigma_{\bar{\omega}_{10\%}}$
1	60	16.0	0.3720	0.0028	2.644	0.030	11.50	0.38
2	60	32.0	0.3721	0.0026	2.654	0.027	11.55	0.21
3	60	50.0	0.3728	0.0022	2.643	0.033	11.56	0.15
4	70	12.5	0.3783	0.0058	2.671	0.035	11.53	0.31
5	70	20.0	0.3773	0.0064	2.684	0.019	11.58	0.26
6	70	32.0	0.3777	0.0058	2.686	0.030	11.57	0.20
7	80	8.0	0.3725	0.0026	2.670	0.041	11.69	0.22
8	80	12.5	0.3716	0.0028	2.675	0.027	11.50	0.31
9	80	20.0	0.3731	0.0022	2.681	0.023	11.68	0.21
10	90	6.3	0.3721	0.0036	2.692	0.043	11.67	0.23
11	90	10.0	0.3735	0.0032	2.694	0.028	11.76	0.26
12	90	16.0	0.3734	0.0033	2.695	0.036	11.71	0.26
13	100	4.0	0.3703	0.0039	2.694	0.044	11.78	0.38
14	100	8.0	0.3703	0.0035	2.691	0.045	11.86	0.21
15	100	12.5	0.3704	0.0037	2.694	0.030	11.70	0.18

Statistical comparisons were performed to determine if the measured frequency values at the 90%, 50%, and 10% MTF values varied significantly with x-ray source potential and x-ray source current. The first comparison tested for differences due to x-ray source current (low, medium, and high) in the mean of the measured frequency values for a given MTF value (90%, 50%, or 10%) and a given x-ray source potential (60 kVp, 70 kVp, 80 kVp, 90 kVp, or 100 kVp). This test was performed using analysis of variance (ANOVA) and assumed a significance level of $p < 0.05$ which corresponds to the critical F-statistic $F_{crit} = 3.35$. The results of this analysis for each MTF value and x-ray source energy are summarized in Table 4.8. There were no statistical differences due to x-ray source current in the measured mean frequency at any MTF value or x-ray source energy ($p > 0.05$ for all comparisons). Because this result showed no statistical difference, ad hoc comparisons between the measured mean frequency values for each x-ray source current (e.g., performing the student t-test between the mean frequency measured at 60 kVp, low tube current, 90% MTF, and the mean frequency measured at 60 kVp, high tube current, 90% MTF) were not performed.

Table 4.8: Summary of the ANOVA test for differences in the mean measured frequency due to x-ray source current (low, medium, and high) for a given MTF value and a given x-ray source energy.

Source	**90% MTF**		**50% MTF**		**10% MTF**	
Potential	F	$p-$**value**	F	$p-$**value**	F	$p-$**value**
60 kVp	0.28	0.76	0.39	0.68	0.13	0.88
70 kVp	0.07	0.93	0.81	0.46	0.10	0.90
80 kVp	0.94	0.40	0.30	0.74	1.83	0.18
90 kVp	0.57	0.57	0.02	0.98	0.32	0.73
100 kVp	0.01	0.99	0.03	0.97	0.93	0.40

The second comparison tested for differences due to x-ray source potential (60 kVp, 70 kVp, 80 kVp, 90 kVp, or 100 kVp) in the mean of the measured frequency values for a given MTF value (90%, 50%, or 10%). Because no statistical difference was found as a function of x-ray source current (low, medium, or high), all of the frequency values measured for a given MTF value and a given energy were used in the comparison between x-ray source energies. This test was also performed using ANOVA with an assumed significance level of $p < 0.05$ ($F_{crit} = 2.43$), with the results summarized in Table 4.9.

Table 4.9: Summary of the ANOVA test for differences in the mean measured frequency due to x-ray source potential (60 kVp, 70 kVp, 80 kVp, 90 kVp, and 100 kVp) for a given MTF value.

	90% MTF		**50% MTF**		**10% MTF**	
mAs	$\boldsymbol{F}$	$\boldsymbol{p-\text{value}}$	$\boldsymbol{F}$	$\boldsymbol{p-\text{value}}$	$\boldsymbol{F}$	$\boldsymbol{p-\text{value}}$
All	16.23	< 0.0001	10.38	< 0.0001	4.77	0.0012

The results in Table 4.9 indicate that at least one of the x-ray source energies had a significantly higher or lower mean frequency value for each of the three MTF points. Ad hoc statistical comparisons were performed between each x-ray source energy for each MTF value using the student t-test. For each MTF value, there were 10 inter-energy comparisons (e.g., comparing 60 kV to 70 kV), and so a Bonferroni correction was applied the assumed significance level of $p < 0.05$, resulting in a significance level of $p < 0.005$.

The trends in mean frequency values as a function of x-ray source energy for each MTF value are shown in the box plots in Fig. 4.24, Fig. 4.25, and Fig. 4.26. The mean frequency value at which the MTF was reduced to 90% was significantly higher for 70 kVp than for the other x-ray source potentials. The MTF was reduced to 90% at $\bar{\omega} = 0.378\,\text{mm}^{-1}$ for 70 kVp and at $\bar{\omega} = 0.370\,\text{mm}^{-1}$ for 100 kVp; 100 kVp had the smallest mean frequency value for the 90% MTF. While this result was significant, it is overall a small difference ($0.008\,\text{mm}^{-1}$). The mean frequency values at which the MTFs were reduced to 50% and 10% generally increased as energy increased.

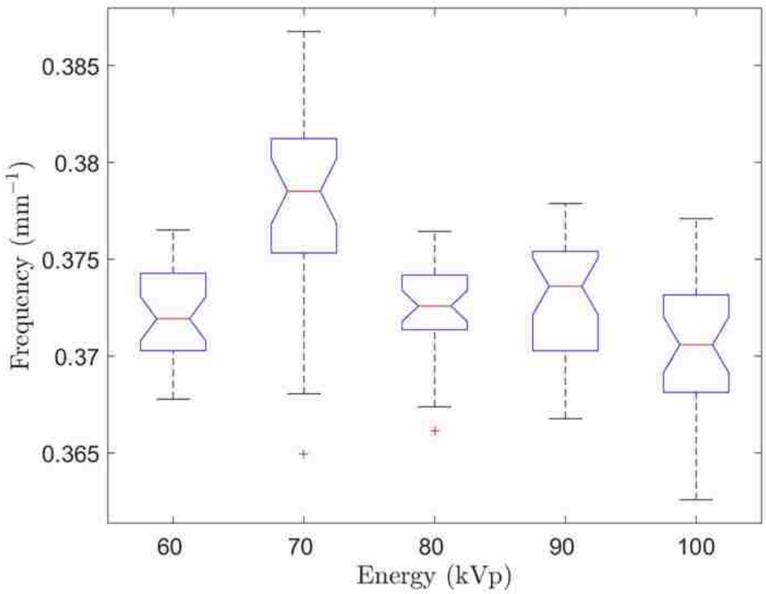

Figure 4.24: Box plot showing median frequency value (red line) at which the detector MTF was reduced to 90% for each x-ray source energy. The notches on the boxes represent the 95% confidence interval, the bottom and top of the box are the 25^{th} and the 75^{th} percentiles, respectively, the whiskers extend to approximately $\pm 2.7\sigma$ which contains 99% of normally distributed data, and the red plus symbols indicate outliers.

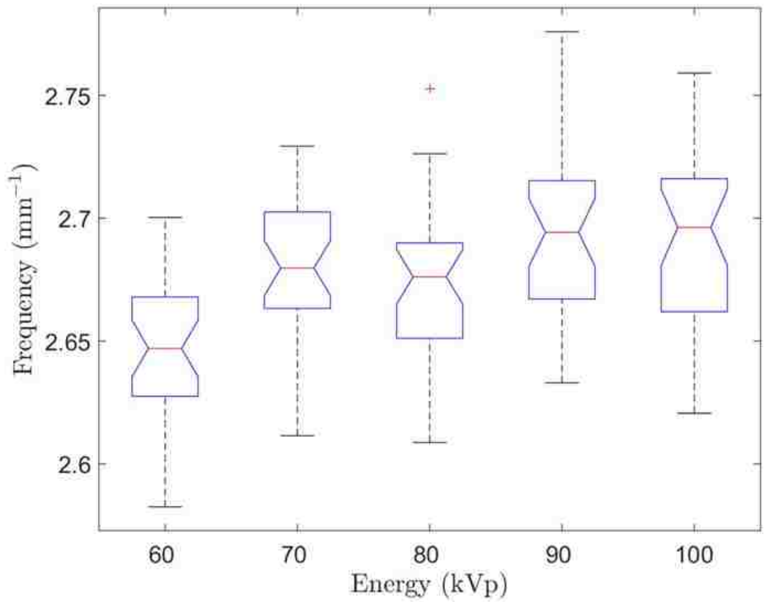

Figure 4.25: Box plot showing median frequency value (red line) at which the detector MTF was reduced to 50% for each x-ray source energy. The notches on the boxes represent the 95% confidence interval, the bottom and top of the box are the 25^{th} and the 75^{th} percentiles, respectively, the whiskers extend to approximately $\pm 2.7\sigma$ which contains 99% of normally distributed data, and the red plus symbols indicate outliers.

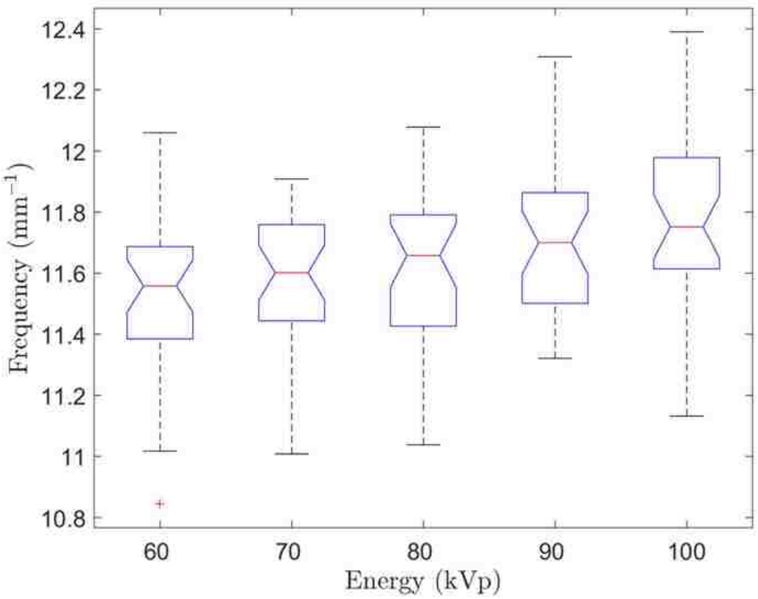

Figure 4.26: Box plot showing median frequency value (red line) at which the detector MTF was reduced to 10% for each x-ray source energy. The notches on the boxes represent the 95% confidence interval, the bottom and top of the box are the 25^{th} and the 75^{th} percentiles, respectively, the whiskers extend to approximately $\pm 2.7\sigma$ which contains 99% of normally distributed data, and the red plus symbols indicate outliers.

Fig. 4.27 compares $\mathrm{MTF}_{\mathrm{endoDPT}}$ at 80 kVp and 12.5 mAs for SAA, BP, and FBP with x-ray source travel of ± 40 cm and 2 cm step size. The acquisition parameters shown here (80 kVp, ± 40 cm, 2 cm source spacing) are those also used for measurement of the NPS, ASF, and dose. Table 4.10 compares the mean frequencies at which $\mathrm{MTF}_{\mathrm{endoDPT}}$ was reduced to 90%, 50%, and 10% for three x-ray source current settings. The mean frequencies at which $\mathrm{MTF}_{\mathrm{endoDPT}}$ was reduced to 90% and 50% for FBP were not assessed due to the filtration process removing the low-frequency information. The FBP $\mathrm{MTF}_{\mathrm{endoDPT}}$ was a relative measure that demonstrated an artificially improved frequency response in comparison to BP. The SAA and BP MTFs were normalized to $\mathrm{MTF}_{\mathrm{recon}}(0)$.

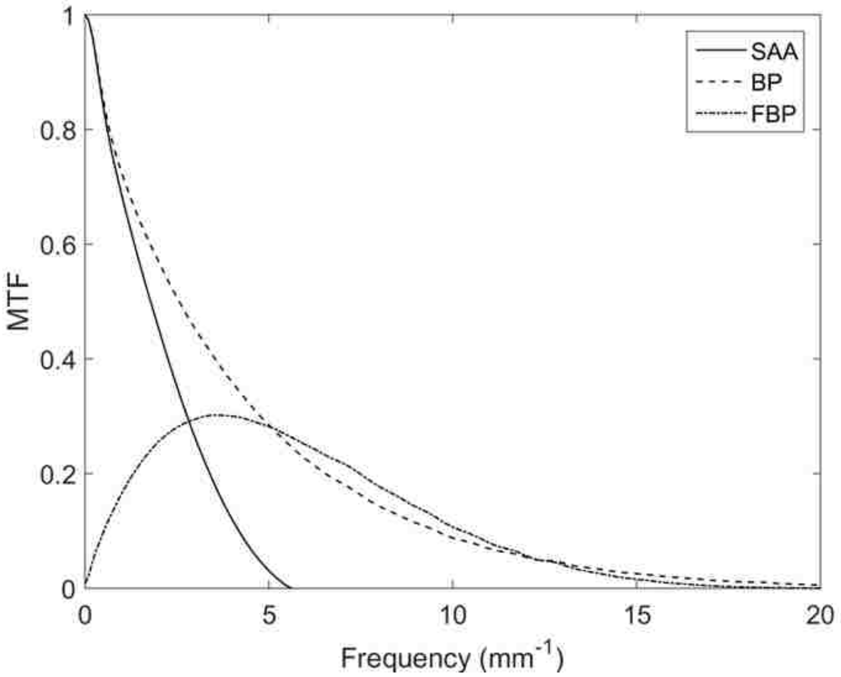

Figure 4.27: $\mathrm{MTF}_{\mathrm{endoDPT}}$ at 80 kVp and 12.5 mAs for each reconstruction method. The reconstruction used 41 images taken in 2 cm increments from $x_{S_i} = -40$ to 40 cm.

Table 4.10: Mean frequencies at which $\mathrm{MTF}_{\mathrm{endoDPT}}$ was reduced 90%, 50%, and 10% versus x-ray source current and reconstruction algorithm. Reconstruction used 41 images taken in 2 cm increments from $x_s = -40$ to 40 cm.

mAs	**Frequency (mm^{-1}) of the 90%, 50% and 10% SAA MTF**					
	$\bar{\omega}_{90\%}$	$\sigma_{\bar{\omega}_{90\%}}$	$\bar{\omega}_{50\%}$	$\sigma_{\bar{\omega}_{50\%}}$	$\bar{\omega}_{10\%}$	$\sigma_{\bar{\omega}_{10\%}}$
8.0	0.3558	0.0010	1.7869	0.0017	4.1811	0.0008
12.5	0.3551	0.0011	1.7846	0.0019	4.1841	0.0009
20.0	0.3564	0.0008	1.7867	0.0016	4.1804	0.0009
mAs	**Frequency (mm^{-1}) of the 90%, 50% and 10% BP MTF**					
	$\bar{\omega}_{90\%}$	$\sigma_{\bar{\omega}_{90\%}}$	$\bar{\omega}_{50\%}$	$\sigma_{\bar{\omega}_{50\%}}$	$\bar{\omega}_{10\%}$	$\sigma_{\bar{\omega}_{10\%}}$
8.0	0.3712	0.0011	2.5572	0.0038	9.5071	0.0032
12.5	0.3703	0.0011	2.5635	0.0029	9.5501	0.0031
20.0	0.3719	0.0009	2.5672	0.0025	9.5568	0.0025
mAs	**Frequency (mm^{-1}) of the 90%, 50% and 10% FBP MTF**					
	$\bar{\omega}_{90\%}$	$\sigma_{\bar{\omega}_{90\%}}$	$\bar{\omega}_{50\%}$	$\sigma_{\bar{\omega}_{50\%}}$	$\bar{\omega}_{10\%}$	$\sigma_{\bar{\omega}_{10\%}}$
8.0	N/A				10.3280	0.0049
12.5					10.2650	0.0032
20.0					10.2840	0.0033

The measured $\mathrm{MTF_{CT}}$ is plotted in Fig. 4.28. The frequencies for the 90%, 50%, and 10% MTF levels are reported in Table 4.11.

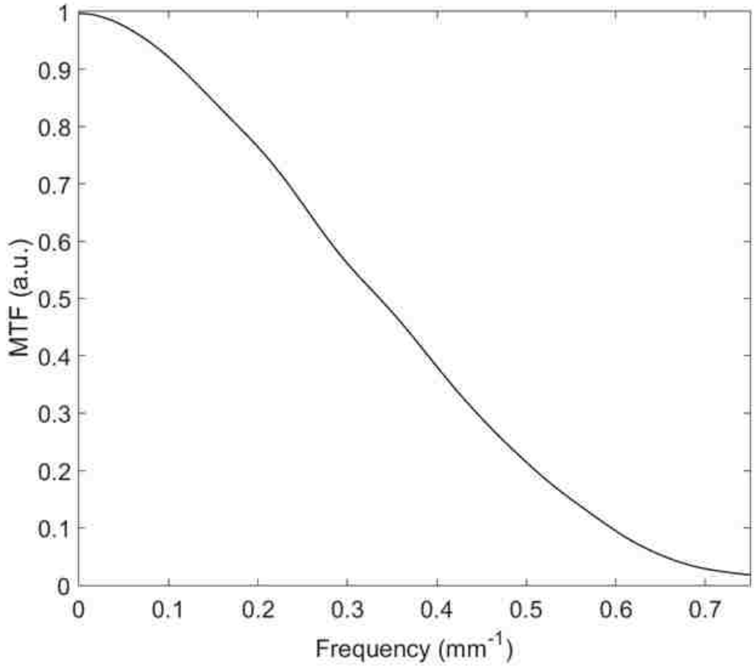

Figure 4.28: $\mathrm{MTF_{CT}}$ (pre-sampled, helical scan, 120 kVp, 1.25 mm slice thickness, 0.938 pitch, 512 by 512 matrix, 0.488 mm voxel size, automatic x-ray source current).

Table 4.11: Mean frequencies at which $\mathrm{MTF_{CT}}$ was reduced 90%, 50%, and 10%.

Frequency (mm^{-1}) of the 90%, 50% and 10% CT MTF					
$\bar{\omega}_{90\%}$	$\sigma_{90\%}$	$\bar{\omega}_{50\%}$	$\sigma_{50\%}$	$\bar{\omega}_{10\%}$	$\sigma_{10\%}$
0.144	0.029	0.408	0.039	0.718	0.033

The frequencies at which $\mathrm{MTF_{endoDPT}}$ and $\mathrm{MTF_{CT}}$ were reduced to 90%, 50%, and 10% were statistically compared using a one-tailed student t-test with a significance level of $p < 0.05$. The multiple parameters used to compute $\mathrm{MTF_{endoDPT}}$ ($\mathrm{MTF_{detector}}$ measured at 8.0 mAs, 12.5 mAs, and 20.0 mAs, and $\mathrm{MTF_{recon}}$ measured for SAA, BP, and FBP) were compared to $\mathrm{MTF_{CT}}$. The results of the statistical comparison are reported in Table 4.12, Table 4.13, and Table 4.14. In all cases, endoDPT had significantly higher resolution than CT. For comparison a single $\mathrm{MTF_{endoDPT}}$ curve and the $\mathrm{MTF_{CT}}$ curve are plotted in Fig. 4.29.

Table 4.12: Statistical comparison of frequencies at which $\mathrm{MTF}_{\mathrm{endoDPT}}$ (8.0 mAs) and $\mathrm{MTF}_{\mathrm{CT}}$ were reduced to 90%, 50%, and 10%. Freq. stands for frequency.

MTF Value	**Freq. (mm^{-1}) of SAA MTF**		**Freq. (mm^{-1}) of CT MTF**		**p-value**
	$\bar{\omega}$	$\sigma_{\bar{\omega}}$	$\bar{\omega}$	$\sigma_{\bar{\omega}}$	
90%	0.356	0.001	0.144	0.030	< 0.0001
50%	1.787	0.002	0.408	0.039	< 0.0001
10%	4.181	0.001	0.718	0.033	< 0.0001
MTF Value	**Freq. (mm^{-1}) of BP MTF**		**Freq. (mm^{-1}) of CT MTF**		**p-value**
	$\bar{\omega}$	$\sigma_{\bar{\omega}}$	$\bar{\omega}$	$\sigma_{\bar{\omega}}$	
90%	0.371	0.001	0.144	0.030	< 0.0001
50%	2.557	0.004	0.408	0.039	< 0.0001
10%	9.507	0.003	0.718	0.033	< 0.0001
MTF Value	**Freq. (mm^{-1}) of FBP MTF**		**Freq. (mm^{-1}) of CT MTF**		**p-value**
	$\bar{\omega}$	$\sigma_{\bar{\omega}}$	$\bar{\omega}$	$\sigma_{\bar{\omega}}$	
90%	N/A		0.144	0.030	N/A
50%			0.408	0.040	N/A
10%	10.328	0.005	0.718	0.033	< 0.0001

Table 4.13: Statistical comparison of frequencies at which $\mathrm{MTF}_{\mathrm{endoDPT}}$ (12.5 mAs) and $\mathrm{MTF}_{\mathrm{CT}}$ were reduced to 90%, 50%, and 10%. Freq. stands for frequency.

MTF Value	**Freq. (mm^{-1}) of SAA MTF**		**Freq. (mm^{-1}) of CT MTF**		**p-value**
	$\bar{\omega}$	$\sigma_{\bar{\omega}}$	$\bar{\omega}$	$\sigma_{\bar{\omega}}$	
90%	0.355	0.001	0.144	0.030	< 0.0001
50%	1.785	0.002	0.408	0.039	< 0.0001
10%	4.184	0.001	0.718	0.033	< 0.0001
MTF Value	**Freq. (mm^{-1}) of BP MTF**		**Freq. (mm^{-1}) of CT MTF**		**p-value**
	$\bar{\omega}$	$\sigma_{\bar{\omega}}$	$\bar{\omega}$	$\sigma_{\bar{\omega}}$	
90%	0.370	0.001	0.144	0.030	< 0.0001
50%	2.565	0.003	0.408	0.039	< 0.0001
10%	9.550	0.003	0.718	0.033	< 0.0001
MTF Value	**Freq. (mm^{-1}) of FBP MTF**		**Freq. (mm^{-1}) of CT MTF**		**p-value**
	$\bar{\omega}$	$\sigma_{\bar{\omega}}$	$\bar{\omega}$	$\sigma_{\bar{\omega}}$	
90%	N/A		0.144	0.030	N/A
50%			0.408	0.040	N/A
10%	10.328	0.005	0.718	0.033	< 0.0001

Table 4.14: Statistical comparison of frequencies at which $\mathrm{MTF_{endoDPT}}$ (20.0 mAs) and $\mathrm{MTF_{CT}}$ were reduced to 90%, 50%, and 10%. Freq. stands for frequency.

MTF Value	**Freq. ($\mathrm{mm^{-1}}$) of SAA MTF**		**Freq. ($\mathrm{mm^{-1}}$) of CT MTF**		**p-value**
	$\bar{\omega}$	$\sigma_{\bar{\omega}}$	$\bar{\omega}$	$\sigma_{\bar{\omega}}$	
90%	0.356	0.001	0.144	0.030	< 0.0001
50%	1.787	0.002	0.408	0.039	< 0.0001
10%	4.180	0.001	0.718	0.033	< 0.0001

MTF Value	**Freq. ($\mathrm{mm^{-1}}$) of BP MTF**		**Freq. ($\mathrm{mm^{-1}}$) of CT MTF**		**p-value**
	$\bar{\omega}$	$\sigma_{\bar{\omega}}$	$\bar{\omega}$	$\sigma_{\bar{\omega}}$	
90%	0.372	0.001	0.144	0.030	< 0.0001
50%	2.567	0.003	0.408	0.039	< 0.0001
10%	9.557	0.003	0.718	0.033	< 0.0001

MTF Value	**Freq. ($\mathrm{mm^{-1}}$) of FBP MTF**		**Freq. ($\mathrm{mm^{-1}}$) of CT MTF**		**p-value**
	$\bar{\omega}$	$\sigma_{\bar{\omega}}$	$\bar{\omega}$	$\sigma_{\bar{\omega}}$	
90%	N/A		0.144	0.030	N/A
50%			0.408	0.040	N/A
10%	10.284	0.003	0.718	0.033	< 0.0001

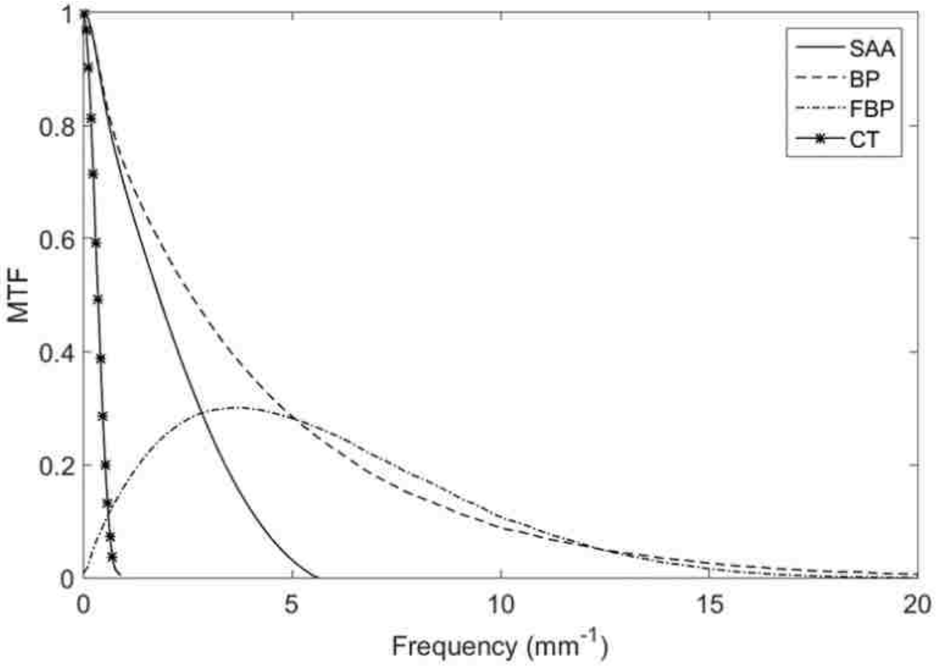

Figure 4.29: Comparison of $\mathrm{MTF_{endoDPT}}$ (80 kVp, 12.5 mAs, 41 images taken in 2 cm increments from $x_s = -40$ to 40 cm) for all reconstruction algorithms used and $\mathrm{MTF_{CT}}$ (helical scan, 120 kVp, 1.25 mm slice thickness, 0.938 pitch, 512 by 512 matrix, 0.488 mm voxel size, automatic x-ray source current).

4.8.2 endoDPT NPS and NEQ

The NPS measured at $z = 1.5$ for three x-ray source currents (25 mAs, 50 mAs, and 100 mAs) are shown in Fig. 4.30 for SAA, Fig. 4.31 for BP, and Fig. 4.32 for FBP. Higher x-ray source currents resulted in lower amplitude of NPS for a given reconstruction method.

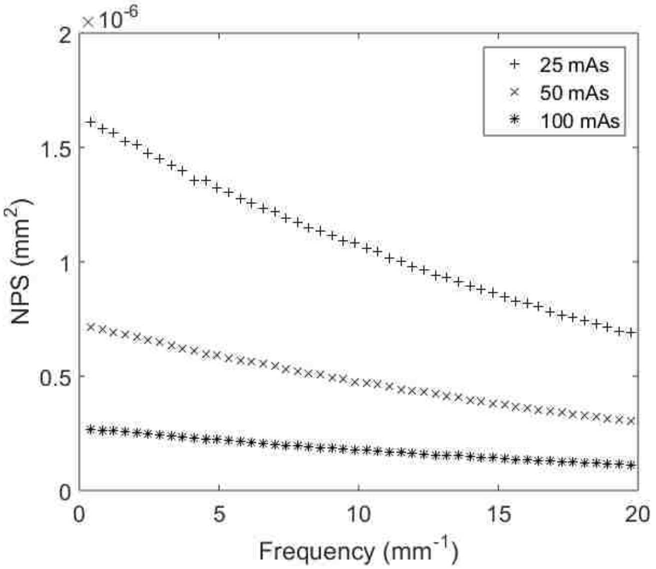

Figure 4.30: SAA NPS measured at 80 kVp using 41 images taken in 2 cm increments for $x_{S_i} = \pm 40$ cm.

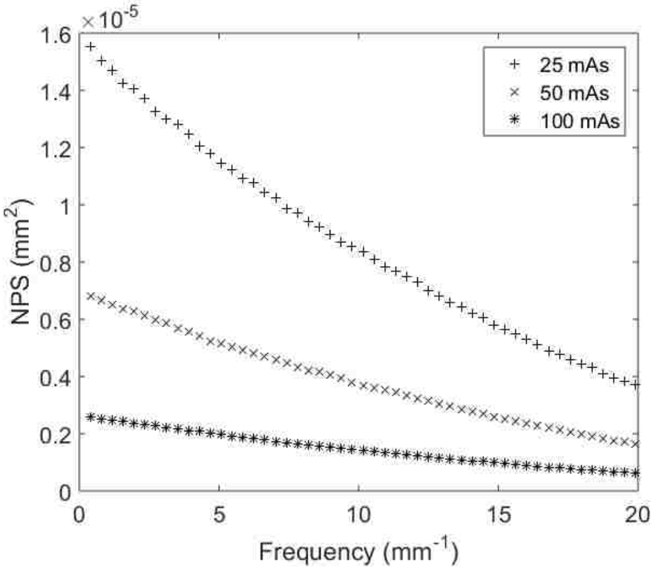

Figure 4.31: BP NPS measured at 80 kVp using 41 images taken in 2 cm increments for $x_{S_i} = \pm 40$ cm.

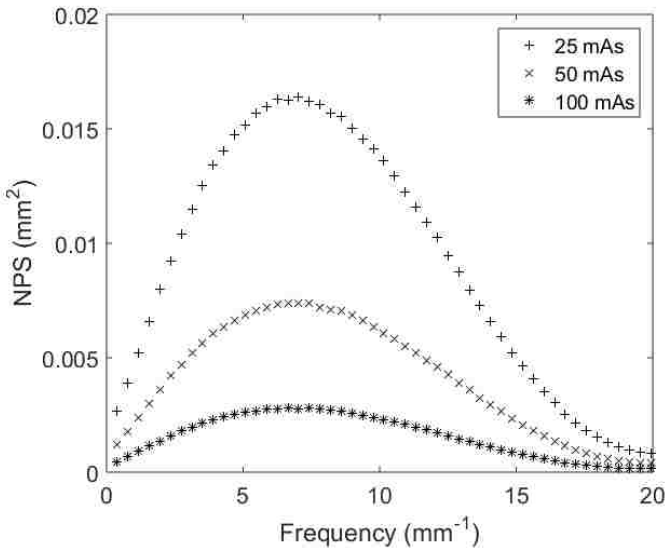

Figure 4.32: FBP NPS measured at 80 kVp using 41 images taken in 2 cm increments for $x_{S_i} = \pm 40$ cm.

The NEQ provides a metric that can be used to compare the three endoDPT reconstruction algorithm for each x-ray source current. Fig. 4.33, Fig. 4.34, and Fig. 4.35 show the NEQ for SAA, BP, and FBP, respectively, for the three levels of x-ray source current used to find $\mathrm{MTF}_{\mathrm{endoDPT}}$ and the NPS. The reported x-ray source currents were not the same between the MTF and NPS scans used to compute the NEQ; for 80 kVp, the low, medium, and high x-ray source current values were 8.0 mAs, 12.5 mAs, and 20 mAs for measurement of $\mathrm{MTF}_{\mathrm{detector}}$ and were 25 mAs, 50 mAs, and 100 mAs for measurement of NPS. For each level of x-ray source current (e.g., the low x-ray source current setting at 8.0 mAs for measurement of $\mathrm{MTF}_{\mathrm{detector}}$ and 25 mAs for measurement of NPS), the XDR sensor was approximately constant. This was appropriate because it resulted in approximately the same incident exposure to the detector for measurement of both $\mathrm{MTF}_{\mathrm{detector}}$ and the NPS; additionally, the limited latitude of the XDR sensor did not allow for an open-air measurement of $\mathrm{MTF}_{\mathrm{detector}}$ (for the half of the sensor that was not under the edge phantom) at 80 kVp with an x-ray source current of greater than 20 mAs without saturating the sensor.

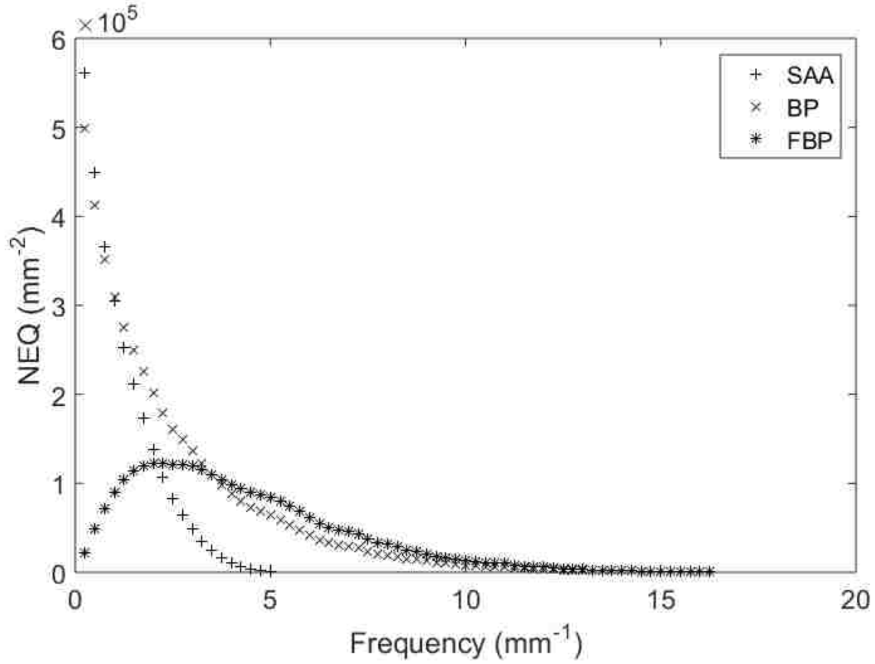

Fig. 4.33: NEQ for the $\mathrm{MTF}_{\mathrm{detector}}$ and NPS measured at 80 kVp for the low x-ray source current setting.

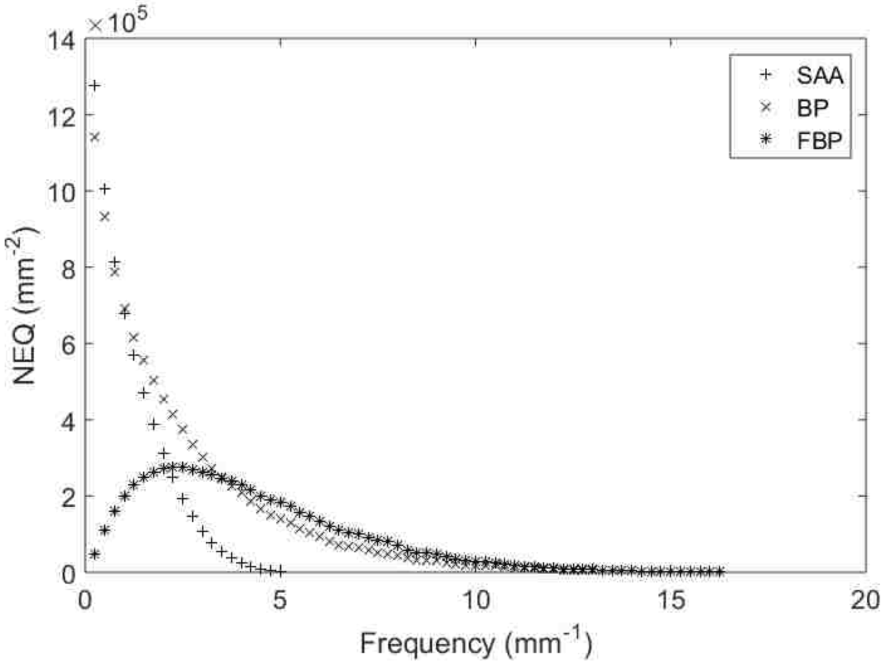

Fig. 4.34: NEQ for the $\mathrm{MTF}_{\mathrm{detector}}$ and NPS measured at 80 kVp for the medium x-ray source current setting.

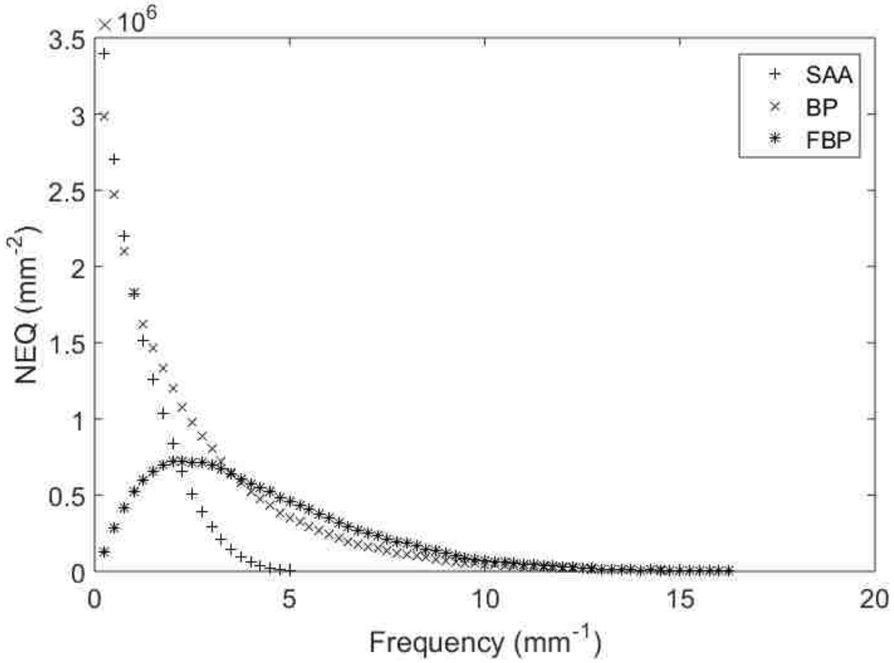

Fig. 4.35: NEQ for the $\mathrm{MTF}_{\mathrm{detector}}$ and NPS measured at 80 kVp for the high x-ray source current setting.

4.8.3 endoDPT ASF

The z-location of each of the six BBs was taken to be the z-plane where the mean value of each BB ROI was at a maximum value. These z-locations are summarized in Table 4.15. The SAA z-locations of the BBs differed marginally (several tenths of a mm) from the BP and FBP z-locations at small z. At large z, the effect became larger (variation by up to 1 mm). This effect occurred due to the parallel beam assumption of SAA.

Table 4.15: BB heights above the XDR sensor for each reconstruction algorithm.

BB	z (cm), SAA	z (cm), BP	z (cm), FBP
1	1.26	1.24	1.24
2	1.56	1.54	1.54
3	1.95	1.91	1.91
4	2.43	2.38	2.38
5	2.95	2.88	2.88
6	3.44	3.33	3.33

Fig. 4.36, Fig. 4.37, and Fig. 4.38 show the ASF for all 6 BBs using SAA, BP, and FBP, respectively. The ASF is only shown for the high (100 mAs) x-ray source current because there was no discernable difference in the ASF as a function of x-ray source current. Fig. 4.39 compares the ASF across reconstruction algorithms for BB 6, which was representative of all BBs.

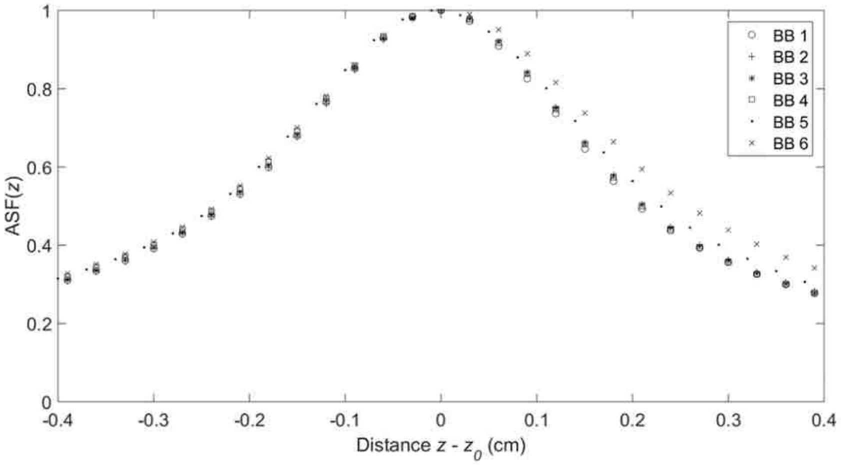

Figure 4.36: ASF for SAA using the 100 mAs x-ray source current and full endoDPT scan (41 source locations, with x_{S_i} nominally ranging from -40 cm to 40 cm in 2 cm increments, $y_S = 0$ cm, and $z_S = 100$ cm).

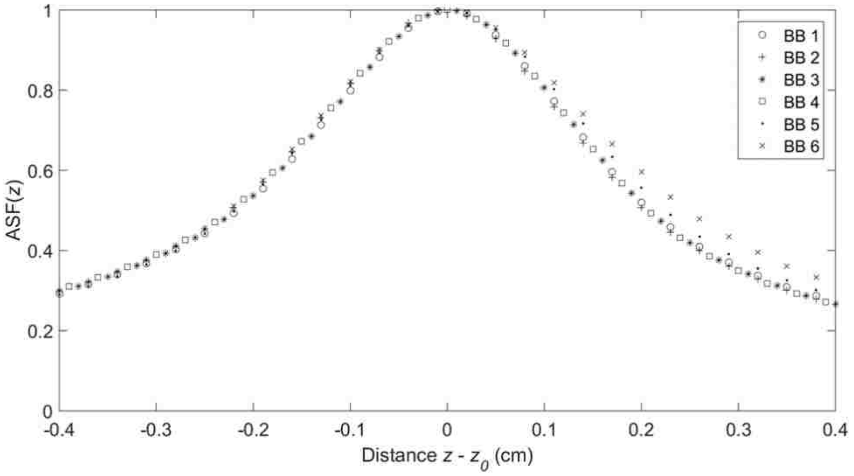

Figure 4.37: ASF for BP using the 100 mAs x-ray source current and full endoDPT scan (41 source locations, with x_{S_i} nominally ranging from -40 cm to 40 cm in 2 cm increments, $y_S = 0$ cm, and $z_S = 100$ cm).

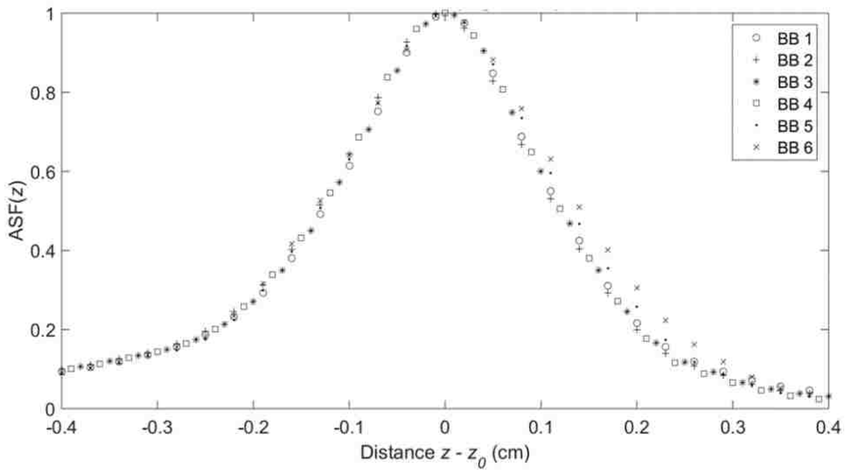

Figure 4.38: ASF for FBP using the 100 mAs x-ray source current and full endoDPT scan (41 source locations, with x_{S_i} nominally ranging from -40 cm to 40 cm in 2 cm increments, $y_S = 0$ cm, and $z_S = 100$ cm).

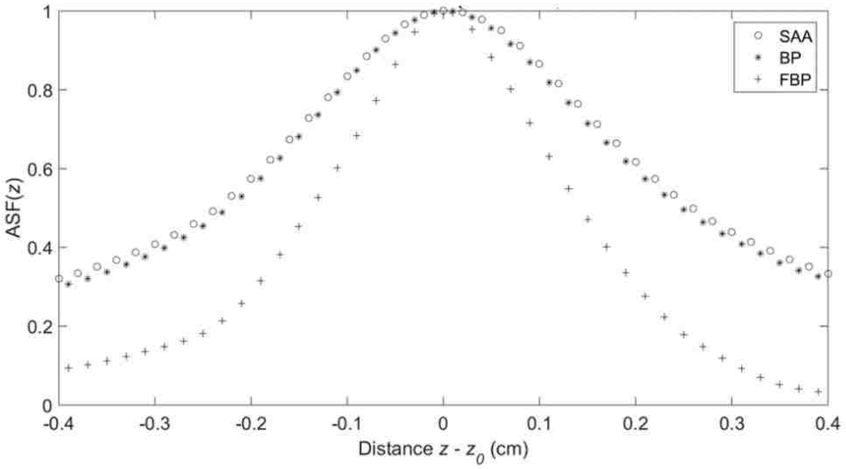

Figure 4.39: ASF for BB 6 for SAA, BP, and FBP using the 100 mAs x-ray source current and full endoDPT scan (41 source locations, with x_{S_i} nominally ranging from -40 cm to 40 cm in 2 cm increments, $y_S = 0$ cm, and $z_S = 100$ cm).

4.8.4 Dose

Fig. 4.40, Fig. 4.41, and Fig. 4.42 report the doses measured at the surface plane, mid plane, and detector plane, respectively for a single CT scan and for single endoDPT scans taken at 100 mAs, 50 mAs, and 25 mAs. Statistical comparisons were performed between the CT and endoDPT measurements using a two-tailed student t-test. $p < 0.05$ was the threshold for significant difference.

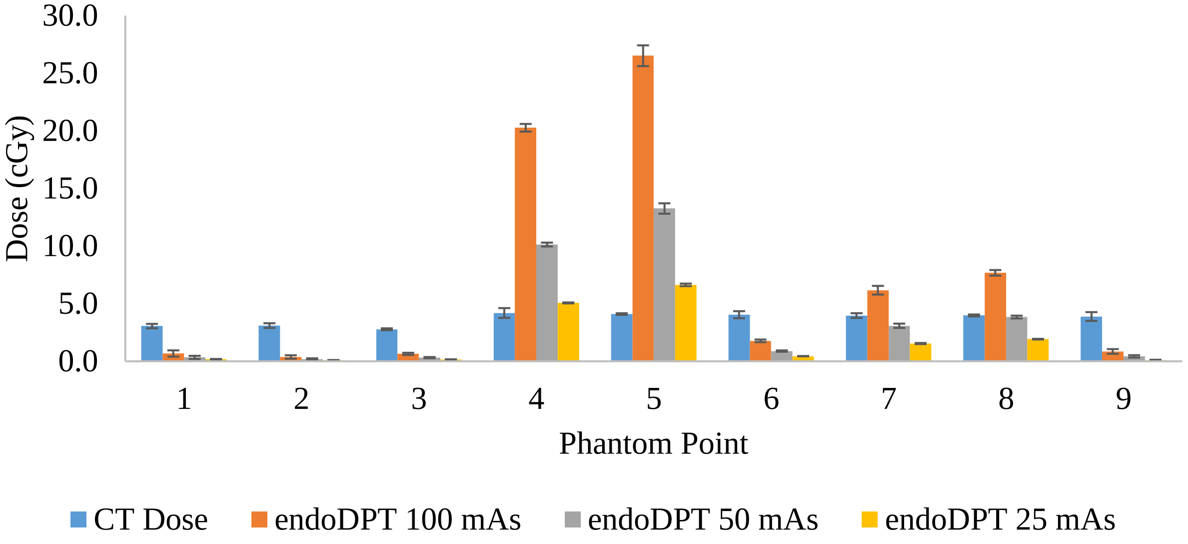

Figure 4.40: Mean dose at each TLD point on the dose phantom surface for a single CT scan and for three discrete endoDPT scans acquired at different x-ray source currents. The vertical error bars represent the standard deviation. Note the y-axis is 0-30 cGy.

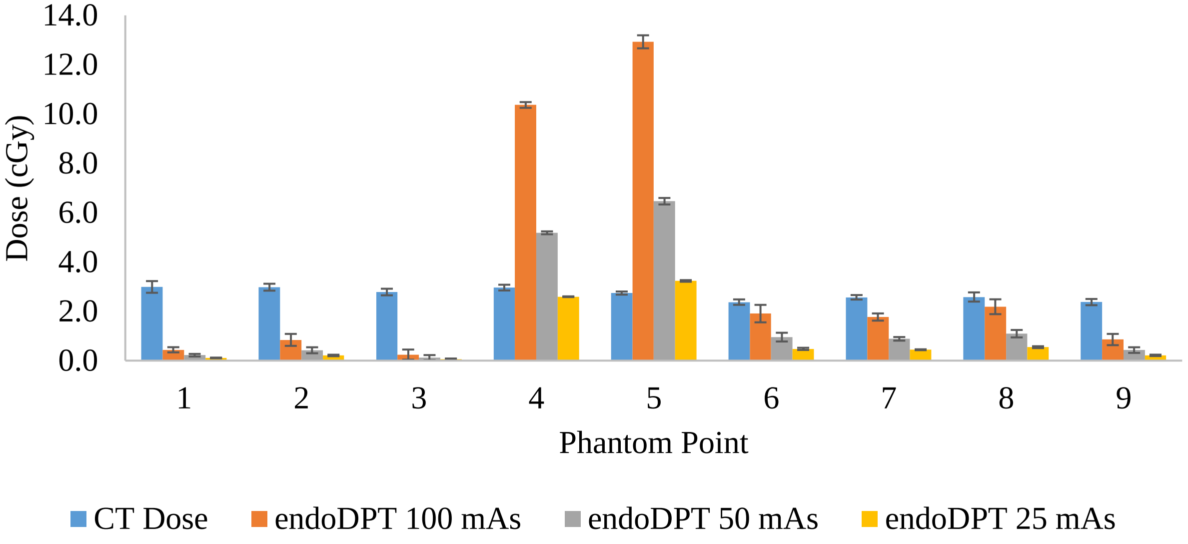

Figure 4.41: Mean dose at each TLD point on the dose phantom mid plane for a single CT scan and for three discrete endoDPT scans acquired at different x-ray source currents. The vertical error bars represent the standard deviation. Note the y-axis is 0-14 cGy.

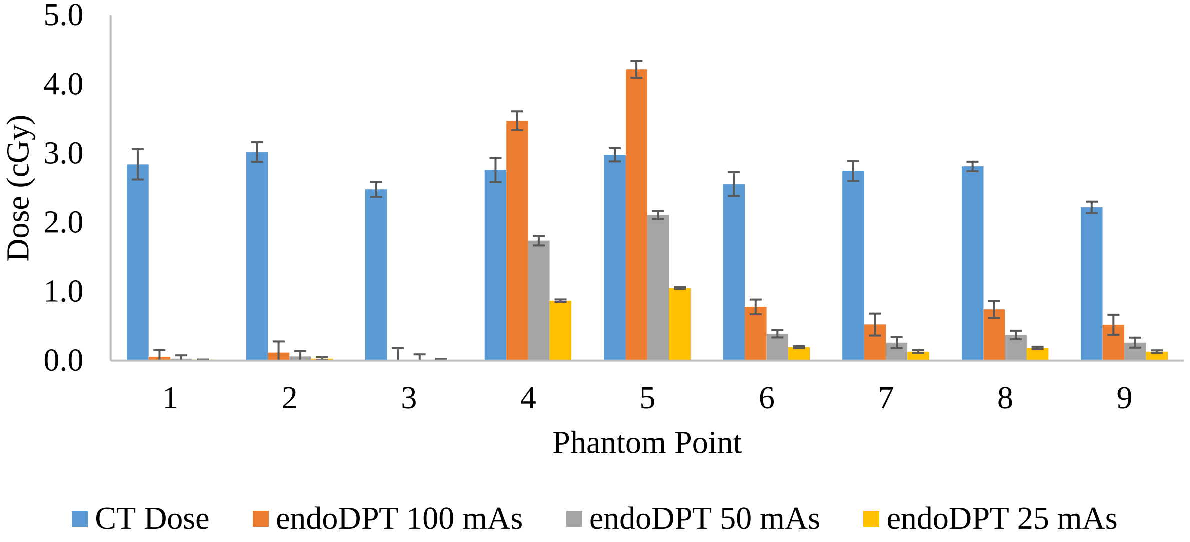

Figure 4.42: Mean dose at each TLD point on the dose phantom detector plane for a single CT scan and for three discrete endoDPT scans acquired at different x-ray source currents. The vertical error bars represent the standard deviation. Note the y-axis is 0-5 cGy.

Table 4.16, Table 4.17, and Table 4.18 report the mean doses ($\bar{D}$), the standard deviations ($\sigma_{\bar{D}}$), and the *p*-values (between CT and endoDPT) for each point in the surface plane, mid plane, and detector plane, respectively.

Table 4.16: Surface plane mean doses for CT and endoDPT. endoDPT doses highlighted in green, yellow, or red indicated the dose at that point was significantly less than, was not different from, or was significantly higher than the CT dose measured at that point, respectively.

	Dose (cGy) at Surface Plane										
Point	CT Dose		endoDPT 100 mAs			endoDPT 50 mAs			endoDPT 25 mAs		
	$\bar{D}$	$\sigma_{\bar{D}}$	$\bar{D}$	$\sigma_{\bar{D}}$	*p*-value	$\bar{D}$	$\sigma_{\bar{D}}$	*p*-value	$\bar{D}$	$\sigma_{\bar{D}}$	*p*-value
1	3.058	0.190	0.68	0.27	0.001	0.34	0.14	0.000	0.17	0.03	0.000
2	3.099	0.205	0.37	0.15	0.000	0.19	0.07	0.000	0.09	0.02	0.000
3	2.777	0.084	0.64	0.09	0.000	0.32	0.05	0.000	0.16	0.01	0.000
4	4.193	0.425	20.27	0.33	0.000	10.13	0.17	0.000	5.07	0.04	0.000
5	4.099	0.073	26.52	0.90	0.000	13.26	0.45	0.000	6.63	0.11	0.000
6	4.044	0.306	1.77	0.11	0.004	0.89	0.06	0.000	0.44	0.01	0.000
7	3.971	0.204	6.17	0.38	0.003	3.08	0.19	0.007	1.54	0.05	0.000
8	3.978	0.086	7.68	0.24	0.000	3.84	0.12	0.108	1.92	0.03	0.000
9	3.886	0.382	0.85	0.20	0.004	0.43	0.10	0.000	0.11	0.03	0.000

Table 4.17: Mid plane mean doses for CT and endoDPT. endoDPT doses highlighted in green, yellow, or red indicated the dose at that point was significantly less than, was not different from, or was significantly higher than the CT dose measured at that point, respectively.

	Dose (cGy) at Mid Plane										
	CT Dose		endoDPT 100 mAs			endoDPT 50 mAs			endoDPT 25 mAs		
Point	$\bar{D}$	$\sigma_{\bar{D}}$	$\bar{D}$	$\sigma_{\bar{D}}$	*p*-value	$\bar{D}$	$\sigma_{\bar{D}}$	*p*-value	$\bar{D}$	$\sigma_{\bar{D}}$	*p*-value
1	2.988	0.237	0.44	0.10	0.002	0.22	0.05	0.000	0.11	0.01	0.000
2	2.978	0.140	0.84	0.24	0.001	0.42	0.12	0.000	0.21	0.03	0.000
3	2.782	0.134	0.24	0.21	0.000	0.12	0.10	0.000	0.06	0.03	0.000
4	2.961	0.116	10.37	0.12	0.000	5.18	0.06	0.000	2.59	0.01	0.000
5	2.740	0.064	12.93	0.26	0.000	6.46	0.13	0.000	3.23	0.03	0.001
6	2.372	0.110	1.91	0.35	0.113	0.95	0.18	0.003	0.48	0.04	0.000
7	2.568	0.092	1.77	0.15	0.003	0.88	0.07	0.000	0.44	0.02	0.000
8	2.581	0.187	2.19	0.30	0.129	1.09	0.15	0.002	0.55	0.04	0.000
9	2.374	0.126	0.86	0.23	0.002	0.43	0.11	0.001	0.21	0.03	0.000

Table 4.18: Detector plane mean doses for CT and endoDPT. endoDPT doses highlighted in green, yellow, or red indicated the dose at that point was significantly less than, was not different from, or was significantly higher than the CT dose measured at that point, respectively.

	Dose (cGy) at Detector Plane										
	CT Dose		endoDPT 100 mAs			endoDPT 50 mAs			endoDPT 25 mAs		
Point	$\bar{D}$	$\sigma_{\bar{D}}$	$\bar{D}$	$\sigma_{\bar{D}}$	*p*-value	$\bar{D}$	$\sigma_{\bar{D}}$	*p*-value	$\bar{D}$	$\sigma_{\bar{D}}$	*p*-value
1	2.841	0.219	0.05	0.10	0.001	0.03	0.05	0.000	0.01	0.00	0.000
2	3.020	0.141	0.12	0.16	0.000	0.06	0.08	0.000	0.03	0.02	0.000
3	2.480	0.108	0.01	0.17	0.000	0.01	0.08	0.000	0.00	0.02	0.000
4	2.761	0.176	3.47	0.14	0.007	1.74	0.07	0.001	0.87	0.02	0.000
5	2.980	0.096	4.22	0.12	0.001	2.11	0.06	0.001	1.05	0.02	0.000
6	2.556	0.172	0.78	0.11	0.000	0.39	0.05	0.000	0.19	0.01	0.000
7	2.746	0.144	0.52	0.16	0.000	0.26	0.08	0.000	0.13	0.02	0.000
8	2.811	0.069	0.74	0.12	0.000	0.37	0.06	0.000	0.19	0.02	0.000
9	2.220	0.082	0.52	0.14	0.000	0.26	0.07	0.000	0.13	0.02	0.000

4.9 Discussion

For all x-ray source energies, the physical $\mathrm{MTF}_{\mathrm{detector}}$ fell to 90%, 50%, and 10% at approximately $0.37\ \mathrm{mm}^{-1}$, $2.67\ \mathrm{mm}^{-1}$, and $11.50\ \mathrm{mm}^{-1}$, respectively. The physical

$\mathrm{MTF_{detector}}$ demonstrated a sharper falloff at low frequencies than at higher frequencies, which is typical for the MTF measured for high resolution indirect x-ray sensors using an opaque edge (Illers 2005) and is also consistent with the known resolution limits (10% $\mathrm{MTF_{detector}} \geq 10\ \mathrm{mm}^{-1}$) of intraoral x-ray sensors (Brennan 2002, Farman 2005a, Brullmann 2015). Several studies have assessed $\mathrm{MTF_{detector}}$ of intraoral x-ray sensors that have a scintillating layer using slit MTF methods (Welander 1994, Irsigler 1999, Farman 2005b) and edge MTF methods (Chen 1994, Kim 2004, Hong 2005). Overall, those results were similar to the $\mathrm{MTF_{detector}}$ measured for the XDR sensor. The most comparable result to endoDPT was the study by Kim *et al.* in which an x-ray sensor constructed using a scintillating layer and a CCD chipset with 22 μm pixels was used (Kim 2004). In that study, the measured $\mathrm{MTF_{detector}}$ fell to 90%, 50%, and 10% at $0.25\ \mathrm{mm}^{-1}$, $2.50\ \mathrm{mm}^{-1}$, and $10.00\ \mathrm{mm}^{-1}$, respectively (Kim 2004), which was very similar to the $\mathrm{MTF_{detector}}$ of endoDPT. Due to the proprietary nature of intraoral x-ray sensor technology and because the hardware of these sensors has been previously well characterized, there is little published literature regarding resolution measurements of newer sensors using MTF analysis. There is some literature regarding intraoral x-ray sensor resolution on various manufacturers websites, but these are limited to MTF plots or images of line-pair phantoms, with little explanation of the measurement process.

The physical $\mathrm{MTF_{detector}}$ did not extend to the same high frequency range as the computational $\mathrm{MTF_{detector}}$ (Chapter 3), because the computational $\mathrm{MTF_{detector}}$ assumed ideal x-ray imaging conditions: x-ray scatter was not modeled, a point source was used, the central ray of the x-ray beam was perpendicular to the edge, the edge was modeled in contact with the computational x-ray sensor (no gap due to the scintillating layer or detector casing), and blur and scatter from the imaging process was ignored. Direct detection x-ray detectors used in DBT, which do not use a scintillating layer, result in a $\mathrm{MTF}_{\mathrm{detector}}$ more similar to the endoDPT computational $\mathrm{MTF}_{\mathrm{detector}}$ (Ren 2005, Chen 2007a).

This study found no dependency of the physical $\mathrm{MTF}_{\mathrm{detector}}$ on x-ray source current for a given x-ray source potential. The ability to reduce x-ray source current without reducing resolution is a positive result because lower x-ray source currents will reduce patient dose in a linear relationship (Bushberg 2012). However, the endoDPT NPS measurement did show that reducing the x-ray source current increased noise in the reconstructed images. While NPS was measured here, the effect of noise on image quality (e.g., on contrast) was not directly assessed. The images used to analyze both the $\mathrm{MTF}_{\mathrm{detector}}$ and ASF were high-contrast measurements where there was no observed dependence on x-ray source current. It will be important in future work to quantitatively evaluate the effect of noise on image quality, such as through measurement of the contrast-to-noise ratio, to determine how noise modifies the ability of endoDPT to visually assess differences in various tissues in the prostate region (e.g., adipose, prostatic, and muscular). The visibility of these different tissues was qualitatively assessed in Chapter 5.

This study found that the physical $\mathrm{MTF}_{\mathrm{detector}}$ had a small but significant dependence the x-ray source potential. The mean frequency at which $\mathrm{MTF}_{\mathrm{detector}}$ was reduced to 90% was significantly higher at 70 kVp than other x-ray source energies. Information from the sensor manufacturer suggested this was due to the XDR sensor's designed operational energy of approximately 70 kV[ii]. The details of the XDR sensor construction (detection efficiency for a given photon energy, exact thickness and diameters of scintillating needles, and other properties) was not available. The mean frequency at which $\mathrm{MTF}_{\mathrm{detector}}$ was reduced to 50% was higher at 70 kVp than 60 kVp or 80 kVp, but lower than 90 kVp and 100 kVp. The mean frequency at which

---

[ii] Dr. Doug Yoon (XDR Radiology), personal communication, September 3, 2015

$\mathrm{MTF}_{\mathrm{detector}}$ was reduced to 10% level showed the $\mathrm{MTF}_{\mathrm{detector}}$ increasing as a function of energy. The slight increase in MTF at higher energies (maximum increase $\ll$ 1%) was most probably due to increased photon transmission through the edge device. Previous studies have shown that measurement of $\mathrm{MTF}_{\mathrm{detector}}$ with radiolucent edge device results in larger $\mathrm{MTF}_{\mathrm{detector}}$ values in the high frequency range compared to measuring the $\mathrm{MTF}_{\mathrm{detector}}$ with an opaque edge (Neitzel 2004, Illers 2005).

The calculation of $\mathrm{MTF}_{\mathrm{endoDPT}}$ from $\mathrm{MTF}_{\mathrm{detector}}$ and $\mathrm{MTF}_{\mathrm{recon}}$ demonstrated that significantly higher resolution is achievable with endoDPT in comparison to the resolution found using a typical CT protocol, noting that $\mathrm{MTF}_{\mathrm{CT}}$ measured in this study was consistent with the results of a similar study (Kayugawa 2013). The mean frequency at which $\mathrm{MTF}_{\mathrm{endoDPT}}$ was reduced to 90% was about 2.5 times and 2.6 times higher than the mean frequency at which $\mathrm{MTF}_{\mathrm{CT}}$ was reduced to 90% for SAA and BP, respectively. The mean frequency at which $\mathrm{MTF}_{\mathrm{endoDPT}}$ was reduced to 50% was about 4.3 times higher and 6.2 times higher than the mean frequency at which $\mathrm{MTF}_{\mathrm{CT}}$ was reduced to 50% for SAA and BP, respectively. The mean frequency at which $\mathrm{MTF}_{\mathrm{endoDPT}}$ was reduced to 10% was about 5.8 times higher and 13.3 times higher than the mean frequency at which $\mathrm{MTF}_{\mathrm{CT}}$ was reduced to 10% for SAA and BP, respectively. Due to the use of filtration in FBP, the frequency values at which $\mathrm{MTF}_{\mathrm{endoDPT}}$ was reduced to 90% and 50% could not be assessed, similar to experience from DBT (Chen 2007a). The mean frequency at which $\mathrm{MTF}_{\mathrm{endoDPT}}$ was reduced to 10% was about 14.3 times higher than the mean frequency at which $\mathrm{MTF}_{\mathrm{CT}}$ was reduced to 10% for FBP. This result was artificially increased because the FBP $\mathrm{MTF}_{\mathrm{recon}}$ was a relative measure normalized to the maximum value and not to MTF(0).

There were several limitations of the measurement of $\mathrm{MTF}_{\mathrm{endoDPT}}$ and subsequent comparison to $\mathrm{MTF}_{\mathrm{CT}}$. The first is that $\mathrm{MTF}_{\mathrm{endoDPT}}$ was assumed to consist of only two stages, $\mathrm{MTF}_{\mathrm{recon}}$ and

$\mathrm{MTF}_{\mathrm{detector}}$. Important parameters such as the effect of scatter (analogous to the water surrounding the wire in measurement of $\mathrm{MTF}_{\mathrm{CT}}$) and the effect of oblique incidence of photons on the XDR sensor were not considered. Other studies have shown that incorporating these additional stages reduces the MTF, but not to a large degree (Mainprize 2006, Zhao 2008, Acciavatti 2011, Chen 2013). Measurement of $\mathrm{MTF}_{\mathrm{endoDPT}}$ using a thin wire phantom (diameter $\ll$ endoDPT pixel size) suspended in water or an equivalent material would provide a fairer comparison to $\mathrm{MTF}_{\mathrm{CT}}$, but was beyond the scope of this study.

Measurements of the ASF, NPS, and dose of endoDPT utilized an x-ray source potential 80 kVp, although the 90% level of $\mathrm{MTF}_{\mathrm{detector}}$ demonstrated the highest mean frequency at 70 kVp. 80 kVp was chosen for these measurements to maintain commonality with typical radiographic procedures of soft tissue in the pelvic and abdominal region (Parry 1999, Bushberg 2012), to increase the penetrating power of the beam which reduced dose to the phantom surface, and to remain within the intraoral dental sensor manufacturers stated guidelines of using x-ray source energies between 60 kV and 80 kV[iii]. While the improved resolution at 70 kVp was significant, it was also small (the increase in the 70 kVp 90% MTF was a maximum of $0.005\ \mathrm{mm}^{-1} \rightarrow 0.008\ \mathrm{mm}^{-1}$ compared to other energies). This slight increase in resolution is not expected to have a significant impact in improving the discernibility of structures in the image.

The endoDPT NPS was measured using a different phantom material, different detector, and different x-ray source from similar studies in DBT, and so the endoDPT NPS was not directly comparable to other studies. However, the shape of the endoDPT NPS was consistent with these previous studies (Chen 2007a, Zhao 2008). The primary motivation for measurement of the endoDPT NPS was to assess differences in the endoDPT reconstruction algorithms, to verify that

---

[iii] Dr. Doug Yoon (XDR Radiology), personal communication, September 3, 2015

FBP improved the NEQ at high frequency values, and to provide baseline measurements for future studies. The endoDPT NPS measurements showed that for a given reconstruction algorithm, higher x-ray source currents reduced the magnitude of noise in the reconstructed images. Using NPS, $\mathrm{MTF}_{\mathrm{detector}}$, and $\mathrm{MTF}_{\mathrm{recon}}$, the NEQ for endoDPT was computed for SAA, BP, and FBP. The NEQ can be used to compare reconstruction algorithms. In endoDPT, BP outperformed SAA, most probably due to the incorporation of beam divergence. Similar to the results in DBT (Chen 2007a) and chest tomosynthesis (Godfrey 2009) FBP had a low NEQ at low frequencies (due to removal of low frequency information by filtration), but outperformed BP at higher frequencies, which was expected as FBP reduces the blurring artifact of the BP process.

The ASF provided a measure of how OOP structures affected a given reconstructed plane as a function of distance from the plane. Due to the nature of tomosynthesis, the contribution of these OOP structures can never be removed, but they can be reduced. In this work, filtering was used to reduce the contribution of OOP structures to a given reconstructed plane. The plots of ASF for endoDPT were shown for planes within ± 4 mm of the plane in which the BBs resided, which was in total 10 times larger than the diameter of each BB (0.79 mm). FBP demonstrated improved removal of the OOP structure compared to SAA and BP, which was expected due to filtering. This result was consistent with similar ASF measurements (Wu 2003). The ASF fell off slightly less for $+\hat{z}$ planes compared to $-\hat{z}$ planes for all reconstructions. This result was also seen in a similar study (Zhang 2006). The current study found no dependence on x-ray source current. For BBs 5 and 6, which were located at relatively large z, the ASF did not fall off as quickly for $+\hat{z}$ planes; this effect occurred because at large z fewer projections were used to reconstruct each voxel due to the limited FoV of the detector, which worsens the ASF. For BBs that were reconstructed from all projection images (BBs 1, 2, 3, and 4), there was no dependency on the ASF as a function of

BB z-location which was also reported in a similar study using thin aluminum discs (Nosratieh 2012).

The point at which the ASF falls to 50% can be used as a metric to estimate the resolution in the $\hat{z}$ direction (Wu 2003). For both SAA and BP, the ASF fell to 50% at approximately $(z - z_0) = -2.2$ mm and $(z - z_0) = +2.3$ mm (approximately ± 2.8 BB diameter). For FBP, the ASF fell to 50% at approximately $(z - z_0) = -1.3$ mm and $(z - z_0) = +1.4$ mm (approximately ± 1.7 BB diameter). This method is only an estimate of resolution in $\hat{z}$ because the ASF is dependent on both object size, shape, and density (Nosratieh 2012). Other studies using metal spheres or approximately spherical masses showed similar results for BP and FBP. Wu *et al.* reported 50% ASF for a 10 mm diameter mass in a breast phantom to be 19 mm (approximately ± 1.9 mass diameter) for BP and of 14 mm (approximately ± 1.4 mass diameter) for FBP (Wu 2003). Zhang *et al.* measured the 50% ASF for a 0.5 mm diameter speck of calcium carbonate in a breast phantom to be 1 mm (approximately ± 2 speck diameter) for BP (Zhang 2006). These results showed improved $\hat{z}$ resolution compared endoDPT. This was probably due to the masses being less dense than tungsten BBs. A study by Hu *et al.* measured the 50% ASF for a 0.4 mm diameter steel BB to be 1 mm (approximately ± 2.5 BB diameter) for FBP (Hu 2008), which is a worse $\hat{z}$ resolution than the result of the current work.

One primary source of error in the ASF analysis is x-ray source localization relative to the XDR sensor. Precise and accurate knowledge of the imaging geometry is required to accurately reconstruct the imaged volume (Mainprize 2011). The method used to determine x-ray source location relative to the XDR sensor utilized several assumptions that could impact the fidelity of geometry determination, such as assuming the FlashPad detector and the XDR sensor were both located in the $(\hat{x}, \hat{y})$ plane, and assuming y_S and z_S were constant for each scan. X-ray source locations were determined with uncertainties on the order of 2-7 mm. Uncertainties in source location using external fiducials in similar imaging methods have reported uncertainties of 0.3-3 mm (Jain 2005, Lee 2011, Kuo 2014), demonstrating the method used for source localization in the current work could be improved.

The dose was measured solely to assess the differences in dose between endoDPT and CT. The dose of endoDPT and CT was measured in a comparative manner using TLDs placed on and in a common phantom. For regions outside the endoDPT beam path, the dose of endoDPT was always less than CT. For regions inside the endoDPT beam path at the detector plane, the 100 mAs/image endoDPT scan was higher than CT at points 4 and 5 (all endoDPT beams intersected these points) but was lower at 50 mAs/image and 25 mAs/image. All other points in the detector plane had lower dose for endoDPT at all x-ray source currents. In contrast, the dose at the surface of the phantom for TLDs within the beam path was found to be high for endoDPT. The lowest x-ray source current setting of endoDPT resulted in doses greater than CT by a factor of about 1.5 for points 4 and 5. The highest x-ray source current setting of endoDPT resulted in doses greater than CT by a factor of about 6 for points 4 and 5.

Using the calibration curve generated from a LINAC, the dose due to CT ranged from minimum of 2.2 cGy within the phantom to a maximum of 4.2 cGy at the phantom surface. These dose values are likely larger than the actual values due to the energy dependence of TLD100; kV photons have about 1.1 times more luminescence for a given dose than MV (Attix 1986). The values are still reasonable, as reported doses from CT range from 0.6 cGy to 6 cGy, depending on the size of the phantom, the point of measurement within the phantom, and the parameters of the protocol (Parry 1999, Smith-Bindman 2009, Bushberg 2012). The doses in a given plane closest to the phantom edges in $\hat{y}$, which was along the axis of the CT scanner, were lower than the dosimeters near the center of the phantom because they had less scatter contribution (Bushberg 2012). The doses on the periphery of the phantom (in $\hat{x}$ and $\hat{z}$) were higher than the doses towards the phantom's center due to attenuation of the kV photons in the phantom material (Bushberg 2012).

The doses from endoDPT showed a much greater spatial variation than CT because some TLDs in the phantom were not in the beam path for any x_{s_i} and because all beams from endoDPT entered through the anterior of phantom. TLDs located outside of the beam path at the detector plane had measured doses as low as indistinguishable from background for the 25 mAs/image scan. TLDs located on the phantom surface that were in the beam path for many of the x-ray source locations had measured doses as high as 26.5 cGy for the 100 mAs/image scan. Regions deeper in the phantom received less dose due to attenuation of the kV x-ray beam, and regions further from the beam paths or in the path of fewer beams received proportionally lower doses. Like CT, the doses in endoDPT were likely higher than actual due to the energy dependence of TLD100 (Attix 1986). A 26.5 cGy appears very high compared to CT but is consistent with previously measured entrance skin doses (ESD) in abdominal and pelvic radiography. For AP radiography of the abdomen and pelvis using 70-85 kVp, 20-40 mAs, 100 cm SID, and a 23 cm thick patient (77 cm source to surface distance), ESDs range from 0.06 cGy to 0.5 cGy per image (Parry 1999, Hall 2006). Multiplying these values by 41 images (a typical endoDPT scan), 2.5 (100 mAs/image endoDPT divided by 40 mAs/image radiography), and $(100/85)^2/(100/77)^2 = 0.82$ (85 cm to endoDPT phantom surface compared to 77 cm to radiography patient surface), the endoDPT ESD would be expected to range from 5.0 cGy to 42.0 cGy. This assumes the x-ray source in endoDPT remains fixed at $x_S = 0$. Because the source moves along $\hat{x}$, both the source to surface distance is increasing and all surface TLDs move out of the beam for certain x_{s_i}.

Overall, the dosimetric results showed that for regions outside of the endoDPT beam, the dose to the phantom was less than CT. This was due to small field size of endoDPT and demonstrates that a lower total whole-body dose than CT may be achievable. At the detector plane, the dose from endoDPT was in most cases lower than CT (it was only higher than CT at two points that were in the path of all beams). This also demonstrates that endoDPT may be able to reduce dose at the level of the rectum, prostate, and bladder compared to a typical CT scan. However, because the endoDPT beams all enter through the anterior of the patient, the dose to the phantom surface was high compared to CT.

4.10 Conclusion

In this aim, the endoDPT system was physically developed using an intraoral dental x-ray sensor and a standard radiography unit. The $\mathrm{MTF}_{\mathrm{detector}}$, NPS, ASF, and dose of endoDPT were measured, providing a set of base measurements for future work. Additionally, The MTF and dose were measured for a common CT scanner using a typical scan protocol. The MTFs and doses of endoDPT and CT were compared, which tested the hypothesis of this research effort. $\mathrm{MTF}_{\mathrm{endoDPT}}$ demonstrated endoDPT is capable of high resolution imaging. This result was verified by comparing MTFs of endoDPT to CT, it was found that the frequencies at which $\mathrm{MTF}_{\mathrm{endoDPT}}$ was reduced to 90%, 50%, and 10% were significantly higher than the frequencies at which $\mathrm{MTF}_{\mathrm{CT}}$ was reduced to 90%, 50%, and 10%. This confirmed the resolution of endoDPT was significantly higher than CT. endoDPT also demonstrated a reduction in dose compared to CT in regions outside the endoDPT FoV. For low x-ray source currents, the dose within the endoDPT FoV was in general lower than or comparable to CT, but in several instances, was up to 50% higher. For higher x-ray source currents, the dose of endoDPT in the FoV, and especially at the surface of the phantom, was significantly higher than CT (up to 600% higher). A reduction in this dose, or the modification of scanning parameters to reduce dose, may be required for clinical implementation of endoDPT.

In summary, this aim demonstrated endoDPT provides high resolution and that the dose of endoDPT is in most cases less than CT in a common phantom. This places endoDPT in a favorable position for future research and design efforts.

Chapter 5. Aim 3: Image Clinically Relevant Prostatic Structures in Phantoms

5.1 Overview

The purpose of this aim was to demonstrate the high-resolution imaging capability of endoDPT. Two small nuts were imaged with endoDPT to show the ability to visualize fine detail. Then, imaging studies were performed of three approximations of clinical scenarios encountered in PCa management: post-implant imaging of LDRBT seed implants, imaging of the PPAT layer, and contrast enhanced imaging of PCa vasculature. *Ex vivo* canine prostate specimens were used to represent these three clinical scenarios. These phantoms were additionally scanned using a typical CT scanner and a typical MRI scanner. Visual aspects of image quality relevant to each scenario were assessed and compared.

5.2 Imaging Systems

The endoDPT and CT imaging systems were described previously (Section 4.2 and Section 4.3). A GE Discovery 750W 3T MRI scanner (General Electric Company, Waukesha, WI) was used in this study (Fig. 5.1). This MRI scanner has a 3-tesla field strength and a 75 cm bore diameter. A 32-channel head coil was used for all acquisitions. This MRI scanner located at Pennington Biomedical Research Center. The acquisition protocols for each approximation of clinical scenarios is discussed in Section 5.5.3.

Figure 5.1: GE Discovery 750W 3T MRI scanner. Image from www.gehealthcare.com.

5.3 Canine Prostate Specimens

Nine canine prostate specimens with diameters of 2.5 cm to 3.5 cm were used in this study. Canine prostates are excellent biological surrogates for human prostates (Starkey 2005) and a typical canine prostate specimen shown in Fig. 5.2. The canine prostate specimens used in this study were fixed in formalin and were donated by the Louisiana State University Biology Department. The Biology Department previously used these prostates in a comparative anatomy course and followed all required compliances regarding use of animal specimens[iv]. No additional approval, such as from an institutional review board or the Institutional Animal Care and Use Committee (IACUC), was required for this work.

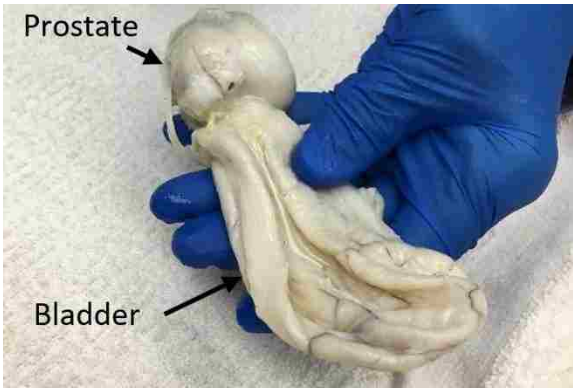

Figure 5.2: Example of canine prostate specimen with attached bladder.

5.4 Phantom Preparation

5.4.1 Nut Phantoms

A pecan (3.5 cm long, 2 cm diameter) and a pistachio (1.5 cm diameter) were imaged in the sample holder plate with no surrounding carrageenan gel (4.76 mm acrylic separated the nut phantoms from the XDR sensor). The set up for both phantoms is shown in Fig. 5.3. These nuts were chosen in part for their small size; they fit in the FoV which reduced the truncation artifact

---

[iv] Dr. Dominique Homberger and Bradley Wood (LSU Biology Dept.), personal communication, December 16, 2015

seen when imaging objects larger than the detector FoV. The pecan and pistachio had well-differentiated internal structure and external borders (shells) that when imaged could highlight the high resolution of endoDPT. Similar examples using tomosynthesis to image fruit have been previously reported (Levakhina 2013).

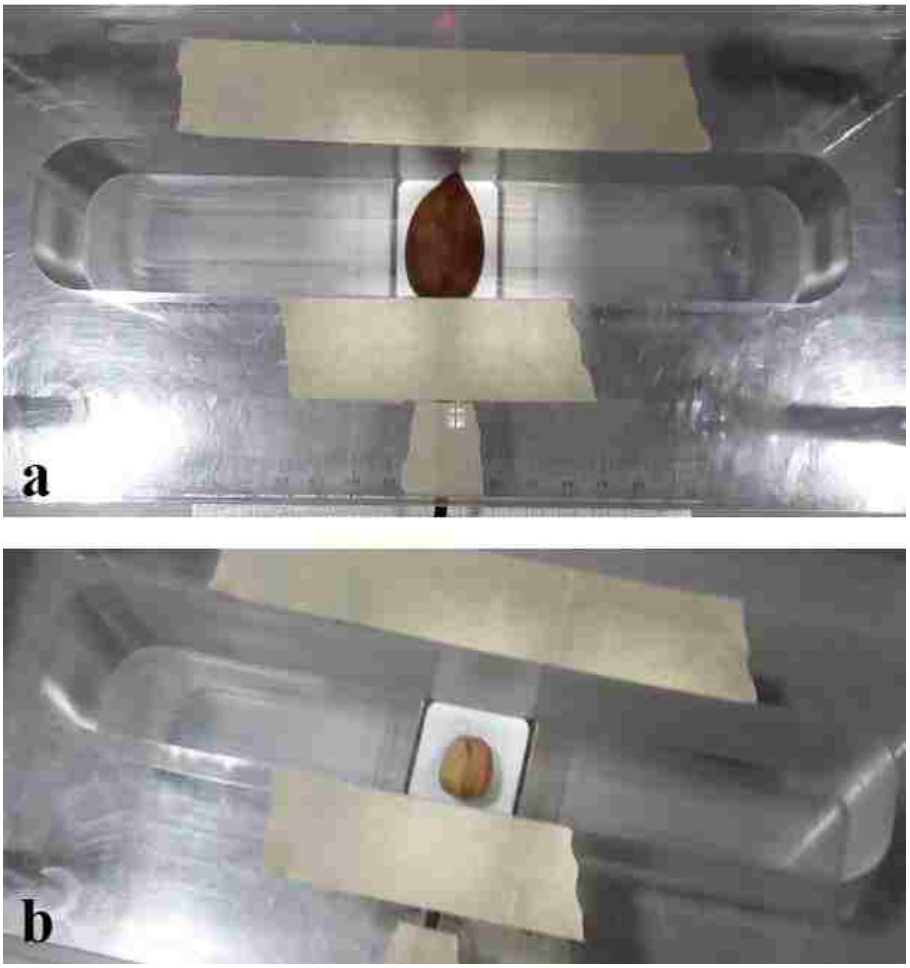

Figure 5.3: (a) Pecan in place in the sample holder plate. (b) Pistachio in place in the sample holder plate.

5.4.2 LDRBT Seed Phantoms

Three prostate specimens were implanted with 27, 30, and 33 BRACHYSOURCE® STM-1251 ^{125}I LDRBT seeds (Bard Medical, Inc., Covington, Georgia), respectively, using hollow needles. The number of implanted seeds was similar to previous studies about imaging of seeds using an endorectal gamma camera (30 seeds) (Alnaghy 2017), CT (17 to 47 seeds) (Siebert 2006, Siebert 2007), and tomosynthesis (45 seeds) (Brunet-Benkhoucha 2009). The seed construction was a titanium shell (0.05 mm thick, 4.5 mm length, 0.8 mm outer diameter) covering a radiopaque silver core (3 mm active length, 0.5 mm diameter) (Khan 2014). More than 10 half-lives of ^{125}I had elapsed since seed manufacture, so the seeds were no longer radioactive and safe to handle.

The seeds were implanted in the canine prostate specimens using a procedure similar to previously described methodologies (Yu 1999, Ellis 2002). Two to five seeds were each loaded into 10 hollow implant needles either end-to-end (0.5 cm spacing between seed center points) or with a plastic spacer (0.5 cm length) between seed ends (1.0 cm spacing between seed center points). The placement of seeds end-to-end or with spacers was random. A predrilled template was used to guide the 10 loaded needles into the prostate, with the needles oriented to be parallel to the urethra. Uniform seed loading of the prostate was utilized with a needle-to-needle spacing of 0.5 cm to 1.0 cm. The needles were removed from the prostate, leaving the seeds and spacers. The seed locations were not planned to achieve a specific dose distribution. The seeds were in some cases closer together than the 1 cm seed spacing typically used for LDRBT PCa treatment (Yu 1999, Zaorsky 2016). After the seeds were implanted in the prostate, each prostate was placed at the bottom of the cavity in the sample holder plate directly above the center of the XDR sensor. The remainder of the cavity in the sample holder plate was filled with carrageenan gel to surround the prostate. Each prostate was made into a separate phantom.

5.4.3 PPAT Phantoms

Because the canine prostates used in the study did not have an attached PPAT layer, thinly sliced porcine fat, which is similar in composition to human fat (Sumitomo 2010), was wrapped around two canine prostates and was cut into small sections and arranged near small sections of a third canine prostate. To create the PPAT layer, a 5 mm thick layer of porcine fat and a 2.5 mm thick layer of porcine fat were sliced from a pork leg that had been obtained at a local grocer. One canine prostate was wrapped completely in the 5 mm thick fat layer and one canine prostate was wrapped completely in the 2.5 mm thick fat layer. To ensure the fat layer remained securely wrapped around the prostate, the open ends of the fat wrappings were closed with surgical sutures. After the fat wrapping, each prostate was placed at the bottom of the cavity in the sample holder plate directly above the center of the XDR sensor. The remainder of the cavity in the sample holder plate was filled with carrageenan gel to surround the prostates. Each prostate was made into a separate phantom.

The third canine prostate was sectioned into small cubes of approximately 5 mm by 5 mm by 5mm and into 1 mm to 2.5 mm thick slabs with lengths ranging from 1 cm to 2 cm. Porcine fat was sectioned into cubes and slabs of similar dimensions. Cubes and slabs of both materials were interspersed in a stack on the sample holder plate directly above the center of the XDR sensor. Carrageenan gel was poured around these cubes and slabs to suspend the prostate and fat tissues.

5.4.4 Tissue Vascularity

Because the prostates used in the study were harvested from decedent canines, perfusion imaging and angiographic imaging using vasculature within the prostate were not possible (dead tissue does not perfuse and the vasculature collapses quickly after death). To simulate angiographic imaging, high-purity silicone rubber tubing with inner/outer diameters (ID/OD) of 0.012”/0.025” (0.30 mm/0.64 mm), 0.02”/0.037” (0.51 mm/0.94 mm), and 0.025”/0.047” (0.64 mm/1.19 mm) were embedded in canine prostates and filled with contrast agents. OMNIPAQUE™ (General Electric Company, Waukesha, Wisconsin), an iodine contrast agent, was diluted with distilled water and used as the contrast agent for endoDPT and CT imaging. $\mathrm{GdCl_3 \cdot 6H_2O}$ (Section 4.4.2), containing gadolinium, a common MRI contrast agent (Prince 1994, Maki 1998), was diluted with distilled water and used as the contrast agent for MRI.

Previous studies have demonstrated that after an injection of iodine contrast agents, contrast-enhanced blood in vessel lumens have CT numbers on the order of 300 Hounsfield units (HU) (Cademartiri 2005). During magnetic resonance angiography (MRA), gadolinium contrast agent results in the blood in vessel lumens have a T1W signal intensity approximately two to three times greater than normal blood (Prince 1994, Maki 1998).

To determine the concentration of iodine in distilled water required to produce a CT number = 300 HU, OMNIPAQUE™ (350 mg I/mL in 755 mg Iohexol/mL) was diluted with distilled water to create five iodine concentrations. The amounts of OMNIPAQUE™ and distilled water mixed to create 120 mL solutions, and the resulting concentrations iodine are listed in Table 5.1. Three 25 mL plastic vials were filled with each of these solutions and imaged with a CT scanner with acquisition parameters of 120 kVp, automatic x-ray source current, 0.938 pitch, and 1.25 mm slice thickness. A representative CT slice through the vials is shown in Fig. 5.4. Circular ROIs (radius of 10 voxels) were drawn in the center of each vial. The mean value of the ROI over five slices (15 total measurements for each concentration) determined the CT number and uncertainty for each concentration (Table 5.1). From this data, the nominal concentration of 10 mg I/mL (vials in column 3) was selected for the simulated angiographic imaging (see below).

Table 5.1: Concentrations of iodine solutions and measured CT number (HU column).

Vial Row	**Planned Concentration (mg I/mL)**	**OMNIPAQUE™ (g)**	**Water (g)**	**Actual Concentration (mg I/mL)**	**HU**	$\sigma_{\mathbf{HU}}$
1	0	0.000	120.000	0	-12.6	4.0
2	5	3.003	118.306	4.991	159.1	2.0
3	10	6.060	116.935	10.043	307.7	2.8
4	15	9.002	114.878	15.000	457.5	6.7
5	20	12.063	113.164	20.044	615.9	9.6

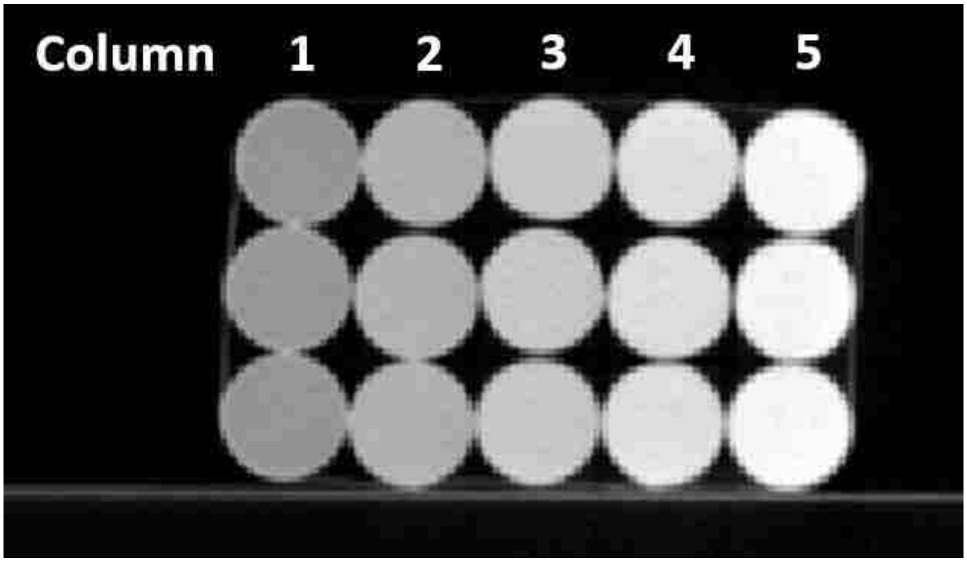

Figure 5.4: CT slice of vials filled with planned concentrations of 0 mg I/mL, 5 mg I/mL, 10 mg I/mL, 15 mg I/mL, and 20 mg I/mL in rows 1 to 5, respectively. Each column comprised three vials of the same concentration. Column three (10 mg I/mL) produced the desired target CT numbers.

A similar procedure was used to determine the concentration of gadolinium in distilled water to produce a T1W signal intensity 2-3 times greater than distilled water. Solutions of $GdCl_3$ in distilled water were created for nominal gadolinium concentrations of 0 mg Gd/mL, 0.15 mg Gd/mL, 0.30 mg Gd/mL, 0.76 mg Gd/mL, 1.5 mg Gd/mL, 2.9 mg Gd/mL, and 6.9 mg Gd/mL. These concentrations were comparable to diluting a 10-mL bottle of OMNISCAN™ (General Electric Company, Waukesha, Wisconsin), a common MRI contrast agent containing 287 mg Gd/mL, with water to 5 L, 2.5 L, 1.0 L, 0.5 L, 0.25 L, and 0.1 L volumes, respectively; however, OMNISCAN™ could not be readily obtained for this study. $GdCl_3$ is not often used clinically because it is not chelated, which can result in high degrees of normal tissue toxicity (Aime 2009, Natalin 2010), but can be used safely in phantoms. $GdCl_3$ has been previously used for magnetic resonance (MR) imaging of human blood samples (Rogosnitzky 2016) and in small animal imaging (Aime 2009).

Table 5.2 lists the masses of distilled water and $GdCl_3 \cdot 6H_2O$ mixed to produce 50 mL of each nominal concentration. The $GdCl_3$ solutions were thoroughly stirred and then 25 mL glass vials were filled with each concentration. A T1W spin echo scan was collected with TR = 650 ms, TE = 9.48 ms, and 2 mm slice thickness. A T1W slice through the vials is shown in Fig. 5.5. Circular ROIs (radius of 10 voxels) were drawn in the center of each vial. An additional ROI was drawn in the air above the vials. The mean value of the ROI over five slices is reported as the T1W signal intensity for each concentration in Table 5.2. From this data, the nominal concentration of 0.30 mg Gd/mL (vial 3) was selected for the simulated angiographic imaging (see below).

Table 5.2: Concentrations of gadolinium solutions and measured T1W signal intensities at 3T.

Vial	**Planned Concentration (mg Gd/mL)**	**$GdCl_3 \cdot 6H_2O$ (mg) used**	**Additional Water (g)**	**Actual Concentration (mg Gd/mL)**	**T1W Signal Intensity (S.I.)**	**$\sigma_{S.I.}$**
1	0	0.000	50.003	0.000	555	62
2	0.15	18.102	50.012	0.153	1120	113
3	0.30	35.752	49.985	0.303	1495	148
4	0.76	89.422	49.975	0.757	1402	116
5	1.5	176.956	49.921	1.498	1286	117
6	2.9	346.705	49.911	2.933	324	71
7	6.9	818.862	49.752	6.930	203	19
Air	0	0	0	0	167	18

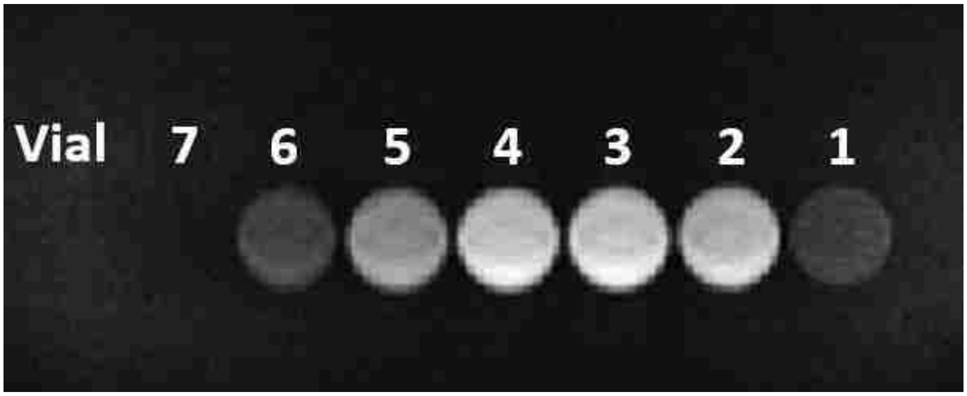

Figure 5.5: T1W slice of vials containing nominal concentrations of 0 mg Gd/mL, 0.15 mg Gd/mL, 0.30 mg Gd/mL, 0.76 mg Gd/mL, 1.5 mg Gd/mL, 2.9 mg Gd/mL, and 6.9 mg Gd/mL (from right to left). Vial 7 was not visible (the signal was indistinguishable from air at this concentration).

Three canine prostates were each sliced into quarters along the coronal and sagittal planes through the prostate center point. One prostate had a piece of 0.64 mm OD silicone rubber tubing placed in each of the sagittal and coronal planes in arbitrary curved paths. The tubing was lightly sutured to the prostate, and the prostate quarters were re-assembled and sutured together. The prostate was placed at the bottom of the cavity in the sample holder plate directly above the center of the XDR sensor, such that both ends of each piece of tubing emerged from the top of the cavity. The remainder of the cavity in the sample holder plate was filled with carrageenan gel to surround the prostate, taking care that the free ends of the tubing did not become submerged. This procedure was repeated for two other prostates using the 0.94 mm OD and the 1.19 mm OD silicone rubber tubing, respectively.

Prior to imaging with endoDPT and CT, the tubing was filled with the iodine contrast agent that produced a CT number of 300 HU (10 mg I/mL) and was tied off. After the scans using x-rays, the ends of the tubing were opened, flushed thoroughly with distilled water, and refilled with the gadolinium contrast agent that resulted in the best enhancement in T1W images (0.30 mg Gd/mL).

5.5 Phantom Imaging

5.5.1 endoDPT

endoDPT scans of all the samples described in Section 5.4 were acquired in the normal manner as described in Chapter 4 with 41 images, with $x_{S_i} = \pm 40$ cm in 2 cm increments, $y_S = 0$ cm, and $z_S = 100$ cm, with the central ray of the x-ray source always directed to $(x_D, y_D, z_D) = (0,0,0)$. Settings of 80 kVp and 0.6 mm focal spot were used. A tube current of 8.0 mAs/image was used for the nut phantoms. The prostate phantoms were imaged at 100 mAs/image.

For all phantoms, image planes above and parallel to the XDR sensor were reconstructed in 1 mm increments from $z = 0.5$ cm to $z = 4.5$ cm using SAA, BP, and FBP (see Section 3.5). A 1 mm separation of image planes was chosen because that is a common plane separation distance in DBT (Sechopoulos 2013b). For display purposes, each image in Section 5.6 is linearly scaled independently such that the minimum value in the image is set to black and the maximum value in each image is set to white. Areas corresponding to insensitive regions of the XDR sensor (e.g., the triangular black voids) were not considered during the display scaling

5.5.2 CT

CT scans of the canine prostate phantoms were acquired using helical scanning at 120 kVp, 1.25 mm slice thickness, 0.938 pitch, small (25 cm) reconstruction FoV for 512 by 512 matrix and 0.488 mm voxel size, and automatic x-ray source current. For all CT images shown in the following sections, the images were independently scaled so that within the prostate/carrageenan gel in the CT image the minimum voxel intensity was black and the maximum voxel intensity was white. The phantom was oriented in the CT scanner such that the $\hat{y}$ axis of the phantom (in endoDPT geometry) was oriented along the axis of the scanner. The same scan protocol was used for all samples to maintain consistency with the measurements made in Chapter 4.

5.5.3 MRI

T1W and T2W MRI scans of the canine prostates were acquired using a 32-channel head coil. The gel slabs containing the prostate samples representing a given clinical scenario (LDRBT seeds, PPAT, or vasculature) were removed from the acrylic sample holder plate and all were imaged together during a single MRI scan. The prostate and gel slabs were oriented in the MR scanner such that the $\hat{x}$ axis of the phantom (in endoDPT geometry) was oriented along the axis of the scanner; this orientation was chosen so that the slabs fit in the head coil. Coronal and sagittal image slices were acquired; The coronal image slices (2 mm slice thickness) were the same view as the endoDPT reconstructed images while the sagittal image slices (4 mm slice thickness) were in the same orientation as the CT axial image slices. All MRI image slices were acquired using a 512 by

512 matrix over a 25 cm FoV (0.488 mm reconstructed voxel size) and used 4 image acquisitions. All MRI images had their grayscale values adjusted the same as the CT images. For the T1W scans, TE (echo time) was specified as ‘min full.’ TE = ‘min full’ calculates the minimum TE value required for full echo acquisition and was recommended for use in this study[v]. Each of the three distinct features in this aim (LDRBT seeds, PPAT, and vasculature) were otherwise imaged using parameters chosen to match similar studies and are summarized in Table 5.3. For vasculature imaging, the TR (repetition time) and TE reproduce parameters for anatomic imaging; the T1W imaging parameters for magnetic resonance angiography were not used because magnetic resonance angiography requires the use of very short TR/TE (≈3 ms/≈1 ms) for dynamic scans (Rosenkrantz 2013, Wu 2016).

Table 5.3: MRI parameters used for imaging the three clinical scenarios of PCa imaging discussed in this dissertation. The parameters were matched to similar studies (footnotes).

Clinical scenario	**T1W**		**T2W**	
	TR (ms)	**TE (ms)**	**TR (ms)**	**TE (ms)**
LDRBT[vi]	247	9.48	2700	100
PPAT[vii]	836	9.48	3400	100
Vasculature[viii]	650	9.48	4500	93

5.6 Results

5.6.1 Nut Phantoms

Fig. 5.6, Fig. 5.7, and Fig. 5.8 show representative tomosynthesis image planes through the pecan at $z = 1.0$ cm and $z = 1.5$ cm, reconstructed with SAA, BP, and FBP, respectively. In all cases, the structures in the pecan are most visible when they are perpendicular to the tomosynthesis image (e.g., when the shell is orientated perpendicular to tomosynthesis image at $z = 1.5$ cm it is

---

[v] Kevin McKlveen, (Pennington Biomedical Research Center), private communication, January 15, 2018

[vi] (De Brabandere 2012)

[vii] (Woo 2015)

[viii] (Hara 2005, Kitajima 2010, Rosenkrantz 2013, Wu 2016)

much sharper compared to when the shell is more angled relative to the tomosynthesis image at $z = 1.0$ cm). Both the SAA and BP tomosynthesis images demonstrate the expected blur artifact which is compensated in the FBP tomosynthesis image. The pecan appears to be slightly wider in the SAA image compared to BP and FBP; due to the parallel beam assumption of SAA the reconstructed plane is slightly magnified. Otherwise, the SAA and the BP images are qualitatively similar. The FBP tomosynthesis images are much sharper due to the reconstruction filter, but are also noisier. The FBP images display the expected overshoot artifact at the air/shell boundary in the direction of scan motion (red arrows). The FBP images display an artifact from the triangular voids in each projection image corner; these voids were excluded from the backprojection process. This artifact could be reduced or eliminated by changing how these regions are handled in the reconstruction process for object sizes that are comparable to the detector FoV.

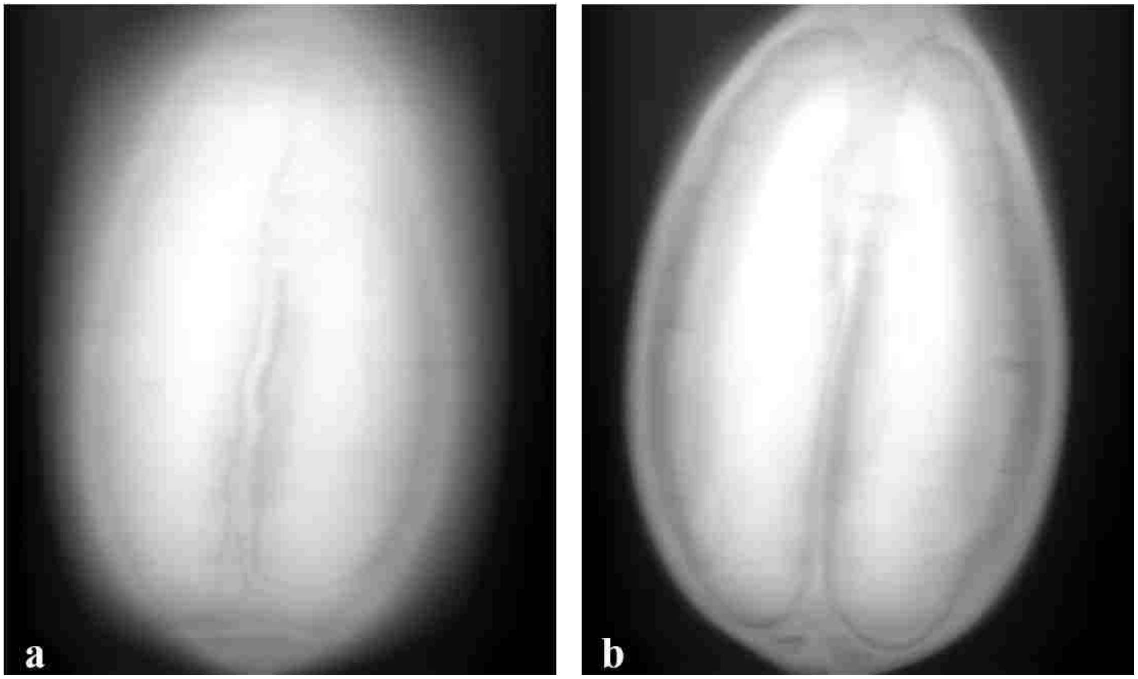

Figure 5.6: SAA pecan tomosynthesis image at $z = 1.0$ cm above the detector face (a) and at $z = 1.5$ cm above detector face (b) with 19 µm voxel size (1368 by 1700 voxels).

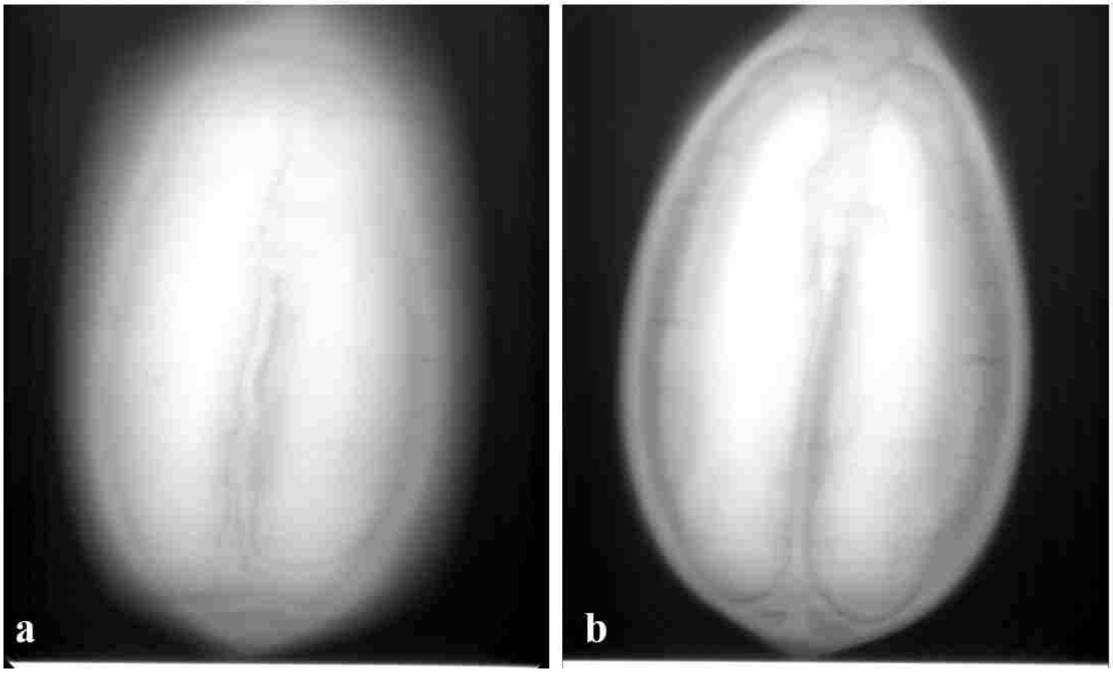

Figure 5.7: BP pecan tomosynthesis image at $z = 1.0$ cm above detector face (a) and at $z = 1.5$ cm above detector face (b) with 20 µm voxel size (1400 by 1700 voxels).

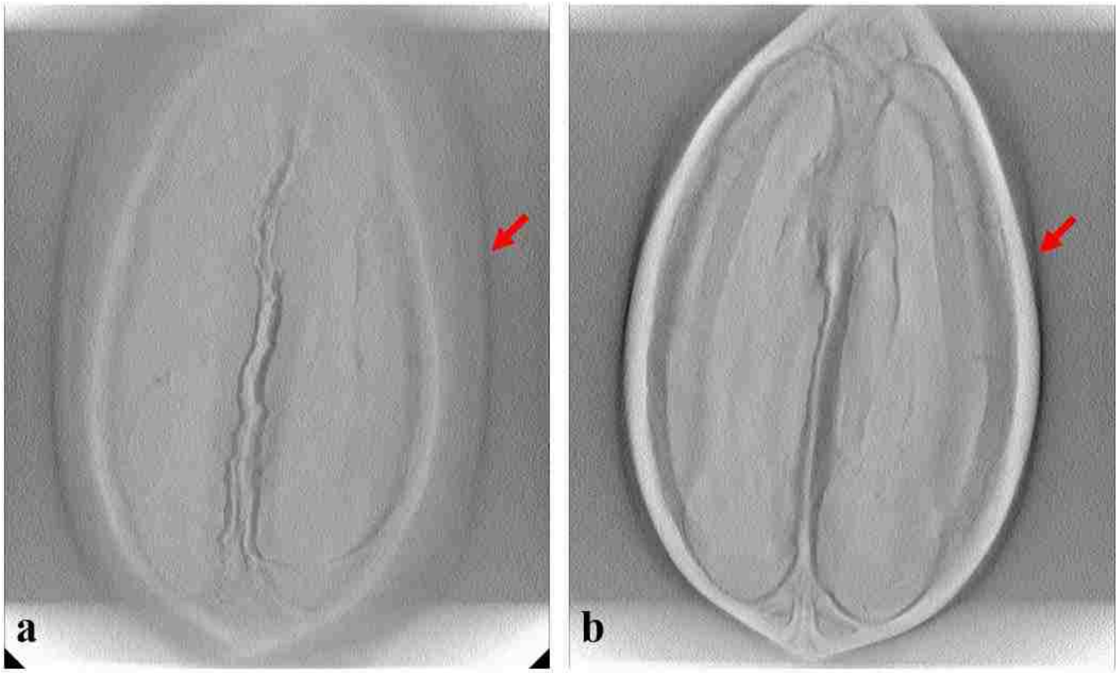

Figure 5.8: FBP pecan tomosynthesis image at $z = 1.0$ cm above detector face (a) and at $z = 1.5$ cm above detector face (b) with 20 µm voxel size (1400 by 1700 voxels). The red arrows point to the overshoot artifact. A reconstruction artifact caused by caused by the triangular voids in the projection images resulted in brighter bands at the top and bottom of the images.

Fig. 5.9, Fig. 5.10, and Fig. 5.11 show tomosynthesis images through the pistachio at $z = 1.1$ cm, 1.2 cm, and 1.3 cm, reconstructed with SAA, BP, and FBP, respectively. These images display the same qualitative features as the pecan for each reconstruction algorithm, except that the artifact from the triangular voids in each projection image is avoided in the FBP reconstruction because the object is smaller.

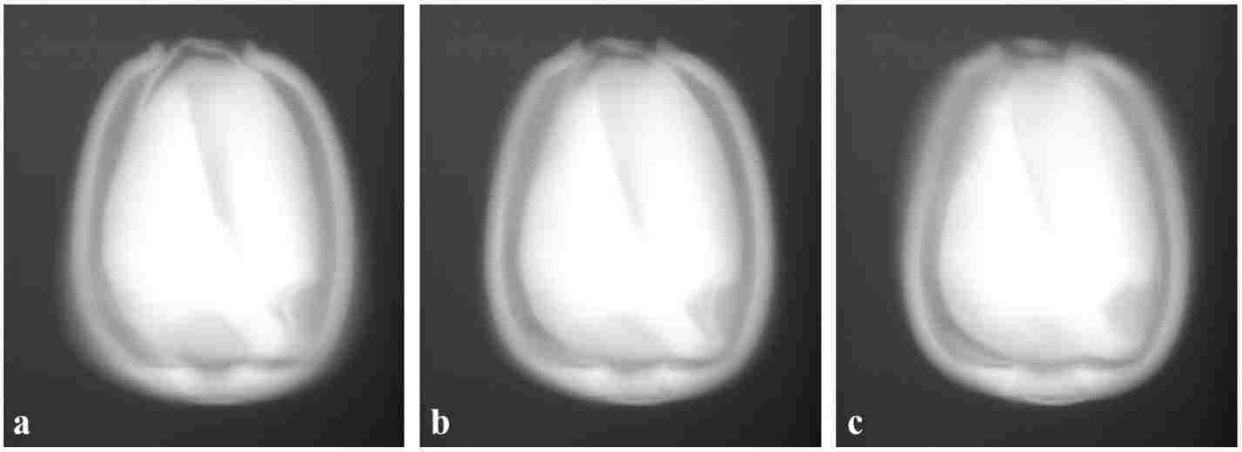

Figure 5.9: SAA pistachio tomosynthesis images at $z = 1.1$ cm (a), 1.2 cm (b), and 1.3 cm (c) above detector face. Images have voxel size of 19 µm (1000 by 1100 voxels).

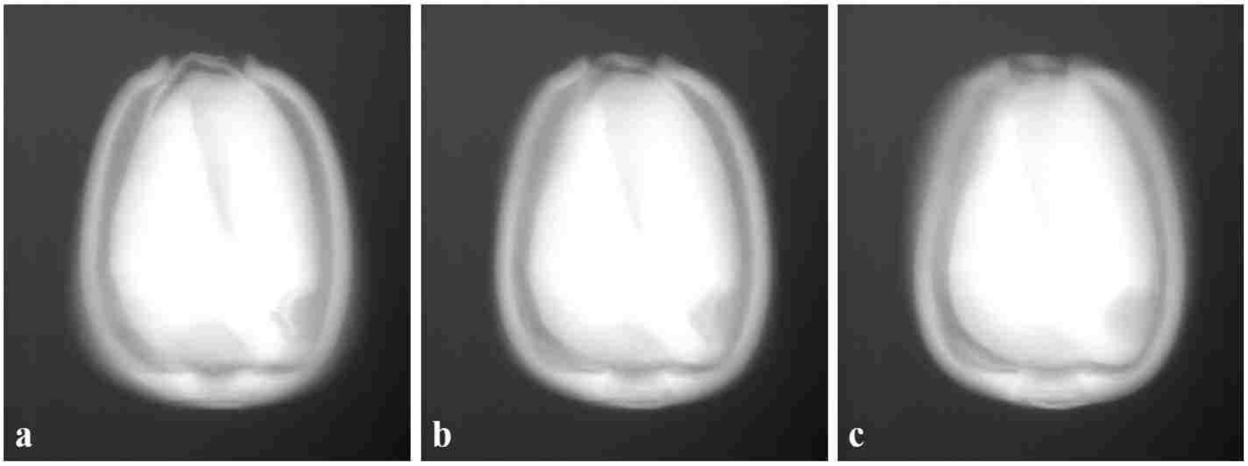

Figure 5.10: BP pistachio tomosynthesis images at $z = 1.1$ cm (a), 1.2 cm (b), and 1.3 cm (c) above detector face. Images have voxel size of 20 µm (1000 by 1100 voxels).

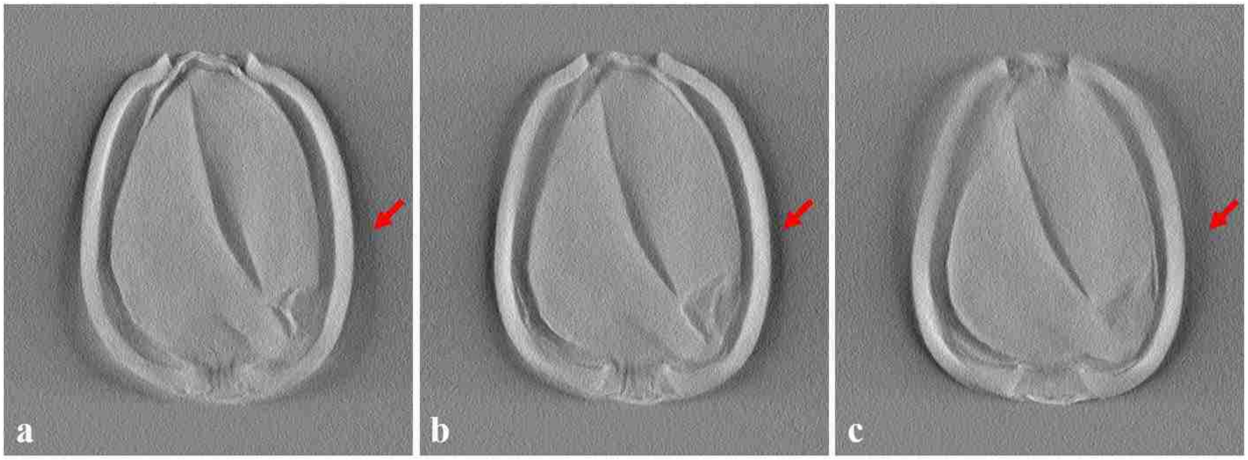

Figure 5.11: FBP pistachio tomosynthesis images at z =1.1 cm (a), 1.2 cm (b), and 1.3 cm (c) above detector face (left to right). Images have voxel size of 20 µm (1000 by 1100 voxels). The red arrows point to the overshoot artifact.

5.6.2 LDRBT Seed Phantoms

Because the SAA and BP images were qualitatively similar, only the BP and FBP endoDPT images are shown for the LDRBT seed phantoms. Fig. 5.12 and Fig. 5.13 show the tomosynthesis image plane through the prostate implanted with 30 LDRBT seeds at $z = 2.3$ cm, reconstructed with BP and FBP, respectively. This tomosynthesis image is representative of all the prostates implanted with LDRBT seeds. An air pocket is visible in the center of both the BP and FBP images.

The BP tomosynthesis image demonstrates the expected blur artifact, in addition to a truncation artifact visible on the image edge in the direction of scan motion. FBP reduces the blur artifact but results in more noise. The expected overshoot artifact enhances the seed edges. The truncation artifact is less visible in FBP due to the increased noise. Due to the high contrast between seeds and prostate tissue, the artifact due to the triangular voids is not as pronounced as in the images of the pecan. Unlike the nut phantoms, the seeds are small and thus reconstruct sharply at each height above the XDR sensor; Fig. 5.14 for FBP tomosynthesis images reconstructed at $z = 1.1$ cm, 1.4 cm, and 1.7 cm.

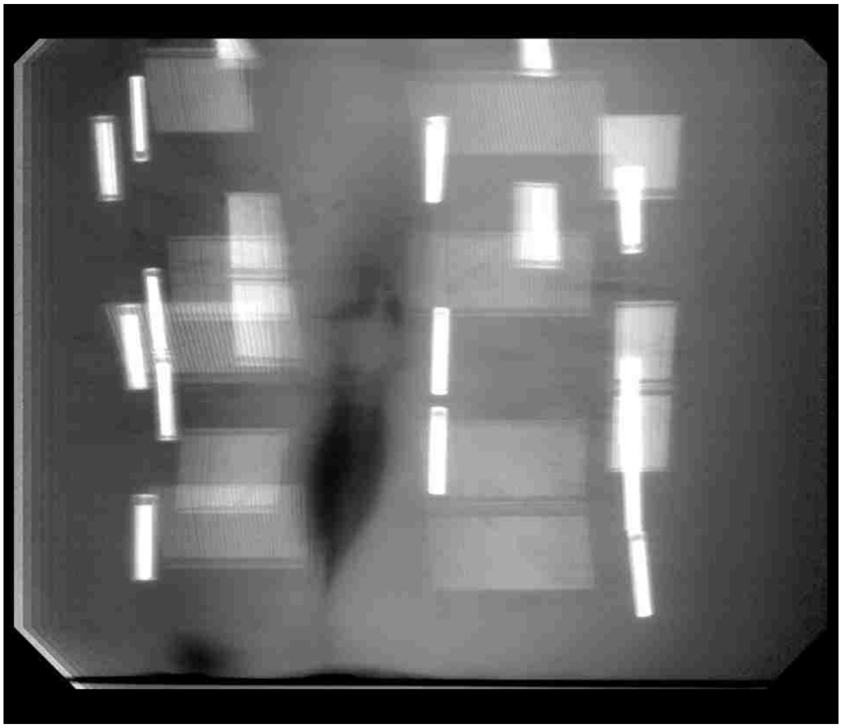

Figure 5.12: BP tomosynthesis image at $z = 2.3$ cm above detector face of the prostate implanted with 30 LDRBT seeds. Images have voxel size of 20 µm (2200 by 1896 voxels).

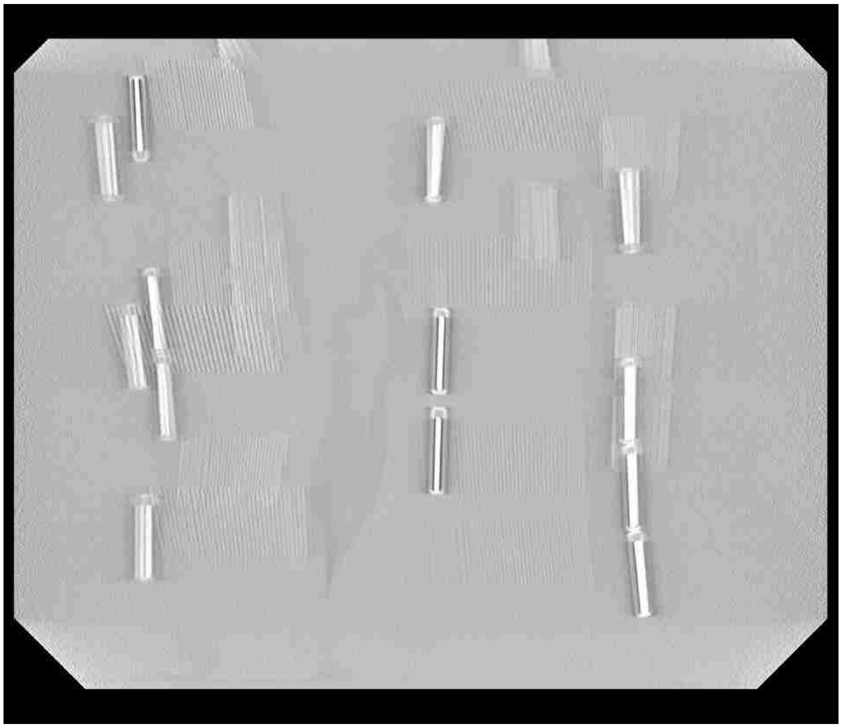

Figure 5.13: FBP tomosynthesis image plane at $z = 2.3$ cm above detector face of the prostate implanted with 30 LDRBT seeds. Images have voxel size of 20 µm (2200 by 1896 voxels).

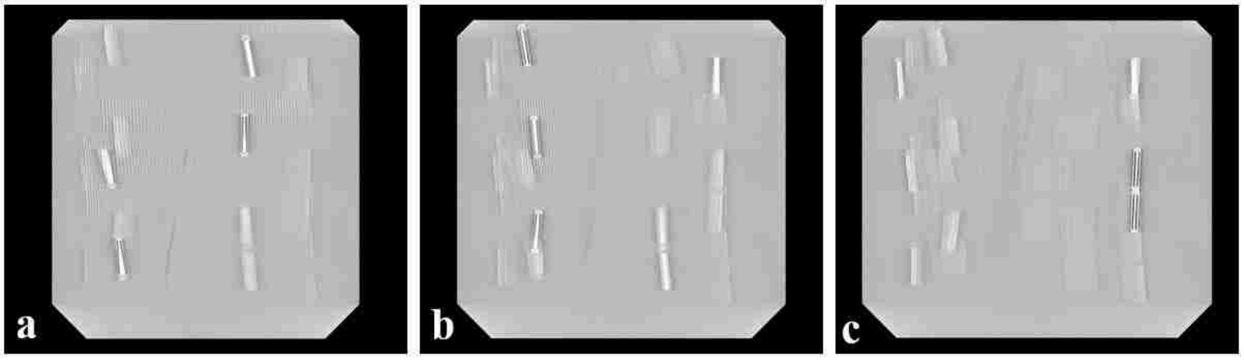

Figure 5.14: FBP tomosynthesis image at $z = 1.1$ cm (a), 1.4 cm (b), and 1.7 cm (c) above the above detector face of the prostate implanted with 30 LDRBT seeds. Images have voxel size of 20 µm (2200 by 1896 voxels).

Fig. 5.15 shows a representative axial CT axial image slice (in the $(\hat{x}, \hat{z})$ image plane of endoDPT geometry) through the prostate implanted with 30 LDRBT seeds. The seeds are easily identifiable and show slight streaking artifacts expected from high spatial density objects. The air pocket seen in the endoDPT images is visible in the center of the prostate region. Because the seeds are high density and because the carrageenan gel is of similar density to the prostate, the prostate border is not visible at the window and level setting of Fig. 5.15. If the window and level are adjusted to allow for visualization of the prostate border, the streaking artifacts are more pronounced.

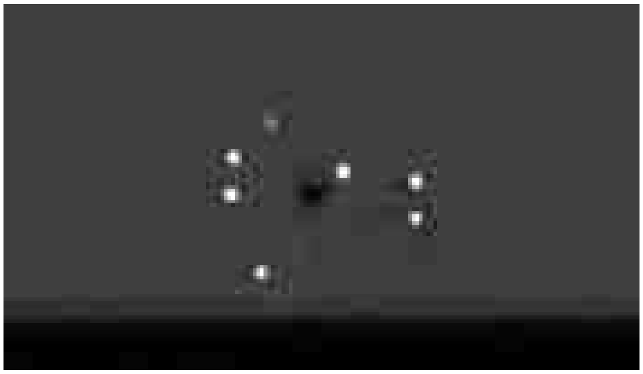

Figure 5.15: CT axial image slices of the prostate implanted with 30 LDRBT seeds.

Fig. 5.16 shows T1W and T2W axial image slices (in the $(\hat{x}, \hat{z})$ plane of endoDPT geometry) for the same prostate specimen. The location of this slice is at the same approximate location as the axial CT slice shown in Fig. 5.15. Fig. 5.17 shows T1W and T2W coronal image slices (in the $(\hat{x}, \hat{y})$ plane of endoDPT geometry) through the prostate implanted with 30 LDRBT seeds. The location of this slice is at the same approximate location ($z = 2.3$ cm) as the endoDPT planes shown in the Fig. 5.12 and Fig. 5.13. The MR images more clearly show prostate anatomy compared to CT and endoDPT, but there is obvious magnetic susceptibility artifact (voids and regions of high signal) around the seeds. These artifacts severely impact the ability to differentiate individual seeds.

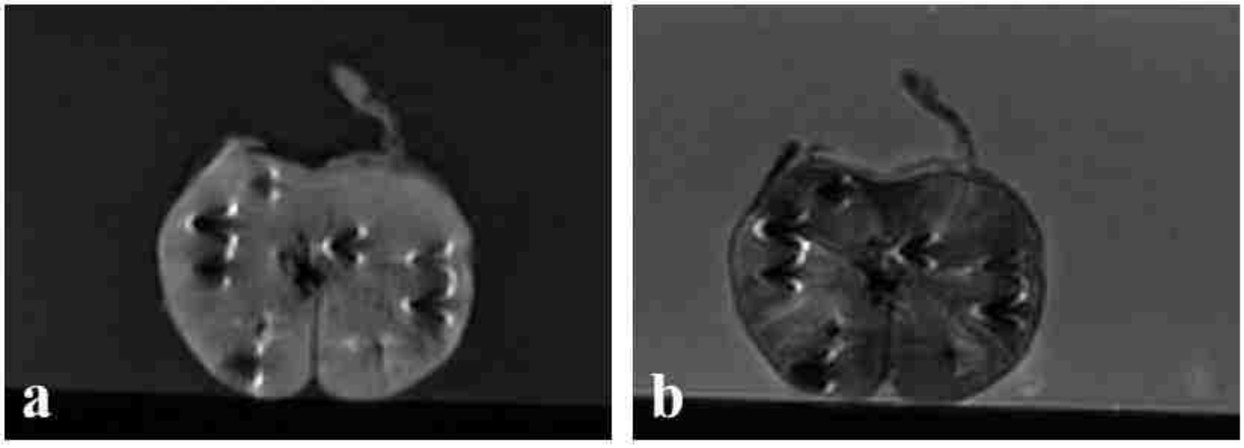

Figure 5.16: T1W (a) and T2W (b) axial image slices of the prostate implanted with 30 LDRBT seeds.

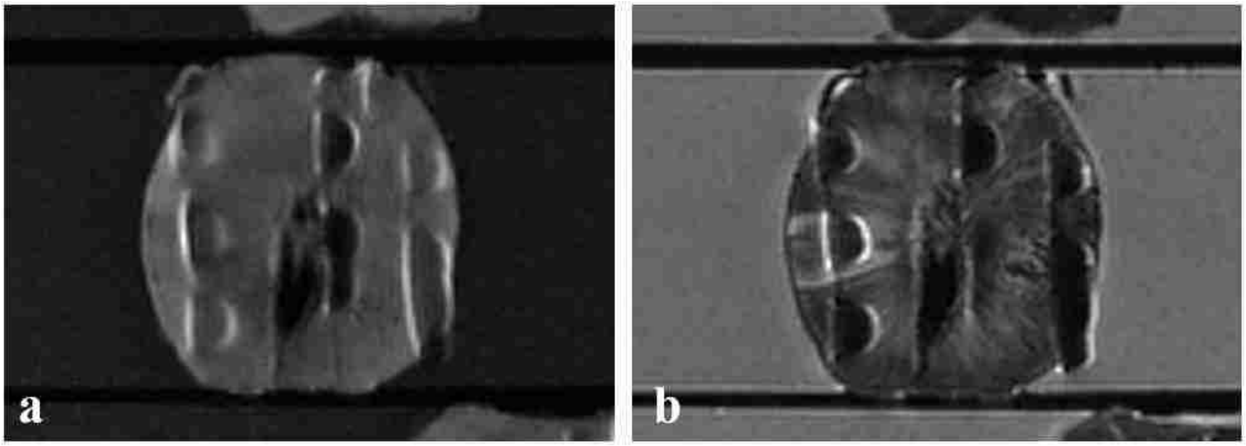

Figure 5.17: T1W (a) and T2W (b) coronal image slices of the prostate implanted with 30 LDRBT seeds.

In addition to the qualitative images shown above for the prostate specimen implanted with 30 LDRBT seeds, the number of LDRBT seeds in each of the three prostates implanted with LDRBT seeds were counted using the FBP endoDPT image set, the CT image set, and the T1W image sets. The FBP endoDPT image set was used for counting because it provided the best differentiation between nearby seeds. The T1W images sets were used because the reference used for MRI LDRBT seed imaging (De Brabandere 2013) used T1W images for seed identification. To count the number of LDRBT seeds, a marker was manually placed at the approximate center of each differentiable seed. The results of the LDRBT seed counting for each imaging modality are given in Table 5.4.

Table 5.4: LDRBT seed counts using endoDPT, CT, and MRI image sets. Cor. represents the coronal image set and Ax. represents the axial image set.

	Number of seeds counted		
Modality	**Prostate 1 (27 seeds)**	**Prostate 2 (30 seeds)**	**Prostate 3 (33 seeds)**
endoDPT (FBP)	27	30	33
CT	24	27	31
MRI (T1, Cor.)	23	22	27
MRI (T1, Ax.)	23	25	30

All LDRBT seeds were identifiable using endoDPT. In CT, the seed count was lower by two to three seeds in all cases. This was because some of the seeds were implanted end-to-end, and it was impossible to tell if one or two seeds were occupying a series of adjacent slices due to 1.25 mm slice thickness. More seeds were identified in the T1W axial view compared to the T1W coronal view. Overall, the seed count was lower by between three and eight seeds for MRI for all prostates.

5.6.3 PPAT Phantoms

Because the SAA and BP images were qualitatively similar, only the BP and FBP endoDPT images are shown for the PPAT prostate phantoms. Fig. 5.18 and Fig. 5.19 show tomosynthesis image planes through the prostate surrounded by the 5 mm thick PPAT layer at $z = 1.5$ cm and $z = 2.0$ cm reconstructed with BP and FBP, respectively. Fig. 5.20 and Fig. 5.21 show the tomosynthesis image plane through the prostate surrounded by the 2.5 mm thick PPAT at the heights of $z = 2.0$ cm and $z = 3.0$ cm, reconstructed with the BP and FBP, respectively. Fig. 5.22 and Fig. 5.23 show the tomosynthesis image plane through the sections of prostate tissue and porcine fat at the heights of $z = 1.2$ cm and $z = 3.3$ cm, reconstructed with BP and FBP, respectively.

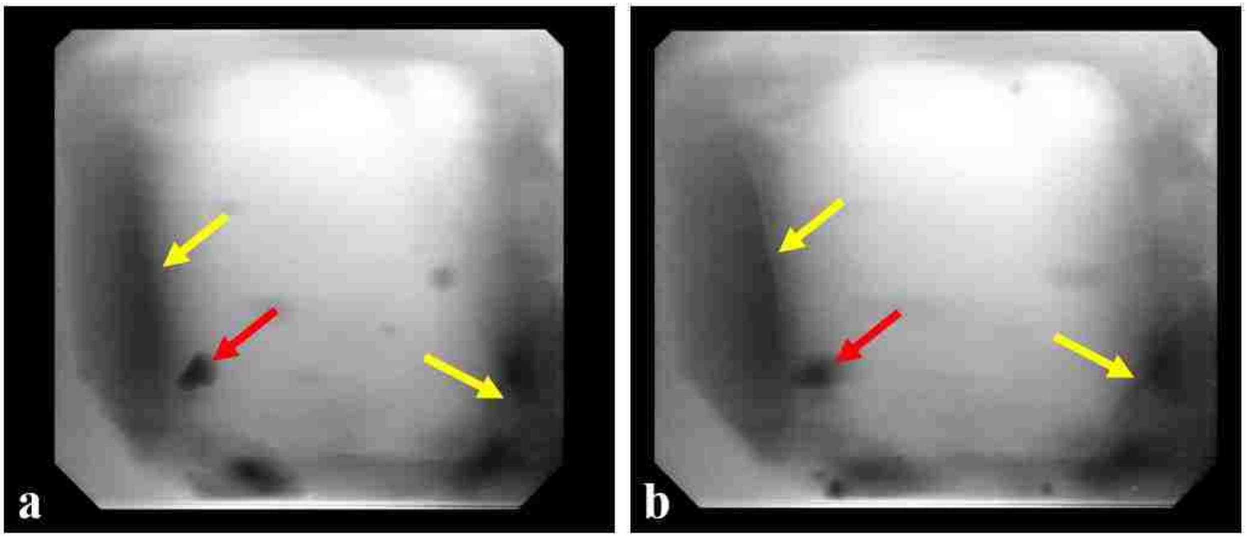

Figure 5.18: BP tomosynthesis image at $z = 1.5$ cm (a) and $z = 2.0$ cm (b) above detector face of the prostate surrounded by a thick layer of porcine fat. The red arrow points to an air pocket and the yellow arrow points to the prostate-PPAT border. Images have voxel size of 20 µm (2200 by 1896 voxels).

In the phantoms with the thick PPAT layer and thin PPAT layer, portions of the PPAT/prostate border can be identified in both tomosynthesis images (yellow arrows) and small air pockets can also be identified (red arrows). The PPAT border is much more distinct when both the PPAT layer and prostate border are perpendicular to the tomosynthesis image. BP results in images with qualitatively improved contrast differentiation at the PPAT/prostate border. However, despite lower contrast, the PPAT/prostate border is still mostly identifiable with FBP as an edge. In the image reconstructed at $z = 3.0$ cm (thin PPAT layer), the truncation artifact is visible throughout the BP reconstruction, and is visible in the FBP reconstruction in the artifact caused by the triangular voids in the corners of the projection images.

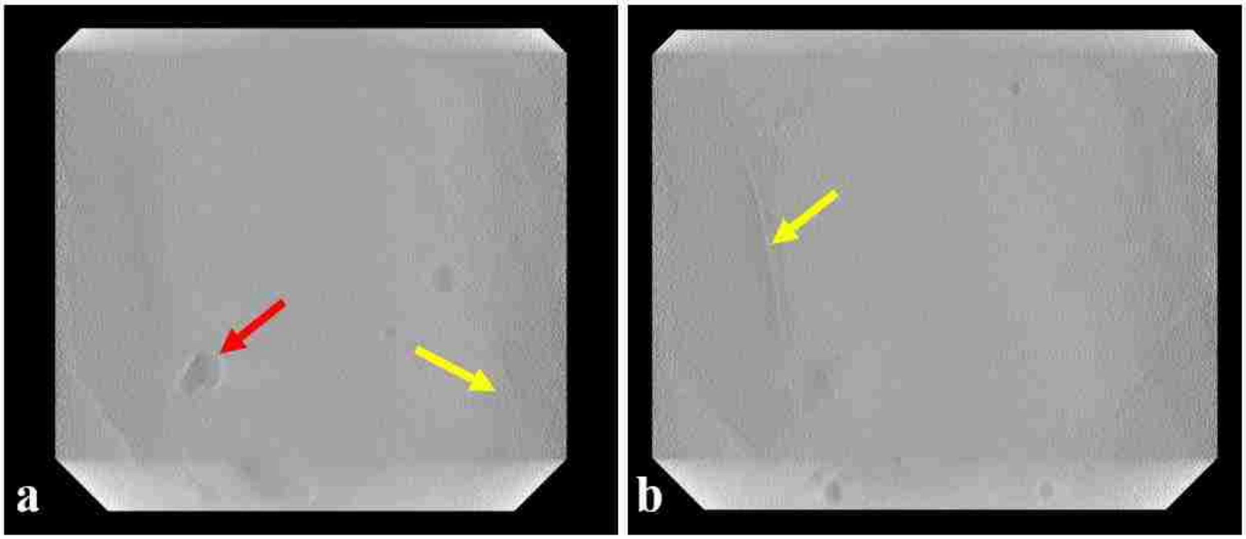

Figure 5.19: FBP tomosynthesis image at $z = 1.5$ cm (a) and 2.0 cm (b) above detector face of the prostate surrounded by a thick layer of porcine fat. The red arrow points to an air pocket and the yellow arrow points to the prostate-PPAT border. Images have voxel size of 20 µm (2200 by 1896 voxels).

In the phantom with the embedded sections of fat and prostate tissues, the tomosynthesis image at $z = 1.2$ cm contains two cubes of fat (visibly distinct from gel) and two cubes of prostate tissue (not visibly distinct from gel). The tomosynthesis image at $z = 3.3$ cm contains one large, triangularly-shaped slab of fat. The borders of the fat are visible (yellow arrows), but the prostate tissue and carrageenan gel cannot be differentiated. At $z = 3.3$ cm, the OOP blur artifact is apparent in the BP reconstructed image and so is the truncation artifact. In FBP, the contrast is reduced and the noise is increased, but blur and the contribution from OOP structures is reduced; the small air pockets show up much more clearly. The triangular void artifact is also visible. In addition, there is a small, unknown, high-density structure located at $z \approx 3.0$ cm that shows up as a series of repeated structures in the $z = 1.2$ cm planes and as a bright spot in the $z = 3.3$ cm planes (white arrow). At the bottom of the image, a dark line is also visible, which is an air gap between the carrageenan gel and the acrylic sample holder.

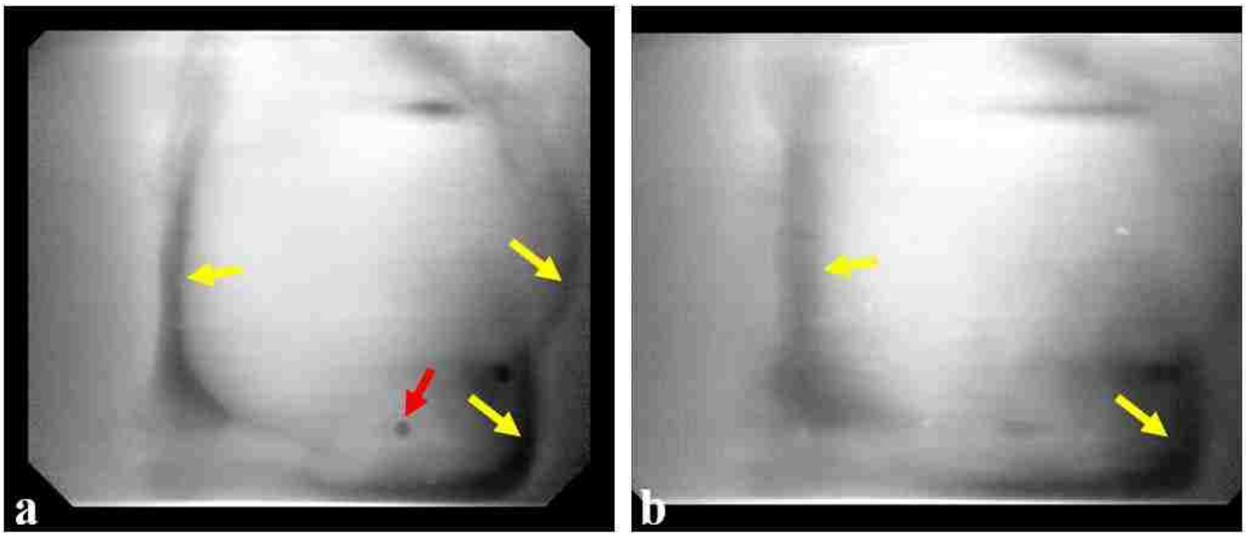

Figure 5.20: BP tomosynthesis image at $z = 2.0$ cm (a) and $z = 3.0$ cm (b) above detector face of the prostate surrounded by a thin layer of porcine fat. The red arrow points to an air pocket and the yellow arrows point to the prostate-PPAT border. Images have voxel size of 20 µm (2200 by 1896 voxels).

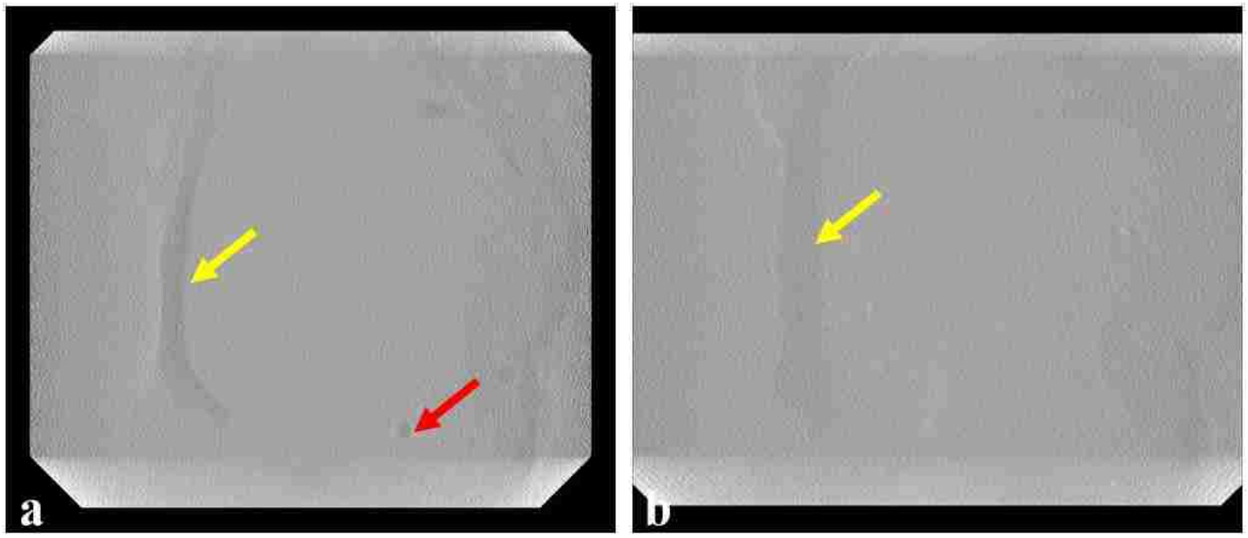

Figure 5.21: FBP tomosynthesis image plane at $z = 2.0$ cm (a) and $z = 3.0$ cm (b) above detector face of the prostate surrounded by a thin layer of porcine fat. The red arrow points to an air pocket and the yellow arrows point to the prostate-PPAT border. Images have voxel size of 20 µm (2200 by 1896 voxels).

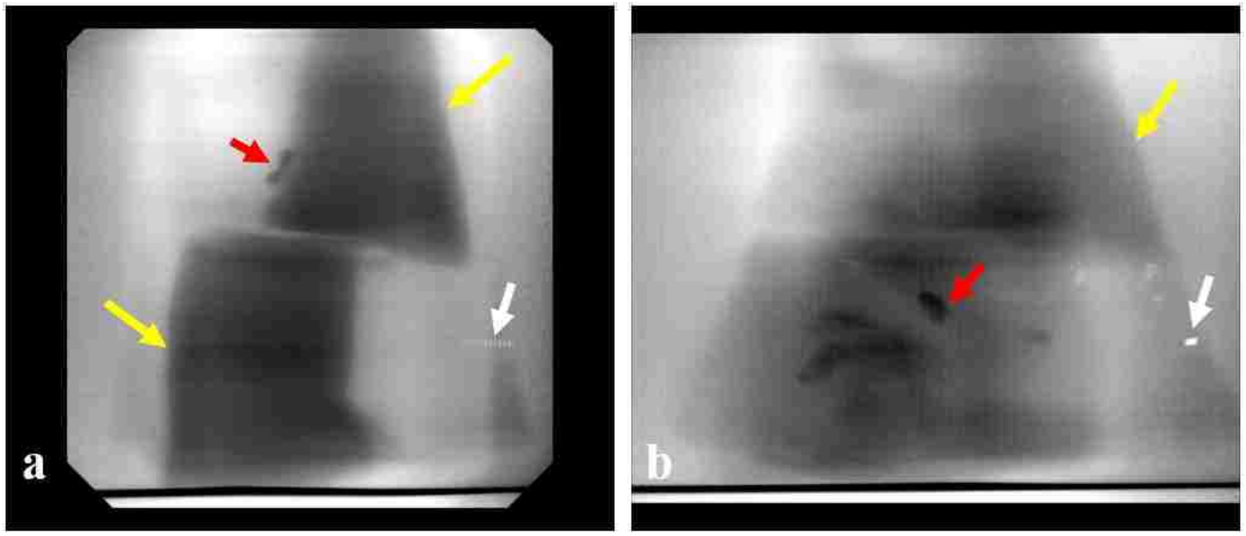

Figure 5.22: BP tomosynthesis image at $z = 1.2$ cm (a) and $z = 3.3$ cm (b) above detector face through the sections of prostate tissue and fat. The red arrows point to air, the yellow arrows point to the fat and prostate or gel border, and the white arrows point towards an unknown high-density structure. Images have 20 µm voxel size (2200 by 1896 voxels).

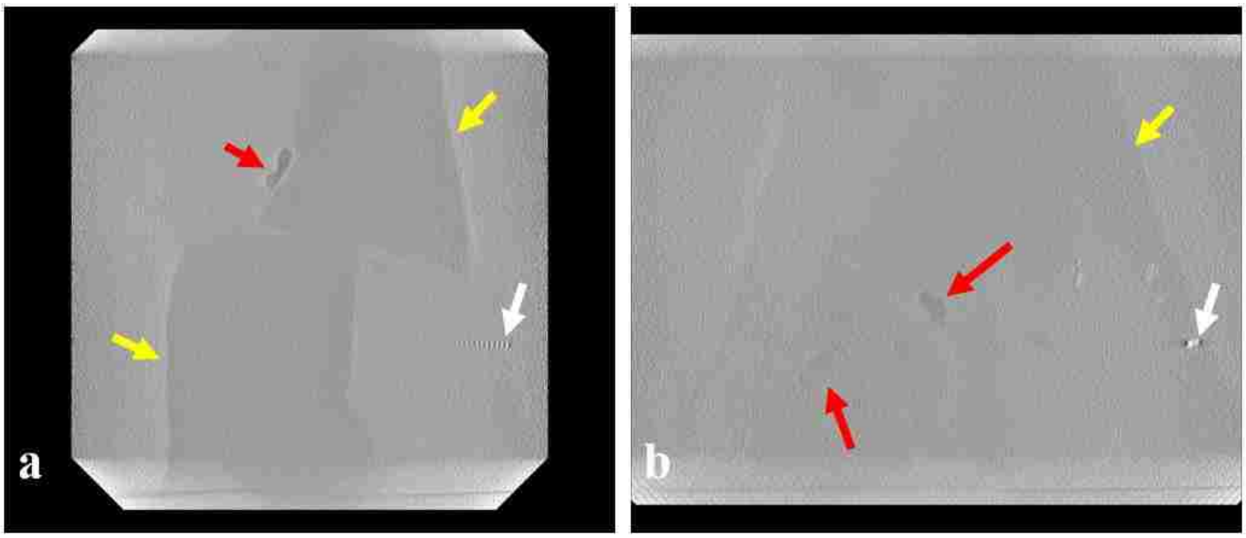

Figure 5.23: FBP tomosynthesis image plane at $z = 1.2$ cm (a) and $z = 3.3$ cm (b) above detector face through the sections of prostate tissue and fat. The red arrows point to air, the yellow arrows point to the fat and prostate or gel border, and the white arrows point towards an unknown high-density structure. Images have 20 µm voxel size (2200 by 1896 voxels).

Fig. 5.24 and Fig. 5.25 show representative axial CT axial image slices (in the $(\hat{x}, \hat{z})$ image plane of endoDPT geometry) for the specimens surrounded by the 5 mm thick and 2.5 mm PPAT layers. Fig. 5.26 shows the phantom made of slabs and cubes of prostate tissue and fat. Because fat is lower density than both the prostate tissue and the carrageenan gel, it is easily differentiable. Due to the similar density of the prostate tissue and carrageenan gel, these two materials cannot be easily differentiated. The image of the prostate/fat sections shows the cubes of fat and prostate tissue (although the prostate tissue is barely visible) near the bottom of the sample holder cavity, and the slabs of fat above the cubes.

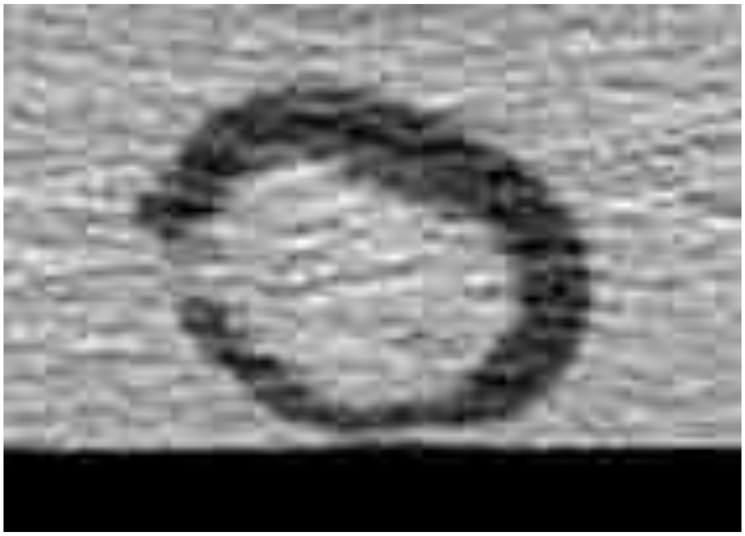

Figure 5.24: CT axial image slices of the prostate surrounded by the 5 mm thick fat layer.

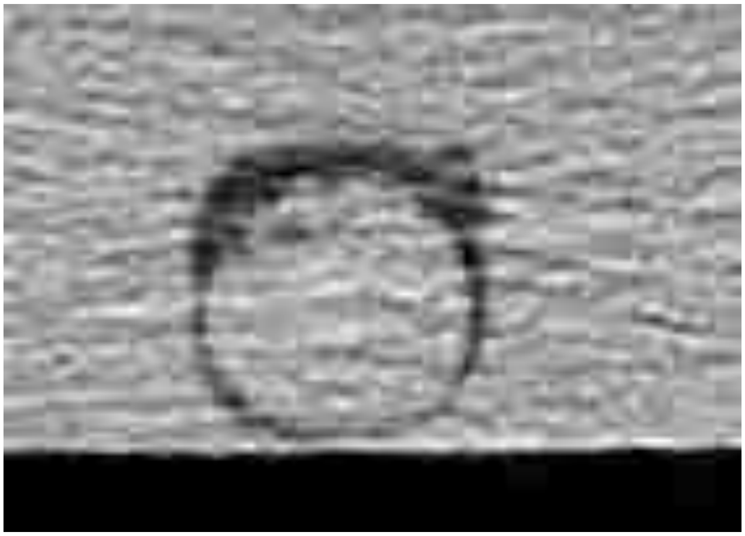

Figure 5.25: CT axial image slices of the prostate surrounded by the 2.5 mm thick fat layer.

Figure 5.26: CT axial image slices of the sections of prostate tissue and fat.

Fig. 5.27 and Fig. 5.28 show T1W and T2W axial image slices (in the $(\hat{x}, \hat{z})$ plane of endoDPT geometry) for the specimens surrounded by the 5 mm thick and 2.5 mm PPAT layers. Fig. 5.29 shows the phantom made of slabs and cubes of prostate tissue and fat. The locations of the slices are in the same approximate locations as the CT images shown in Fig. 5.26, Fig. 5.27, and Fig. 5.28, respectively. These axial MR images show that T2W images show the differences between fat tissue, prostatic tissue, and the carrageenan gel more clearly than the T1W images, which was expected from the TR/TE chosen for this study (Woo 2015). Because of this, only the coronal T2W images are shown in Fig. 5.30, Fig. 5.31, and Fig. 5.32.

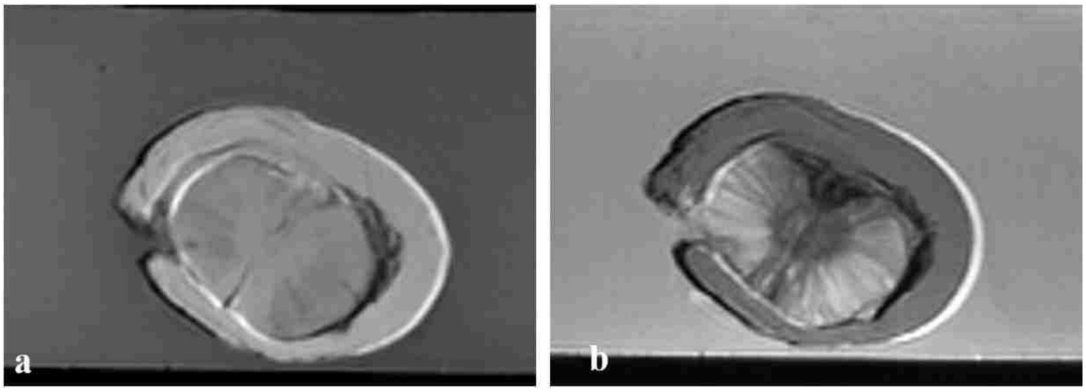

Figure 5.27: T1W (a) and T2W (b) axial slices of prostate wrapped in 5 mm thick fat layer.

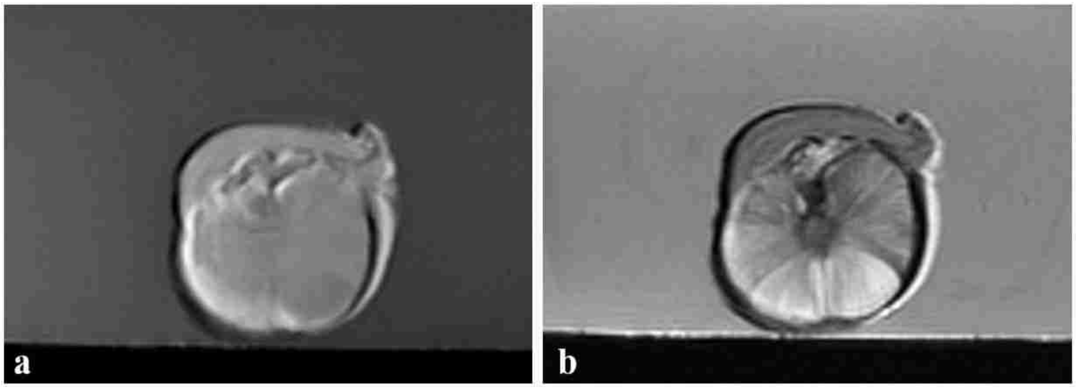

Figure 5.28: T1W (a) and T2W (b) axial slices of prostate wrapped in 2.5 mm thick fat layer.

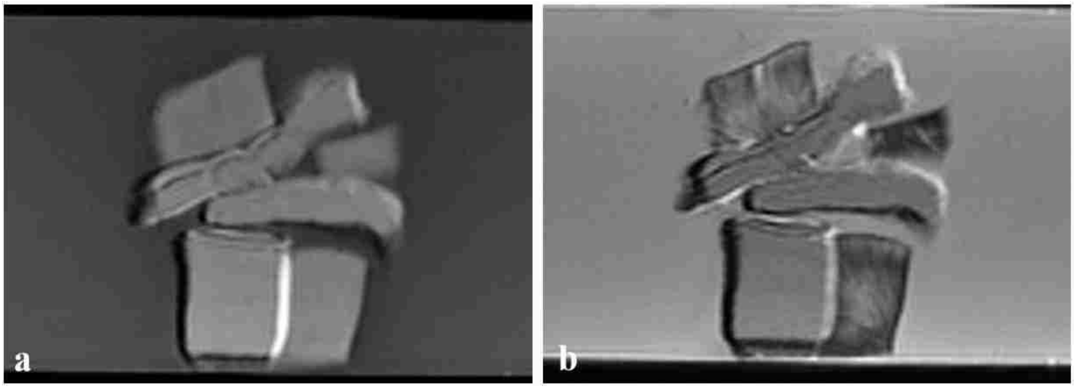

Figure 5.29: T1W (a) and T2W (b) axial image slices through the sections of prostate tissue and fat tissue.

Fig. 5.30 shows the T2W image slices (in the $(\hat{y}, \hat{z})$ plane of endoDPT geometry) through the prostate surrounded by the 5 mm thick PPAT layer at approximately $z = 1.5$ cm and $z = 2.0$ cm. These z locations are in the same planes as the endoDPT tomosynthesis images shown in Fig. 5.18 and Fig. 5.19. Fig. 5.31 shows the T2W image slices in the $(\hat{x}, \hat{y})$ plane of endoDPT geometry through the prostate surrounded by the 2.5 mm thick PPAT layer at approximately $z = 2.0$ cm and $z = 3.0$ cm. These z locations are in the same planes as the endoDPT tomosynthesis images shown in Fig. 5.20 and Fig. 5.21. Fig. 5.32 shows the T2W coronal image slices in the $(\hat{x}, \hat{y})$ plane of endoDPT geometry through the fat tissue and prostate tissue sections at approximately $z = 1.2$

cm and $z = 3.3$ cm. These z locations are in the same planes as the endoDPT tomosynthesis images shown in Fig. 5.22 and Fig. 5.23.

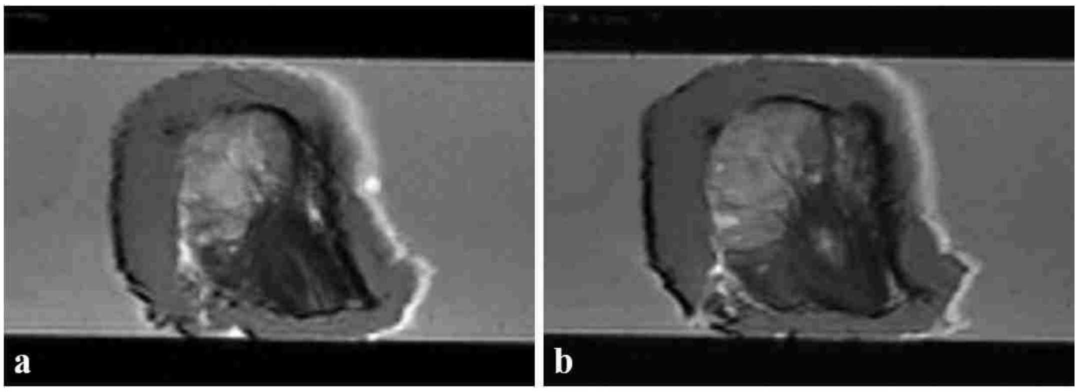

Figure 5.30: T2W coronal slices of prostate surrounded by 5 mm thick fat layer at approximately $z = 1.5$ cm (a) and $z = 2.0$ cm (b).

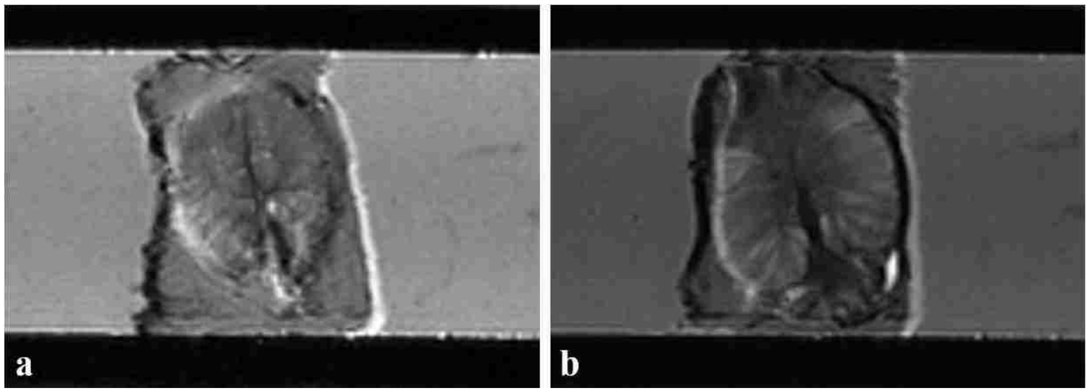

Figure 5.31: T2W coronal slices of prostate surrounded by 2.5 mm thick fat layer at approximately $z = 2.0$ cm (a) and $z = 3.0$ cm (b).

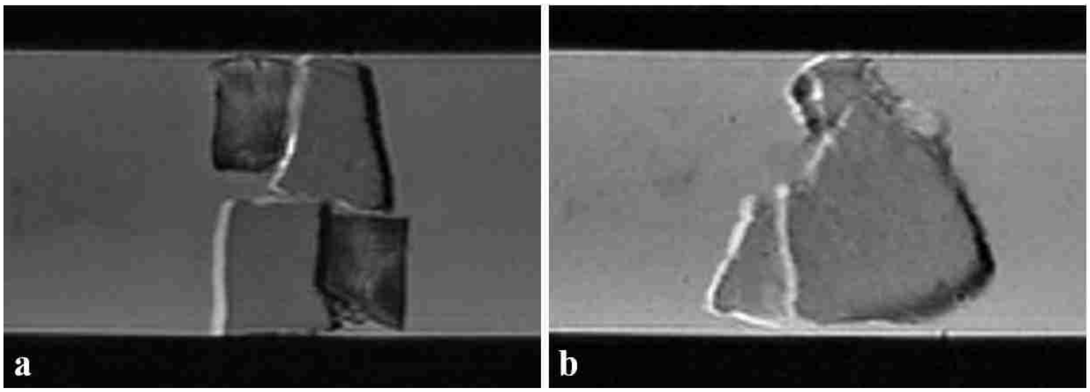

Figure 5.32: T2W coronal image slices through the sections of prostate tissue and fat tissue at approximately $z = 1.2$ cm (a) and $z = 3.3$ cm (b).

For the axial MRI slices, both the T1W and T2W images show a significant chemical shift artifact due to Larmor frequency differences in the fat and prostate/carrageen gel materials[ix]. The T2W images show better soft tissue contrast of the prostate, which is particularly evident in the prostate tissue and fat tissue sections (the prostate tissue is visible in the MR images compared to gel, whereas it was not clearly visible in the endoDPT and CT images). In all cases for prostates surrounded by a PPAT layer, the PPAT is visible and easily differentiable from both the prostatic tissue and the carrageenan gel.

Because the PPAT thickness was not identifiable in all endoDPT images, a measurement of PPAT thickness for the prostates wrapped in the thick and thin fat layers using the endoDPT images was not performed. For the CT and MR images of prostates with the thin and thick PPAT layers, the mean thickness of the PPAT layers was measured. 10 PPAT thicknesses were manually measured in random locations over 10 slices in the axial CT images and over three slices in the axial T2W images. The mean PPAT thickness for the thick PPAT layer was 4.86 ± 1.67 mm for CT and 5.76 ± 1.28 mm for MRI. The mean PPAT thickness for the thin fat layer was 2.14 ± 1.18 mm for CT and 2.49 ± 1.16 mm for MRI. These thicknesses are approximate as the images of the prostates wrapped in the thick and thin PPAT layers show that the thickness of the PPAT varies significantly even in single slices.

5.6.4 Tissue Vascularity

Because the SAA and BP images were qualitatively similar, only the BP and FBP images are shown for prostate phantoms embedded with silicone rubber tubing filled with iodine contrast agent. Fig. 5.33 and Fig. 5.34 show the BP and FBP tomosynthesis image planes through the prostate with embedded 0.64 mm OD silicone rubber tubing at $z =$ 1.0 cm and 2.0 cm. Fig. 5.35

[ix] Kevin McKlveen, (Pennington Biomedical Research Center), private communication, January 15, 2018

and Fig. 5.36 show the BP and FBP tomosynthesis image planes through the prostate with embedded 0.94 mm OD silicone rubber tubing at $z = 1.5$ cm and 2.6 cm. Fig. 5.37 and Fig. 5.38 show the BP and FBP tomosynthesis image planes through the prostate with embedded 1.19 mm OD silicone rubber tubing at $z = 1.5$ cm and 2.0 cm.

In all of the endoDPT tomosynthesis images, the tubing is visible. However, the tubing appears solid – there is no differentiation between the silicone rubber walls and the internal iodine contrast agent. This is because silicone rubber has very similar attenuation properties to the concentration of iodine used to fill the tubing. Choi *et al.* reported silicone rubber having a CT number $= 278 \pm 120$ HU (Choi 2010) and Mardis *et al.* reported that silicone rubber stents with similar diameters to the tubing used in this study had CT numbers ranging from 125 to 360 HU (Mardis 1993). To verify that the tubing seen in the endoDPT images was the entire silicone rubber tubing diameter and not just the inner lumen, 10 tubing diameters were measured over 10 FBP tomosynthesis images for each of the prostate samples. The mean diameters found for the tubing with nominal ODs of 0.64 mm, 0.94 mm, and 1.19 mm were 0.66 ± 0.05 mm, 0.95 ± 0.07 mm, and 1.18 ± 0.11 mm, respectively. The measured tubing ODs all agreed well with the nominal tubing ODs.

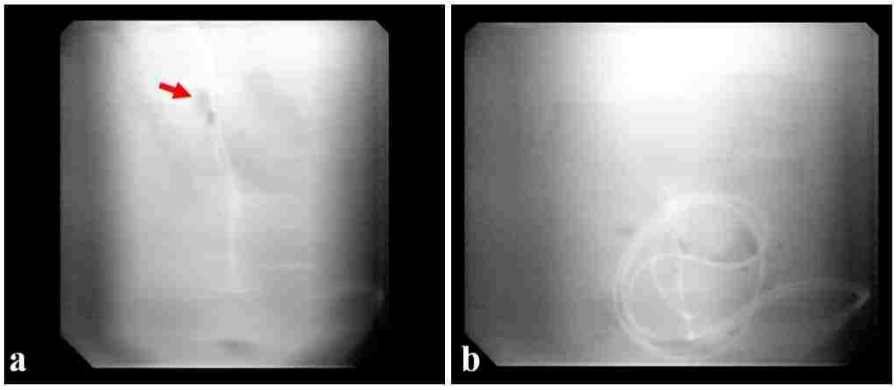

Figure 5.33: BP tomosynthesis image at $z = 1.0$ cm (a) and $z = 2.0$ cm (b) above detector face of prostate with 0.64 mm OD tubing. The red arrow points to an air pocket. Images have voxel size of 20 μm (2200 by 1896 voxels).

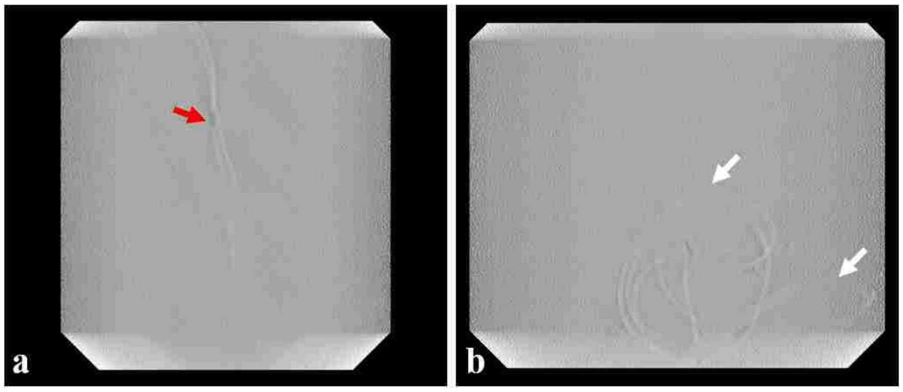

Figure 5.34: FBP tomosynthesis image at $z = 1.0$ cm (a) and $z = 2.0$ cm (b) above detector face of prostate with 0.64 mm OD tubing. The red arrow points to an air pocket. The white arrows point to a masking artifact. Images have voxel size of 20 µm (2200 by 1896 voxels).

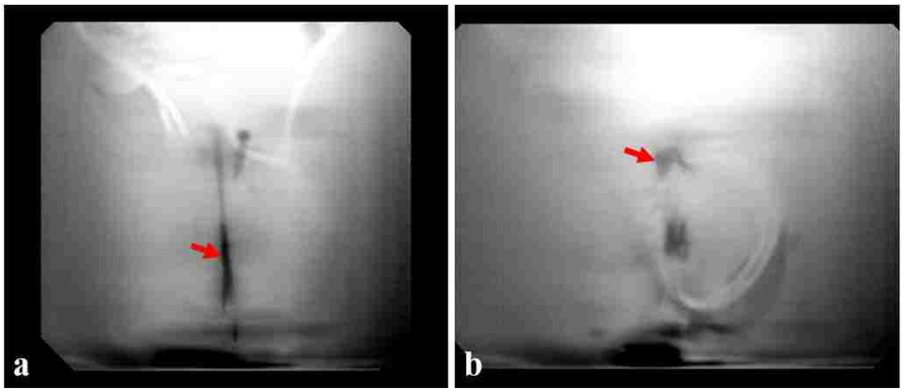

Figure 5.35: BP tomosynthesis image at $z = 1.5$ cm (a) and $z = 2.6$ cm (b) above detector face of prostate with 0.94 mm OD tubing. The red arrow points to an air pocket. Images have voxel size of 20 µm (2200 by 1896 voxels).

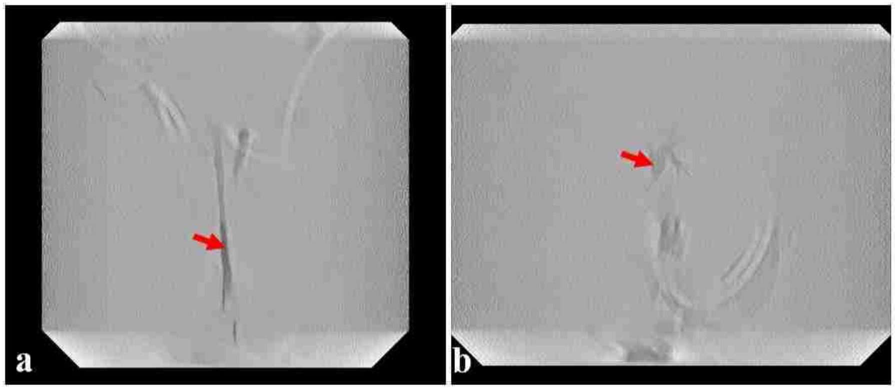

Figure 5.36: FBP tomosynthesis image at $z = 1.5$ cm (a) and $z = 2.6$ cm (b) above detector face of prostate with 0.94 mm OD tubing. The red arrow points to an air pocket. Images have voxel size of 20 µm (2200 by 1896 voxels).

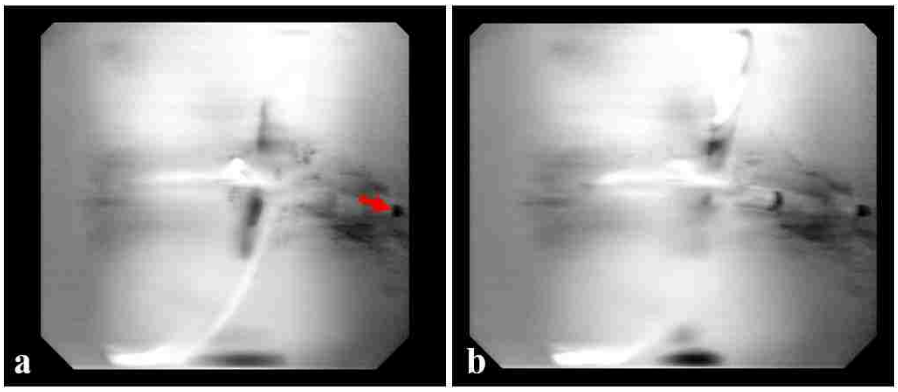

Figure 5.37: BP tomosynthesis image at $z = 1.5$ cm (a) and $z = 2.0$ cm (b) above detector face of the prostate that had tubing (OD = 1.19 mm) filled with iodine contrast agent. The red arrow points to an air pocket. Images have voxel size of 20 µm (2200 by 1896 voxels).

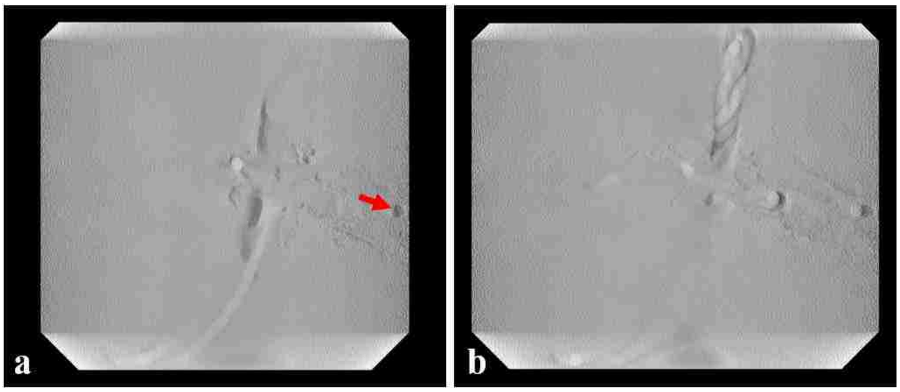

Figure 5.38: FBP tomosynthesis image at $z = 1.5$ cm (a) and $z = 2.0$ cm (b) above detector face of the prostate that had tubing (OD = 1.19 mm) filled with iodine contrast agent. The red arrow points to an air pocket. Images have voxel size of 20 µm (2200 by 1896 voxels).

Similar to the LDRBT implant and PPAT prostate scenarios, small air pockets were visible in both BP and FBP reconstruction (red arrows). Regions where the tubing was perpendicular to the tomosynthesis image were well resolved. The prostate border was not visible because the prostatic tissue and carrageenan gel have very similar attenuation properties. The truncation artifact was seen in some of the BP tomosynthesis images, and for thicker tubing, the blur artifact seen in BP became much more severe. The overshoot artifact was not very apparent in FBP, but the artifact from the triangular voids in the projection images was visible. One additional artifact noted with

FBP in these images (white arrows) was that for tubing with a long axis along the direction of scan motion, the tubing washed out and had low contrast.

The silicone rubber tubing containing iodine contrast agent was visible for the largest tubing diameter (1.19 mm OD) in the CT images. A single CT slice of the prostate with the 1.19 mm OD tubing is shown in Fig. 5.39 (in the $(\hat{x}, \hat{z})$ image plane of endoDPT geometry). At this window and level, the prostate border is not visible. Large air pockets within the prostate are visible.

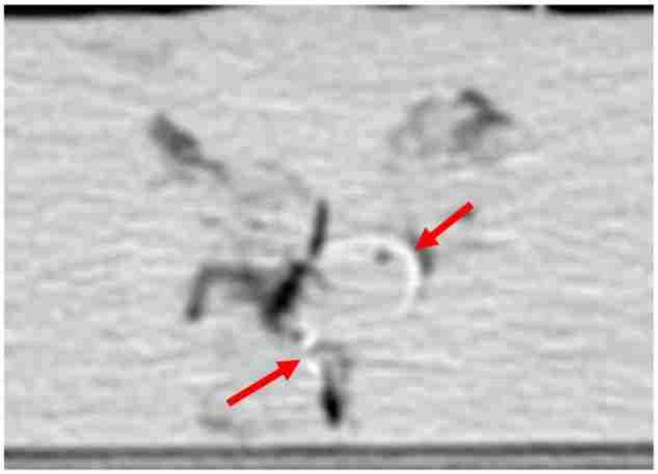

Figure 5.39: CT axial image slices through the prostate with embedded silicone rubber tubing (1.19 mm OD). The red arrows point to the tubing.

The silicone rubber tubing filled with gadolinium contrast agent was difficult to see in most MR images. Fig. 5.40 shows T1W and T2W coronal image slices (in the $(\hat{x}, \hat{y})$ plane of endoDPT geometry) for the prostate that had 0.64 mm OD silicon rubber tubing. The location of this slice is at the same approximate location as the endoDPT planes at $z = 2.0$ cm (Fig. 5.33 and Fig. 5.34). Fig. 5.41 shows the T1W and T2W coronal image slices (in the $(\hat{x}, \hat{y})$ plane of endoDPT geometry) through the prostate that had 0.94 mm OD silicon rubber tubing. The location of this slice is at the same approximate location as the endoDPT planes at $z = 2.6$ cm (Fig. 5.35 and Fig. 5.36). Fig. 5.42 shows the T1W and T2W axial image slices (in the $(\hat{x}, \hat{z})$ plane of endoDPT geometry) through the prostate that had 1.19 mm OD silicon rubber tubing. The location of this slice is at the same approximate location as the CT slice shown in Fig. 5.39. Fig. 5.43 shows the T1W and T2W coronal image slices (in the $(\hat{x}, \hat{y})$ plane of endoDPT geometry) through the prostate that had 1.19 mm OD silicon rubber tubing. The location of this slice is at the same approximate location as the endoDPT planes at $z = 2.0$ cm (Fig. 5.37 and Fig. 5.38).

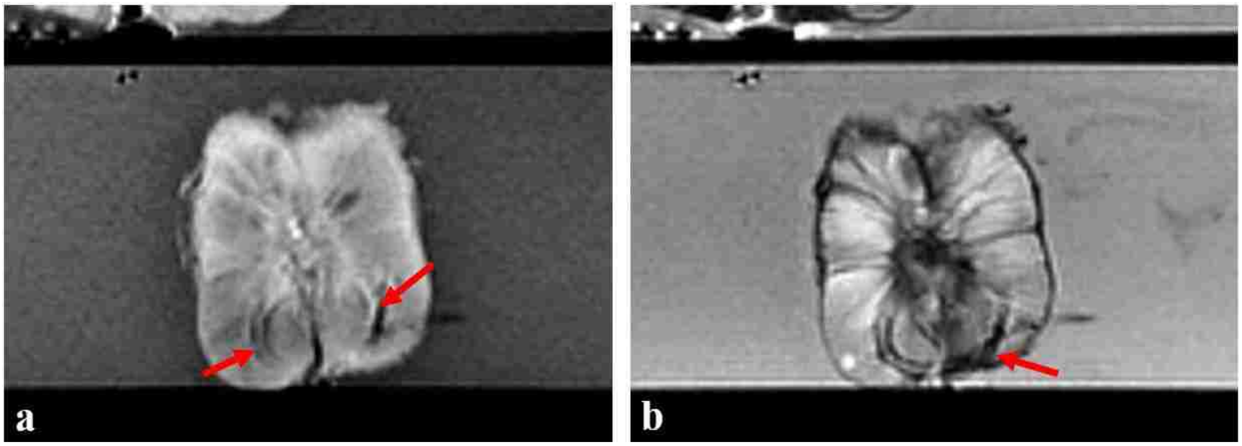

Figure 5.40: T1W (a) and T2W (b) coronal image slices of the that had tubing (OD = 0.64 mm) at approximately $z = 2.0$ cm. The red arrows point to the tubing.

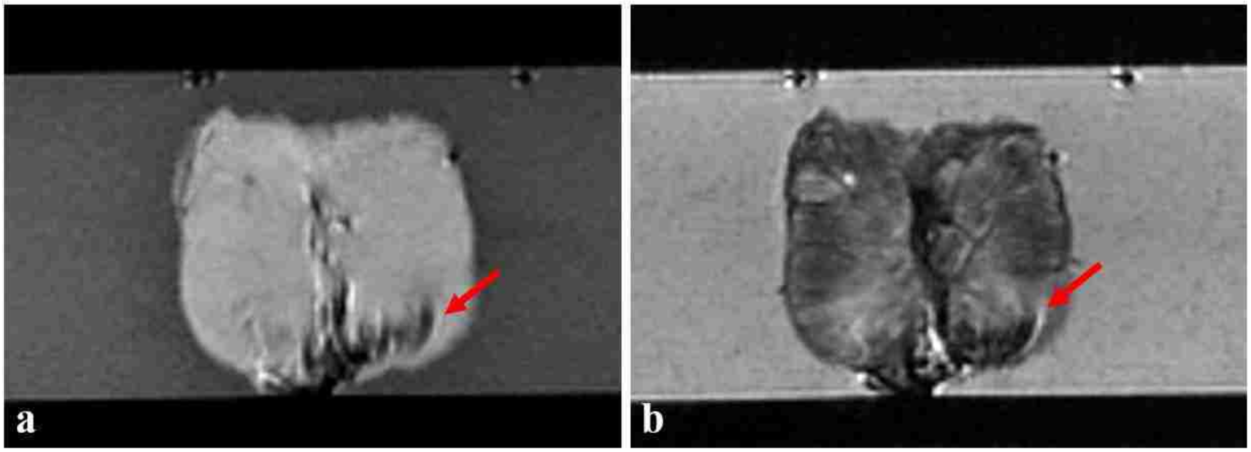

Figure 5.41: T1W (a) and T2W (b) coronal image slices of the that had silicon tubing (OD = 0.94) at approximately $z = 2.6$ cm. The red arrows point to the tubing.

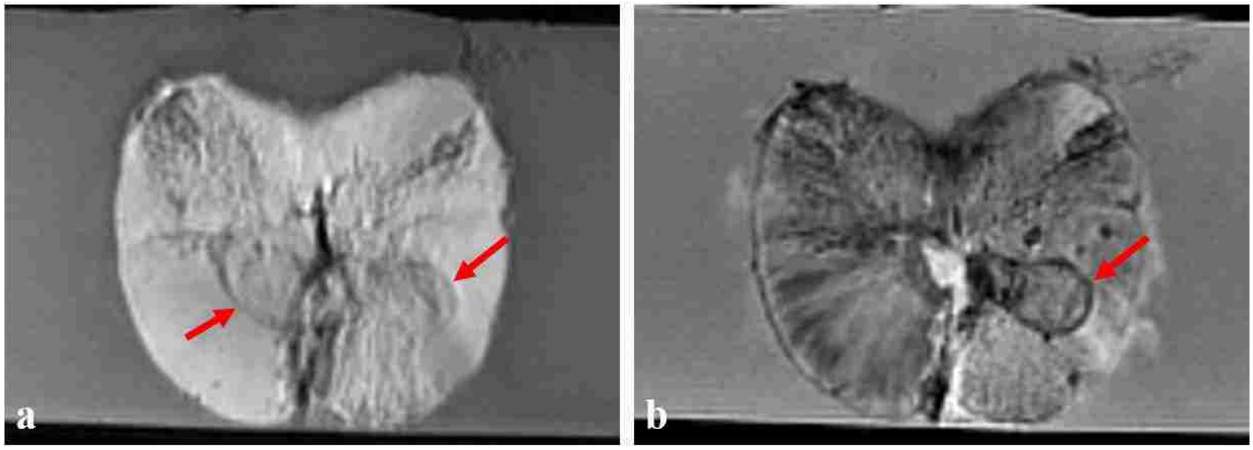

Figure 5.42: T1W (a) and T2W (b) axial image slices of the that had silicon tubing (OD = 1.19 mm). The red arrows point to the tubing.

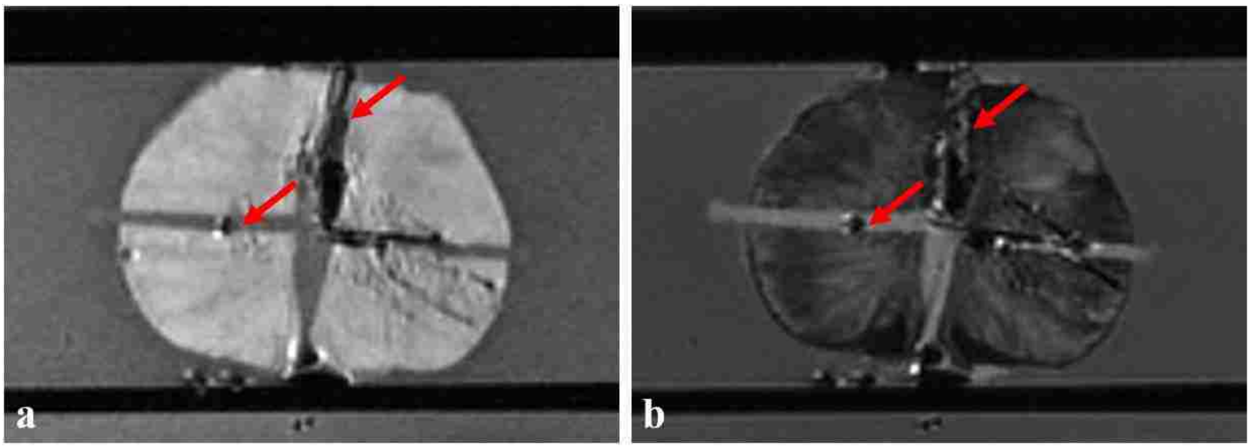

Figure 5.43: T1W (a) and T2W (b) coronal image slices of the that had silicon tubing (OD = 1.19 mm) at approximately $z = 2.0$ cm. The red arrows point to the tubing.

All of the tubing appeared hypointense in the prostate phantoms. Per volume, there was more silicone rubber in the tubing wall than gadolinium contrast agent in the lumen; previous studies have noted that silicone rubber tubing (stents) are hypointense in both T1W and T2W MR images (Yunker 2013). The tubing with a 0.94 mm OD did exhibit a hyperintense region, but this was located near an air pocket which appeared to distort the image. Overall, the tubing did not enhance due to the gadolinium.

5.7 Discussion

endoDPT imaging of the pecan and pistachio nuts demonstrated that high resolution is achievable using this imaging method. Structures of the nut, such as the shell and meat, were clearly visible, particularly in the midplane. However, the anterior and posterior portions of the nut were more difficult to visualize. These nut phantoms also demonstrated several artifacts due to tomosynthesis reconstruction and the imaging hardware. SAA and BP had the expected blur artifact (Dobbins 2003). FBP removed much of the blur artifact, producing a cleaner but noisier image. The FBP images also displayed a banding artifact at the top and bottom of the images; this banding artifact manifested because the triangular voids in the projection images are not used to reconstruct the images. This banding artifact occurred due to the filtration process; at image edges, the signal was artificially increased by the filter. Despite removing 1 mm along all edges of the projection images after filtering, including the voids, the edge enhancement was still evident, particularly when fewer additions per voxel occurred. The effect of this artifact can be reduced by removing more of the edge, but this further reduces the already small FoV of the detector.

The most significant artifact seen in FBP was the overshoot (edge enhancement) artifact that was particularly evident at the low-density air and high-density shell interfaces. This edge artifact is due to the interplay of limited sampling (endoDPT sampled the imaged volume over $\approx \pm 21.8°$) with the filtration process (Chen 2005, Chen 2007a, Chen 2008, Cong 2011, Mertelmeier 2014). When the imaged volume is not fully sampled, the negative side lobes of the spatial domain point impulse inversion filter result in edge enhancement between structures with substantially different densities. Use of more advanced analytic filters (e.g., incorporate filter weighting for divergent beam) or iterative/algebraic reconstruction algorithms, in addition to sampling over a larger angular range, can reduce this artifact. Similar edge enhancement artifacts have been noted when imaging other phantoms (an apple) (Levakhina 2013).

The endoDPT images of the LDRBT seeds and the silicone rubber tubing also clearly demonstrated the high-resolution of this new imaging methods. The primary limitations for imaging both scenarios were that the prostate border was not visible, and there were truncation artifacts and artifacts from the triangular voids in the projection images. The images of the prostates wrapped in a PPAT layer demonstrate that prostate border visualization is possible with endoDPT. To improve prostate border visibility and to reduce the truncation artifact, a larger x-ray sensor that allows for detector acquisition FoV would be beneficial. However, a larger sensor would prove challenging for endorectal imaging.

In the FBP endoDPT images of the LDRBT seeds, the core and shell of each seed was clearly identifiable, which is a metric of high image quality and resolution (Rozenfeld 2012). For BP, the blur artifact made it difficult to differentiate the shell from the core. Because the seeds are high-density, there was a substantial blur artifact from OOP seeds for all reconstruction methods. This blur was reduced with FBP because filtration reduced the effect OOP structures, as was observed in the measurement of the ASF. Similar to imaging the pecan and pistachio, FBP resulted in an edge-enhancement artifact. LDRBT seed orientation and geometry were easily discernable with endoDPT. While not studied in this work, it is possible that improved knowledge of LDRBT seed orientation could improve dosimetry of the LDRBT treatment. Dosimetric differences in the treated prostate volume of up to 1.6% have been reported when comparing one-dimensional (point source) to two-dimensional (line source) dose calculations using TG-43 formalism (Chng 2012); incorporating variations in LDRBT seed tilt in post-implant dosimetry has been reported to change dose to OAR by up to 10% (Collins Fekete 2014).

In CT, the LDRBT seeds appeared as easily identifiable bright spots in the axial images of the canine prostates; it is for this reason that CT is considered the gold standard imaging method for

LDRBT (Amdur 1999, Mehrmohammadi 2014). For seeds that were end-to-end, it was difficult to differentiate seeds, and seed orientation (tilt) was not identifiable. A streaking artifact was present in the images, which is typical in CT images of LDRBT seeds due to the high-density seed cores and titanium shells (Han 2003a, De Brabandere 2006, Siebert 2007, Robertson 2012). Because a thin slice (1.25 mm thick) was used, and because the carrageenan gel and prostate tissue had similar attenuation properties, the prostate border was difficult to discern. This problem is not a consequence of the tissue-equivalent gel used here, as other studies have reported that CT has difficulty in differentiating the prostate from nearby soft tissues such as the pelvic floor muscles (Amdur 1999, Mehrmohammadi 2014). Overall, these canine prostate images were similar to post-implant images of human prostates (Amdur 1999, De Brabandere 2012, Mehrmohammadi 2014).

Unlike both endoDPT and CT, the LDRBT seeds in the MR images were not directly visible. The seeds appeared as distorted voids of signal due to the magnetic susceptibility artifact; it was impossible to identify seed tilt or orientation. Such voids of signal are typical in MR imaging of LDRBT seeds (De Brabandere 2006, Thomas 2009, Robertson 2012) and are primarily due to the titanium shell, which is highly paramagnetic (Thomas 2009). The shell distorts the magnetic field which induces a magnetic susceptibility artifact; this artifact presents as a void of signal with nearby bright regions corresponding to signal from the protons in the void being mismapped (Thomas 2009). Overall, the seeds heavily distorted the MR images and were not easily identifiable, but the undistorted portions of the images clearly showed the internal prostate anatomy and prostate border, which is consistent with the findings of other groups (Amdur 1999, De Brabandere 2012, Robertson 2012). While not studied in this work, novel pulse sequences and MR specific contrast markers have some utility in improving LDRBT seed imaging (Lamberto 2014, Lim 2016).

To compare seed differentiability between endoDPT, CT, and MRI, all visible independent seeds were counted. All seeds could be identified in endoDPT. Similar studies have reported 100% seed identification success rates with tomosynthesis using an external x-ray sensor (Tutar 2003). In this study, all LDRBT seeds were located within the endoDPT FoV. However, for larger prostates (such as in men suffering from PCa and BPH) or for migrated the small FoV of endoDPT may preclude 100% seed counts. Up to 40% of patients experience seed migration (Wang 2015). CT had seeds counts that missed two to three seeds and MRI had seed counts that missed three to eight seeds. For CT, this was because some of the seeds were spaced end-to-end, and it was impossible to determine if it was a single seed or two seeds spanning four to five slices. A larger number of seeds were missed in MRI due to the magnetic susceptibility (void) artifact obscuring signals from seeds near each other, making it impossible to differentiate closely-spaced seeds. The results of seed counting with CT and MRI were comparable to a study performed by Bloch *et al.* where he reported seed identification success rates of 91.5% with T1W MRI and 96.7% with CT (Bloch 2007).

The images of the silicone rubber tubing filled with iodine contrast agent also served to highlight the high resolution of endoDPT. The tubing was readily visible in all endoDPT images, although the larger diameter tubing was very blurred in the BP reconstructions. Due to similarity in the attenuation of silicone rubber (Mardis 1993, Choi 2010) and the iodine contrast solution used in this work, the tubing wall was indistinguishable from the tubing lumen, which was verified by measuring the diameters of the tubing in the endoDPT images. The expected blur and truncation artifacts were seen in the BP images. Because the density of the silicone rubber tubing filled with iodine contrast was much less than the density of LDRBT seeds, the overshoot artifact was not as pronounced in the FBP images. However, the artifact from the triangular voids in the projection images was still visible in FBP, and an additional artifact presented that washed out the signal of tubing that was oriented parallel to the x-ray source motion. The tubing in this orientation has the same appearance as a small structure that is above or below the tomosynthesis image, similar to the OOP BBs in Fig. 4.19. FBP actively works to remove such OOP structure blur artifacts and operates in the same manner on the tubing if it presents in a similar orientation.

The largest diameter tubing was visible in CT and all tubing diameters were visible in at least one MRI view in each image set. The tubing had limited visibility in CT due to a large amount of noise from the thin slice thickness and the poor resolution in comparison to endoDPT. The tubing in the MR images was hypointense and indistinct primarily because of the interplay between the MR signals from the silicone rubber in the tubing walls compared to the gadolinium contrast solution in the tubing lumen. Silicon rubber generally appears hypointense (Yunker 2013). Overall, the visualization of the silicone rubber tubing was poor with MRI and CT. Because no other studies have assessed visibility of contrast agent in silicon tubing or the visibility of individual vessels in the prostate using angiographic techniques, there was no metric of comparison for this result. However, imaging of blood perfusion in the prostate is often performed with both MRI and TRUS (Sankineni 2016) and is under clinical investigation with CT (Luczynska 2014). This study did not image perfusion because the use of *ex vivo* canine prostate specimens precluded diffusion of the contrast medium (iodine for x-rays and gadolinium for MRI) out of the capillaries into the surrounding extra-cellular space (Padhani 2005).

The endoDPT images of the prostates wrapped in a PPAT layer and of the sections of prostatic tissue near fat tissue demonstrated that soft tissue contrast between the prostate and surrounding fat layer is possible with endoDPT. The images of the prostates wrapped in PPAT were the only endoDPT images that allowed for some visualization of the prostate boarder. Overall, this demonstration of soft-tissue contrast is a positive result for endoDPT and future efforts will focus on improving image contrast to allow for visualization of the prostate border. Overall the prostate/fat images highlighted the largest flaw of endoDPT, which is the difficulty to visualize large structures clearly. The PPAT layer was readily visible in CT as a dark (low-density) band surrounding the prostate, which is consistent with previous studies (van Roermund 2010, van Roermund 2011). There were no obvious artifacts in the CT images, but the images were noisy due to the small slice thickness and reconstructed voxel size; the prostate tissue and carrageenan gel were indistinguishable. The MR images showed excellent soft tissue contrast between the fat, prostate tissue, and gel, with the T2W images also showing zonal anatomy clearly. Comparable results have been observed in previous studies (Amdur 1999, Woo 2015). A chemical shift artifact in the slice selection direction was visible, due to the difference in Larmor frequency between the fat and prostate/carrageenan gel.

5.8 Conclusion

The objective of this aim was to qualitatively demonstrate the high resolution of endoDPT in comparison to CT and MRI, two common methods of prostate imaging. The results of this aim showed that small structures, such as the internal details of nut phantoms, LDRBT seeds implanted in canine prostates, and small diameter silicone rubber tubing filled with contrast agent, were visible with high resolution using endoDPT. A limitation of endoDPT was that the prostate border was not clearly visualized in these images. In CT the prostate border was usually discernable, while MRI provided the best visualization of the prostate border and internal prostate anatomy. In CT, the LDRBT seed implants were easily identifiable, but the seed shell and core were not differentiable; seeds oriented end-to-end made seed counting difficult. The silicon rubber tubing had very poor visibility in CT. In MRI, the seeds presented as voids of signal due to a large magnetic susceptibility artifact, and precise knowledge of seed location or orientation was impossible to ascertain. The silicon rubber had more visibility in MRI than CT, but not as much as endoDPT. Images of the prostates wrapped in a PPAT layer demonstrated the primary limitation of endoDPT, which is difficulty in discerning larger structures due to the small size of the XDR sensor. CT and MRI provided much better visualization of the prostate and the fat layer.

Chapter 6. Conclusion

6.1 Summary of Results

Currently, the prostate region is imaged using CT, MRI, TRUS, PET, and SPECT (Kelloff 2009, Sankineni 2016), which typically have spatial resolutions on the order of 0.3 to 5.0 mm (Bushberg 2012). The purpose of this work was to explore endoDPT, an imaging method that uses an endorectal x-ray sensor and external x-ray source to produce high-resolution images of the prostate region using tomosynthesis. While endorectal imaging of the prostate is clinically performed or is under investigation using MRI, TRUS, PET, and SPECT (Mukdadi 2014, Musico 2016, Sankineni 2016), the method of imaging described in the previous chapters as endoDPT has not been previously explored.

This study clearly demonstrated both computationally and by measurement that endoDPT is a high-resolution imaging method in comparison to the typical resolutions reported for CT, MRI, TRUS, PET, and SPECT prostate imaging. Results showed that the 90%, 50%, and 10% MTF occurred at significantly higher ($p < 0.0001$) frequencies than CT for all endoDPT parameters. These improvements in resolution were achievable at endoDPT ionizing radiation doses that were significantly less ($p < 0.002$) than CT outside the beam FoV and ranged from significantly less than to significantly higher than CT in the endoDPT beam FoV.

The high resolution of endoDPT was further demonstrated by using endoDPT to image two types of nuts, canine prostates implanted with LDRBT seeds, and canine prostates embedded with small-diameter silicone rubber tubing filled with contrast agent. endoDPT could clearly identify the LDRBT seeds, including identification of both the seed shell and core for seeds in-plane. The seed cores were readily visible on CT and presented as void of signal on MRI; for both modalities, it was difficult to differentiate seeds in close proximity. The current detector size used here limited the ability of endoDPT to clearly identify large structures, such as fat layers or prostate borders.

Both the fat layer and prostate border were visible with CT and MRI, although differentiation of the prostate border from the carrageenan gel was difficult in CT due to similar attenuation in both materials. Like the LDRBT seeds, endoDPT could clearly identify the silicone tubing, including finding the OD of the tubing to within 0.02 mm. These small diameter silicon rubber tubes were difficult or impossible to see in both CT and MRI. This work has overall demonstrated resolution improvements compared to CT and MRI.

6.2 Response to Hypothesis

We hypothesized that the in-plane resolution of endoDPT was significantly higher than the in-plane resolution of a typical CT scanner at an ionizing radiation dose significantly less than the ionizing radiation dose of a typical CT scan. For the former portion of the hypothesis, the null hypothesis that endoDPT had the same or significantly lower resolution than CT was rejected. endoDPT demonstrated that the 90%, 50%, and 10% levels of MTF occurred at significantly higher frequencies than CT ($p < 0.0001$) for all endoDPT parameters tested.

The latter portion of the hypothesis did not allow for complete rejection of the null hypothesis that endoDPT radiation dose was the same as or significantly greater than CT radiation dose. The dose outside of the endoDPT FoV was significantly less than CT ($p < 0.002$) at all endoDPT x-ray source currents (100 mAs, 50 mAs, and 25 mAs) at all planes of measurement. The dose measured near the endoDPT FoV and within the endoDPT FoV ranged from significantly lower to significantly higher than CT. Future clinical studies will need to address whether the improved resolution at the cost of increased ionizing radiation dose is a trade-off that benefits the patient. Some dose reduction may be achieved by optimizing endoDPT scan parameters (such as using a smaller x-ray source travel distance and fewer projection images) and hardware (such as using a harder x-ray beam or a detector that requires less exposure).

6.3 Recommendation

This study clearly demonstrated through quantitative and qualitative evaluation that endoDPT has high in-plane image resolution. The results of this work indicate that endoDPT has some favorable characteristics compared to other prostate imaging techniques, whether as a standalone method or paired with other imaging modalities. While this study provided baseline data for endoDPT, more development and optimization are required before endoDPT can be evaluated as a clinical technique for PCa management. Our primary recommendation is to improve the endoDPT system design through development of a prototype system that allows for automated endoDPT scan acquisition, image reconstruction, and x-ray source localization. An endoDPT scan currently takes approximately 1 hour to complete due to manual positioning of the x-ray source and low frame rate of the XDR sensor. With an automated prototype system, optimizing scan parameters and pre-clinical studies become both efficient and feasible.

6.4 Limitations of the Study

The primary limitations of this study were the manual positioning of the x-ray source and the small detector size. Because the x-ray source was manually positioned for each discrete projection image, scan times were long and the potential for error in positioning of the source was high. This limited the number of scan parameters that were tested, for example, for measurement of NPS, ASF, and dose, only one x-ray source kVp setting was used. While the slow frame-rate of the XDR sensor of 5-7 seconds per image was not a limiting factor in the current study (in comparison to manual tube positioning), in a clinical environment, short scan times are important so a frame-rate of 5-7 seconds per image would represent a severe limitation.

The manual source positioning resulted in x-ray source locations that could deviate from the nominal x-ray source locations. Errors in source location degrade reconstructed image quality. Fiducial wires were used to identify and correct source position errors, but this method was manual and thus time intensive. An automated, reproducible x-ray source positioning method, with actual source locations integrated in real-time image reconstruction software, would be desirable for clinical implementation of endoDPT.

The small detector FoV resulted in a significant truncation artifact, particularly in the SAA and BP reconstructions. The limited FoV made it difficult to visualize the prostate border. A larger detector size that allowed for full-field imaging of the prostate would alleviate this artifact and would improve visualization of the prostate border. However, the detector size is limited both by manufacturing (it is difficult and expensive to produce large area, high resolution CCD or CMOS imaging sensors) and by the endorectal insertion profile. Increasing the detector size while maintaining a viable endorectal insertion profile may prove to be the largest challenge in moving endoDPT into clinical workflow. It may be necessary to combine endoDPT with another clinical imaging technology and utilize a fusion technique, such that endoDPT provides high-resolution images and another modality, such as TRUS, provides the prostate border and other large details. Ultrasound sensors have been fitted onto similar endorectal gamma-ray detection devices (Rozenfeld 2012).

6.5 Future Work

This study provided baseline data for endoDPT and demonstrated that endoDPT is a high-resolution imaging method. The primary recommendation for this work is to move forward in development of a prototype system that allows for automated image acquisition. It is expected such work will include design of a probe system with an x-ray sensor optimized for endoDPT, development of a protocol for existing radiography systems that allows for automated endoDPT scan acquisition, and a refined method of x-ray source localization relative to the endoDPT x-ray sensor. With such a prototype, pre-clinical testing becomes feasible.

The primary goal in endorectal probe and detector design should be maintaining a small insertion profile while maximizing the detector FoV. One possible solution for this goal is development of a detector with a small insertion profile that expands within the rectum, similar to endorectal MRI coils. The insertion profile must be small as the anal sphincter is where pain occurs in endorectal imaging techniques (Koprulu 2012). After the anal sphincter is bypassed, a detector within the rectum can move or expand relatively freely; this is utilized during DREs to palpate the lateral regions of the gland and not just the portion of the prostate proximal to the rectum (Balkissoon 2009). The expanding detector could be created by patching together multiple imaging chips, which can be accomplished with gaps in the imaging plane of less than one pixel (Mertelmeier 2014). Endorectal gamma-ray sensors, such as BrachyView, use multiple imaging chips in a single probe (Petasecca 2013, Safavi-Naeini 2013, Loo 2014, Safavi-Naeini 2015, Alnaghy 2017), although in a somewhat more linear arrangement than needed for endoDPT. The larger FoV afforded by an x-ray sensor larger than the XDR sensor would increase image quality and improve visualization of the prostate border, as well as reducing the severity of the truncation artifact.

Development of an automated endoDPT imaging system represents less of a challenge than large FoV detector design, because automated tomosynthesis imaging systems have been previously developed for chest and breast imaging (Goodsitt 2014). Adaption to endoDPT should be straight forward. Similarly, source localization methods for endoDPT should not prove challenging, due to the large scope of work previously published for localization of fluoroscopy, C-arm, and CT sources using external or internal fiducial markers (Jain 2005, Kuo 2014, Lee 2017).

References

(Acciavatti 2011). Acciavatti, R. J. and A. D. Maidment (2011). "Optimization of phosphor-based detector design for oblique x-ray incidence in digital breast tomosynthesis." **Medical Physics** 38(11): 6188-6202.

(Adolfsson 2008). Adolfsson, J. (2008). "Watchful waiting and active surveillance: the current position." **BJU International** 102(1): 10-14.

(Aime 2009). Aime, S. and P. Caravan (2009). "Biodistribution of gadolinium-based contrast agents, including gadolinium deposition." **Journal of Magnetic Resonance Imaging** 30(6): 1259-1267.

(Alnaghy 2017). Alnaghy, S., D. L. Cutajar, J. A. Bucci, K. Enari, M. Safavi-Naeini, M. Favoino, M. Tartaglia, F. Carriero, J. Jakubek, S. Pospisil, M. Lerch, A. B. Rosenfeld and M. Petasecca (2017). "BrachyView: Combining LDR seed positions with transrectal ultrasound imaging in a prostate gel phantom." **Physica Medica** 34: 55-64.

(Amdur 1999). Amdur, R. J., D. Gladstone, K. A. Leopold and R. D. Harris (1999). "Prostate seed implant quality assessment using MR and CT image fusion." **International Journal of Radiation Oncology Biology Physics** 43(1): 67-72.

(Attix 1986). Attix, F. H. (1986). Introduction to radiological physics and radiation dosimetry. New York, Wiley.

(Ayala 1989). Ayala, A. G., J. Y. Ro, R. Babaian, P. Troncoso and D. J. Grignon (1989). "The Prostatic Capsule - Does It Exist - Its Importance in the Staging and Treatment of Prostatic-Carcinoma." **American Journal of Surgical Pathology** 13(1): 21-27.

(Balkissoon 2009). Balkissoon, R., K. Blossfield, L. Salud, D. Ford and C. Pugh (2009). "Lost in translation: unfolding medical students' misconceptions of how to perform a clinical digital rectal examination." **American Journal of Surgery** 197(4): 525-532.

(Barentsz 2016). Barentsz, J. O., J. C. Weinreb, S. Verma, H. C. Thoeny, C. M. Tempany, F. Shtern, A. R. Padhani, D. Margolis, K. J. Macura, M. A. Haider, F. Cornud and P. L. Choyke (2016). "Synopsis of the PI-RADS v2 Guidelines for Multiparametric Prostate Magnetic Resonance Imaging and Recommendations for Use." **European Urology** 69(1): 41-49.

(Bhavsar 2014). Bhavsar, A. and S. Verma (2014). "Anatomic imaging of the prostate." **BioMed Research International** 2014: 1-10.

(Bhindi 2012). Bhindi, B., G. Trottier, M. Elharram, K. A. Fernandes, G. Lockwood, A. Toi, K. M. Hersey, A. Finelli, A. Evans, T. H. van der Kwast and N. E. Fleshner (2012). "Measurement of peri-prostatic fat thickness using transrectal ultrasonography (TRUS): a new risk factor for prostate cancer." **BJU International** 110(7): 980-986.

(Bigler 1993). Bigler, S. A., R. E. Deering and M. K. Brawer (1993). "Comparison of Microscopic Vascularity in Benign and Malignant Prostate Tissue." **Human Pathology** 24(2): 220-226.

(Bilusic 2016). Bilusic, M. (2016). "Castration Resistant Prostate Cancer: Role of Chemotherapy". <u>Prostate Cancer: Science and Clinical Practice</u>. J. H. Mydlo and C. J. Godec. London, Elsevier/AP: 509-514.

(Bittencourt 2014). Bittencourt, L. K., D. Hausmann, N. Sabaneeff, E. L. Gasparetto and J. O. Barentsz (2014). "Multiparametric magnetic resonance imaging of the prostate: current concepts." **Radiologia Brasileira** 47(5): 292-300.

(Bloch 2007). Bloch, B. N., R. E. Lenkinski, T. H. Helbich, L. Ngo, R. Oismueller, S. Jaromi, K. Kubin, R. Hawliczek, I. D. Kaplan and N. M. Rofsky (2007). "Prostate postbrachytherapy seed distribution: comparison of high-resolution, contrast-enhanced, T1- and T2-weighted endorectal magnetic resonance imaging versus computed tomography: initial experience." **International Journal of Radiation Oncology Biology Physics** 69(1): 70-78.

(Borre 1998). Borre, M., B. V. Offersen, B. Nerstrom and J. Overgaard (1998). "Microvessel density predicts survival in prostate cancer patients subjected to watchful waiting." **British Journal of Cancer** 78(7): 940-944.

(Brawer 1993). Brawer, M. K., R. E. Deering, M. Brown, S. D. Preston and S. A. Bigler (1993). "Predictors of pathologic stage in prostatic carcinoma. The role of neovascularity." **Cancer** 73(3): 678-687.

(Brennan 2002). Brennan, J. (2002). "An introduction to digital radiography in dentistry." **Journal of Orthodontics** 29(1): 66-69.

(Brullmann 2015). Brullmann, D. and R. K. W. Schulze (2015). "Spatial resolution in CBCT machines for dental/maxillofacial applications-what do we know today?" **Dentomaxillofacial Radiology** 44(1): 1-8.

(Brunet-Benkhoucha 2009). Brunet-Benkhoucha, M., F. Verhaegen, S. Lassalle, D. Beliveau-Nadeau, B. Reniers, D. Donath, D. Taussky and J. F. Carrier (2009). "Clinical implementation of a digital tomosynthesis-based seed reconstruction algorithm for intraoperative postimplant dose evaluation in low dose rate prostate brachytherapy." **Medical Physics** 36(11): 5235-5244.

(Bushberg 2012). Bushberg, J. T. (2012). <u>The essential physics of medical imaging</u>. Philadelphia, Wolters Kluwer Health/Lippincott Williams & Wilkins.

(Cademartiri 2005). Cademartiri, F., N. R. Mollet, A. van der Lugt, E. P. McFadden, T. Stijnen, P. J. de Feyter and G. P. Krestin (2005). "Intravenous contrast material administration at helical 16-detector row CT coronary angiography: effect of iodine concentration on vascular attenuation." **Radiology** 236(2): 661-665.

(Catalona 1994). Catalona, W. J. (1994). "Management of cancer of the prostate." **The New England Journal of Medicine** 331(15): 996-1004.

(Chen 1994). Chen, S. K. and L. Hollender (1994). "Modulation transfer function of a digital dental x-ray system." **Oral Surgery, Oral Medicine, Oral Pathology, Oral Radiology** 77(3): 308-313.

(Chen 2007a). Chen, Y. (2007a). Digital Breast Tomosynthesis (DBT) - A Novel Imaging Technology to Improve Early Breast Cancer Detection: Implementation, Comparison, and Optimization. PhD Dissertation, Duke University.

(Chen 2013). Chen, Y. (2013). "Breast Tomosynthesis". Physics of Mammographic Imaging. M. K. Markey, CRC Press: 39-52.

(Chen 2006). Chen, Y., J. Y. Lo, J. A. Baker and J. T. Dobbins III (2006). "Gaussian frequency blending algorithm with Matrix Inversion Tomosynthesis (MITS) and Filtered Back Projection (FBP) for better digital breast tomosynthesis reconstruction". *Medical Imaging 2006: Physics of Medical Imaging*, San Diego, SPIE.

(Chen 2005). Chen, Y., J. Y. Lo and J. T. Dobbins III (2005). "Impulse response analysis for several digital tomosynthesis mammography reconstruction algorithms". *Medical Imaging 2005: Physics of Medical Imaging*, San Diego, SPEI.

(Chen 2007b). Chen, Y., J. Y. Lo and J. T. Dobbins, 3rd (2007b). "Importance of point-by-point back projection correction for isocentric motion in digital breast tomosynthesis: relevance to morphology of structures such as microcalcifications." **Medical Physics** 34(10): 3885-3892.

(Chen 2008). Chen, Y., J. Y. Lo and J. T. Dobbins, 3rd (2008). "Impulse response and Modulation Transfer Function analysis for Shift-And-Add and Back Projection image reconstruction algorithms in Digital Breast Tomosynthesis (DBT)." **International Journal of Human Nutrition and Functional Medicine** 1(2): 189-204.

(Chen 2014). Chen, Y., W. Zhou and J. T. Dobbins III (2014). "Fourier-domain methods for optimization of tomosynthesis (NEQ)". Tomosynthesis Imaging. I. Reiser and S. Glick. Boca Raton, FL, CRC Press, Taylor & Francis Group, LLC: 135-145.

(Chipollini 2016). Chipollini, J. and S. Punnen (2016). "Salvage Cryoablation of the Prostate". Prostate Cancer: Science and Clinical Practice. J. H. Mydlo and C. J. Godec. London, Elsevier/AP: 543-549.

(Chng 2012). Chng, N., I. Spadinger, R. Rasoda, W. J. Morris and S. Salcudean (2012). "Prostate brachytherapy postimplant dosimetry: seed orientation and the impact of dosimetric anisotropy in stranded implants." **Medical Physics** 39(2): 721-731.

(Choi 2010). Choi, H. J., H. J. Lee and S. G. Kang (2010). "The Clinical Significance of Hounsfield Number of Metallic and Non-Metallic Foreign Bodies in the Soft Tissue." **Soonchunhyang Medical Science** 16(2): 226-230.

(Choi 2015). Choi, S., S. Lee, Y.-J. Lee, Y.-S. Kim, H.-H. Lee and H.-J. Kim (2015). "Feasibility of ray- and pixel-driven projector/back-projector in linear motion tomosynthesis". *Physics of Medical Imaging*, Orlando, SPEI.

(Claus 2004). Claus, B. E. H. and J. W. Eberhard (2004). Generalized Filtered Backprojection in Digital Tomosynthesis. USPTO. USA. 6,707,878 B2.

(Claus 2006). Claus, B. E. H., J. W. Eberhard, A. Schmitz, P. Carson, M. Goodsitt and H. P. Chan (2006). "Generalized filtered back-projection reconstruction in breast tomosynthesis." **Digital Mamography, Proceedings** 4046: 167-174.

(Collins Fekete 2014). Collins Fekete, C. A., M. Plamondon, A. G. Martin, E. Vigneault, F. Verhaegen and L. Beaulieu (2014). "Quantifying the effect of seed orientation in postplanning dosimetry of low-dose-rate prostate brachytherapy." **Medical Physics** 41(10): 1017041-1017049.

(Colsher 1977). Colsher, J. G. (1977). "Iterative 3-Dimensional Image-Reconstruction from Tomographic Projections." **Computer Graphics and Image Processing** 6(6): 513-537.

(Cong 2011). Cong, L., Y. Chen and W. Zhou (2011). "Effects of slice thickness filter in filtered backprojection reconstruction with parallel breast tomosynthesis imaging configuration". *IEEE International Workshop on Genomic Signal Processing and Statistics*, San Antonio, TX.

(Davis 2012). Davis, B. J., E. M. Horwitz, W. R. Lee, J. M. Crook, R. G. Stock, G. S. Merrick, W. M. Butler, P. D. Grimm, N. N. Stone, L. Potters, A. L. Zietman and M. J. Zelefsky (2012). "American Brachytherapy Society consensus guidelines for transrectal ultrasound-guided permanent prostate brachytherapy." **Brachytherapy** 11(1): 6-19.

(De Angelis 2007). De Angelis, G., H. G. Rittenhouse, S. D. Mikolajczyk, L. Blair Shamel and A. Semjonow (2007). "Twenty Years of PSA: From Prostate Antigen to Tumor Marker." **Reviews in Urology** 9(3): 113-123.

(De Brabandere 2013). De Brabandere, M., B. Al-Qaisieh, L. De Wever, K. Haustermans, C. Kirisits, M. A. Moerland, R. Oyen, A. Rijnders, F. Van den Heuvel and F. A. Siebert (2013). "CT- and MRI-based seed localization in postimplant evaluation after prostate brachytherapy." **Brachytherapy** 12(6): 580-588.

(De Brabandere 2012). De Brabandere, M., P. Hoskin, K. Haustermans, F. Van den Heuvel and F. A. Siebert (2012). "Prostate post-implant dosimetry: interobserver variability in seed localisation, contouring and fusion." **Radiotherapy and Oncology** 104(2): 192-198.

(De Brabandere 2006). De Brabandere, M., C. Kirisits, R. Peeters, K. Haustermans and F. Van den Heuvel (2006). "Accuracy of seed reconstruction in prostate postplanning studied with a CT- and MRI-compatible phantom." **Radiotherapy and Oncology** 79(2): 190-197.

(de Rooij 2014). de Rooij, M., E. H. Hamoen, J. J. Futterer, J. O. Barentsz and M. M. Rovers (2014). "Accuracy of multiparametric MRI for prostate cancer detection: a meta-analysis." **American Journal of Roentgenology** 202(2): 343-351.

(de Rooij 2016). de Rooij, M., E. H. Hamoen, J. A. Witjes, J. O. Barentsz and M. M. Rovers (2016). "Accuracy of Magnetic Resonance Imaging for Local Staging of Prostate Cancer: A Diagnostic Meta-analysis." **European Urology** 70(2): 233-245.

(Dobbins 1990). Dobbins, J. T., 3rd (1990). Matrix inversion tomosynthesis improvements in longitudinal X-ray slice imaging. USPTO. USA. 4,903,204.

(Dobbins 2009a). Dobbins, J. T., 3rd (2009a). "Tomosynthesis imaging: at a translational crossroads." **Medical Physics** 36(6): 1956-1967.

(Dobbins 1995). Dobbins, J. T., 3rd, D. L. Ergun, L. Rutz, D. A. Hinshaw, H. Blume and D. C. Clark (1995). "DQE(f) of four generations of computed radiography acquisition devices." **Medical Physics** 22(10): 1581-1593.

(Dobbins 2003). Dobbins, J. T., 3rd and D. J. Godfrey (2003). "Digital x-ray tomosynthesis: current state of the art and clinical potential." **Physics in Medicine & Biology** 48(19): R65-106.

(Dobbins 2009b). Dobbins, J. T., 3rd and H. P. McAdams (2009b). "Chest tomosynthesis: technical principles and clinical update." **European Journal of Radiology** 72(2): 244-251.

(Dulaney 2016). Dulaney, C. R., D. O. Osula, E. S. Yang and S. Rais-Bahrami (2016). "Prostate Radiotherapy in the Era of Advanced Imaging and Precision Medicine." **Prostate Cancer** 2016: 1-10.

(Eifler 2016). Eifler, J. B. and J. A. Smith Jr (2016). "Management of PSA Recurrences After Radical Prostatectomy". <u>Prostate Cancer: Science and Clinical Practice</u>. J. H. Mydlo and C. J. Godec. London, Elsevier/AP: 451-458.

(Ellis 2002). Ellis, W. J. (2002). "Prostate brachytherapy". <u>Prostate Cancer: New Horizons in Research and Treatment</u>. M. L. Cher, A. Raz and K. V. Honn. Dordrecht, Kluwer Academic Publishers: 345-349.

(Erhard 2012). Erhard, K., M. Grass, S. Hitziger, A. Iske and T. Nielsen (2012). "Generalized Filtered Backprojection for Digital Breast Tomosynthesis Reconstruction". *Medical Imaging 2012: Physics of Medical Imaging*, San Diego, SPIE.

(Errico 2015). Errico, C., J. Pierre, S. Pezet, Y. Desailly, Z. Lenkei, O. Couture and M. Tanter (2015). "Ultrafast ultrasound localization microscopy for deep super-resolution vascular imaging." **Nature** 527(7579): 499-502.

(Farman 2005a). Farman, A. G. and T. T. Farman (2005a). "A comparison of 18 different x-ray detectors currently used in dentistry." **Oral Surgery, Oral Medicine, Oral Pathology, Oral Radiology** 99(4): 485-489.

(Farman 2005b). Farman, T. T., R. H. Vandre, J. C. Pajak, S. R. Miller, A. Lempicki and A. G. Farman (2005b). "Effects of scintillator on the modulation transfer function (MTF) of a digital imaging system." **Oral Surgery, Oral Medicine, Oral Pathology, Oral Radiology** 99(5): 608-613.

(Ferrara 2007). Ferrara, K., R. Pollard and M. Borden (2007). "Ultrasound microbubble contrast agents: fundamentals and application to gene and drug delivery." **Annual Review of Biomedical Engineering** 9: 415-547.

(Finley 2009). Finley, D. S., V. S. Calvert, J. Inokuchi, A. Lau, N. Narula, E. F. Petricoin, F. Zaldivar, R. Santos, D. R. Tyson and D. K. Ornstein (2009). "Periprostatic adipose tissue as a modulator of prostate cancer aggressiveness." **Journal of Urology** 182(4): 1621-1627.

(Folkman 1990). Folkman, J. (1990). "What Is the Evidence That Tumors Are Angiogenesis Dependent." **Journal of the National Cancer Institute** 82(1): 4-6.

(Freedland 2007). Freedland, S. J., E. B. Humphreys, L. A. Mangold, M. Eisenberger, F. J. Dorey, P. C. Walsh and A. W. Partin (2007). "Death in patients with recurrent prostate cancer after radical prostatectomy: Prostate-specific antigen doubling time subgroups and their associated contributions to all-cause mortality." **Journal of Clinical Oncology** 25(13): 1765-1771.

(Futterer 2015). Futterer, J. J., A. Briganti, P. De Visschere, M. Emberton, G. Giannarini, A. Kirkham, S. S. Taneja, H. Thoeny, G. Villeirs and A. Villers (2015). "Can Clinically Significant Prostate Cancer Be Detected with Multiparametric Magnetic Resonance Imaging? A Systematic Review of the Literature." **European Urology** 68(6): 1045-1053.

(Futterer 2006). Futterer, J. J., S. W. T. P. J. Heijmink, T. W. J. Scheenen, J. Veltman, H. J. Huisman, P. Vos, C. A. Hulsbergen-Van De Kaa, J. A. Witjes, P. F. M. Krabbe, A. Heerschap and J. O. Barentsz (2006). "Prostate cancer localization with dynamic contrast-enhanced MR imaging and proton MR spectroscopic imaging." **Radiology** 241(2): 449-458.

(Garrison 1969). Garrison, J. B., D. G. Grant, W. H. Guier and R. J. Johns (1969). "Three dimensional roentgenography." **The American Journal of Roentgenology, Radium Therapy, and Nuclear Medicine** 105(4): 903-908.

(Gennaro 2016). Gennaro, G. (2016). "Physics and Radiation Dose of Digital Breast Tomosynthesis". <u>Digital Breast Tomosynthesis: A Practical Approach</u>. A. Tagliafico, N. Houssami and M. Calabrese, Springer: 1-10.

(Gleason 1966). Gleason, D. F. (1966). "Classification of prostatic carcinomas." **Cancer Chemotherapy Reports** 50(3): 125-128.

(Gleason 1974). Gleason, D. F. and G. T. Mellinger (1974). "Prediction of prognosis for prostatic adenocarcinoma by combined histological grading and clinical staging." **Journal of Urology** 111(1): 58-64.

(Godfrey 2009). Godfrey, D. J., H. P. McAdams and J. T. Dobbins (2009). "Stochastic noise characteristics in matrix inversion tomosynthesis (MITS)." **Medical Physics** 36(5): 1521-1532.

(Godfrey 2006a). Godfrey, D. J., H. P. McAdams and J. T. Dobbins, 3rd (2006a). "Optimization of the matrix inversion tomosynthesis (MITS) impulse response and modulation transfer function characteristics for chest imaging." **Medical Physics** 33(3): 655-667.

(Godfrey 2006b). Godfrey, D. J., F. F. Yin, M. Oldham, S. Yoo and C. Willett (2006b). "Digital tomosynthesis with an on-board kilovoltage imaging device." **International Journal of Radiation Oncology Biology Physics** 65(1): 8-15.

(Gomella 2016). Gomella, L. G. and C. Kundavaram (2016). "Radical Retropubic Prostatectomy". <u>Prostate Cancer: Science and Clinical Practice</u>. J. H. Mydlo and C. J. Godec. London, Elsevier/AP: 265-273.

(Goodsitt 2014). Goodsitt, M. M. (2014). "The history of tomosynthesis". <u>Tomosynthesis Imaging</u>. I. Reiser and S. J. Glick. London, CRC Press: 3-18.

(Grant 1972). Grant, D. G. (1972). "Tomosynthesis: a three-dimensional radiographic imaging technique." **IEEE Transactions on Biomedical Engineering** 19(1): 20-28.

(Groh 1977). Groh, G. (1977). "Tomosynthesis and Coded Aperture Imaging - New Approaches to 3-Dimensional Imaging in Diagnostic Radiography." **Proceedings of the Royal Society Series B-Biological Sciences** 195(1119): 299-306.

(Haerer 2002). Haerer, W., G. Lauritsch and M. Zellerho (2002). Method for Reconstructing a Three-Dimensional Image of an Object Scanned in the Context of Tomosynthesis, and an Apparatus for Tomosynthesis. U. S. P. Office. United States. US 6,442,288 B1.

(Haider 2008). Haider, M. A., P. Chung, J. Sweet, A. Toi, K. Jhaveri, C. Menard, P. Warde, J. Trachtenberg, G. Lockwood and M. Milosevic (2008). "Dynamic contrast-enhanced magnetic resonance imaging for localization of recurrent prostate cancer after external beam radiotherapy." **International Journal of Radiation Oncology Biology Physics** 70(2): 425-430.

(Hall 2006). Hall, E. J. and A. J. Giaccia (2006). <u>Radiobiology for the radiologist</u>. Philadelphia, Lippincott Williams & Wilkins.

(Halpern 2006). Halpern, E. J. (2006). "Contrast-enhanced ultrasound imaging of prostate cancer." **Reviews in Urology** 8 Suppl 1: S29-37.

(Han 2003a). Han, B. H., K. Wallner, G. Merrick, K. Badiozamani and W. Butler (2003a). "The effect of interobserver differences in post-implant prostate CT image interpretation on dosimetric parameters." **Medical Physics** 30(6): 1096-1102.

(Han 2003b). Han, B. H., K. Wallner, G. Merrick, W. Butler, S. Sutlief and J. Sylvester (2003b). "Prostate brachytherapy seed identification on post-implant TRUS images." **Medical Physics** 30(5): 898-900.

(Hara 2005). Hara, N., M. Okuizumi, H. Koike, M. Kawaguchi and V. Bilim (2005). "Dynamic contrast-enhanced magnetic resonance imaging (DCE-MRI) is a useful modality for the precise detection and staging of early prostate cancer." **The Prostate** 62(2): 140-147.

(Harvey 2012). Harvey, C. J., J. Pilcher, J. Richenberg, U. Patel and F. Frauscher (2012). "Applications of transrectal ultrasound in prostate cancer." **British Journal of Radiology** 85 Spec No 1: 3-17.

(Hattori 2013). Hattori, K., Y. Ikemoto, W. Takao, S. Ohno, T. Harimoto, S. Kanazawa, M. Oita, K. Shibuya, M. Kuroda and H. Kato (2013). "Development of MRI phantom equivalent to human tissues for 3.0-T MRI." **Medical Physics** 40(3): 032303.032301-032303.032311.

(Heijmink 2011). Heijmink, S. W., J. J. Futterer, S. S. Strum, W. J. Oyen, F. Frauscher, J. A. Witjes and J. O. Barentsz (2011). "State-of-the-art uroradiologic imaging in the diagnosis of prostate cancer." **Acta Oncologica** 50 Suppl 1: 25-38.

(Hong 2005). Hong, S., H. Jung, K. D. Kim, S. G. So, J. H. Kim, S. K. Yoo, H. S. Yoo and H. J. Kim (2005). "Development and evaluation of a CMOS sensor-based digital intra-oral radiographic system." **IEEE Transactions on Nuclear Science** 52(1): 256-261.

(Horvath 2016). Horvath, A., P. Wolf, J. Nagy, A. Kelemen, G. Horvath, D. Hadhazi, A. Horvath, B. Czetenyi, Z. Sutto and K. Szondy (2016). "Overview of a Digital Tomosynthesis Development: New Approaches for Low-Dose Chest Imaging." **Radiation Protection Dosimetry** 169(1-4): 171-176.

(Howlader 2016). Howlader, N., A. M. Noone, M. Krapcho, D. Miller, K. Bishop, S. F. Altekruse, C. L. Kosary, M. Yu, J. Ruhl, Z. Tatalovich, A. Mariotto, D. R. Lewis, H. S. Chen, E. J. Feuer and K. A. Cronin (2016). SEER Cancer Statistics Review, 1975-2013, National Cancer Institute, Section: Prostate. Bethesda, MD.

(Hsieh 2009). Hsieh, J. (2009). Computed tomography: principles, design, artifacts, and recent advances. Hoboken, N.J., Wiley Interscience; SPIE Press.

(Hu 2008). Hu, Y.-H., W. Zhao, T. Mertelmeier and J. Ludwig (2008). Image Artifact in Digital Breast Tomosynthesis and Its Dependence on System and Reconstruction Parameters. Digital Mammography, 9th International Workshop. E. A. Krupinski. 2008.

(Humphrey 2004). Humphrey, P. A. (2004). "Gleason grading and prognostic factors in carcinoma of the prostate." **Modern Pathology** 17(3): 292-306.

(IEC 2003). IEC (2003). Medical electrical equipment – Characteristics of digital X-ray imaging devices. International Standard 62220-1. Geneva, Switzerland: 36.

(Illers 2005). Illers, H., E. Buhr, S. Gunther-Kohfahl and U. Neitzel (2005). "Measurement of the modulation transfer function of digital X-ray detectors with an opaque edge-test device." **Radiation Protection Dosimetry** 114(1-3): 214-219.

(Irsigler 1999). Irsigler, R., J. Andersson, J. Alverbro, J. Borglind, C. Frojdh, P. Helander, S. Manolopoulos, H. Martijn, V. O'Shea and K. Smith (1999). "X-ray imaging using a 320 x 240 hybrid GaAs pixel detector." **IEEE Transactions on Nuclear Science** 46(3): 507-512.

(Ives 2005). Ives, E. P., M. A. Burke, P. R. Edmonds, L. G. Gomella and E. J. Halpern (2005). "Quantitative computed tomography perfusion of prostate cancer: correlation with whole-mount pathology." **Clinical Prostate Cancer** 4(2): 109-112.

(Jain 2005). Jain, A. K., T. Mustafa, Y. Zhou, C. Burdette, G. S. Chirikjian and G. Fichtinger (2005). "FTRAC--a robust fluoroscope tracking fiducial." **Medical Physics** 32(10): 3185-3198.

(Jung 2012). Jung, A. J. and A. C. Westphalen (2012). "Imaging prostate cancer." **Radiologic Clinics of North America** 50(6): 1043-1059.

(Kayugawa 2013). Kayugawa, A., M. Ohkubo and S. Wada (2013). "Accurate determination of CT point-spread-function with high precision." **Journal of Applied Clinical Medical Physics** 14(4): 216-226.

(Kelloff 2009). Kelloff, G. J., P. Choyke and D. S. Coffey (2009). "Challenges in clinical prostate cancer: role of imaging." **American Journal of Roentgenology** 192(6): 1455-1470.

(Khan 2014). Khan, F. M. and J. P. Gibbons (2014). The physics of radiation therapy. Philadelphia, PA, Lippincott Williams & Wilkins/Wolters Kluwer.

(Kim 2004). Kim, J.-H., S.-G. So and K.-S. Joo (2004). "Development and Performances of a Dental Digital Radiographic System Using a High Resolution CCD Image Sensor". *Nuclear Science Symposium Conference Record*.

(Kitajima 2013). Kitajima, K., R. C. Murphy and M. A. Nathan (2013). "Choline PET/CT for imaging prostate cancer: an update." **Annals of Nuclear Medicine** 27(7): 581-591.

(Klotz 1976). Klotz, E. and H. Weiss (1976). "X-ray 3-D coded aperture imaging: displaying the heart." **Applied Optics** 15(8): 1913-1918.

(Klotz 2005). Klotz, L. (2005). "Active surveillance for prostate cancer: for whom?" **Journal of Clinical Oncology** 23(32): 8165-8169.

(Knoll 2010). Knoll, G. F. (2010). Radiation detection and measurement. Hoboken, N.J., John Wiley.

(Koprulu 2012). Koprulu, S., I. Cevik, N. Unlu and O. Dillioglugil (2012). "Size of the transrectal ultrasound probe makes no difference in pain perception during TRUS-Bx under adequate local anesthesia." **International Urology and Nephrology** 44(1): 29-33.

(Krause 2013). Krause, B. J., M. Souvatzoglou and U. Treiber (2013). "Imaging of prostate cancer with PET/CT and radioactively labeled choline derivates." **Urologic Oncology** 31(4): 427-435.

(Kunogi 2015). Kunogi, H., H. Hojo, Y. Wakumoto, A. I. Saito, S. Ishikura, Y. Yamashiro, R. Kuwatsuru and K. Sasai (2015). "A new two-step accurate CT-MRI fusion technique for post-implant prostate cancer." **Journal of Contemporary Brachytherapy** 7(2): 117-121.

(Kuo 2014). Kuo, N., E. Dehghan, A. Deguet, O. Y. Mian, Y. Le, E. C. Burdette, G. Fichtinger, J. L. Prince, D. Y. Song and J. Lee (2014). "An image-guidance system for dynamic dose calculation in prostate brachytherapy using ultrasound and fluoroscopy." **Medical Physics** 41(9): 09172.09171-091712.091713.

(Kuriyama 1981). Kuriyama, M., M. C. Wang, C. I. Lee, L. D. Papsidero, C. S. Killian, H. Inaji, N. H. Slack, T. Nishiura, G. P. Murphy and T. M. Chu (1981). "Use of human prostate-specific antigen in monitoring prostate cancer." **Cancer Research** 41(10): 3874-3876.

(Kuriyama 1980). Kuriyama, M., M. C. Wang, L. D. Papsidero, C. S. Killian, T. Shimano, L. Valenzuela, T. Nishiura, G. P. Murphy and T. M. Chu (1980). "Quantitation of prostate-specific antigen in serum by a sensitive enzyme immunoassay." **Cancer Research** 40(12): 4658-4662.

(Lamberto 2014). Lamberto, M. (2014). A feasability study of ultra-short echo time MRI for positive contrast visualization of prostate brachytherapy permanat seed implants for post implant dosimetry. MS Thesis, Louisiana State University and Agricultural and Mechanical College.

(Laurent 2016). Laurent, V., A. Guerard, C. Mazerolles, S. Le Gonidec, A. Toulet, L. Nieto, F. Zaidi, B. Majed, D. Garandeau, Y. Socrier, M. Golzio, T. Cadoudal, K. Chaoui, C. Dray, B. Monsarrat, O. Schiltz, Y. Y. Wang, B. Couderc, P. Valet, B. Malavaud and C. Muller (2016). "Periprostatic adipocytes act as a driving force for prostate cancer progression in obesity." **Nature Communications** 7: 1-15.

(Lauritsch 1998). Lauritsch, G. and W. H. Haerer (1998). A theoretical framework for filtered backprojection in tomosynthesis. Medical Imaging 1998: Image Processing. San Diego, CA.

(Lee 2011). Lee, J., N. Kuo, A. Deguet, E. Dehghan, D. Y. Song, E. C. Burdette and J. L. Prince (2011). "Intraoperative 3D reconstruction of prostate brachytherapy implants with automatic pose correction." **Physics in Medicine & Biology** 56(15): 5011-5027.

(Lee 2017). Lee, J., O. Y. Mian, Y. Le, H. J. Bae, E. C. Burdette, T. L. DeWeese, J. L. Prince and D. Y. Song (2017). "Intraoperative Registered Ultrasound and Fluoroscopy (iRUF) for dose calculation during prostate brachytherapy: Improved accuracy compared to standard ultrasound-based dosimetry." **Radiotherapy and Oncology** 124(1): 61-67.

(Levakhina 2013). Levakhina, Y. (2013). Three-Dimensional Digital Tomosynthesis. PhD Dissertation, Springer Vieweg.

(Li 2007). Li, B., G. Avinash, B. Claus and S. Mertz (2007). "3-D view weighted cone-beam filtered backprojection reconstruction for digital tomosynthesis". *Proc. of SPIE: Medical Imaging 2007 Physics of Medical Imaging*, Bellingham, WA, SPIE.

(Li 2010). Li, X., Z. Da and B. Liu (2010). "A generic geometric calibration method for tomographic imaging systems with flat-panel detectors--a detailed implementation guide." **Medical Physics** 37(7): 3844-3854.

(Lim 2016). Lim, T. Y., R. J. Kudchadker, J. Wang, T. Bathala, J. Szklaruk, T. J. Pugh, U. Mahmood, G. S. Ibbott and S. J. Frank (2016). "Development of a magnetic resonance imaging protocol to visualize encapsulated contrast agent markers in prostate brachytherapy recipients: initial patient experience." **Journal of Contemporary Brachytherapy** 8(3): 235-242.

(Littleton 1996). Littleton, J. T. and M. Littleton (1996). "Conventional Tomography". A History of the Radiological Sciences. R. Gagliardi and B. L. McClennan, Radiology Centennial, Inc.: 369-401.

(Loo 2014). Loo, K. J., J. Jakubek, J. Zemlicka, M. Petasecca, M. Safavi-Naeini, J. Bucci, M. Zaider and A. B. Rosenfeld (2014). "BrachyView: Feasibility study into the application of Timepix detectors for soft tissue thickness imaging in prostate brachytherapy treatment." **Radiation Measurements** 71: 329-332.

(Luczynska 2014). Luczynska, E., P. Blecharz, S. Dyczek, A. Stelmach, G. Petralia, M. Bellomi, B. A. Jereczek–Fossa and J. Jakubowicz (2014). "Perfusion CT is a valuable diagnostic method for prostate cancer: a prospective study of 94 patients." **ecancer** 8(476): 1-12.

(Mainprize 2011). Mainprize, J. G., A. Bloomquist, X. Wang and M. J. Yaffe (2011). "Dependence of image quality on geometric factors in breast tomosynthesis." **Medical Physics** 38(6): 3090-3103.

(Mainprize 2006). Mainprize, J. G., A. K. Bloomquist, M. P. Kempston and M. J. Yaffe (2006). "Resolution at oblique incidence angles of a flat panel imager for breast tomosynthesis." **Medical Physics** 33(9): 3159-3164.

(Maki 1998). Maki, J. H., T. L. Chenevert and M. R. Prince (1998). "Contrast-enhanced MR angiography." **Abdominal Imaging** 23(5): 469-484.

(Mardis 1993). Mardis, H. K., R. M. Kroeger, J. J. Morton and J. M. Donovan (1993). "Comparative-Evaluation of Materials Used for Internal Ureteral Stents." **Journal of Endourology** 7(2): 105-115.

(McLaughlin 2005). McLaughlin, P. W., V. Narayana, A. Meirovitz, S. Troyer, P. L. Roberson, R. Gonda, Jr., H. Sandler, L. Marsh, T. Lawrence and M. Kessler (2005). "Vessel-sparing prostate radiotherapy: dose limitation to critical erectile vascular structures (internal pudendal artery and corpus cavernosum) defined by MRI." **International Journal of Radiation Oncology Biology Physics** 61(1): 20-31.

(McNeal 1969). McNeal, J. E. (1969). "Origin and development of carcinoma in the prostate." **Cancer** 23(1): 24-34.

(Mcneal 1978). Mcneal, J. E. (1978). "Origin and Evolution of Benign Prostatic Enlargement." **Investigative Urology** 15(4): 340-345.

(McNeal 1981). McNeal, J. E. (1981). "The zonal anatomy of the prostate." **The Prostate** 2(1): 35-49.

(McNeal 1988). McNeal, J. E. (1988). "Normal Histology of the Prostate." **American Journal of Surgical Pathology** 12(8): 619-633.

(Mehrmohammadi 2014). Mehrmohammadi, M., A. Alizad, R. R. Kinnick, B. J. Davis and M. Fatemi (2014). "Feasibility of vibro-acoustography with a quasi-2D ultrasound array transducer for detection and localizing of permanent prostate brachytherapy seeds: a pilot ex vivo study." **Medical Physics** 41(9): 092902.092901-092902.092910.

(Mendhiratta 2016). Mendhiratta, N. and S. S. Taneja (2016). "Focal Therapy for Prostate Cancer". Prostate Cancer: Science and Clinical Practice. J. H. Mydlo and C. J. Godec. London, Elsevier/AP: 563-577.

(Mertelmeier 2014). Mertelmeier, T. (2014). "Filtered backprojection-based methods for tomosynthesis image reconstruction". Tomosynthesis Imaging. I. Reiser and S. Glick. Boca Raton, CRC Press,Taylor & Francis Group: 101-106.

(Mertelmeier 2006). Mertelmeier, T., J. Orman, W. Haerer and M. K. Dudam (2006). "Optimizing filtered backprojection reconstruction for a breast tomosynthesis prototype device". *Medical Imaging 2006: Physics of Medical Imaging*, San Diego, SPIE.

(Miller 1971). Miller, E. R., E. M. McCurry and B. Hruska (1971). "An infinite number of laminagrams from a finite number of radiographs." **Radiology** 98(2): 249-255.

(Miller 1974). Miller, E. R., E. M. Mccurry and B. B. Hruska (1974). "Simplified Procedure for Viewing Multiple Films to Create an Infinite Number of Laminagrams." **Radiology** 110(2): 365-367.

(Mitri 2009). Mitri, F. G., B. J. Davis, M. W. Urban, A. Alizad, J. F. Greenleaf, G. H. Lischer, T. M. Wilson and M. Fatemi (2009). "Vibro-acoustography imaging of permanent prostate brachytherapy seeds in an excised human prostate--preliminary results and technical feasibility." **Ultrasonics** 49(3): 389-394.

(Monn 2016). Monn, M. F., C. K. Flack and M. O. Koch (2016). "High-Intensity Focused Ultrasound". Prostate Cancer: Science and Clinical Practice. J. H. Mydlo and C. J. Godec. London, Elsevier/AP: 551-562.

(Mucci 2009). Mucci, L. A., A. Powolny, E. Giovannucci, Z. Liao, S. A. Kenfield, R. Shen, M. J. Stampfer and S. K. Clinton (2009). "Prospective study of prostate tumor angiogenesis and cancer-specific mortality in the health professionals follow-up study." **Journal of Clinical Oncology** 27(33): 5627-2633.

(Mukdadi 2014). Mukdadi, O., M. Salkini, A. Majewski and J. FProffitt (2014). Endorectal Prostate Probe with Combined PET and US Modalities. USPTO. USA. 2014/0276018 A1.

(Musico 2016). Musico, P. (2016). "The endo-rectal probe prototype for the TOPEM project". *13th Pisa Meeting on Advanced Detectors*, Genova, Italy.

(Natalin 2010). Natalin, R. A., M. R. Prince, M. E. Grossman, D. Silvers and J. Landman (2010). "Contemporary applications and limitations of magnetic resonance imaging contrast materials." **Journal of Urology** 183(1): 27-33.

(Nath 1997). Nath, R., L. L. Anderson, J. A. Meli, A. J. Olch, J. A. Stitt and J. F. Williamson (1997). "AAPM TG56: Code of practice for brachytherapy physics: Report of the AAPM Radiation Therapy Committee Task Group No. 56." **Medical Physics**: 1557-1598.

(Nath 2009). Nath, R., W. S. Bice, W. M. Butler, Z. Chen, A. S. Meigooni, V. Narayana, M. J. Rivard, Y. Yu and M. American Association of Physicists in (2009). "AAPM recommendations on dose prescription and reporting methods for permanent interstitial brachytherapy for prostate cancer: report of Task Group 137." **Medical Physics** 36(11): 5310-5322.

(Neitzel 2004). Neitzel, U., E. Buhr, G. Hilgers and P. R. Granfors (2004). "Determination of the modulation transfer function using the edge method: influence of scattered radiation." **Medical Physics** 31(12): 3485-3491.

(Nett 2007). Nett, B. E., S. Leng and G.-H. Chen (2007). "Planar tomosynthesis reconstruction in a parallel-beam framework via virtual object reconstruction". *Medical Imaging 2007: Physics of Medical Imaging*, San Diego, SPIE.

(Niklason 1997). Niklason, L. T., B. T. Christian, L. E. Niklason, D. B. Kopans, D. E. Castleberry, B. H. Opsahl-Ong, C. E. Landberg, P. J. Slanetz, A. A. Giardino, R. Moore, D. Albagli, M. C. DeJule, P. F. Fitzgerald, D. F. Fobare, B. W. Giambattista, R. F. Kwasnick, J. Liu, S. J. Lubowski, G. E. Possin, J. F. Richotte, C. Y. Wei and R. F. Wirth (1997). "Digital tomosynthesis in breast imaging." **Radiology** 205(2): 399-406.

(Nosratieh 2012). Nosratieh, A., K. Yang, S. Aminololama-Shakeri and J. M. Boone (2012). "Comprehensive assessment of the slice sensitivity profiles in breast tomosynthesis and breast CT." **Medical Physics** 39(12): 7254-7261.

(Orman 2006). Orman, J., T. Mertelmeier and W. Haerer (2006). "Adaptation of image quality using various filter setups in the filtered backprojection approach for digital breast tomosynthesis." **Digital Mamography, Proceedings** 4046: 175-182.

(Osimani 2012). Osimani, M., D. Bellini, C. Di Cristofano, G. Palleschi, V. Petrozza, A. Carbone and A. Laghi (2012). "Perfusion MDCT of prostate cancer: correlation of perfusion CT parameters and immunohistochemical markers of angiogenesis." **American Journal of Roentgenology** 199(5): 1042-1048.

(Padhani 2005). Padhani, A. R., C. J. Harvey and D. O. Cosgrove (2005). "Angiogenesis imaging in the management of prostate cancer." **Nature Clinical Practice. Urology** 2(12): 596-607.

(Parry 1999). Parry, R. A., S. A. Glaze and B. R. Archer (1999). "The AAPM/RSNA physics tutorial for residents. Typical patient radiation doses in diagnostic radiology." **Radiographics** 19(5): 1289-1302.

(Petasecca 2013). Petasecca, M., K. J. Loo, M. Safavi-Naeini, Z. Han, P. E. Metcalfe, S. Meikle, S. Pospisil, J. Jakubek, J. A. Bucci, M. Zaider, M. L. Lerch, Y. Qi and A. B. Rosenfeld (2013). "BrachyView: proof-of-principle of a novel in-body gamma camera for low dose-rate prostate brachytherapy." **Medical Physics** 40(4): 041709.041701-041709.041709.

(Petralia 2010). Petralia, G., L. Preda, G. D'Andrea, S. Viotti, L. Bonello, R. De Filippi and M. Bellomi (2010). "CT perfusion in solid-body tumours. Part I: Technical issues." **La radiologia medica** 115(6): 843-857.

(Porten 2014). Porten, S. P., A. Smith, A. Y. Odisho, M. S. Litwin, C. S. Saigal, P. R. Carroll, M. R. Cooperberg and U. D. A. Project (2014). "Updated trends in imaging use in men diagnosed with prostate cancer." **Prostate Cancer and Prostatic Diseases** 17(3): 246-251.

(Prando 2000). Prando, A. and S. Wallace (2000). "Helical CT of prostate cancer: early clinical experience." **American Journal of Roentgenology** 175(2): 343-346.

(Prince 1994). Prince, M. R. (1994). "Gadolinium-Enhanced Mr Aortography." **Radiology** 191(1): 155-164.

(Qaseem 2013). Qaseem, A., M. J. Barry, T. D. Denberg, D. K. Owens, P. Shekelle and P. Clinical Guidelines Committee of the American College of (2013). "Screening for prostate cancer: a guidance statement from the Clinical Guidelines Committee of the American College of Physicians." **Ann Intern Med** 158(10): 761-769.

(Qian 2013). Qian, X. (2013). "Fundementals of Digital Mammography". Physics of Mammographic Imaging. M. K. Markey, CRC Press: 3-10.

(Quivrin 2015). Quivrin, M., R. Loffroy, L. Cormier, F. Mazoyer, A. Bertaut, D. Chambade, E. Martin, P. Maingon, P. Walker and G. Crehange (2015). "Multiparametric MRI and post implant CT-based dosimetry after prostate brachytherapy with iodine seeds: The higher the dose to the dominant index lesion, the lower the PSA bounce." **Radiotherapy and Oncology** 117(2): 258-261.

(Radon 1917). Radon, J. (1917). Über die Bestimmung von Funktionen durch ihre Integralwerte längs gewisser Mannigfaltigkeiten. Berichte über die Verhandlungen der Königlich-Sächsischen Akademie der Wissenschaften zu Leipzig, Mathematisch-Physische Klasse. Leipzig: 262-277.

(Reese 2016). Reese, A. C. (2016). "Clinical and Pathologic Staging of Prostate Cancer". Prostate Cancer: Science and Clinical Practice. J. H. Mydlo and C. J. Godec. London, Elsevier/AP: 353-360.

(Reiser 2007). Reiser, I., J. Bian, R. M. Nishikawa, E. Y. Sidky and X. Pan (2007). "Comparison of reconstruction algorithms for digital breast tomosynthesis". *9th International Meeting* *on Fully Three-Dimensional Image Reconstruction and HPIR Workshop*, Lindau, Germany.

(Reiser 2014). Reiser, I., B. Lau and R. M. Nishikawa (2014). "Tomosynthesis system modeling". Tomosynthesis Imaging. I. Reiser and S. J. Glick. London, CRC Press: 81-95.

(Ren 2005). Ren, B., C. Ruth, J. Stein, A. Smith, I. Shaw and Z. Jing (2005). "Design and performance of the prototype full field breast tomosynthesis system with selenium based flat panel detector". *Proc. of SPIE: Medical Imaging 2005 Physics of Medical Imaging*, Bellingham, WA.

(Ribeiro 2012). Ribeiro, R., C. Monteiro, V. Cunha, M. J. Oliveira, M. Freitas, A. Fraga, P. Principe, C. Lobato, F. Lobo, A. Morais, V. Silva, J. Sanches-Magalhaes, J. Oliveira, F. Pina, A. Mota-Pinto, C. Lopes and R. Medeiros (2012). "Human periprostatic adipose tissue promotes prostate cancer aggressiveness in vitro." **Journal of Experimental & Clinical Cancer Research** 31(32): 1-11.

(Robertson 2012). Robertson, A. K., P. S. Basran, S. D. Thomas and D. Wells (2012). "CT, MR, and ultrasound image artifacts from prostate brachytherapy seed implants: the impact of seed size." **Medical Physics** 39(4): 2061-2068.

(Roehrborn 2005). Roehrborn, C. G. (2005). "Benign prostatic hyperplasia: an overview." **Reviews in Urology** 7 Suppl 9: S3-S14.

(Rogosnitzky 2016). Rogosnitzky, M. and S. Branch (2016). "Gadolinium-based contrast agent toxicity: a review of known and proposed mechanisms." **Biometals** 29(3): 365-376.

(Roobol 2015). Roobol, M. J. (2015). "Perspective: Enforce the Clinical Guidelines." **Nature** 528(7582 Suppl.): S123.

(Rosenkrantz 2013). Rosenkrantz, A. B., S. Kim, R. P. Lim, N. Hindman, F. M. Deng, J. S. Babb and S. S. Taneja (2013). "Prostate cancer localization using multiparametric MR imaging: comparison of Prostate Imaging Reporting and Data System (PI-RADS) and Likert scales." **Radiology** 269(2): 482-492.

(Rozenfeld 2012). Rozenfeld, A. and J. Jakubek (2012). Imaging Method and System. USPTO. USA, University of Wollongong. US 2012/0230574 Al.

(Safavi-Naeini 2015). Safavi-Naeini, M., Z. Han, S. Alnaghy, D. Cutajar, M. Petasecca, M. L. Lerch, D. R. Franklin, J. Bucci, M. Carrara, M. Zaider and A. B. Rosenfeld (2015). "BrachyView, a novel in-body imaging system for HDR prostate brachytherapy: Experimental evaluation." **Medical Physics** 42(12): 7098-7107.

(Safavi-Naeini 2013). Safavi-Naeini, M., Z. Han, D. Cutajar, S. Guatelli, M. Petasecca, M. L. Lerch, D. R. Franklin, J. Jakubek, S. Pospisil, J. Bucci, M. Zaider and A. B. Rosenfeld (2013). "BrachyView, a novel inbody imaging system for HDR prostate brachytherapy:

design and Monte Carlo feasibility study." **Medical Physics** 40(7): 071715.071711-071715.071711.

(Samei 1998). Samei, E., M. J. Flynn and D. A. Reimann (1998). "A method for measuring the presampled MTF of digital radiographic systems using an edge test device." **Medical Physics** 25(1): 102-113.

(Sankineni 2016). Sankineni, S., P. L. Choyke, P. Pinto and B. Turkbey (2016). "Imaging in Localized Prostate Cancer". <u>Prostate Cancer: Science and Clinical Practice</u>. J. H. Mydlo and C. J. Godec. London, Elsevier/AP: 91-99.

(Sano 2011). Sano, F., H. Terao, T. Kawahara, Y. Miyoshi, T. Sasaki, K. Noguchi, Y. Kubota and H. Uemura (2011). "Contrast-enhanced ultrasonography of the prostate: various imaging findings that indicate prostate cancer." **BJU International** 107(9): 1404-1410.

(Saunders 2003). Saunders, R. S., Jr. and E. Samei (2003). "A method for modifying the image quality parameters of digital radiographic images." **Medical Physics** 30(11): 3006-3017.

(Saunders 2005). Saunders, R. S., Jr., E. Samei, J. L. Jesneck and J. Y. Lo (2005). "Physical characterization of a prototype selenium-based full field digital mammography detector." **Medical Physics** 32(2): 588-599.

(Scarpato 2016). Scarpato, K. R. and P. C. Albertsen (2016). "Prostate-Specific Antigen Screening Guidelines". <u>Prostate Cancer: Science and Clinical Practice</u>. J. H. Mydlo and C. J. Godec. London, Elsevier/AP: 111-116.

(Schieda 2015). Schieda, N., L. Avruch, W. M. Shabana and S. C. Malone (2015). "Multi-echo gradient recalled echo imaging of the pelvis for improved depiction of brachytherapy seeds and fiducial markers facilitating radiotherapy planning and treatment of prostatic carcinoma." **Journal of Magnetic Resonance Imaging** 41(3): 715-720.

(Sechopoulos 2013a). Sechopoulos, I. (2013a). "A review of breast tomosynthesis. Part I. The image acquisition process." **Medical Physics** 40(1): 014301.014301-014301.014312.

(Sechopoulos 2013b). Sechopoulos, I. (2013b). "A review of breast tomosynthesis. Part II. Image reconstruction, processing and analysis, and advanced applications." **Medical Physics** 40(1): 014302.014301-014302.014316.

(Sharma 2014). Sharma, S. (2014). "Imaging and intervention in prostate cancer: Current perspectives and future trends." **Indian Journal of Radiology and Imaging** 24(2): 139-148.

(Siddon 1985). Siddon, R. L. (1985). "Fast calculation of the exact radiological path for a three-dimensional CT array." **Medical Physics** 12(2): 252-255.

(Siebert 2007). Siebert, F. A., M. De Brabandere, C. Kirisits, G. Kovacs and J. Venselaar (2007). "Phantom investigations on CT seed imaging for interstitial brachytherapy." **Radiotherapy and Oncology** 85(2): 316-323.

(Siebert 2006). Siebert, F. A., P. Kohr and G. Kovacs (2006). "Comparison of CT- and radiograph-based post-implant dosimetry for transperineal 125I prostate brachytherapy using single seeds and a commercial treatment-planning software." **Strahlentherapie und Onkologie** 182(2): 96-101.

(Siegal 1995). Siegal, J. A. and M. K. Brawer (1995). "Topography of Neovascularity in Human Prostate Carcinoma." **Cancer** 75(10): 2545-2551.

(Siegel 2017). Siegel, R. L., K. D. Miller and A. Jemal (2017). "Cancer Statistics, 2017." **CA: A Cancer Journal for Clinicians** 67(1): 7-30.

(Silberman 1997). Silberman, M. A., A. W. Partin, R. W. Veltri and J. I. Epstein (1997). "Tumor angiogenesis correlates with progression after radical prostatectomy but not with pathologic stage in Gleason sum 5 to 7 adenocarcinoma of the prostate." **Cancer** 79(4): 772-779.

(Smith-Bindman 2009). Smith-Bindman, R., J. Lipson, R. Marcus, K. P. Kim, M. Mahesh, R. Gould, A. Berrington de Gonzalez and D. L. Miglioretti (2009). "Radiation dose associated with common computed tomography examinations and the associated lifetime attributable risk of cancer." **Archives of Internal Medicine** 169(22): 2078-2086.

(Sobel 1968). Sobel, I. and G. Feldman (1968). A 3x3 Isotropic Gradient Operator for Image Processing. Stanford Artificial Intelligence Project.

(Sone 1991). Sone, S., T. Kasuga, F. Sakai, J. Aoki, I. Izuno, Y. Tanizaki, H. Shigeta and K. Shibata (1991). "Development of a high-resolution digital tomosynthesis system and its clinical application." **Radiographics** 11(5): 807-822.

(Sone 1993). Sone, S., T. Kasuga, F. Sakai, H. Hirano, K. Kubo, M. Morimoto, K. Takemura and M. Hosoba (1993). "Chest imaging with dual-energy subtraction digital tomosynthesis." **Acta Radiologica** 34(4): 346-350.

(Starkey 2005). Starkey, M. P., T. J. Scase, C. S. Mellersh and S. Murphy (2005). "Dogs really are man's best friend--canine genomics has applications in veterinary and human medicine!" **Briefings in Functional Genomics** 4(2): 112-128.

(Stevens 2001). Stevens, G. M., R. Fahrig and N. J. Pelc (2001). "Filtered backprojection for modifying the impulse response of circular tomosynthesis." **Medical Physics** 28(3): 372-380.

(Strazdina 2011). Strazdina, A., G. Krumina and M. Sperga (2011). "The Value and Limitations of Contrast-enhanced Ultrasound in Detection of Prostate Cancer." **Anticancer Research** 31(4): 1421-1426.

(Su 2004). Su, Y., B. J. Davis, M. G. Herman and R. A. Robb (2004). "Prostate brachytherapy seed localization by analysis of multiple projections: identifying and addressing the seed overlap problem." **Medical Physics** 31(5): 1277-1287.

(Sumitomo 2010). Sumitomo, M., J. Asakuma, H. Yoshii, A. Sato, A. Horiguchi, K. Ito, K. Nagakura and T. Asano (2010). "Anterior perirectal fat tissue thickness is a strong predictor of recurrence after high-intensity focused ultrasound for prostate cancer." **International Journal of Urology** 17(9): 776-782.

(Sutcliffe 2015). Sutcliffe, S. and M. A. Pontari (2015). "Inflammation and Infection in the Etiology of Prostate Cancer". Prostate Cancer: Science and Clinical Practice. J. H. Mydlo and C. J. Godec. London, Elsevier/AP: 13-20.

(Szczykutowicz 2016). Szczykutowicz, T. P., Z. E. Labby, N. Rubert and C. Wallace (2016). "Technical Note: Confirming the prescribed angle of CT localizer radiographs and c-arm projection acquisitions." **Medical Physics** 43(2): 865-869.

(Tan 2015). Tan, C. H., B. P. Hobbs, W. Wei and V. Kundra (2015). "Dynamic contrast-enhanced MRI for the detection of prostate cancer: meta-analysis." **American Journal of Roentgenology** 204(4): 439-448.

(Tang 2016). Tang, V., D. G. Murphy and D. Moon (2016). "Management of Locally Advanced (Nonmetastatic) Prostate Cancer". Prostate Cancer: Science and Clinical Practice. J. H. Mydlo and C. J. Godec. London, Elsevier/AP: 467-477.

(Thomas 2009). Thomas, S. D., K. Wachowicz and B. G. Fallone (2009). "MRI of prostate brachytherapy seeds at high field: A study in phantom." **Medical Physics** 36(11): 5228-5234.

(Thompson 2014). Thompson, J. E., D. Moses, R. Shnier, P. Brenner, W. Delprado, L. Ponsky, M. Pulbrook, M. Bohm, A. M. Haynes, A. Hayen and P. D. Stricker (2014). "Multiparametric magnetic resonance imaging guided diagnostic biopsy detects significant prostate cancer and could reduce unnecessary biopsies and over detection: a prospective study." **Journal of Urology** 192(1): 67-74.

(Tortora 2014). Tortora, G. J. and M. T. Nielsen (2014). Principles of human anatomy. Hoboken, NJ, Wiley.

(Tretiakova 2013). Tretiakova, M., T. Antic, D. Binder, M. Kocherginsky, C. Liao, J. B. Taxy and A. Oto (2013). "Microvessel density is not increased in prostate cancer: digital imaging of routine sections and tissue microarrays." **Human Pathology** 44(4): 495-502.

(Tutar 2003). Tutar, I. B., R. Managuli, V. Shamdasani, P. S. Cho, S. D. Pathak and Y. Kim (2003). "Tomosynthesis-based localization of radioactive seeds in prostate brachytherapy." **Medical Physics** 30(12): 3135-3142.

(Udeh 1982). Udeh, F. N. (1982). "Structure and architecture of the prostatic capsule." **International Urology and Nephrology** 14(1): 35-43.

(van Roermund 2010). van Roermund, J. G., G. H. Bol, J. A. Witjes, J. L. Ruud Bosch, L. A. Kiemeney and M. van Vulpen (2010). "Periprostatic fat measured on computed tomography as a marker for prostate cancer aggressiveness." **World Journal of Urology** 28(6): 699-704.

(van Roermund 2011). van Roermund, J. G., K. A. Hinnen, C. J. Tolman, G. H. Bol, J. A. Witjes, J. L. Bosch, L. A. Kiemeney and M. van Vulpen (2011). "Periprostatic fat correlates with tumour aggressiveness in prostate cancer patients." **BJU International** 107(11): 1775-1779.

(Venkatasubramanian 2014). Venkatasubramanian, P. N., C. B. Brendler, B. A. Plunkett, S. E. Crawford, P. S. Fitchev, G. Morgan, M. L. Cornwell, M. S. McGuire, A. M. Wyrwicz and J. A. Doll (2014). "Periprostatic adipose tissue from obese prostate cancer patients promotes tumor and endothelial cell proliferation: a functional and MR imaging pilot study." **The Prostate** 74(3): 326-335.

(Wang 2015). Wang, Y., N. J. Nasser, J. Borg and E. P. Saibishkumar (2015). "Evaluation of the dosimetric impact of loss and displacement of seeds in prostate low-dose-rate brachytherapy." **Journal of Contemporary Brachytherapy** 7(3): 203-210.

(Weidner 1993). Weidner, N., P. R. Carroll, J. Flax, W. Blumenfeld and J. Folkman (1993). "Tumor Angiogenesis Correlates with Metastasis in Invasive Prostate Carcinoma." **American Journal of Pathology** 143(2): 401-409.

(Weinreb 2015). Weinreb, J. C., J. O. Barentsz, P. L. Choyke, F. Cornud, M. A. Haider, K. J. Macura, D. Margolis, M. D. Schnall, F. Shtern, C. M. Tempany, H. C. Thoeny and S. Verma (2015). "PI-RADS Prostate Imaging - Reporting and Data System: 2015, Version 2." **European Urology** 69(1): 16-40.

(Welander 1994). Welander, U., W. D. Mcdavid, G. C. H. Sanderink, G. Tronje, A. C. Morner and B. Dove (1994). "Resolution as Defined by Line Spread and Modulation Transfer-Functions for 4 Digital Intraoral Radiographic Systems." **Oral Surgery, Oral Medicine, Oral Pathology, Oral Radiology** 78(1): 109-115.

(Wells 2006). Wells, P. N. (2006). "Ultrasound imaging." **Physics in Medicine & Biology** 51(13): R83-98.

(West 2001). West, A. F., M. O'Donnell, R. G. Charlton, D. E. Neal and H. Y. Leung (2001). "Correlation of vascular endothelial growth factor expression with fibroblast growth factor-8 expression and clinico-pathologic parameters in human prostate cancer." **British Journal of Cancer** 85(4): 576-583.

(Woo 2015). Woo, S., J. Y. Cho, S. Y. Kim and S. H. Kim (2015). "Periprostatic fat thickness on MRI: correlation with Gleason score in prostate cancer." **American Journal of Roentgenology** 204(1): 43-47.

(Wu 2016). Wu, G., T. Jin, T. Li, J. Morelli and X. M. Li (2016). "High spatial resolution time-resolved magnetic resonance angiography of lower extremity tumors at 3T: Comparison with computed tomography angiography." **Medicine** 95(37).

(Wu 2004). Wu, T., R. H. Moore, E. A. Rafferty and D. B. Kopans (2004). "A comparison of reconstruction algorithms for breast tomosynthesis." **Medical Physics** 31(9): 2636-2647.

(Wu 2003). Wu, T., A. Stewart, M. Stanton, T. McCauley, W. Phillips, D. B. Kopans, R. H. Moore, J. W. Eberhard, B. Opsahl-Ong, L. Niklason and M. B. Williams (2003). "Tomographic mammography using a limited number of low-dose cone-beam projection images." **Medical Physics** 30(3): 365-380.

(Yakar 2010). Yakar, D., T. Hambrock, H. Huisman, C. A. Hulsbergen-van de Kaa, E. van Lin, H. Vergunst, C. M. Hoeks, I. M. van Oort, J. A. Witjes, J. O. Barentsz and J. J. Futterer (2010). "Feasibility of 3T dynamic contrast-enhanced magnetic resonance-guided biopsy in localizing local recurrence of prostate cancer after external beam radiation therapy." **Investigative Radiology** 45(3): 121-125.

(Yoo 2009). Yoo, S., Q. J. Wu, D. Godfrey, H. Yan, L. Ren, S. Das, W. R. Lee and F. F. Yin (2009). "Clinical evaluation of positioning verification using digital tomosynthesis and bony anatomy and soft tissues for prostate image-guided radiotherapy." **International Journal of Radiation Oncology Biology Physics** 73(1): 296-305.

(Yu 1999). Yu, Y., L. L. Anderson, Z. Li, D. E. Mellenberg, R. Nath, M. C. Schell, F. M. Waterman, A. Wu and J. C. Blasko (1999). "Permanent prostate seed implant brachytherapy: report of the American Association of Physicists in Medicine Task Group No. 64." **Medical Physics** 26(10): 2054-2076.

(Yunker 2013). Yunker, B. E., D. Cordes, A. L. Scherzinger, G. D. Dodd, R. Shandas, Y. S. Feng and K. S. Hunter (2013). "An investigation of industrial molding compounds for use in 3D ultrasound, MRI, and CT imaging phantoms." **Medical Physics** 40(5): 052905.052901-052905.052908.

(Zaorsky 2016). Zaorsky, N. G. and E. M. Horwitz (2016). "Brachytherapy for Prostate Cancer: An Overview". Prostate Cancer: Science and Clinical Practice. J. H. Mydlo and C. J. Godec. London, Elsevier/AP: 399-411.

(Zhang 2006). Zhang, Y., H. P. Chan, B. Sahiner, J. Wei, M. M. Goodsitt, L. M. Hadjiiski, J. Ge and C. Zhou (2006). "A comparative study of limited-angle cone-beam reconstruction methods for breast tomosynthesis." **Medical Physics** 33(10): 3781-3795.

(Zhao 2008). Zhao, B. and W. Zhao (2008). "Three-dimensional linear system analysis for breast tomosynthesis." **Medical Physics** 35(12): 5219-5232.

(Zhao 2013). Zhao, H. X., C. X. Xia, H. X. Yin, N. Guo and Q. Zhu (2013). "The value and limitations of contrast-enhanced transrectal ultrasonography for the detection of prostate cancer." **European Journal of Radiology** 82(11): 641-647.

(Zhou 2007). Zhou, J., B. Zhao and W. Zhao (2007). "A computer simulation platform for the optimization of a breast tomosynthesis system." **Medical Physics** 34(3): 1098-1109.

(Zhou 2015). Zhou, W., J. Lu, O. Zhou and Y. Chen (2015). "Evaluation of back projection methods for breast tomosynthesis image reconstruction." **Journal of Digital Imaging** 28(3): 338-345.

(Ziedses des Plantes 1935). Ziedses des Plantes, B. G. (1935). "Seriescopie, een röntgen graphische methode welke het mogelijk maakt achtereenvolgens een oneindig aantal evenwijdige vlakken van het te onderzoeken voorwerp afzonderlijk te beschouwen." **Nederlands Tijdschrift Voor Geneeskunde** 79: 5852-5856.

(Ziedses Des Plantes 1938). Ziedses Des Plantes, B. G. (1938). "Serieskopie. Eine röntgenographische Methode, welche ermöglicht, mit Hilfe einiger Aufnahmen, eine unendliche Reihe paralleler Ebenen in Reihenfolge gesondert zu betrachten." **Fortschr Röntgenstr** 57(1938).

Appendix A: Focal Spot Blur Reduction

Focal spot blurring occurs due to the finite size of the focal spot (e.g., 0.6 mm by 0.6 mm). This results in the bremsstrahlung x-rays produced in the anode emanating not from a point source, as is often assumed, but from a finite area. Larger focal spots decrease image resolution due to the blurring effect. This effect is illustrated in Fig. A.1.

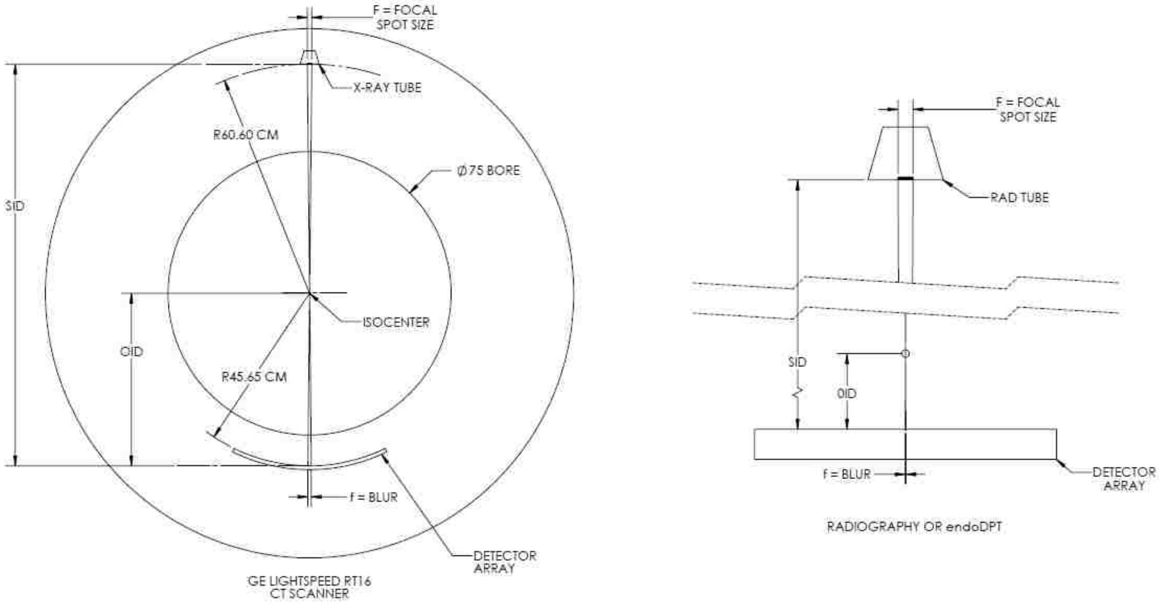

Figure A.1: The focal spot blur effect for CT and for radiography. A large SID and a small OID result in minimal focal spot blur, improving image quality. The size of the focal spot has been increased by a factor of 10 for clarity.

In this example, the CT scanner and x-ray source used in this study are illustrated. A radiopaque point at the location of the prostate using these two imaging modalities is modeled. The focal spot blur is simply the size of the radiographic shadow cast from the radiopaque point due to x-rays emanating from a finite area. In the ideal case, the x-rays emanate from a point and the radiographic shadow is simply a magnified image of the radiopaque point with sharp borders. For a finite sized focal spot, the focal spot blur is an edge gradient, f, is given by

$$f = F * \frac{OID}{SID - OID} = F * \frac{OID}{SOD} \tag{A.1}$$

where F is the size of the focal spot, SID is the source to image plane distance, OID is the object to image plane distance, and SOD is the source to object plane distance. For clarity, Eq. A.1 is given in one dimension. To reduce focal spot blur, imaged anatomy should be placed as close as possible to the image plane (unless magnification is required, as in magnification mammography) and the smallest focal spot should be used (Bushberg 2012).

Table A.1 compares the focal spot blur in one dimension of a typical CT scanner (GE Lightspeed RT16), a typical radiograph of the prostate in the pelvis (GE Proteus XR/a radiography unit), and endoDPT. For endoDPT, x-ray source parameters from the standard radiography unit (GE Proteus XR/a) are used. Focal spot blur would be further reduced by use of a higher resolution x-ray source with a smaller focal spot (the Hologic Selenia Dimensions mammography unit has focal spot sizes of 0.1 mm and 0.3 mm). In this example, it is assumed that the CT detector array is planar rather than curved.

Table A.1: Illustration of focal spot blur in CT, radiography, and endoDPT.

Modality	**F (mm)**	**SID (mm)**	**OID (mm)**	**f (mm)**
CT	1.2	1063	456.5	0.515
Radiography	0.6	1000	100	0.060
endoDPT	0.6	1000	15	0.009

Appendix B: The Logarithmic Transform

For a monoenergetic, parallel photon beam traveling the distance l_t through a material t with photon attenuation coefficient μ_t, the incident signal (the line integral, I) assumes the form

$$I_t = I_0 e^{-\mu_t l_t} \tag{B.1}$$

where I_0 is the incident signal on the pixel if the beam is not attenuated. This is illustrated in Fig. B.1.

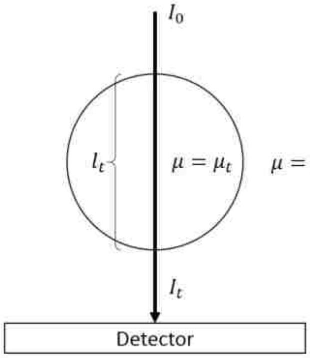

Figure B.1. Attenuation of x-ray beam through material t.

The reconstruction algorithms used in this work reconstruct an approximate attenuation value in the reconstructed image plane through the addition of pixel values from every projection image. Addition of the line integrals to find an approximate attenuation coefficient is not a linear process whereas addition of the logarithmic transformed data (which removes the exponential term) is. Dobbins and Godfrey proved this is true in tomosynthesis, and their result is rederived below (Dobbins 2003).

If the photon beam from the previous example now passes through a non-uniform volume consisting of materials t and b, as shown in Fig. B.2, the incident signal on the detector now becomes

$$I_{t,b} = I_0 e^{-\mu_t l_t - \mu_b l_b} \tag{B.2}$$

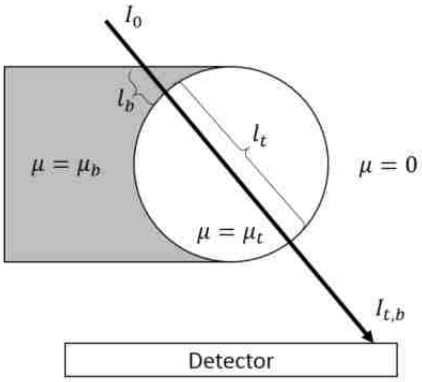

Figure B.2. Attenuation of x-ray beam passing through materials t and b.

Using a backprojection process, an approximate attenuation coefficient can be reconstructed at the intersection of the rays shown in Fig. B.1 and Fig B.2 by simply adding together pixel values where the ray falls on the detector (I_t and $I_{t,b}$). If the projections are added together, the result is

$$P = I_t + I_{t,b} = I_0 e^{-\mu_t l_t} + I_0 e^{-\mu_t l_t - \mu_b l_b} = I_0 e^{-\mu_t l_t}(1 - e^{-\mu_t l_b}) \qquad (\mathrm{B}.3)$$

which is not linear. If the logarithmic transform of the data is taken, the result is linear, given by

$$P = \ln(I_t) + \ln\left(I_{t,b}\right) = \ln(I_0 e^{-\mu_t l_t}) + \ln(I_0 e^{-\mu_t l_t - \mu_b l_b}) = \\ 2\ln(I_0) - 2\mu_t l_t - \mu_b l_b \qquad (\mathrm{B}.4)$$

Appendix C: Carrageenan Gel Recipe Example

The required quantities of ingredients given in Table C.1 for a 500 g batch of the carrageenan gel mixture from Section 4.4.2 are derived below. 500 g of gel was an adequate amount to fill the cavity of the sample holder acrylic plate. The mass of $\mathrm{GdCl_3 \cdot 6H_2O}$ required was calculated using the following equations in conjunction

$$55\frac{\mu\mathrm{mol}}{\mathrm{kg}}\ \mathrm{GdCl_3} * \frac{1\mathrm{kg}}{1000\mathrm{g}} * 500\mathrm{g} = 27.5\mu\mathrm{mol}\ \mathrm{GdCl_3} \tag{C.1}$$

and

$$27.5\mu\mathrm{mol}\ \mathrm{GdCl_3} * 263.61\frac{\mathrm{g}}{\mathrm{mol}}\ \mathrm{GdCl_3} * \frac{1\ \mathrm{mol}}{10^6\mu\mathrm{mol}} = 0.00725\mathrm{g}\ \mathrm{GdCl_3} \tag{C.2}$$

and

$$0.00725\mathrm{g}\ \mathrm{GdCl_3} * \frac{371.70\frac{\mathrm{g}}{\mathrm{mol}}\ \mathrm{GdCl_3 \cdot 6H_2O}}{263.61\frac{\mathrm{g}}{\mathrm{mol}}\ \mathrm{GdCl_3}} = 0.010\mathrm{g}\ \mathrm{GdCl_3 \cdot 6H_2O} \tag{C.3}$$

The mass of the $\mathrm{NaN_3}$ aqueous solution was calculated using

$$0.03\%\ \mathrm{NaN_3} * 500\mathrm{g\ sample} * \frac{1\mathrm{g\ water}}{0.05g\ \mathrm{NaN_3}} = 3\mathrm{g\ aqueous\ solution} \tag{C.4}$$

Table C.1: Amounts of materials required for one 500g batch of phantom material. Agarose, carrageenan, and NaCl we added simply as w/w. The remainder of the mixture was distilled water.

Material	Nominal concentration	Quantity Required for 500*g* w/w
Agarose	1.200% w/w	6.000g
$\mathrm{GdCl_3 \cdot 6H_2O}$	55.0 µmol/kg (of $\mathrm{GdCl_3}$)	0.010g
Carrageenan	3% w/w	15.000g
NaCl	0.291% w/w	1.455g
$\mathrm{NaN_3}$ aqueous solution	0.03% w/w	3.00g
Water	Remainder	474.535g

Vita

Joseph R. Steiner was born in San Diego, California, and was raised throughout much of the United States because his father was active duty military. Joseph attended Buffalo State College, Buffalo, New York, and received a Bachelor of Science degree in physics (summa cum laude) in 2010. Upon graduation, Joseph worked in mechanical engineering for three years. In August of 2013, Joseph enrolled in the Graduate School at Louisiana State University in Baton Rouge to work towards a Doctor of Philosophy degree in Medical Physics. Upon successfully completion of all degree requirements in June of 2018, Joseph will enter the diagnostic imaging medical physics residency program at the Henry Ford Health System located in Detroit, Michigan.